NTNU – Trondheim
Norwegian University of
Science and Technology

Alternative methods of realizing the sea spectrum for time-domain simulations of marine structures in irregular seas

Eivind Bækkedal

Marine Technology
Submission date: June 2014
Supervisor: Jørgen Amdahl, IMT

Norwegian University of Science and Technology
Department of Marine Technology

NTNU
Norges teknisk-naturvitenskapelige universitet
Institutt for marin teknikk

MASTER THESIS 2014

for

Stud. Techn. Eivind Bækkedal

Alternative methods of realizing the sea spectrum for time-domain simulation of marine structures in irregular seas

Alternative metoder for å simulere bølgespektrum for tidsplananalyse av marine konstruksjoner i irregulær sjø

For dynamically sensitive marine structures or marine structures subjected to large displacements the extreme response is often determined on the basis of short term time domain simulation of extreme sea states using the environmental contour line method. A challenge with time-domain analysis is the representation of the sea spectrum. For linear analysis and small displacements is common to use fast Fourier transform (FFT) of the sea spectrum. In order to avoid repetition of the wave history several thousand of uniformly spaced wave components may be needed. For nonlinear time domain simulations the computational requirements of FFT will become prohibitive. An alternative to FFT is to use a few wave components based on equal area principle. This implies that emphasis is placed on the energy rich parts of the wave spectrum. The accuracy of this method must be demonstrated. Using the computer program USFOS it was shown in a previous master thesis work that this method is quite good for floating structures with eigenperiods far away from the energy rich periods of the wave spectrum, but less accurate for structures with eigenperiods in the range of 4-5 seconds. The results depend also on whether the wave forces are mass dominated or drag dominated. It has been suggested that the accuracy may be improved by increasing the subdivision of the wave spectrum in the vicinity of the structure eigenperiod(s).

In USFOS the built-in algorithm for realisation of irregular seas states is based upon linear wave theory and extrapolation of wave kinematics to the instantaneous sea surface (Wheeler stretching). Improved accuracy is obtained by using 2nd order wave theory for surface elevation Wheeler stretching of linear wave kinematics to the surface, and the user may specify the frequency components of the discretised wave spectrum in the input. Most correct is to base wave kinematics completely on 2nd order theory. In USFOS pre-calculated wave kinematics may be represented on a 3D grid and interpolation to actual structure coordinates. It is of interest to compare these methods with respect to extreme response for dynamically sensitive structures.

The following topics should be addressed in the project work:

1. Project revisited. The "FFT" method used as to produce "exact" results shall be re-assessed. It is suggested that similar analysis be performed with software NIRWANA, which uses a true FFT-approach. Convergence of the extreme value estimates shall be investigated by increasing the number of sea state simulation for selected cases. Statistics

of wave elevation, wave particle speed and acceleration shall be recorded. It may also be considered to compare the results with those based on pre-calculated wave kinematics on a 3-D grid.

2. Alternative methods of simulating the sea spectrum shall be investigated: Constant $\Delta\omega$, but random phase angle and constant $\Delta\omega$ and random wave amplitude and phase angle. Further discretization close to structural natural periods may also be considered. It shall be documented that repetition of wave elevation does not occur. Analysis shall be conducted for both drag and mass dominated structure.

3. Investigate alternative procedures to obtain extreme response values, e.g. spool-to-extreme-wave method, dynamic design wave etc.

4. Conduct review of theory for 2^{nd} order wave kinematics to be used in simulation of irregular seas. Develop a MATLAB algorithm for generation of wave kinematics according to this theory.

5. Implement the wave kinematics as a grid wave in USFOS. Compare the kinematics, loads and responses of a bottom fixed cylinder to those of a linear irregular sea. Analysis shall be conducted for both drag and mass dominated structure.

6. An alternative to a complete 2nd order simulation might be to perform a simulation of the linear irregular sea to assess the location of extreme response, and conduct a second order analysis only at a time interval around this point. The dynamics can be set up approximately by simulating the linear sea up to, say 15 seconds before the extreme time. Comparisons between the results and those found under (5) shall be done. Analysis shall be conducted for both drag and mass dominated structure.

7. Conclusions and recommendation for further work

Literature studies of specific topics relevant to the thesis work may be included.

The work scope may prove to be larger than initially anticipated. Subject to approval from the supervisors, topics may be deleted from the list above or reduced in extent.

In the thesis the candidate shall present his personal contribution to the resolution of problems within the scope of the thesis work.

Theories and conclusions should be based on mathematical derivations and/or logic reasoning identifying the various steps in the deduction.

The candidate should utilise the existing possibilities for obtaining relevant literature.

Thesis format
The thesis should be organised in a rational manner to give a clear exposition of results, assessments, and conclusions. The text should be brief and to the point, with a clear language. Telegraphic language should be avoided.

The thesis shall contain the following elements: A text defining the scope, preface, list of contents, summary, main body of thesis, conclusions with recommendations for further work, list of symbols and acronyms, references and (optional) appendices. All figures, tables and equations shall be numerated.

The supervisors may require that the candidate, in an early stage of the work, presents a written plan for the completion of the work. The plan should include a budget for the use of computer and laboratory resources which will be charged to the department. Overruns shall be reported to the supervisors.

The original contribution of the candidate and material taken from other sources shall be clearly defined. Work from other sources shall be properly referenced using an acknowledged referencing system.

The report shall be submitted in two copies:

- Signed by the candidate
- The text defining the scope included
- In bound volume(s)
- Drawings and/or computer prints which cannot be bound should be organised in a separate folder.
- The report shall also be submitted in pdf format along with essential input files for computer analysis, spreadsheets, MATLAB files etc in digital format.
-

Ownership
NTNU has according to the present rules the ownership of the thesis. Any use of the thesis has to be approved by NTNU (or external partner when this applies). The department has the right to use the thesis as if the work was carried out by a NTNU employee, if nothing else has been agreed in advance.

Thesis supervisor

Prof. Jørgen Amdahl

Deadline: June 10, 2014

Trondheim, January 14, 2014

Jørgen Amdahl

Preface

This report is the result of a master thesis conducted at the Department of Marine Technology at the Norwegian University of Science and Technology (NTNU). The scope of work was formulated by Professor Jørgen Amdahl.

This report deals with time-domain simulation of a vertical bottom fixed cylinder with varying eigenperiods exposed to ocean waves. Simplified approaches for simulating the surface and kinematics are first tested for a linear sea realization, and thereafter applied to a complete second order simulation. A review of the theoretical basis, calculation models and program is also given.

It was initially thought to perform studies in both the computer software *USFOS* and *NIRWANA* to verify results and identify discrepancies. This involved some complications, and, as an alternative, some algorithms were developed in *MATLAB* to produce statistical values for comparison with *USFOS* results.

I would like to thank Professor Jørgen Amdahl for his help and guidance during the semester. I am also grateful to Tore Holmås from the *USFOS* support team for help regarding specific functions of *USFOS*. Finally I would thank Professor II Sverre Haver for sharing his knowledge and ideas regarding second order wave kinematics.

Trondheim, June 11, 2014

Eivind Bækkedal

Abstract

For dynamically sensitive structures or marine structures subjected to large displacements the extreme response is often determined on the basis of short term time domain simulation of extreme sea states using the environmental contour line method. A challenge with time-domain simulation is the representation of the sea spectrum. For linear analysis and small displacements it is common to use Fast Fourier Transform (FFT) of the sea spectrum. For non linear simulations the computational requirements of the FFT becomes prohibitive. The purpose of this report is to contribute to the development and verification of simplified methods of realizing the sea spectrum for time domain analysis.

The report consists of three parts. First, a review of theoretical models used in the simulation is performed. It is focused on the probabilistic modelling of ocean waves, methods of establishing kinematics and also various methods of simulating the sea spectrum. From these theories, a *MATLAB* algorithm is created to perform a second order surface realization and estimate the associated kinematics.

The next part consists of a set of introductory studies. The objective was to identify possible methods of reducing the computational efforts of a second order process. Alternative ways of simulating the wave spectrum for a linear process with few frequency components have been investigated, and also the required length of initiation time to avoid transient behaviour. Furthermore a test case for the mentioned *MATLAB* algorithm was performed, and comparisons were made with both linear approximations and by fitting a Stokes V wave to the extreme crest.

In the final part of the work, a short term analysis of quasi-static and dynamic response was carried out for a vertical bottom fixed cylinder, using 30 seed variations. Two different methods for representing the sea spectrum are compared, the FFT and peaked EAP. The simulations were conducted using both linear and second order wave theory, and additionally a combination of these where the second order contributions are only included around the largest linear response, referred to as *Spool-to-Extreme-Linear-Response* (SELR).

From the linear simulations of the various spectral decompositions it is found that the method using an equal area principle with increased representation around the structure's eigenfrequency has best agreement with the commonly applied FFT. While the other few-component methods suffer from large underestimations for some of the cylinders compared to the FFT, the results from this method is consistently in agreement when the number of wave components are larger or equal to 100. This provides a marked reduction in computer efforts as compared to the 1000 component FFT method.

The results from the test simulation of the *MATLAB* algorithm show a kinematic profile and static load calculation which agrees very well with that of a Stokes' V wave. It is also found that the well known weakness of the Wheeler stretching of linear and second order theory are also present for these tests, hence confirming the second order calculations.

The extreme value statistics obtained in the final study show that second order contributions can be neglected for mass loads, but must be included when drag loads are dominating. The alternative methods of simulating a second order process, by peaked EAP or by the SELR, show both very good agreement with the complete second order simulation of the 500 component FFT. The time savings of these methods are substantial, hence these methods could provide an efficient way of simulating second order seas.

Sammendrag

For dynamisk sensitive marine konstruksjoner, eller marine konstruksjoner utsatt for store forskyvninger, blir responsen under ekstreme forhold ofte beregnet ved en korttids tidsplan-analyse ved bruk av konturlinje metoden. En utfordring ved tidsplananalyser er korrekt representasjon av bølgespekteret. For lineære analyser og små forskyvninger er det vanlig å bruke Fast Fourier Transform (FFT) av spekteret. En fin inndeling er nødvendig for å unngå repetisjon av bølgetoget. For ikkelineære analyser vil antallet regne-operasjoner stige, og beregningskravene til FFT vil bli uoverkommelige. Formålet med dette prosjektet er å bidra til utvikling og verifisering av forenklede metoder å realisere bølgespektrum for numerisk simulering i tidsplanet.

Denne rapporten består av tre deler. I den første delen blir det gitt en gjennomgang av teoretiske modeller som brukes i simuleringene. Det er fokusert på probabilistiske modeller for havoverflaten, beregningsmodeller for bølgekinematikk og forskjellige metoder å simulere bølgespekteret. Ut fra de teoretiske modellene er en *MATLAB* algoritme laget for a utføre en andre ordens realisering av havoverflaten og estimere bølge kinematikken.

Den neste delen består av en rekke innledende studier. Formålet var å identifisere mulige metoder å redusere de nødvendige operasjonene for en andre ordens prosess. Alternative måter å simulere bølge-spektrum for en lineær prosess med få frekvenskomponenter er blitt undersøkt, og også den nødvendige initieringstiden for å unngå transient respons. Videre er en test kjøring av textit MATLAB algoritmen utført, og sammenligninget med både lineære tilnærminger og ved å tilpasse en Stokes V bølge til den ekstreme bølgetoppen.

I den siste delen av rapporten, ble en kortsiktig analyse av kvasi-statisk og dynamisk respons utført med 30 forskjellige frø for en vertikal sylinder fast innspent i havbunnen. To forskjellige fremgangsmåter for å representere bølgespekteret sammenlignes, FFT, og EAP med økt fokus rundt egenperioden. Simuleringene ble utført med både lineær og andre ordens teori, og for en kombinasjon av disse, der andre ordens bidrag kun blir inkludert rundt den største lineære respons, kalt *Spol-Til-Ekstrem-Lineær-Respons*(SELR).

Fra de lineære simuleringer av forskjellige spektrale dekomponeringer er det funnet at fremgangsmåten ved hjelp av et konstant areal prinsipp (EAP) med økt representasjon rundt konstruksjonens egenfrekvens har best overensstemmelse med vanlig FFT. De fleste av de forenklede metodene gjør store, ikke konservative, feil i spesifikke simuleringer i forhold til FFT, men denne metoden gir konsistent gode approksimasjoner av FFT når man bruker fler enn 100 komponenter.

Resultatene fra prøve simuleringen av *MATLAB* algoritmen viser en kinematisk profil og kvasi-statisk belastning i overenstemmelse med Stokes V bølgen. Ved sammenligning med Wheeler strekking observeres det at de velkjente feilene denne metoden gjør er tilstede. Disse observasjonene gir grunn til å tro at algoritmen fungerer.

Ekstremverdistatikken for responsen i den endelige studien viser at andre ordens effekter er neglisjerbare når massekrefter dominerer, men er betydelige for drag krefter. De alternative metodene for å simuler andre ordens kinematikken, EAP-p og SELR stemmer meget bra overens med FFT tilnærmingen. Tidsbesparelsene ved disse metodene er store, og kan dermed danne grunnlag for en effektiv måte å utføre simuleringer av andre ordens irregulær sjø.

Contents

List of Figures

List of Tables

Abbreviations

	Full name	Explanation
EAP	Equal Area Principle	A method of obtaining the wave components for time domain simulation, where the wave components have the same variance (amplitudes)
FFT	Fast Fourier Transformation	Here used mainly as a method of obtaining the wave components for time domain simulation where the components have equally spaced frequencies, $\Delta\omega$ is constant.
SELR	Spool to Extreme Linear Response	A method of obtaining response where second order kinematics are included only in a limited area around the largest linear response
PDF	Probability Density Function	
CDF	Cumulative Density Function	

Nomenclature

α_1	Rayleigh damping coefficient [Mass]
α_2	Rayleigh damping coefficient [Stiffness]
α_F	Forristal distribution parameter
α_G	Gumbel parameter
$\bar{\mu}_X^{(n)}$	N'th central moment of pdf
β	Free parameter of the Newmark-β method of numerical integration
β_F	Forristal distribution parameter
β_G	Gumbel parameter
$\boldsymbol{C}$	Damping matrix
$\boldsymbol{K}$	Stiffness matrix
$\boldsymbol{M}$	Mass matrix
$\ddot{r}$	Structural acceleration
Δt	Time increment in time-domain simulation
$\Delta\omega$	Frequency width
$\dot{r}$	Structural velocity
ϵ	Bandwidth parameter
γ	Euler's constant 0.5772
γ	Free parameter of the Newmark-β method of numerical integration
γ_1	Skewness parameter for a stochastic process
γ_2	Kurtosis parameter for a stochastic process
λ	Wave length
λ_i	Damping ratio
μ_x	Mean of the variable x
$\mu_X^{(n)}$	N'th moment of pdf
ω	Angular frequency
ω_{cut}	Truncation frequency of the wave spectrum (also ω_{max})
ω_{m01}	The middle frequency of the spectrum
ω_{m02}	Mean zero crossing frequency of a spectrum
Φ	Gaussian cumulative distribution function

ϕ	Velocity potential
ρ	Density of a fluid $[kg/m^3]$
σ_x	Standard deviation of the variable x
σ_x^2	Variance of parameter x
ε	Phase angle
$\zeta(t)$	Surface elevation
ζ_A	Amplitude of the wave [m]
ζ_{glob}	Global maximum surface elevation
ζ_{loc}	Local maximum surface elevation
c	Crest height
C_D	Drag coefficient
C_M	Mass coefficient
d	Sea depth
$d\omega$	angular frequency increment
E	Total energy
$f(x)$	Probability density function
$F_{X_n}(x_n)$	Cumulative density function of surface maxima x_n
$f_{X_n}(x_n)$	Probability density function of surface maxima x_n
$f_X(x)$	Probability density function for the variable x
g	Gravitational acceleration $[kgm/s^2]$
H_Γ	Transfer function of response quantity Γ
H_S	Significant wave height
k	Wave number
m_i	i'th spectral moment
N_y	Total number of samples
p	Pressure
r	Structural displacement
$R(\tau)$	Autocorrelation function
$S1$	Steepnessparameter
t	Time
T_r	Return period[yr]

T_{m01}	Middle period of spectrum
T_{m02}	Mean zero crossing period of spectrum
T_{SS}	Simulation of sea state [hr]
U_r	Ursell number
x	Rice distribution parameter

1 Introduction

The sea surface is irregular and changes continuously. An exact mathematical representation of it is not possible, but through probabilistic models one can make predictions of the sea a marine structure will be operating in. By using the theory of stochastic processes it is possible to describe the sea, and thus determine certain statistical extreme values for design considerations.

The loads and response of a structure are not only dependent on the characteristic statistical values, such as the most probable highest wave. The period of the loads will significantly impact the response, both as being a parameter in the size of the wave force, and, equally important, because the dynamic response is strongly dependent on the load frequency. It is therefore not sufficient to calculate deterministic extreme values from wave statistics. One of the tools for dynamic calculations is a time-domain simulation where the equation of motion is solved for each time step of the simulation.

A challenge with time-domain analysis is the representation of the sea spectrum. For linear analysis and small displacements it is common to use an inverse *Fast Fourier Transform* (FFT) of the sea spectrum. In order to avoid repetition of the wave history, and to adequately represent the linear sea, several thousand wave components may be needed. For each time step the forces are found from the kinematics of the N components. For simulations of a second order sea with associated kinematics, the computational requirements become prohibitive, as N^2 operations must be performed at every time step. It is therefore desirable to look into alternative methods of representing the sea spectrum with fewer components, and ways to reduce the necessary simulation time.

This report addresses possible ways of simplifying the time domain analysis of a bottom fixed vertical cylinder subject to Morrison's based wave forces, and illustrates the effect in statistics of the surface and extreme loads using a linear and a second order sea surface. A *MATLAB* algorithm to calculate second order kinematics of an irregular wave is created and used for the simulations in this work.

The outline of the report is:

Section 2-4 Review of:

- Existing theories for probabilistic modelling of ocean waves as a linear and second order process.
- Existing theories for obtaining kinematics from linear and second order, regular and irregular waves.
- Methods and theoretical basis for the simulation of irregular sea from a wave spectrum.

Section 6 A description of the computer software *USFOS* used for the simulations and the algorithm created to calculate second order wave kinematics.

Section 7 Three separate introductory studies are performed to investigate the goodness of the simplifications for a linear sea. A fourth introductory study is performed to compare kinematics from a linear, second order and a Stokes V wave fitted to extreme crest.

Section 8 30 realizations of two sea states with different steepness is furthermore conducted for linear, second order and simplified methods of establishing the kinematics.

Some concluding remarks and recommendations are given in Section 9.

2 Review of Statistical Theories on Ocean Waves

The random nature of ocean waves are usually described by probabilistic models. As the statistical variables of the ocean changes much more slowly than the wave elevation one can assume that the surface process is stationary over a short time, typically taken as three hours. The most common approach is therefore to split the overall variation in the surface in two parts, the short term variability of the surface given the environment, i.e. a conditional variability, and a long term variability of the environment. In this section both sources of variability are addressed, with main focus on the short term variability. The current report deals with the simulation of a sea state with given statistical variables, hence the focus is on the short term variability.

2.1 Short term model for ocean waves

Surface elevation data sampled within a short time (or over a large area at a time instant) are found to nearly depict that of a Gaussian process. Due to the simplicity of the Gaussian model it is commonly used to describe the surface process. The surface elevation ζ will then follow the *probability density function* (pdf) given by:

$$f_\zeta(\zeta) = \frac{1}{\sigma_\zeta\sqrt{2\pi}} e^{-\frac{(\zeta-\mu_\zeta)^2}{2\sigma_\zeta^2}} \tag{1}$$

where σ_ζ and μ_ζ are the standard deviation and mean value, respectively, and when introducing $\zeta = 0$ at the mean water level, μ_ζ becomes zero. The only unknown parameter is σ_ζ, i.e. the tendency to have large waves (large deviations from zero). This parameter changes over time, described by the long term variation of the surface. The assumption for short term probabilistic models is that this value, along with other environmental parameters, can be considered constant over a short time interval.

2.1.1 Statistical parameters of a Gaussian process

The properties of a stochastic distribution can be examined by the moments of its probability density function, defined as:

Moments: $\mu_X^{(n)} = \int_{-\infty}^{\infty} x^n f_X(x)dx$

Central Moments: $\bar{\mu}_X^{(n)} = \int_{-\infty}^{\infty} (x-\mu_x)^n f_X(x)dx$

Depending on the distribution the variable follows, a number of the moments must be included to completely describe it. For a Gaussian variable the second order moments are sufficient. The definition of some statistical parameters, their relation to the spectral moments, and their value for the Gaussian distribution (and trends for measured values from actual seas) are presented in the following.

Expectation Value

The *expectation value* is the first order moment of the pdf, representing the *center of gravity* of the distribution. It is given by:

$$\mu_x^{(1)} = E[X] = \int_{-\infty}^{\infty} x f_X(x)dx \tag{2}$$

For a standard Gaussian distribution the mean value is zero.

The expectation value of a sample of a stochastic variable, ie. a sample of the surface elevation, can be estimated by:

$$E[X] = \frac{1}{N}\sum_{i=1}^{N} x_i \tag{3}$$

Variance

The *variance* is the second order central moment of the PDF, and is used to express the spreading of the distribution. It is found as:

$$\sigma_x^2 = \bar{\mu}_x^{(2)} = E[(X - E[X])^2] = \int_{-\infty}^{\infty} (x - \mu_x)^2 f_X(x) dx \tag{4}$$

It can also be expressed by the first and second *moment*, which for the surface elevation reduces to the second moment. An equally important parameter is the standard deviation, σ_x, which is the square root of the variance.

The *unbiased* variance of a stochastic variable, can be estimated by a sample of the variable:

$$Var[X] = \frac{1}{N-1}\sum_{i=1}^{N}(x_i - E[X])^2 \tag{5}$$

Skewness

The third moment yields the *skewness* coefficient. It gives a description of the symmetry of the distribution, being 0 if the distribution is completely symmetric. The parameter, denoted γ_1 is defined as:

$$\gamma_1 = \frac{\bar{\mu}_x^{(3)}}{(\bar{\mu}_x^{(2)})^{3/2}} = \frac{\bar{\mu}_x^{(3)}}{\sigma_x^3} \tag{6}$$

A standard Gaussian distribution will have a skewness parameter of zero. This is however an area where the Gaussian distribution deviates from real surface measurements, as they tend to have a slightly positive skewness, representing higher peaks than troughs.

The skewness of a sample can be estimated by:

$$\gamma_1 = \frac{\frac{1}{N}\sum_{i=1}^{N}(x_i - E[X])^3}{(Var[X])^{3/2}} \tag{7}$$

Kurtosis

The fourth moment defines the *kurtosis*, also named the *flatness coefficient*, which is a parameter of the peakedness of the distribution.

$$\gamma_2 = \frac{\bar{\mu}_x^{(4)}}{(\bar{\mu}_x^{(2)})^2} = \frac{\bar{\mu}_x^{(4)}}{\sigma_x^4} \tag{8}$$

For the standard Gaussian distribution, the kurtosis coefficient $\gamma_2 = 3$. Kurtosis is also commonly presented as excess kurtosis, i.e. related to the kurtosis of the standard Gaussian distribution (3). The kurtosis of a sample is:

$$\gamma_2 = \frac{\frac{1}{N}\sum_{i=1}^{N}(x_i - E[X])^4}{(Var[X])^2} \tag{9}$$

2.1.2 The wave spectrum

If the Gaussian assumption is assumed to hold for the surface elevation, waves can be resolved as a sum of infinite number of harmonic wave components with infinitesimal amplitudes and random phases by virtue of the central limit theorem. The surface elevation of short crested seas, $\zeta(t,x)$ can then be expressed as:

$$\zeta(t,x) = \sum_{i=1}^{\infty} \zeta_{A,i}\, cos(k_i x - \omega_i t + \varepsilon_i) \tag{10}$$

where $\zeta_{A,i}$ is the amplitude, k_i the wave number, ω_i the frequency and ε_i the phase related to the i'th component. The wave number is related to the wavelength λ by $k = \frac{2\pi}{\lambda}$, and to the frequency ω through the *dispersion relation*.

The energy (kinetic+potential) in a wave is completely described by the amplitude of the wave, and the length of the wave. The energy per unit length can be expressed as:

$$E_i = \frac{\rho g \zeta_{A,i}^2}{2} \tag{11}$$

As a structures response to loads are largely impacted by the load frequency, it can be convenient to find the energy at the different frequencies. Combining Eqs. 10 and 11 provides the *wave energy spectrum*, or simply *wave spectrum*.

$$\frac{E}{\rho g} = \sum_{i=1}^{\infty} \frac{1}{2}\zeta_{A,i}^2 = \sum_{i=1}^{\infty} S(\omega_i)\Delta\omega \tag{12}$$

The inverse form of the last equality provides a relation between wave energy and surface elevation. It is frequently used as the basis of simulation of an irregular sea with a predefined wave spectrum, described in detail in Section 4. The amplitude of the i'th wavelet is then expressed by:

$$\zeta_{A,i} = \sqrt{2S(\omega_i)\Delta\omega} \tag{13}$$

It is found that the wave spectra tend to have certain similarities, and standardisations have therefore been estimated. The spectrum can be established based on a few environmental parameters, typically wind speed at a certain height, mean of the 1/3 highest waves (*significant wave height* H_s), mean frequency of the waves or the frequency containing the bulk of the energy (*peak frequency*, ω_p). Some of the most commonly used standardised spectra are the Pierson-Moskowitz (PM) and JONSWAP spectrum presented here:

PM The PM spectrum applies to deep water conditions and fully developed wind sea. It is found through observations of steep front for low frequencies, and an exponentially decay rate for higher frequencies. It is given on the form:

$$S(\omega) = \frac{A}{\omega^5} e^{-B/\omega^4} \tag{14}$$

Where A and B are functions of one or more of the above mentioned parameters, set together in a fashion which maintains the dimension of the wave spectrum (S $[m^2 s]$). A method where the significant wave height and peak frequency are used as parameters is the ISSC spectrum:

$$A_1 = 0.11 H_s^2 \qquad B_1 = \frac{5}{4}\omega_p^4 \tag{15}$$

JONSWAP Based on measurements at shallow waters in the North Sea in 1968-1969, it was observed that the spectrum were more peaked than the PM spectrum allowed. Hence some corrections were introduced. The B is kept similar to the above B_1, while the A is changed, and in practice must be decided through location specific considerations. However, in many practical applications, such as the USFOS software [40], it is simplified, and approximated by:

$$A_2 = \frac{5}{32\pi} H_s^2 T_p (\frac{\omega_p}{\omega})^5 [1 - 0.287 ln(\gamma)] \tag{16}$$

Additionally, the spectrum is peaked by multiplication with:

$$\gamma^{exp\left[-\frac{1}{2}\left(\frac{\omega-\omega_p}{\sigma\omega_p}\right)^2\right]} \tag{17}$$

γ is a peakedness factor, relating the maximum energy in the JONSWAP spectrum to the PM spectrum given by the same A and B coefficients. It is often taken as 3.3. σ is the variance on each side of the spectral peak, typically taken as 0.07 for frequencies below the peak, and 0.09 for frequencies above. Assembling the different coefficients, the total JONSWAP spectrum is given by.

$$S(\omega) = \frac{5}{32\pi} H_s^2 T_p (\frac{\omega_p}{\omega})^5 e^{-\frac{5}{4}(\frac{\omega_p}{\omega})^4} [1 - 0.287 ln(\gamma)] \gamma^{e^{\frac{(\frac{\omega}{\omega_p}-1)^2}{2\sigma^2}}} \tag{18}$$

This form of the JONSWAP spectrum will hence be a three parameter spectrum, with the γ in addition to H_s and T_p. As the multiplication term in Eq. 17 is larger than 1 for all frequencies, the resulting spectrum will have more energy than the initial PM spectrum from A and B. The underlying PM spectrum is hence not a good approximation for a PM spectrum with the given H_s and T_p.

A comparison between these spectra are given in Figure 1, where the environmental parameters are the same for both PM and JONSWAP. Note the difference in the underlying PM for the JONSWAP spectrum and the ISSC version of the PM spectrum. The peak of the JONSWAP spectrum is 3.3 times as high as the underlying PM spectrum.

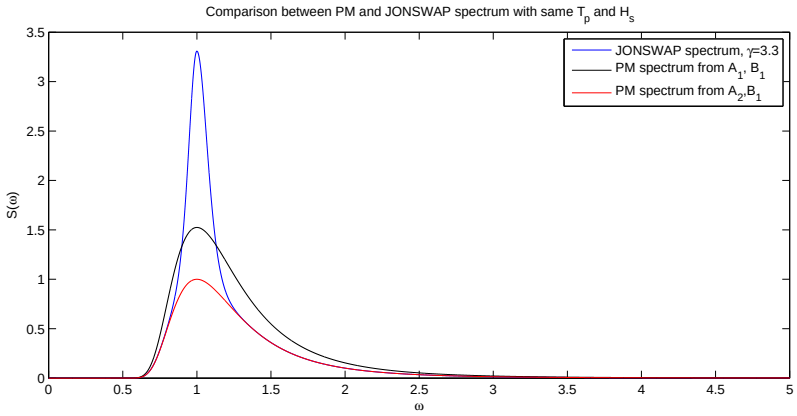

Figure 1: JONSWAP, underlying PM and *correct* PM for $H_s = 12m$ and $T_p = 14s$

These spectra presented are *single peaked*, and are used to describe *local wind* generated seas. In open waters *swell* seas must also be accounted for, and can not be adequately described by

the single peaked spectra. Swell sea is basically waves that are generated far from the location, and are not directly influenced by the wind system at the site. These waves tend to have long wavelengths, which results in a second peak in the low frequency part of the wave spectra. An example of such a *double peaked* standard wave spectrum is the Torsethaugen. For information regarding this spectrum, sea e.g. [30]

Similarly to the moments of the probability density function, moments of the wave energy spectrum can be established and used to find important information of the surface process:

$$m_n = \int_0^\infty \omega^n S(\omega) d\omega \tag{19}$$

Some important values can be established through these moments, such as:

m_0 is the variance of the sea state, equal to those of the Gaussian estimates $m_0 = \sigma_\zeta^2$

$H_S = 4\sqrt{m_0} = 4\sigma_\zeta$ is the height of the 1/3 highest waves, and an important parameter for describing irregular waves

$\omega_{m01} = \frac{m_1}{m_0}$ is the mean frequency of the spectrum.

$T_{m01} = \frac{2\pi}{\omega_{m01}}$ is the mean period of the spectrum.

$\omega_{m02} = \sqrt{\frac{m_2}{m_0}}$ is the mean zero-up-crossing frequency of the spectrum. It is important for calculating the total number of global maxima in a time interval

$T_{m02} = \frac{2\pi}{\omega_{m02}}$ is the mean zero-up-crossing period of the spectrum.

$T_{m24} = 2\pi\sqrt{\frac{m_2}{m_4}}$ is the mean period between local maxima. The difference between T_{m02} and T_{m24} describes how narrow banded a surface process is,i.e. the tendency to have several peaks between each zero crossing.

The wave spectrum $S(\omega)$ can be set up directly from the probability density function of the surface process, through a Fourier transform of the *autocorrelation function* $R(\tau) = E[\zeta(t) \cdot \zeta(t+\tau)]$, i.e.:

$$S_t(\omega) = \int_{-\infty}^\infty R(\tau) e^{-i\omega\tau} d\tau \tag{20}$$

Here $S(\omega)$ is defined as both positive and negative frequencies, and the physical realisable spectral density is therefore $S(\omega) = 2S_t(\omega)$, where ω is strictly positive.

2.1.3 Distribution of surface maxima

In many practical applications it is of interest to find the distributions of the maxima (or minima) of the surface process $\zeta(t)$. A *local* maxima or minima is a point where the derivative of the surface process is zero, denoted ζ_{loc}. For a broad banded process there might be several local maxima and minima between each zero-up-crossing, the largest of these the *global* maxima, ζ_{glob}. Assuming that the process is Gaussian, a theoretical model for the local maxima has been derived by Cartwright and Longuet-Higgins [3], and results in a Rice distribution:

$$f_X(x) = \frac{1}{\sqrt{2\pi}}\epsilon \cdot e^{-\frac{1}{2}(\frac{x}{\epsilon})^2} + \sqrt{1-\epsilon^2}x \cdot e^{-\frac{1}{2}x^2} \cdot \Phi(\frac{x}{\epsilon}\sqrt{1-\epsilon^2}) \tag{21}$$

where:

$$\begin{aligned} x &= \frac{\zeta_{loc}}{\sigma_\zeta} \\ \epsilon^2 &= 1 - \frac{m_2^2}{m_1 m_4}, \qquad 0 \leq \epsilon \leq 1 \end{aligned} \tag{22}$$

x is the standardised local maxima, i.e. scaled using the standard deviation of the surface process (σ_ζ). In the following one will continue to use the standardised process, the corresponding expectations are found by multiplying with the standard deviation, σ_ζ. ϵ is a bandwidth parameter describing the tendency to have several peaks between each zero crossing. The extremities, $\epsilon = 0$ and $\epsilon = 1$ results in the Gaussian and Rayleigh distributions respectively. Φ is the Gaussian cumulative distribution. The m_i are given by the wave spectrum described in the previous section. The mean and variance of x is found by the moments of Eq. 21:

$$\begin{aligned} \mu_x &= \sqrt{\frac{\pi}{2}(1-\epsilon^2)} \\ \sigma_x^2 &= 1 - \left(\frac{\pi}{2} - 1\right)\left(1-\epsilon^2\right) \end{aligned} \tag{23}$$

The largest maximum in a train of waves is an important value in engineering. Assuming that all individual maxima x_i are identically distributed and statistically independent (which is a slightly conservative assumption), the cumulative distribution of the largest of N local maxima, denoted x_N are found as:

$$F_{X_N}(x) = \Pi_{i=1}^N P[x_i \leq x] = (P[x_i \leq x])^N = [F_X(x)]^N \tag{24}$$

The x_N is asymptotically Gumbel distributed as N approach infinity. Cartwright and Longuet Higgins, has shown that the mode, expectation value and standard deviation of the largest among N local maxima, when N becomes large are given by:

$$\begin{aligned} Mode &= \sqrt{2ln(\sqrt{1-\epsilon^2}\cdot N)} \\ \mu_{x_N} &= \sqrt{2}\left[\sqrt{ln(\sqrt{1-\epsilon^2}\cdot N)} + \frac{\gamma}{2\sqrt{ln(\sqrt{1-\epsilon^2}\cdot N)}}\right] \\ \sigma_{x_N} &= \frac{\pi}{\sqrt{6}}\frac{1}{\sqrt{2ln(\sqrt{1-\epsilon^2}\cdot N)}} \end{aligned} \tag{25}$$

Where γ is the Euler's constant, =0.5772...

For the Rice model, N is the number of *local peaks*, given by the period T_{m24}, not to be confused with the number of zero-up-crossings associated with the period T_{m02}.

The error of the expectation value is of the order $O[(ln(\sqrt{1-\epsilon^2}\cdot N))^{-\frac{3}{2}}]$.

If $\zeta(t)$ is assumed to be narrow banded, i.e only one peak between each zero-crossing ($\epsilon \longrightarrow 0$),i.e. $\zeta_{loc} = \zeta_{glob}$, the distribution of maxima assumes the Rayleigh model.

$$f_X(x) = xe^{-\frac{x^2}{2}} \tag{26}$$

The corresponding mode, mean and variance are found from Eq. 23, using $\epsilon = 0$. Similar expressions to Eq. 25 can be assembled for the narrow banded waves, with N the number of zero crossing waves, and $\epsilon = 0$. It can be shown that the extreme amplitudes x_N predicted from both Rayleigh and Rice distributions coincide. Denoting N the number of local maxima, and N_0 the number of global maxima (or zero crossing waves), one can show that the modes (or $exp(Mode^2/2)$) are the same:

$$\begin{aligned} &Rice: && \sqrt{1-\epsilon^2}\cdot N = \sqrt{1-\left(1-\frac{m_2^2}{m_0 m_4}\right)}\cdot\frac{t}{T_{m24}} = \sqrt{\frac{m_2^2}{m_0 m_4}}\cdot\frac{t}{2\pi\sqrt{\frac{m_2}{m_4}}} = \frac{t}{2\pi\sqrt{\frac{m_0}{m_2}}} \\ &Rayleigh: && N_0 = \frac{t}{T_{m02}} = \frac{t}{2\pi\sqrt{\frac{m_0}{m_2}}} \end{aligned} \tag{27}$$

The expected extremes of a simulation is therefore uniquely defined by the length t, mean zero-up-crossing period T_{m02} and standard deviation of the surface process σ_ζ (or equivalent $H_s = 4\sigma_\zeta$). The short term distribution of extreme surface elevation can therefore be considered conditional on the environmental parameters T_{m02} and H_s when the surface process is assumed Gaussian.

Due to the simplicity of the Rayleigh distributions, and the complexity of handling high order spectral moments (as the integration limits will influence the size of high order spectral moments, such as m_4), one often assumes the Rayleigh model. The extreme and standard deviation is, expressed by N_0:

$$\begin{aligned} Mode &= \sqrt{2ln(N_0)} \\ E\left[x_N\right] &= \sqrt{2}\left[\sqrt{ln(N_0)} + \frac{\gamma}{2\sqrt{ln(N_0)}}\right] \\ \sigma_{x_n} &= \frac{\pi}{\sqrt{6}}\frac{1}{\sqrt{2ln(N_0)}} \end{aligned} \tag{28}$$

If one wants the largest deviation from surface mean, i.e. either positive or negative, the number of occurrences N_0 must be taken as twice the mean zero up-crossing waves.

Under the Rayleigh assumption the wave heights, i.e. the distance between consecutive troughs and peaks will also follow the Rayleigh model, and be given by $H = 2x$. The standardised distribution of wave heights will then be of the form:

$$F_H(h) = 1 - e^{-\left(\frac{h^2}{8}\right)} \tag{29}$$

And, consequently, the expected largest (standardized) is found as twice the surface elevation

$$H_{max} = 2x_N \tag{30}$$

When using this assumption on a broad banded process, the results will be somewhat conservative. The reason for this is that the largest peak is not necessarily followed by the largest trough. Other models exist which better depict the real broadband surface, two of which are discussed in the following

2.1.4 Two higher order models for the surface process

The real surface does not follow a Gaussian distribution therefore the maxima does not follow a Rayleigh model. The Gaussian surface can be considered as the first order approximation of the irregular sea, this will be discussed in Sections 3 and 4. The real surface tends to have larger crests, and shallower troughs. A result is that the trough and crests does no longer follow the same probabilistic models. For most structural considerations the most important parameter is the the expected largest crest height, c_{max}, therefore two models to account for the higher order terms of the crest are presented here.

2.1.4.1 Modification of the Rayleigh model

The Rayleigh model tend to predict extreme crest accurately when the significant wave height is low, i.e. the waves are not steep. This is not the case for, say, the 100 year return period sea state. Stansberg [28] presented a modification to the Rayleigh model to account for the increased steepness, introducing a steepness parameter of the sea state, k_pc, where k_p is the wave number corresponding to the spectral peak period, and c is the standardized crest height found through the Rayleigh model, Eq. 28 (i.e. $c = x$). The correction term is based on second-order regular wave theory, where the total crest height is divided in a linear and a second order correction term: $c' = c(1 + 1/2k_pc)$. This is accounted for by a modified Rayleigh distribution model for short-time statistics of nonlinear peaks c' [28]:

$$F(c') = 1 - e^{-\frac{[c'(1-1/2k_pc)]^2}{2}} \tag{31}$$

The extremes of N_0 crests can be found and expressed in terms of the extreme Rayleigh crest height, c_r as [28]:

$$\mu_{c_{max}} \quad = c_r\,(1 + 1/2k_pc_r) \tag{32}$$

The simple equation have been shown by Stansberg [28] to compare well with second order simulations.

2.1.4.2 Forristall crest height model

Through a large number of simulations for various values of sea state steepness and depths, Forristall [8] established a probabilistic model for the crest heights. The model is a 2 parameter Weibull model conditional on h_s and t_{m01}:

$$F_{C|H_s,T_{m01}}(c|h_s, t_{m01}) = 1 - e^{-\left(\frac{c}{\alpha_F h_s}\right)^{\beta_F}} \tag{33}$$

Where the Forristall parameters α_F and β_F for long crested seas are:

$$\begin{aligned} \alpha_F &= 0.3536 + 0.2892 \cdot S_1 + 0.1060 \cdot U_r \\ \beta_F &= 2 - 2.1597 \cdot S_1 + 0.0968 \cdot U_r^2 \end{aligned} \tag{34}$$

Where S_1 and U_r are the steepness parameter and Ursell number, respectively:

$$S_1 = \frac{2\pi}{g}\frac{h_s}{t_{m01}^2} \qquad U_r = \frac{h_s}{d^3 k_{m01}^2} \tag{35}$$

With t_{m01} the mean wave period, calculated from m_0 and m_1, and k_{m01} is the associated wave number, d is the depth. For infinite depth the Forristall parameters are nearly the same for short crested seas, Haver [10].

The crests and troughs does no longer follow the same model, and the height can not be considered as $2 \cdot c$. Forrstall established therefore a distribution of the wave heights h which more correctly models the narrow banded seas:

$$F_{H|H_s}(h|h_s) = 1 - e^{-2.263\left(\frac{h}{h_s}\right)^{2.126}} \tag{36}$$

While being a bit more tedious to work with, the Foristall crest height model give a better prediction of the real surface, with crests modelled correctly to the second order. The crest heights predicted using Foristall is larger than those one get from the Rayleigh or Rice models, which are non-conservative compared to the real surface. No second order trough model is presented here, as troughs in general are less important. One can assume that the trough will be slightly over predicted by the Rayleigh and Rice models. One can find the mode of the largest of N_0 crests as the value superseded once every n times:

$$F_C(c) = 1 - \frac{1}{N_0} = \left(1 - e^{-\left(\frac{c}{\alpha_F h_s}\right)^{\beta_F}}\right) \quad \leftrightarrow \quad c_n = h_s \cdot \alpha_F \cdot ln(N_0)^{\frac{1}{\beta_F}} \tag{37}$$

Here N_0 represent the number of zero-up-crossings, corresponding to T_{m02}. The Forristall model will yield an extreme value distribution that follows a Gumbel model, similar to the Rayleigh and Rice. Knowing the mode one can find the expected maximum and standard deviation (standardised by using $H_s = 4\sigma_\zeta$ and divide by σ_ζ), see e.g. [18]:

$$\begin{aligned} \mu_{c_{max}} &= 4\alpha_F \left[ln(N_0)^{\frac{1}{\beta_F}} + \frac{\gamma}{\beta ln(N_0)^{\frac{\beta_F - 1}{\beta_F}}} \right] \\ \sigma_{c_{max}} &= \frac{\pi}{\sqrt{6}} \cdot \frac{4\alpha_F}{\beta_F \left[ln(N_0)\right]^{\frac{\beta_F - 1}{\beta_F}}} \end{aligned} \tag{38}$$

A special case of this is when $S_1 = U_r = 0$, the Rayleigh distribution appears, and its extremes and standard deviations can be found from Eqs. 25 or 28 with the same outcome.

There exist several other models for higher order seas, but the predictions differ considerable. The Forristall model have been seen to fit well with observed measurements, and will therefore be used when predicting second order extremes. Nevertheless one should beware of the fact that at the largest crests even higher order effects might influence the problem significantly, and a safety adjustment should therefore always be introduced in the calculations.

2.1.5 Gumbel extreme value distribution

Any exponential distribution of a single event, such as normal, exponential, Weibull, Rayleigh, Rice, Forristall etc., will result in the Gumbel extreme distribution. Consequently, the extreme values of the surface elevation follows asymptotically a Gumbel distribution. The cdf and pdf of the Gumbel model of extreme value x_n are given in Eqs. 39 and 40.

$$F_{X_n}(x_n) = e^{-e^{-\frac{(x_n-\alpha_G)}{\beta_G}}} \tag{39}$$

$$f_{X_n}(x_n) = \frac{1}{\beta_G} e^{-\frac{(x_n-\alpha_G)}{\beta_G} - e^{-\frac{(x_n-\alpha_G)}{\beta_G}}} \tag{40}$$

Where α_G and β_G are the Gumbel parameters, given by:

$$\beta_G = \frac{\sigma_{x_n}\sqrt{6}}{\pi}, \qquad \alpha_G = \mu_{x_n} - 0.5772 \cdot \beta_G \tag{41}$$

μ_{x_n} and σ_{x_n} are the expected value and standard deviation, respectively, of the largest among n waves, given in Eq. 25.

The Gumbel model is also frequently used to depict the distribution of a given response quantity from a sample of extremes, when the underlying distributions are not theoretically available. The mean and variance of the samples of extreme response are used to calculate the values, and the resulting distribution is plotted in a *Gumbel probability paper*, along with the cumulative distribution of the samples. A probability paper is a graph with the axis tuned so as to yield a straight line if the distribution is correct. For the Gumbel distribution, this is found by linearising Eq. 39:

$$-ln(-ln(F)) = \frac{(x-\alpha_G)}{\beta_G} \tag{42}$$

The Gumbel probability paper is therefore a graph with $-log(-log(F))$ on the y-axis and the x (surface max, response max, etc.) on the x-axis. The sample cumulative density function is found as :

$$F_i = \frac{i}{1+N} \tag{43}$$

Where N is the total number of samples of x, and i runs from one to N. The F_i's are plotted against the sorted x's, in the Gumbel paper, and if the x's follow a Gumbel distribution, should result in a nearly straight line.

There are, however, no clear practise for how large deviations from the straight line should be accepted, and the method is therefore subjective. Nevertheless, the method presents a simple and effective tool for preliminary assessment of a tentative model, and is therefore frequently used in practical applications.

2.2 Long term variation and estimation of extreme response

The theories discussed above are in the family of *short term* wave statistics. The assumption that the sea environment is a stationary process with constant statistical properties is only valid for short time periods (less than three hours). These values will vary significantly throughout a structures lifetime and this variability is a vital part of assessing the environmental loads and hence the extreme responses. The short-term distribution of wave or crest height can be considered conditioned to the governing environmental parameters, typically taken as H_s ant T_p. In order to find the cumulative long term distribution of wave heights, used for instance in calculating amplitudes of a certain return period (typically 100 or 10 000 year), one must include the variation in sea characteristics through a *joint probability density function* (jpdf). It is convenient (albeit not strictly necessary) to assume that the environmental parameters is stationary over three hours, and use the three hour maximum crest height as the stochastic variable. The long term cdf of crest height is then given by:

$$F_{C_{3h}}(c) = \int_{h_s}\int_{t_p} \overbrace{F_{C_{3h}|H_s,T_p}(c|h_s,t_p)}^{\text{Short term variation}} \cdot \overbrace{f_{H_s,T_p}(h_s,t_p)}^{\text{Long term variation}} \, dh_s dt_p \tag{44}$$

Where f_{H_s,T_p} is the jpdf of H_s and T_p. The jpdf is typically set up based on measured or hindcast data of the specific field. Several probabilistic models have been found, with varying fits. One which usually gives a very good fit for H_s to observations is the hybrid model, presented in e.g. Haver [10]. The model consists of a Lognormal distribution of H_s up to a certain threshold, and follows a Weibull model in the upper tail. The distribution of T_p are assumed conditional on H_s, and follow a Lognormal distribution, with parameters dependent on H_s. The pdf's along with example parameters are given in Appendix B.

The conditional three hour crest height is typically found by assuming one of the previously discussed short term models for an individual crest (i.e. Forristall, Rayleigh, etc.), and assume all crests as independent variables drawn from that distribution, i.e.

$$F_{C_{3h}|H_s,T_p}(c|h_s,t_p) = \left(F_{C|H_s,T_p}(c|h_s,t_p)\right)^{N_0(h_s,t_p)} \tag{45}$$

Where N_0 is the total number of zero up-crossing waves in the sea state characterized by t_p and h_s. It is found by dividing the simulation length with the mean zero up-crossing period (found from the two first spectral moments), i.e. $N_0 = \frac{10800}{T_{m02}}$.

With the long-term model assembled, the extreme crests with a return period of n_y years can be found by relating the y-year probability to the three-hour distribution function, by:

$$1 - F_{C_{3h}}(h) = \frac{1}{\frac{n_y \cdot 365 \cdot 24}{3}} \tag{46}$$

Using the Eq.'s presented in this section one can find the y-year crest height, and similarly, the y-year wave height if a proper wave height model is used instead of crest height.

2.2.1 Methods of predicting extreme loads

In addition to the extreme waves a structure will experience, one is typically also interested in the extreme response in terms of forces, moments and motions. The response of a structure is not necessarily related to the largest waves, as they also are influenced by the dynamics in terms of excitation periods, and, if consisting of several members, cancellation of forces on the different parts. Other environmental parameters will also impact the response, such as currents and wind. One can set up a similar equation to that in Eq. 44 for a response quantity $X_{\Gamma_{3h}}$ exhibited to environmental variables H_s and T_p:

$$F_{X_{\Gamma,3h}}(x) = \int_{h_s} \int_{t_p} F_{X_{\Gamma,3h}|H_s,T_p}(x|h_s,t_p) \cdot f_{H_s,T_p}(h_s,t_p) dh_s dt_p \tag{47}$$

One can include other parameters than the significant wave height H_s, peak period T_p, such as current U_c, wind U_w, tide, etc. These are, however, most commonly taken as the values with a certain return period, as specified by NORSOK [23] While the long term variability of the environmental parameters can be estimated from measurements, accurate theoretical models for the short term variability can not allways be established. Simplified methods are often used to establish the extreme structural behaviour with a return period of y years.

2.2.1.1 Design wave method

For structures with small dynamic effects, a design wave approach can be conducted. The idea is that the structure acts static, and the critical load is hence found at the highest crest. The structure investigated is then exposed to a regular wave with crest (or wave-) height found from 44, and period found from the Lognormal distribution of T_p, see e.g. NORSOK N-003 for how to decide the period(s) to be used. Additionally one can include the y-year current, wind etc. The most common wave profile for this method is the Stoke's V, but other models, such as Dean's stream function must be used at very shallow waters.

A quasi-static solution of the equation of motion is conducted as the wave passes through the structure, and the largest response is taken as the y-year extreme value. The limited amount of dynamics is introduced by estimatingthe *dynamic amplification factor*(daf) for a simplified one degree of freedom system with corresponding mass and stiffness. This approach is used in connection with jackets with very low eigenperiods (< 2 sec), where the dynamic amplification factor is than 1.1.

If one shall conduct a design wave approach on structures with more dynamics than this, one must compute the *equivalent dynamic amplification factor*, typically taken as the ratio of the y-year dynamic response of time domain simulations to the y-year static response. The dynamics are introduced as an *equivalent acceleration field* to maintain the amplification of certain response and displacement quantities.

2.2.1.2 Long term analysis (all sea states) -linear system

Certain response values can be considered as having a linear nature, i.e. there exist a linear relation between response and wave amplitude for all frequencies. It will then exist a deterministic relation between the wave process and response, a *transfer function*, $H_\Gamma(\omega)$. The *response spectrum* can be assembled when the transfer function and wave spectrum are known:

$$S_\Gamma(\omega; h_s, t_p) = |H_\Gamma(\omega)|^2 \cdot S_\zeta(\omega; h_s, t_p) \tag{48}$$

Similarly to the wavespectrum, important characteristics such as the variance of the response σ_Γ and mean zero-up-crossing period $T_{m02,\Gamma}$ can be found from the spectral moments, see formulas in Section 2.1.2.

It can be shown that if the underlying wave field can be assumed Gaussian, then the response will also follow a Gaussian distribution. The individual response maxima can hence be reasonably well described by a Rayleigh model, i.e.

$$F_{X_\Gamma|H_s,T_p}(x) = 1 - exp\left[-\frac{1}{2}\left(\frac{x}{\sigma_\Gamma(h_s,t_p)}\right)^2\right] \tag{49}$$

From the distribution of individual response maxima, the distribution of the three-hour extreme $F_{X_{\Gamma,3h}|H_s,T_p}(x)$ can be found. This distribution can be directly inserted in Eq. 47, and used to establish the long term distribution of $F_{X_\Gamma,3h}$. From this distribution, the y-year response value can be found directly. Due to correlation between adjacent waves and correlation between adjacent sea states (i.e. these are not independently distributed in reality), the long term analysis using the all-sea states approach lead to an overestimation of the y-year extreme by 3-5 %, see e.g. Haver [10].

2.2.1.3 Long term analysis (all sea states) - Non linear system

An important condition for the previous mentioned relations to be true is that the response quantity must be of a linear nature, i.e. linear relation between response and wave amplitude, and a linear mechanical system. Many marine applications does not fulfil these requirements, as for instance a slender, drag dominated, structure will have a quadratic relation between force and wave. Additionally, structures which have large motions and hence have a damping and stiffness of non linear nature will not satisfy these criteria. The short term model presented previously is hence not valid for these applications. In order to use Eq. 47, new models of the short term distribution must be found.

A way to establish these (conditional) distributions is to run k 3-hour simulations for a large number of different sea states (h_s/t_p combinations). From each of these k-simulations one extracts the extreme value, and fit these to some continuous distribution. The Gumbel model described in 2.1.5 provides a good fit for many response quantities. The number k must be relatively large, around 20-40, to limit the statistical uncertainties related to stochastic time domain simulations.

From these j sea states, one have j pairs of the Gumbel parameters α_j and β_j:

$$\beta_j(h_{s,j}, t_{p,j}) = \frac{\sigma_{X_{\Gamma,3h}}\sqrt{6}}{\pi}, \qquad \alpha_j(h_{s,j}, t_{p,j}) = \mu_{X_{\Gamma,3h}} - 0.5772 \cdot \beta_j(h_{s,j}, t_{p,j}) \tag{50}$$

Interpolation between these j values will provide continuous parameters, response surfaces, over the whole h_s/t_p domain, i.e. $\alpha(h_s, t_p)$ and $\beta(h_s, t_p)$. One can then assemble the continuous conditional cumulative thee hour short term distribution of the response quantity:

$$F_{X_{\Gamma,3h}|h_s,t_p}(x|h_s,t_p) = e^{-e^{-\frac{(x-\alpha(h_s,t_p)}{\beta(h_s,t_p)}}} \tag{51}$$

Using this short term distribution in Eq. 47 can provide a good estimate of the y-year extreme response, provided there is no abrupt change in load nature (i.e. wave-deck impact). If the deviations from the Gumbel model is too large, one must consider if the extreme response quantity follow a different distribution.

If one must conduct a significant amount of either costly model tests or computationally expensive time domain simulations (i.e. second order waves and non linear structural behaviour), this procedure become prohibitive. For such systems, the environmental contours may represent a convenient approach.

2.2.1.4 The Environmental Contour line method

In the previous section a way to find the long term extreme response using simulation of several sea states were described. In the *environmental contour line* approach, the simulations are limited to a single sea state. It assumes that the short- and long term variation can be decoupled, and use a reliability method to establish contours of the environmental parameters with a return period of y-years. The method is described briefly here, for detailed information see e.g. Winterstein et al. [36].

Assuming that the distribution of H_s and T_p are given by $F_{H_s}(h_s)$ and $F_{T_p|H_s}(t_p|h_s)$, the Rosenblatt transformations into the standard Gaussian space can be described by:

$$\begin{array}{lcll} F_{H_s}(h_s) & = & \Phi(u_1) & \longleftrightarrow \quad u_1 = \Phi^{-1}(F_{H_s}(h_s)) \\ F_{T_p|H_s}(h_s) & = & \Phi(u_2) & \longleftrightarrow \quad u_2 = \Phi^{-1}(F_{T_p|H_s}(t_p|h_s) \end{array} \tag{52}$$

Where Φ is the standard normal distribution, and the transformed variables u_1 and u_2 are independent. The contour lines are determined so that all 3-hour stationary sea states on the contour lines are of the same annual exceedance probability, q. This value is transformed to the standard Gaussian space as:

$$\Phi(\beta) = 1 - q \quad \longleftrightarrow \quad \beta = -\Phi^{-1}(q) \tag{53}$$

The contour lines satisfying an annual probability of exceedance of q in the Gaussian space will be circles, satisfying $\sqrt{u_1^2 + u_2^2} = \beta$. Transforming the Gaussian variables back to physical space, will yield the combinations of H_s and T_p satisfying q annual exceedance probability. The contour lines in standard Gaussian space and physical space are given in Figure 2. Here the hybrid model are adopted for H_s and Lognormal for the conditional distribution of T_p. The parameters in the distributions are found using the Nora10 hindcast data in [44], and presented can be found in Appendix B.

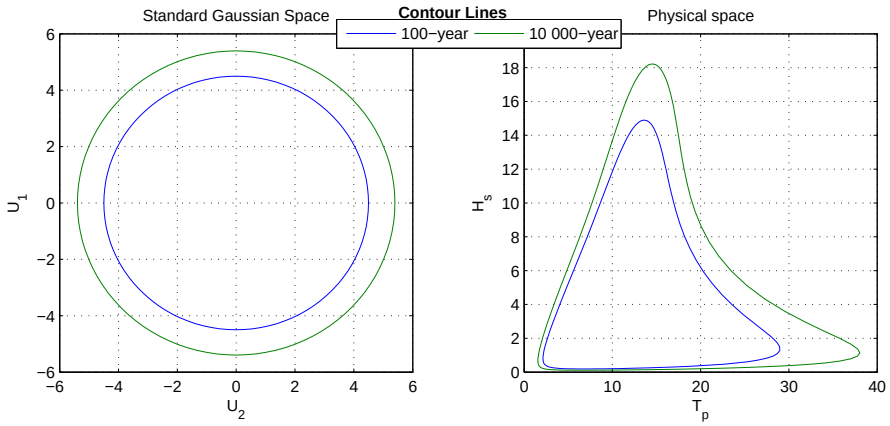

Figure 2: Contour lines for environmental parameters with 100 and 10 000 year return period

From the contour lines one can pick out some seastates which one expects the extreme response to occur, and do 4-5 test simulations of these. Based on these results one picks the worst case, and performs 20-30 more time domain simulations or model tests. These are furthermore fit to an extreme value distribution (typically Gumbel). Because of the neglected short-term variability, one must use a higher percentile for the design value. Typically NORSOK recommends an 85-90 percentile for *ultimate limit state* (ULS, 100 year return period) and 90-95 percentile for *accidental limit state* (ALS, 10 000 year return period). Alternatively one could increase the return period to account for this neglected variability. Regardless, the applied percentile should be verified with some sort of long term simulations.

2.2.1.5 Concluding remarks

Some of the most common methods of finding the extreme response value in y-years have been presented in this section. Many more exist, such as the reliability method and peak over threshold method. The latter is common for hurricane seas, where the extreme response is governed by the occurrence of some few hurricanes. For more information about these, or more in depth information regarding the previously described methods, it is referred to Haver [10].

Many of the methods described include some sort of numerical time domain analysis, where the structure is subjected to irregular waves. For complex systems, these simulations might be tedious and complex, in particular if higher order models for both wave loads and structural behaviour are necessary. This is the motivation for the studies performed later in this report. First, however, it is necessary to understand the complexity of applying a full set of second order wave-particle kinematics to a time domain simulation of irregular sea.

3 Review of Wave theories

A review of existing theories for establishing wave particle kinematics in an undisturbed regular and irregular wave field are here given. Establishing accurate kinematics are paramount for the goodness of force calculations on a marine structure. For small volume structures, that is structures where the wavelength is much larger than the structures dimensions, the forces are found directly from the kinematics of the undisturbed wave field. One can disregard the structure itself, and set up the wave kinematics by solving the wave-wave interaction problem. In this section the solution to the boundary value problem is given for a first and second order regular and irregular wave field. Furthermore specific higher order models which are typically used in combination with a design wave method is given.

The theory of second order wave-wave interaction was first discussed for deep waters by Longuet-Higgins [19] and later extended to arbitrary depth and directional seas by Sharma and Dean [**?**]. The equations and solutions presented in this chapter is a summary of the mentioned papers.

3.1 Governing equations

To correctly describe the sea environment, certain physical conditions must be satisfied. If the effects of viscosity and turbulence can be regarded as small, the fluid can be considered as irrotational, and the flow can be well described by a velocity potential ϕ. The velocities u, v and w can then be described in terms of the gradients of the velocity potential:

$$(u, v, w) = \left(\frac{\partial \phi}{\partial x}, \frac{\partial \phi}{\partial y}, \frac{\partial \phi}{\partial z}\right) \tag{54}$$

As water is incompressible, i.e. $\nabla \cdot \vec{V} = 0$, it follows that the velocity potential must satisfy the Laplace equation

$$\nabla \cdot \vec{V} = \frac{\partial^2 \phi}{\partial x^2} + \frac{\partial^2 \phi}{\partial y^2} + \frac{\partial^2 \phi}{\partial z^2} = \nabla^2 \phi = 0 \tag{55}$$

where $-d \leq z \leq \zeta$, and $-\infty \leq x, y \leq \infty$

In addition to Eq. 55, certain boundary conditions are needed to maintain the physical problem. An illustration of the boundary value problem, along with coordinate systems and visualisations of some of the parameters are shown in Figure 3. It is used a regular sine wave to illustrate the wave parameters.

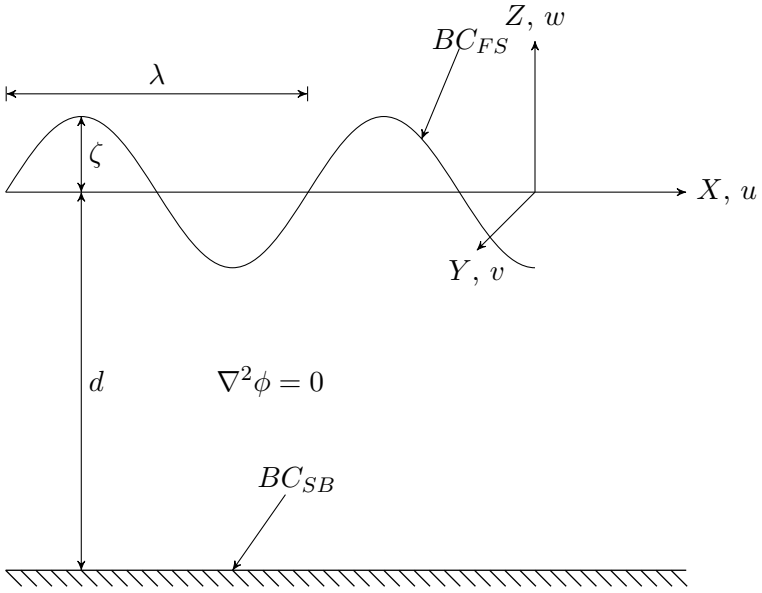

Figure 3: Boundary value problem

Bottom Boundary Condition, BC_{SB} At the seabed, $z = -d$, the velocity normal to the boundary must be zero to sustain the impermeability of the seabed, i.e. $\nabla\phi \cdot \vec{n} = 0$. The seabed are here taken as horizontal, giving:

$$\frac{\partial \phi}{\partial z} = 0, \qquad z = -d \tag{56}$$

Dynamic Free Surface Bounary Condition The water pressure at the free surface is equal to the atmospheric pressure, p_0

$$g\zeta + \frac{1}{2}\underbrace{\left(\left(\frac{\partial \phi}{\partial x}\right)^2 + \left(\frac{\partial \phi}{\partial y}\right)^2 + \left(\frac{\partial \phi}{\partial z}\right)^2\right)}_{nonlinear} + \frac{\partial \phi}{\partial t} + p_0 = p_0, \qquad z = \zeta(x, y, t) \tag{57}$$

Kinematic Free Surface Boundary Condition A water particle on the free surface remains on the free surface, i.e. the vertical velocity is equal to the rate of change of elevation at the free surface.

$$\frac{\partial \zeta}{\partial t} + \underbrace{u\frac{\partial \zeta}{\partial x} + v\frac{\partial \zeta}{\partial y}}_{nonlinear} = w, \qquad z = \zeta(x, y, t) \tag{58}$$

Combined Free Surface Boundary Equation BC_{FS} The Kinematic and Dynamic Free Surface Conditions can be combined, eliminating ζ:

$$-\frac{\partial^2 \phi}{\partial t^2} - g\frac{\partial \phi}{\partial z} - \underbrace{\left(\frac{\partial}{\partial t} + \frac{1}{2}\vec{\nabla}\phi \cdot \vec{\nabla}\right)|\vec{\nabla}\phi|^2}_{nonlinear} = 0, \qquad z = \zeta(x, y, t) \tag{59}$$

3.2 Method of Solution

The perturbation scheme is assumed here for the solution of the boundary value problem. The variables can then be expanded as a convergent power series of a small parameter, and the velocity potential solution to the combined free surface boundary condition can be expanded as a convergent Maclaurin series around z=0. The velocity potential and surface elevation can then be expressed as:

$$\begin{aligned}\phi(x,y,z,t) &= \phi_1(x,y,z,t) + \phi_2(x,y,z,t) + \ \ldots \quad O(\phi_{i+1}) = O\left(\phi_1\left(\frac{H}{\lambda}\right)^i\right) \\ \zeta(x,y,z,t) &= \zeta_1(x,y,z,t) + \zeta_2(x,y,z,t) + \ \ldots \quad O(\zeta_{i+1}) = O\left(\zeta_1\left(\frac{H}{\lambda}\right)^i\right)\end{aligned} \tag{60}$$

Where H and λ are the height and length of the wave. Introducing the perturbation to Eqs. 55 and 56:

$$\nabla^2\phi = \nabla^2\phi_1 + \nabla^2\phi_2 + \ \ldots \tag{61}$$

$$\frac{\partial\phi_1}{\partial z} = 0, \quad \frac{\partial\phi_2}{\partial z} = 0, \qquad z = -d \tag{62}$$

The MacLaurin series of the velocity potential at the free surface can be expressed as

$$\phi(x,y,\zeta,t) = \phi(x,y,0,t) + \zeta\frac{\partial\phi(z,y,0,t)}{\partial z} + \frac{\zeta^2}{2}\frac{\partial^2\phi(x,y,0,t)}{\partial z^2} \ \ldots. \tag{63}$$

In the following sections the results using the first and second order perturbation will be extensively discussed and compared, using both a single and multiple wave components. Higher order perturbations and other more complex versions of the solutions are not used in time domain simulations of irregular seas, and will therefore only be explained briefly at the end of this chapter.

3.3 First order perturbation, linear wave theory

When the surface elevation is considered very small, the linear theory arises. One assumes that the amplitude is far less than the wavelength ($\zeta < \lambda$), leaving the first order error of the velocity potential and surface elevation negligible. This implies that the terms marked as *nonlinear* in Eqs. 57 to 59 are neglected. Only the first term of the MacLaurin series of the velocity potential at the free surface is included as ζ is assumed to be very small and only first order contributions are included. The following equations define the problem:

First-Order Equations

$$\begin{aligned}
\nabla^2\phi_1 &= 0, & -d \leq z \leq 0, -\infty \leq x, y \leq \infty \\
\frac{\partial\phi_1}{\partial z} &= 0, & z = -d \\
\frac{\partial^2\phi_1}{\partial t^2} + g\frac{\partial\phi_1}{\partial z} &= 0, & z = 0 \\
-\frac{1}{g}\left[\frac{\partial\phi_1}{\partial t}\right] &= \zeta_1, & z = 0
\end{aligned} \tag{64}$$

3.3.1 First order solution for a regular wave

The solution to the first order problem was first presented by Airy in 1841. The solution is found by assuming a velocity potential of the form

$$\phi_1 = f(z)sin(k(xcos(\theta) + ysin(\theta)) - \omega t) \tag{65}$$

Where k is the wave number, defined as $k = 2\pi/\lambda$, ω is the angular frequency of oscillation [rad/s] and θ the direction of propagation. For the rest of this report one will assume unidirectional waves, propagating in the positive x direction, i.e. $\theta = 0$. All relations still hold, with x as a vector containing $[xcos(\theta),\ ysin(\theta)]$. By enforcing the boundary conditions given in Eq. 64, the velocity potential is found as:

$$\phi_1 = \frac{g\zeta_A}{\omega}\frac{cosh(k(z+d))}{cosh(kd)}sin(kx - \omega t) \tag{66}$$

Where ζ_A is the amplitude of the wave. The shape of the wave profile will be that of a sine wave with amplitude ζ_A and frequency ω.

$$\zeta(t) = \zeta_A cos(kx - \omega t) \tag{67}$$

The relation between wave frequency and wavenumber are given through the *dispersion relation*

$$\omega^2 = kg\ tanh(kd) \tag{68}$$

With the velocity potential known, important kinematics such as velocity $\vec{v}$, accelerations $\vec{a}$ and dynamic pressure p can be found through differentiation. As the phase of the kinematics are different, they will have maximum at different positions as the wave propagate.

$$\begin{aligned}
\vec{u}_1 = \nabla\phi_1 \quad &= \frac{kg\zeta_A}{\omega cosh(kd)} \cdot \begin{bmatrix} \cosh(k(d+z)) \cdot \ cos(kx-\omega t) \\ \sinh(k(d+z)) \cdot \ sin(kx-\omega t) \end{bmatrix} \\
\vec{a}_1 = \frac{\partial \vec{u}_1}{\partial t} \quad &= \frac{kg\zeta_A}{cosh(kd)} \cdot \begin{bmatrix} \cosh(k(d+z)) \cdot \ sin(kx-\omega t) \\ sinh(k(d+z)) \cdot \ cos(kx-\omega t) \end{bmatrix} \\
p_1 = -\rho\frac{\partial \phi_1}{\partial t} \quad &= \rho g\zeta_A \frac{cosh(k(z+d))}{cosh(kd)} cos(kx-\omega t)
\end{aligned} \tag{69}$$

3.3.2 Wave-wave interactions, linear irregular sea

When linear theory is applied, the superposition principle is valid for interactions between waves. That is, there is no interactions and the solutions of each boundary value problem is summed. The velocity potential and surface elevation can then be expressed as:

$$\begin{aligned}
\phi_1 = \phi_{1,1} + \phi_{1,2} + \ ... \quad &= \sum_i^N \phi_{1,i} \\
\zeta_1 = \zeta_{1,1} + \zeta_{1,2} + \ ... \quad &= \sum_n^N \zeta_{1,n}
\end{aligned} \tag{70}$$

where $\phi_{1,i}$ and $\zeta_{1,i}$ are separate solutions of the first order boundary value problem, defined by their amplitude $\zeta_{A1,i}$, frequency ω_i and a phase angle ε_i to describe the relative phases between the wave components. Similarly, the kinematics under the irregular wave can be found as the sum of the kinematics of each individual wave. A common belief is that the kinematics are not defined for $z > 0$, and some sort of extrapolation or *stretching* from mean water level is necessary to provide kinematics up to the free surface of a crest. It is, however, a misunderstanding that this is a formal requirement of the perturbation formulation, Johannessen [13].

When the wave components are found from a continuous spectrum there might be an issue with the kinematics above mean water level, which arise from the realization that linear velocity itself might not be defined for $z > 0$, refer Johannessen [13]. The issue is depending on the decay rate of the upper tail of the wave spectrum and arises from the fact that the exponential term will converge upon infinity for $z > 0$ as ω increase. It was shown by e.g. Johannessen, that the horizontal velocity from linear components is not defined above mean water level unless the amplitudes of the harmonic wave components in the upper part of the spectrum decays exponentially. It is then necessary to use approximate method to obtain results at the free surface, such as linear extrapolation or Wheeler stretching. The methods are explained after the solution of the second order perturbation.

3.4 Second order perturbation

The second order perturbation is found by including terms up to second order. In addition to the second order velocity potential and surface elevation, one must also include the *nonlinear* parts of equations 57 to 59. Finally the second term of the MacLaurin series of the first order potential must be included. Therefore ϕ and ζ must satisfy, in addition to Eq. 64, the following relations (see e.g. [26]).

Second-Order Equations

$$\begin{aligned}
\nabla^2\phi_2 &= 0, && -d \le z \le 0, -\infty \le x, y \le \infty \\
\frac{\partial\phi_2}{\partial z} &= 0, && z = -d \\
\frac{\partial^2\phi_2}{\partial t^2} + g\frac{\partial\phi_2}{\partial z} &= -\frac{\partial}{\partial t}\left|\vec{\nabla}\phi_1\right|^2 - \zeta_1\frac{\partial}{\partial z}\left[\frac{\partial^2\phi_1}{\partial t^2} + g\frac{\partial\phi_1}{\partial z}\right], && z = 0 \\
\zeta_2 &= -\frac{1}{g}\left[\frac{\partial\phi_2}{\partial t} + \frac{1}{2}\left|\vec{\nabla}\phi\right|^2 + \zeta_1\frac{\partial^2\phi_1}{\partial z\partial t}\right], && z = 0
\end{aligned} \tag{71}$$

3.4.1 Second order solution for a regular wave

The solution to the second order boundary value problem for a single wave, commonly referred to as Stokes 2.nd, were theoretically demonstrated by Stokes in 1847. The complete formula of velocity potential and surface elevation for a wave propagating in positive x-axis are ($\phi = \phi_1 + \phi_2$):

$$\begin{aligned}
\phi = &\frac{g\zeta_A}{\omega}\frac{cosh(k(z+d))}{cosh(kd)} \cdot \left\{ \underbrace{sin(kx-\omega t)}_{linear} + \underbrace{k\zeta_A\frac{3cosh(2k(z+d))}{8sinh^3(kd)} \cdot sin(2(kx-\omega t))}_{sum\ frequency} \right\} \\
&\underbrace{-(k\zeta_A)^2\frac{1}{2sinh(2kd)}\frac{gt}{k}}_{Mean\ drift} \quad + \quad O\left(\left(\frac{\zeta_A}{\lambda}\right)^3\right)
\end{aligned} \tag{72}$$

$$\zeta = \zeta_A\left\{cosk(kx-\omega t) + k\zeta_A\frac{3-tanh^2(kd)}{4tanh^3(kd)}cos(2(kx-\omega t))\right\} \quad + \quad O\left(\left(\frac{\zeta_A}{\lambda}\right)^3\right) \tag{73}$$

From these equation one finds several interesting observations. The finite water velocity potential includes a linear *mean drift* in time, and a sum frequency term. The *mean drift* gives rise to constant forces through the dynamic pressure term, while the sum frequency term cause loads oscillating at twice the frequency of the linear term. For some structures, with low eigenperiods, this oscillatory force might cause large dynamic responses. A third second order correction to the velocity potential arises when waves with different frequencies interact, creating *difference frequency* oscillations. Additionally, a correction to the surface elevation is introduced in Eq. 73. The phase velocity can be shown to be the same for the two surface elevation components, i.e. the wave shape is maintained.

If one assumes an infinite depth both the second and third term of Eq. 72 vanish, as the denominator approach infinity. Similarly the amplitude of the second term of Eq. 73 converges to $\frac{k\zeta_A}{2}$. The only correction of second order theory for a single wave at infinite depth is therefore a correction to the surface elevation, none for the kinematics. It can be shown that first at the fourth

order Stoke's perturbation will a correction to the velocity potential at deep water be introduced.

The relation between wave frequency and wave number, i.e. the dispersion relation, is the same as for the first order solution. The kinematics are found as the derivative of the velocity potential, and presented in Eq. 74. Note that these are the second order correction, and must be added to the first order kinematics in Eq. 69.

$$
\begin{aligned}
\vec{u}_2 &= \frac{3(k\zeta_A)^2 g}{8\omega} \cdot \begin{bmatrix} \left(2\frac{cosh(k(z+d))}{cosh(kd)}\right) \cdot \left(\frac{cosh(2k(z+d))}{sinh^3(kd)}\right) cos(2(kx-\omega t)) \\ \left(\frac{sinh(k(z+d)) + 3sinh(3k(z+d))}{2cosh(kd)\cdot sinh^3(kd)}\right) sin(2(kx-\omega t)) \end{bmatrix} \\
\vec{a}_2 &= \frac{3}{8}(k\zeta_A)^2 g \cdot \begin{bmatrix} \left(4\frac{cosh(k(z+d))}{cosh(kd)}\right) \cdot \left(\frac{cosh(2k(z+d))}{sinh^3(kd)}\right) sin(2(kx-\omega t)) \\ \left(\frac{sinh(k(z+d)) + 3sinh(3k(z+d))}{2cosh(kd)\cdot sinh^3(kd)}\right) cos(2(kx-\omega t)) \end{bmatrix} \\
p_2 &= \rho k \zeta_A^2 g \left[\frac{1}{2sinh(2kd)} + 2\left(\frac{cosh(k(z+d))}{cosh(kd)}\right) \cdot \left(\frac{3cosh(2k(+d))}{8sinh^3(kd)}\right) \cdot cos(2(kx-\omega t))\right]
\end{aligned}
\tag{74}
$$

Similarly to that of Gaussian waves, the velocity potential is valid up to the surface. Approximations to the exact free surface must therefore be introduced for the second order kinematics as well.

3.4.2 Second order wave-wave interaction

The second order perturbation solution to the wave wave interaction problem for arbitrary depths was presented by Sharma and Dean [26]. It involves the first order solution presented previously, and a second order correction. The correction to the velocity potential is:

$$
\begin{aligned}
\phi_2 = \; & \overbrace{\frac{1}{4}\sum_{i=1}^{N}\sum_{j=1}^{N} \frac{g^2 \zeta_{A_{1,i}} \zeta_{A_{1,j}}}{\omega_i \omega_j} \frac{cosh(k_{ij}^-(z+d))}{cosh(k_{ij}^- d)} \cdot \frac{D_{ij}^-}{\omega_i - \omega_j} sin(\psi_i - \psi_j)}^{difference\ \ frequency} \\
+ \; & \underbrace{\frac{1}{4}\sum_{i=1}^{N}\sum_{j=1}^{N} \frac{g^2 \zeta_{A_{1,i}} \zeta_{A_{1,j}}}{\omega_i \omega_j} \frac{cosh(k_{ij}^+(z+d))}{cosh(k_{ij}^+ d)} \cdot \frac{D_{ij}^+}{\omega_i + \omega_j} sin(\psi_i + \psi_j)}_{sum\ \ frequency}
\end{aligned}
\tag{75}
$$

where

$$
\begin{aligned}
k_{ij}^- &= |k_i - k_j| \\
k_{ij}^+ &= |k_i + k_j| \\
\psi_i &= k_i x - \omega_i t + \varepsilon_i \\
D_{ij}^- &= \frac{\left(\sqrt{R_i} - \sqrt{R_j}\right)\left[\sqrt{R_j}\left(k_i^2 - R_i^2\right) - \sqrt{R_i}\left(k_j^2 - R_j^2\right)\right]}{\left(\sqrt{R_i} - \sqrt{R_j}\right)^2 - k_{ij}^- tanh(k_{ij}^- d)} + \frac{2\left(\sqrt{R_i} - \sqrt{R_j}\right)^2 (k_i k_j + R_i R_j)}{\left(\sqrt{R_i} - \sqrt{R_j}\right)^2 - k_{ij}^- tanh(k_{ij}^- d)} \\
D_{ij}^+ &= \frac{2\left(\sqrt{R_i} + \sqrt{R_j}\right)^2 (k_i k_j - R_i R_j)}{\left(\sqrt{R_i} + \sqrt{R_j}\right)^2 - k_{ij}^+ tanh(k_{ij}^+ d)} + \frac{\left(\sqrt{R_i} + \sqrt{R_j}\right)\left[\sqrt{R_i}\left(k_j^2 - R_j^2\right) + \sqrt{R_j}\left(k_i^2 - R_i^2\right)\right]}{\left(\sqrt{R_i} + \sqrt{R_j}\right)^2 - k_{ij}^+ tanh(k_{ij}^+ d)} \\
R_i &= k_i tanh(k_i d)
\end{aligned}
\tag{76}
$$

The second order contribution to the surface elevation are found by:

$$\zeta_2 = \frac{1}{4}\sum_{i=1}^{N}\sum_{j=1}^{N}\zeta_{A1,i}\zeta_{A1,j}\Bigg\{\overbrace{\left(\frac{D_{ij}^{-}-(k_ik_j+R_iR_j)}{\sqrt{R_iR_j}}+(R_i+R_j)\right)cos(\psi_i-\psi_j)}^{difference\ \ frequency} + \underbrace{\left(\frac{D_{ij}^{+}-(k_ik_j-R_iR_j)}{\sqrt{R_iR_j}}+(R_i+R_j)\right)cos(\psi_i+\psi_j)\Bigg\}}_{sum\ \ frequency} \tag{77}$$

For many marine applications one can assume an infinite water depth,i.e. $d \longrightarrow \infty$. Consequently, $tanh(\infty) \longrightarrow 1$, $R_i \longrightarrow k_i$ and $\frac{cosh(k(z+d))}{cosh(kd)} \longrightarrow e^{kz}$. Introducing this into the previous equations, one can show that D_{ij}^{+} becomes zero, and that resulting problem (both first and second order) can be expressed as:

$$\begin{aligned}
\zeta_1 &= \sum_{i=j}^{N}\zeta_{A1,j}cos(\psi_j)\\
\zeta_2 &= \frac{1}{2}\sum_{i=j}^{N}\zeta_{A1,j}k_jcos(2\psi_j)+\frac{1}{2}\sum_{j=1}^{N-1}\sum_{i=j+1}^{N}\zeta_{A1,i}\zeta_{A1,j}\Big((k_i+k_j)cos(\psi_i+\psi_j)-(k_i-k_j)cos(\psi_i-\psi_j)\Big)\\
\phi_1 &= \sum_{j=1}^{N}\zeta_{A1,j}\frac{\omega_j}{k_j}e^{k_jz}sin(\psi_j)\\
\phi_2 &= -\sum_{j=1}^{N-1}\sum_{i=1}^{N}\zeta_{A1,i}\zeta_{A1,j}\omega_ie^{(k_i-k_j)z}sin(\psi_i-\psi_j)
\end{aligned} \tag{78}$$

The equations presented are valid for one or more waves interacting, and can additionally be used in time domain simulations of an irregular sea generated from a wave spectrum. The second order theory includes a significant increase in the complexity of the equations. There is N^2 correction terms to the surface elevation, and also N^2 correction terms to the velocity potential. Particularly the latter is of importance, as the velocity potential must be used at every step to find the appropriate kinematics for force calculations.

Similarly to the issues regarding spectral decay rates for linear surface realizations as mentioned previously apply for second order theory. Special consideration must also be taken when calculating kinematics under a second order realization of a continuous spectrum. Due to interactions between wave components with very different frequencies, the derivatives of surface elevation and velocity potential are not defined if the spectrum is summed up to high frequencies. Discussions around the issue can be found in e.g. Johannessen [13], Zhang & Yue [37] and Zhang et al. [38] In general, Johannessen concludes that a cut off frequency and/or limiting the interact between wave components with very different frequencies are necessary to compute kinematics for realistic wave spectrum.

While the velocity potential and its derivatives in general are defined both below and above mean water level, the issues for a continuous spectrum defined above presents challenges. Two approximate methods of modelling second order kinematics are therefore discussed in the following.

3.5 Approximate methods of estimating wave kinematics under an irregular wave

Several possible ways exist to obtain the linear or second order velocity at the free surface. The most commonly accepted are vertical or linear extrapolation or Wheeler stretching of the kinematics at $z = 0$.

3.5.1 Wheeler stretching

The most commonly used method to estimate kinematics underneath a measured surface is that proposed by Wheeler [35]. The measured surface is here treated as linear, and linear theory is used to calculate the velocities. It was observed that if the velocity potential is applied all the way, the kinematics were significantly overestimated at the free surface. The issues, collectively referred to as *high frequency contamination* are discussed by e.g. Johannessen [13], and reprinted here:

- *By assuming that all the frequency components that make up the surface are linear, it is assumed that each frequency is associated with a wavenumber according to the linear dispersion relation. For a steep wave, a high frequency component contains significant bound waves which are associated with much smaller wavenumbers. As a result, a linear assumption will yield too large contributions for high wavenumbers which control the horizontal velocity profile (e^{kz}).* [13]
- *A fundamental point of superposition theory is that components may be superimposed at z=0. Even assuming that the linear components are correctly identified, this leads to significant inaccuracies: A short wave (with amplitude a and wavenumber K) which is in reality riding on top of a much larger long wave (with amplitude A and wavenumber k), will only have an effect near the top of the long wave. Using linear theory, these are superimposed at z=0 ($Ae^{kz} + ae^{Kz}$ up to $z = a + A$) such that the contribution of the short wave is overestimated.* [13]

In order to correct for the above mentioned issues, two empirical corrections were introduced.

1. The time history of the surface elevation is low pass filtered with a cut-off frequency of $\omega_{cut} = 4\omega_p$.
2. It was observed that the kinematics found from the linear components (of the measured surface) at $z = 0$ corresponded to the measured free surface kinematics, and hence a stretching procedure was suggested:

$$z' = (z - \zeta)\frac{d}{d + \zeta} \tag{79}$$

   Where z' is the z entering in the linear velocity potential.

For a linear realization of a wave spectrum, Wheeler stretching is performed simply from the initial wave components. For a second order sea realization, the surface must first be assembled using the second order surface correction terms, and then a Fourier transform must be applied to obtain a new set of linear wave components. These are assumed to be linear, and kinematics are calculated according to linear theory and stretched to the second order surface. This constitutes a major computational saving, as the second order velocity potential must not be found for all steps in the simulation.

Wheeler stretching will in general produce relatively good surface kinematics when applied to a measured (or second order) surface. There are, however, issues regarding a too low vertical kinematic profiles obtained from this stretching. Additionally, if Wheeler stretching is applied to a linear sea, the kinematics will be underestimated also at the free surface. An illustration and explanation is given in Section 3.6.

3.5.2 Stansberg linear extrapolation

Linear extrapolation is a commonly applied method to avoid issues regarding non-existing velocities above the mean water level. The velocity potential is expanded to the free surface using the MacLaurin series in Eq. 63. For a linear extrapolation, the two first terms are included:

$$\phi(x,z,t) = \phi_1(x,0,t) + \phi_2(x,0,t) + z\frac{\partial \phi_1}{\partial z}(x,0,t) \tag{80}$$

Note that the same expression is valid for a linear extrapolation of the first order surface model, by removing the ϕ_2 term.

The resulting kinematics will follow an exponential profile given by ϕ_1 and ϕ_2 below the free surface, and a linear profile above, given by the z-derivative of the linear velocity potential $z = 0$. For the horizontal velocity, one gets:

$$u(x,z,t) = \frac{\partial \phi_1}{\partial x}(x,0,t) + \frac{\partial \phi_2}{\partial x}(x,0,t) + z \cdot \frac{\partial^2 \phi_1}{\partial x \partial z}(x,0,t), \qquad z > 0 \tag{81}$$

Applying this equation to continuous spectra are, however, still problematic. High derivatives of the surface elevation and the velocity potential are not defined for realistic spectra, ref. Johannessen [13]. A truncation of the wave spectrum is therefore required. A cut-off frequency of the wave spectrum as given in Eq. 82 was proposed by Stansberg [27]. Along with a linear extrapolation of the kinematics, it has shown good compliance to measurements. This is presently the cut-off frequency recommended in e.g. DNV-RP-C205 [5].

$$\omega_{max} = \sqrt{\frac{2g}{H_s}} \tag{82}$$

A disadvantage with this method is that a linear profile is used above mean water level, which will not be able to completely describe the real exponential behaviour. It is shown that this will marginally underestimate the surface velocity at the crest Stansberg [28].

An example of the horizontal velocity under a second order crest using either Wheeler stretching (blue) or Stansberg linear extrapolation (red) is given in Figure 4. The underlying velocity contributions are also shown, using dashed and dotted lines.

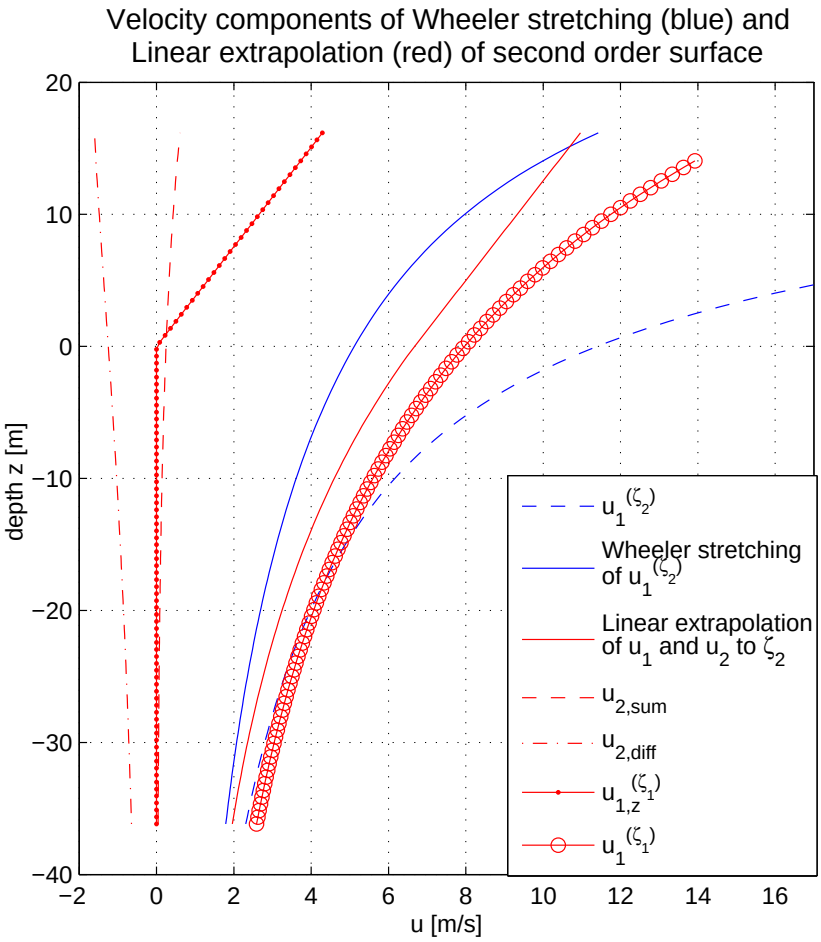

Figure 4: Linear extrapolation of second order kinematics, d=90

Both the underestimation of Wheeler stretching around mean water level, and the slightly low free surface velocity of the Stansberg extrapolation is clearly visible in this plot.

3.6 Comparisons of linear and second order velocity profiles

Several studies discusses the effect of the different ways of modelling the sea surface and kinematics. This section illustrates some of the methods discussed previously. Figure 5 shows the horizontal velocities measured in an experiment by Johannessen & Swan [14], along with the profiles based on the theories discussed here. Note that the initial spectrum is truncated, and the velocity potentials are applied to the free surface, i.e. no linear extrapolation is applied. For more information regarding the set-up, it is referred to Johannessen & Swan [14].

Figure 5a shows the results when the measured surface is treated as linear, by applying ϕ_1 on the linear components from the measured surface, and by a Wheeler stretching of the linear components. Figure 5b illustrates the profiles using ϕ_1 on the underlying linear components (i.e. only from ζ_1), and when using the second order correction term, ϕ_2 along with ϕ_1 of linear components.

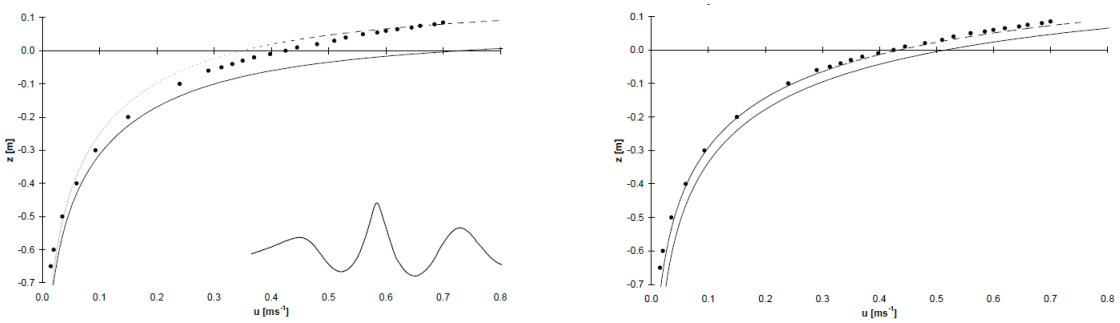

(a) Measurements (dots), Linear based on free surface (solid), Wheeler of linear components from free surface(dashed), Figure from: [14]

(b) Measurements (dots), Linear based on linear surface (solid), Second order using $\phi_1 + \phi_2$ to the free surface (dashed), Figure from: [14]

Figure 5: Comparison of estimated kinematic profiles and measurements

It is observed that Wheeler stretching of the second order surface provides a marked improvement of the surface velocity in Figure 5a, compared to the linear velocity, which is due to the mentioned high frequency contaminations. However, the issues regarding an underestimating of the kinematics around and below the mean water level is clearly illustrated as well. In Figure 5b the second order kinematics provides a remarkably good fit. Also, using the linear velocity potential on the underlying linear components presents a clear improvement of the linear kinematics of the second order components in Figure 5a. An interesting observation here is that the second order velocity correction is in fact a negative correction underneath a large crest, for infinitely deep waters. This can also be seen from previous equations due to the phase shift of the difference frequency contribution to the velocity potential (i.e. it is negative).

It is seen that both Wheeler method in (a), and linear and second order in (b) provides relatively good estimations. The main issue arise when one simulate a linear sea, and use Wheeler stretching of the linear components. That is, one use the linear velocity up to 0 in Figure 5b, and stretch this value to the free surface. This is currently being done in many computer software (such as *USFOS*) and provides a significant underestimation of the velocity both at the free surface and throughout the water column. In order to account for this effect it is recommended to increase the hydrodynamic coefficients, refer NORSOK N-003 [23].

3.7 Higher order perturbations and stream theory for use in design wave approach

The second order model is the most sophisticated model of irregular seas available for routine engineering. However, for regular waves, both higher order perturbation solutions and other theoretical approaches are available. These models are used in design when the dynamic effects are small so that a design wave approach is sufficient.

In this chapter some remarks regarding the higher order Stokes' perturbations and Deans stream function is given.

3.7.1 Stokes waves

The resulting wave problems when exploiting the perturbation scheme are commonly referred to as Stokes waves. In the previous sections the governing equations and solutions of the first two perturbations are given. The series expansion of velocity potential and surface profile is given in Eqs. 83 and 84, while the necessary relations can be found in e.g. [40]:

$$\phi = \sum_{i=1}^{I} \phi_i' cosh\{k(z+d)\} cos(\omega t - kx) \tag{83}$$

$$\zeta = \sum_{i=1}^{I} \zeta_i' \frac{sin\{i(\omega t - kx)\}}{k} \tag{84}$$

Where ϕ_i' and ζ_i' are coefficient for each component of the series expansion, depending on wavelength, and found through an iterative procedure. The resulting wave kinematics is also a result of a series of components, found by differentiating the velocity potential with respect to direction and time. The acceleration and velocity in horizontal direction are given as:

$$u = \frac{d\phi}{dx} = \sum_{i=1}^{I} i\frac{\omega}{k}\phi_i' cosh\{k(z+d)\} sin(\omega t - kx) \tag{85}$$

$$a = \frac{du}{dt} = -\sum_{i=1}^{I} i\frac{\omega^2}{k}\phi_i' cosh\{k(z+d)\} cos(\omega t - kx) \tag{86}$$

The benefits of the Stoke's wave is a more exact representation of the wave shape, thus resulting in more accurate wave kinematics and ultimately loads and responses. The draw backs are a significantly more complex procedure of obtaining the values. Stoke's waves has limitations, and should not be used for $2\zeta_a/\lambda$ less than $1/7$, as the waves will break.

One should always exercise caution when dealing with shallow water waves, as the perturbation scheme fails at a certain depth. The wave profile will be unphysical, in the sense that it gets many local maxima between the peaks, and the shape does not resemble that of an ocean wave. Inspection of the simulated wave profile is therefore necessary to assure that a correct shape is maintained. Other theories can be used for more shallow waters, such as Deans Stream Theory.

3.7.2 Dean Stream function

An alternative theory to describe the wave equations were proposed by Dean [4], and makes use of the *stream function* rather than the velocity potential. A stream function is a vector field which satisfies:

$$\frac{\partial \psi}{\partial x} = -v, \qquad \frac{\partial \psi}{\partial y} = u \tag{87}$$

Stream function wave theory was developed to examine fully non-linear waves numerically by fitting stream functions to waves with known profiles. The theory was later expanded to calculate wave theory based on target wave height, period and depth, see e.g. Rienecker and Fenton [25]. The method is also known as Fourier approximation wave theory. The problem is to find a stream function which satisfies the same boundary conditions as described in Eqs. 56 through 59, i.e.:

1. Laplace equation:
$$\frac{\partial^2 \psi}{\partial x^2} + \frac{\partial^2 \psi}{\partial z^2} = 0 \tag{88}$$
2. Bottom boundary condition:
$$\psi(x, 0) = 0 \tag{89}$$
3. Kinematic free surface condition:
$$\psi(x, \zeta) = -Q \tag{90}$$
4. Dynamic free surface condition:
$$\frac{1}{2}\left[\left(\frac{\partial \phi}{\partial x}\right)^2 + \left(\frac{\partial \phi}{\partial z}\right)^2\right] + \zeta = R \tag{91}$$

The first two equations are satisfied by a stream function of the form:

$$\psi(x, z) = B_0 z + \sum_{j=1}^{N} B_j \frac{sinh(jkz)}{cosh(jk)} cos(jkz) \tag{92}$$

Where k is the wave number, and N is the order of the stream function. k and B_j are chosen so as to satisfy Eqs. 90 and 91. The complexity of the equations, and accuracy of the solution, increase with the number of components N. Typically 3-5 components are satisfactory in deep waters, while in very shallow water the required order can be as high as 30. The kinematics are found as derivatives of the stream function according to Eq. 87.

Deans theory is a best fit method, and provides therefore no truncation like the perturbation theories, which removes contributions higher than the perturbation order. If the terms that is ignored are sizable, then the accuracy of the Stoke perturbation is questionable, and Dean's theory might give better results. When the wave height/depth ratio is less than 0.5 the difference between the stream function and the most common perturbation, Stokes 5th, are negligible [40].

4 Simulation Methods for Irregular Waves

For dynamically sensitive marine structures, or marine structures subjected to large displacements, analytical solution of force interactions is not possible, and some sort of time domain simulation must be conducted to obtain the structural behaviour. This can either be in the form of model simulations, or numerical simulations on a computer. Either way involve a digital simulation in the frequency domain where a number of sine waves are summed to produce an approximate Gaussian process. The components are chosen based on a target spectrum, and summed according to Eq. 93 (for a uni directional case).

$$\zeta(t) = \lim_{N \longrightarrow \infty} \sum_{i=1}^{N} \zeta_{A,i} cos(k_i x - \omega_i t + \varepsilon_i) \tag{93}$$

Where $\zeta_{A,i} = \sqrt{S(\omega_i)\Delta\omega_i}$ and the relation between wave number k_i and frequency ω_i are given through the dispersion relation. The randomly distributed phases ε_i allows for an infinite amount of possible realizations $\zeta(t)$, by using a different random generation between each run. It is here only considered linear waves, where a Gaussian representation is correct, the second order extension is discussed in Section 4.2.

In order to apply Eq. 93 to a physical problem, a finite number of components N must be selected, i.e.:

$$\zeta(t) = \sum_{i=1}^{N} \zeta_{A,i} cos(k_i x - \omega_i t + \varepsilon_i) \tag{94}$$

This leads to a departure from the Gaussian model, hence the statistics of the surface process presented in Section 2 might no longer be valid. Another important effect is that, if the frequencies are chosen with correlated frequencies, i.e. a constant frequency span, the process will repeat itself after a time T, given by:

$$T = \frac{2\pi}{\Delta\omega} = \frac{2\pi N}{\omega_{max} - \omega_{min}} \tag{95}$$

Where ω_{min} and ω_{max} are the cut-off limits of the spectrum (for a Gaussian process 0 and ∞). The lower limit should in theory be set to zero, however for many practical applications the wave spectrum will be zero in a large range, and hence the cut off might be taken higher to remove some components. The influence of the upper limit should be checked for each individual test case. The reason for this is that the derivatives of the velocity potential is significantly influenced by the decay rate in the upper tail, and might not exist in specific cases. This will be further discussed in relation to the second order extension.

Several methods of choosing components so as to best approximate the Gaussian surface exist, with varying computation time and accuracy. In this report several such methods are compared, and their adequacy discussed. In the following sections the methods are described, and their limitations explained.

4.1 Determination of harmonic components

Here two main methods of realising the sea surface are explained, the *constant frequency span method*, commonly referred to as the *fast Fourier transform* (FFT), and the *equal area method* (EAP). Different ways of finding the frequency, amplitude and phase of each method is discussed, along with a suggestion for improvement of the EAP method.

4.1.1 Fast Fourier Transform

The traditional method of representing irregular seas is by discrete Fourier components with constant frequency span. This method is commonly referred to as the *fast Fourier transform* (FFT) of the wave spectrum.

$$\Delta\omega = \frac{\omega_{max} - \omega_{min}}{N_{components}} = constant \tag{96}$$

The general idea is presented in Figure 6, for a procedure using 30 components. Using as few as 30 components are seldom used in combination with the FFT method, as the wave history will repeat in a very short time for a broad banded process.

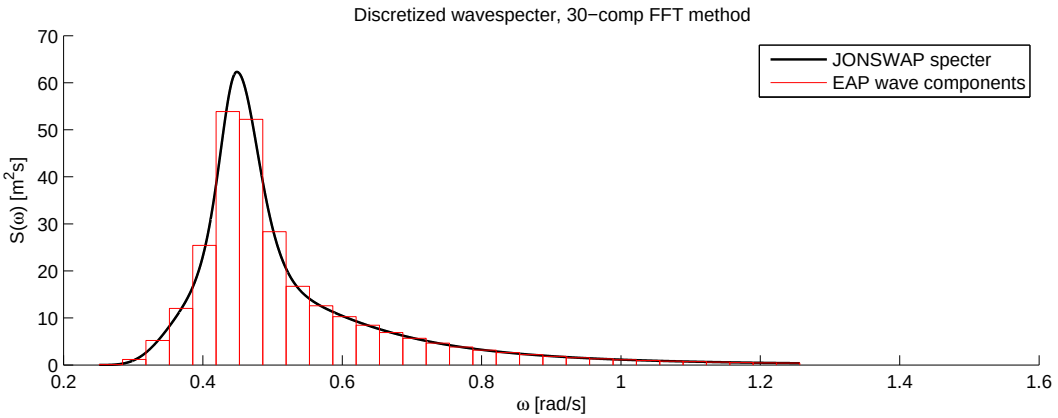

Figure 6: The Fast Fourier Transformation method, with deterministic amplitude

There are essentially three methods of finding the amplitude, phase and frequency of components.

4.1.1.1 Random phase scheme

The most common procedure is to exploit the fact that for sufficiently large N, the limit state behaviour of Eq. 93 is approximately obtained by Eq. 94. It was shown by Elgar et al. [6] that for $N > 1000$ the errors on extreme values made by this assumption were less than 1% for either narrow or a broad banded processes. The harmonic components will then be given by:

$$\begin{aligned} \zeta_{A,i} &= \sqrt{2\int_{\omega_{l,i}}^{\omega_{u,i}} S(\omega)d\omega} \\ \omega_i &= \frac{\omega_{l,i} + \omega_{u,i}}{2} \\ \varepsilon_i &= rand[0,\ 2\pi] \end{aligned} \tag{97}$$

The procedure results in components with varying amplitudes for each wave component, the largest for the components in the energy rich parts of the wave spectrum. However, the uniform spacing of the frequency's result in a repetition of the wave history after a certain time. As there

will be no new information as the wave history is repeated, the length of the simulation is limited by the time until repetition. In order to do long simulations, say three hour, for a spectrum which is truncated ω_max at a frequency around 2 [rad/s], this would require several thousand wave components, even though 1000 components depict the sea satisfactory as a Gaussian process.

4.1.1.2 Random amplitude scheme

Consider how the wave spectrum is created. One measure the ocean waves in a certain area (or over a certain time window), and decompose the sea into various discrete components through the inverse Fourier Transform, and get the wave spectrum at that instant, call it E_i. This procedure is repeated a certain amount of times within a limited time window. The wave spectrum S is then found as the average of the individual spectrum E_i. However, if one were to simulate a number of realizations from Eq. 94 using the deterministic amplitudes of Eq. 97, one would get sea states which, when inversely samples, reproduced the $S(\omega)$ in every sample. This means that some randomness of the real system is lost, and the result is not a Gaussian process.

The theoretical reason is that a Gaussian realisation in its original form is a sum of sine and cosine terms.

$$\zeta(t) = \sum_{i=1}^{N} (a_i cos(\omega_i t) + b_i sin(\omega_i t)) \tag{98}$$

Here a_i and b_i are Gaussian distributed variables with zero mean and a standard deviation of $\sigma_i = \sqrt{2\int_l^u S(\omega)d\omega}$. Eq. 98 assumes the form of Eq. 94 only in the limit $N \longrightarrow \infty$. Through theoretical derivations, Tucker et al. [34] found that to correctly simulate a Gaussian process, the amplitudes of Eq. 94 must be taken as Rayleigh distributed, with a *root-mean-square* value of $\sqrt{2\sigma_i} = \sqrt{2\int_l^u S(\omega)d\omega}$, and the phase randomly distributed as in the previous section. This is also the recommended practice in e.g. *DNV-RP-C205* [5]. Two possible realisations of the surface spectrum when this method is applied are shown in Figure 7, for 1000 components. Notice the large deviations from original spectrum, and also the variance of the simulated spectrum.

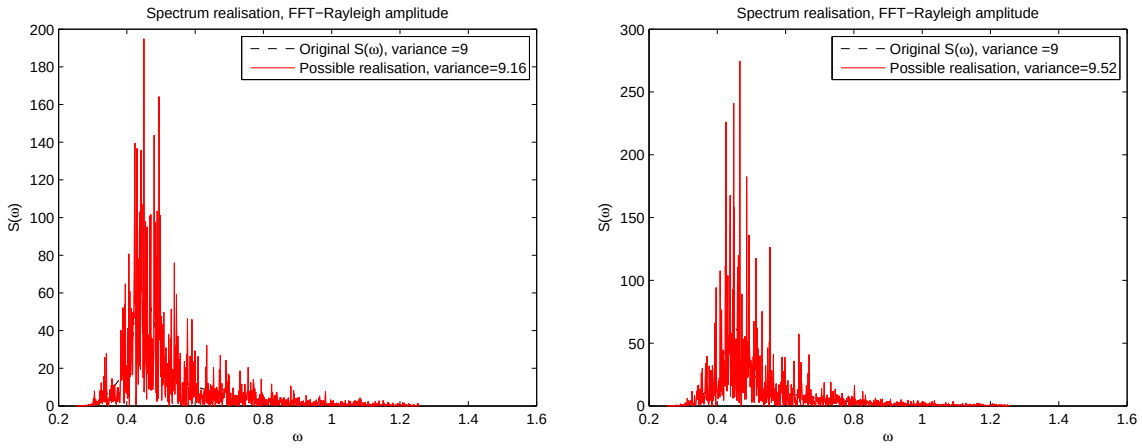

(a) Example 1 (b) Example 2

Figure 7: Variance in spectrum for random amplitude scheme

When averaged over a sufficient number of samples to describe statistical parameters, one finds that the results converge towards the original spectrum. For 1000 simulations the results are shown in Figure 8.

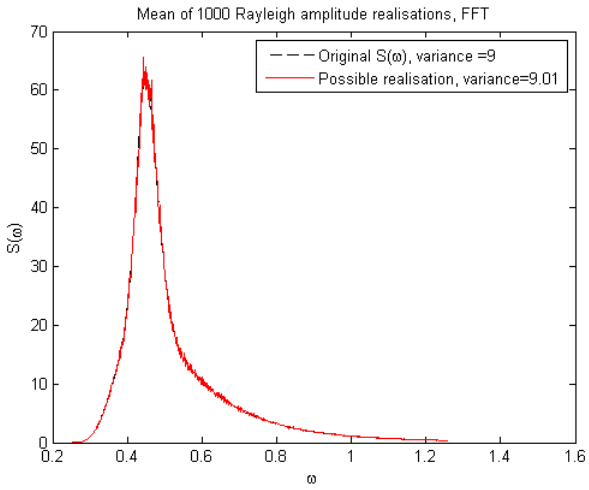

Figure 8: Spectrum of random amplitudes, averaged over 1000 samples

The errors done in assuming a deterministic amplitude is that the variance of the variance of the simulations is underestimated, as the spectral variance is the same in every run. Denoting the variance of a spectrum m_0, the variance of the variance was found by Tucker [33] to be:

$$\sigma_{m0}^2 = \frac{2\pi}{t} \int_0^\infty S^2(\omega) d\omega \tag{99}$$

With t the length of simulation, and S the wave spectrum. Tucker et al. [34] went on to suggest that this loss of variance might lead to a shorter run length of wave groups, which is the length of a period with consecutive high waves in a simulation. This would then be directly related to the extreme predictions of the samples. However, Elgar [6] showed results contradicting the suggestion, as the run lengths were found to have negligible differences for sufficiently large N's. However, for a peaked (narrow banded) spectrum, around 1000 components were required to give similar results in run lengths (2% deviation). The results suggests that for a wave spectrum, which tend to be slightly peaked (i.e. the JONSWAP type), one should use the random amplitude approach.

As the sample variance is underestimated, it is a reasonable suggestion that also the variance of the sample extremes are under predicted by this assumption, as the extremes are theoretically related to the significant wave height, which in turn are related to the variance of the sea state. If the variance of the sea state is constant, the variance of the extremes might then be under predicted compared to that of a random sample variance. The extreme value is, on the other hand, expected to be of the same size given the number of components are sufficient.

4.1.1.3 Random frequency scheme

To avoid the problems of correlated harmonics, it was suggested by Faltinsen and Zhao [7] that the frequencies of each wave component were randomly distributed within the frequency interval of that component. As the frequencies can no longer be expressed in terms of the preceding values, the process will not repeat according to Eq. 95. This method allows therefore for longer simulations with fewer wave components, and thereby a drastic reduction in computing time.

An issue with the method is that when N becomes smaller, the transformation from the limit state to a finite set of components fails. Tucker [34] showed that for a case of 100 components,

the sample variance was under predicted considerably if the amplitudes were chosen deterministically, according to Eq. 97. On the other hand, if the approach with a random amplitude as described in the previous pages were applied, a too large sample variance were predicted as the randomness of each component played a too large part in the total simulation.

On the basis of discussions in the previous section, one would expect a too low extreme value, and, depending on whether the random amplitude scheme or random phase scheme is conducted, one would expect a too low or too high standard deviation of the extremes.

4.1.2 Equal Area Method

The argument behind the Equal Area Method (EAP) is that the energy rich parts of the wave spectrum are most important for the representation of an irregular sea, and therefore the emphasis should be placed here. The angular frequency limits are adjusted so that each component contains the same amount of energy, resulting in a varying $\Delta\omega_i$. The angular frequency of the component is taken as the middle value of the *wave component block*. A deterministic amplitude $\zeta_{A,i}$ depending on the wave component is found as shown in Eq. 100.

$$\zeta_{A,i} = \sqrt{\frac{2\int_{\omega_{min}}^{\omega_{max}} S(\omega)d\omega}{N}} \tag{100}$$

The advantage of this procedure is that the wave components does not have the constant span in frequency, limiting the chance of repetition of the wave history. Therefore a much lower number of components can be used, for instance 30. The procedure is illustrated in Figure 9.

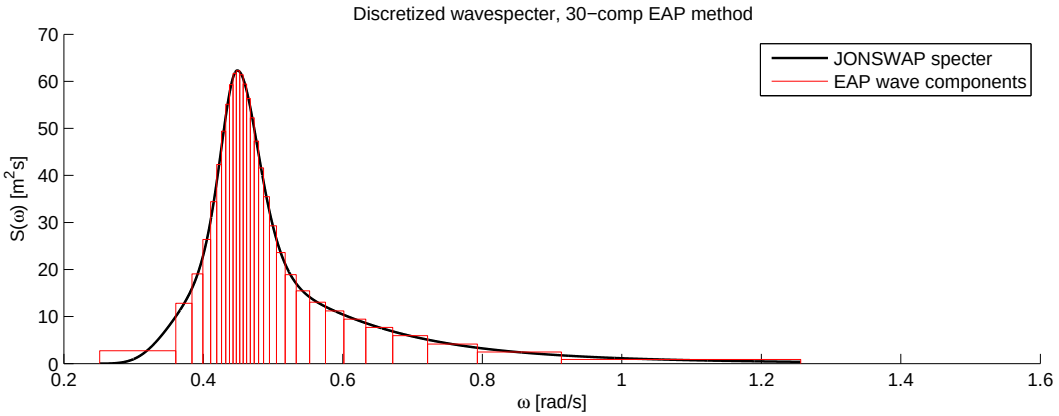

Figure 9: The Equal Area Method, using 30 components

While the EAP has proven to give satisfactory results for a range of applications, some limitations must be acknowledged. While it gives a good representation of the sea spectrum in the energy rich parts of the spectrum, some errors are introduced at the energy dense parts. It was shown by Binner [1] that the response calculations for structures with eigenperiod in the dense parts of the spectrum tend to be significantly under predicted, as the dynamics of the problem are not properly accounted for when modelling a large frequency range with a single wave component.

Another issue is the one addressed regarding a random amplitude scheme of the FFT approach when the number of components become small. The problem is illustrated in Figure 10. The change in variance of the sea state are much larger than those found in Figure 7, which will lead

to a larger variance of the sample variance, and therefore also over predict the variance of the extremes.

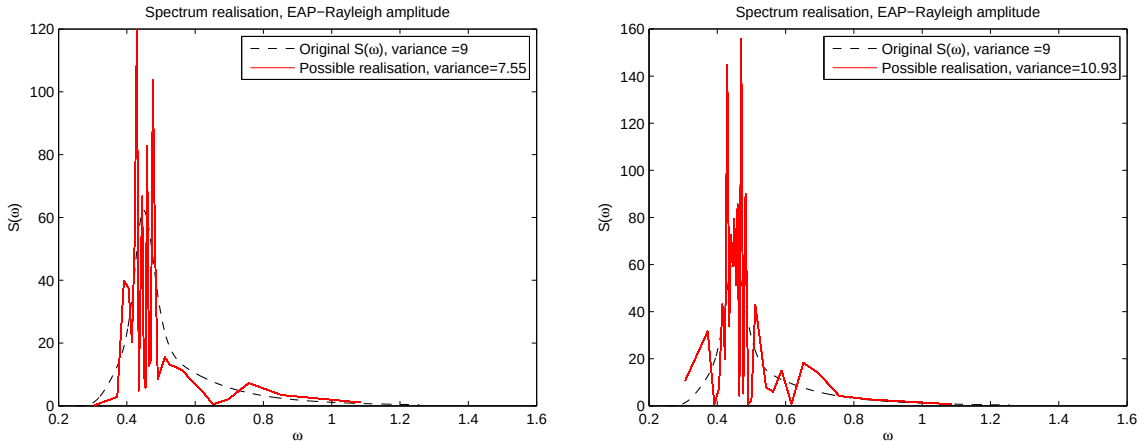

(a) Example 1 (b) Example 2

Figure 10: Variance in spectrum for random amplitude scheme

When these spectra are averaged over 1000 simulations with random seeds, the original spectrum materializes. The mean accurately predicts the initial spectrum, both in shape and total variance of the sea:

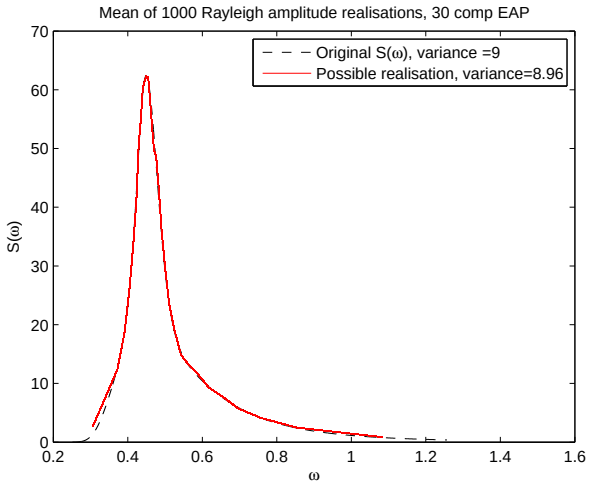

Figure 11: Spectrum of random amplitudes, averaged over 1000 samples

It is believed that as the equal area principle have more components in the high energy parts of the spectrum, the limit state of Eq. 93 will be better approximated by an EAP scheme than by a random frequency FFT scheme with the same total number of components. While this exact method was not investigated in the study Elgar et al. [6] found that the ability to represent the Gaussian sea was directly correlated with the *effective components* in the energy rich parts, rather than the total number of components. This is further illustrated and discussed in Study 2 in Section 7.

4.1.3 Peaked Equal Area Method

The results of a previous master thesis by Binner [1] suggests that a finer mesh around certain important frequencies, such as the eigenfrequency and peak frequency of the spectrum can lead to a more correct force and response calculation of the irregular sea. A possibility of combining these two methods, called the *peaked EAP*, was therefore suggested. The method employs the equal area principle initially, and furthermore increase the representation around the structural eigenfrequency by inserting additional components in this area.

The total number of wave components are split in a number of EAP components, N_{EAP}, and a number of peak components, N_{peak}, by the following relation:

$$N = N_{EAP} + N_{peak} = N \cdot (1 - \rho) + N \cdot \rho \tag{101}$$

Where ρ is the factor describing the percentage of the components to be dedicated to the area around the natural period, a *density factor*. The process is as follows:

1. The equal area method is first used to compute N_{EAP} wave components.
2. The block containing the eigenfrequency ω_n, and its two neighbouring blocks are removed. If the eigenfrequency lies towards either end of the spectrum, only one or none of the neighbouring blocks are removed at that side.
3. The "open" frequency domain is now split into $N_{peak} + 1, 2, 3, 4$ *or* 5 new components. The frequency span of these new methods are chosen so as to decrease towards the eigenfrequency. For the frequencies lower than ω_n, an example is the following:

   $$\Delta\omega_i = (\omega_n - \omega_{min}) \cdot \frac{N_A - i}{N_A \cdot (\frac{N_A+1}{2})} \tag{102}$$

   It can be shown that the sum of these $\Delta\omega_i$ becomes exactly the intended $\omega_n - \omega_{min}$, as

   $$\sum_{i=0}^{N_A-1} \frac{N_A - i}{N_A \cdot (\frac{N_a+1}{2})} = 1 \tag{103}$$

   A similar process is applied for the frequencies higher than the eigenfrequency.
4. The new frequencies, ω_i are found as the mean frequency in the new components, and the amplitude is found by integrating $S(\omega)$ over $\Delta\omega_i$.

The discretized wave components are shown in Figure 12. The dashed, blue line represents the position of the eigenfrequency. In this example $T_n = 9$, the density is set to 0.1, and the total number of components is 40.

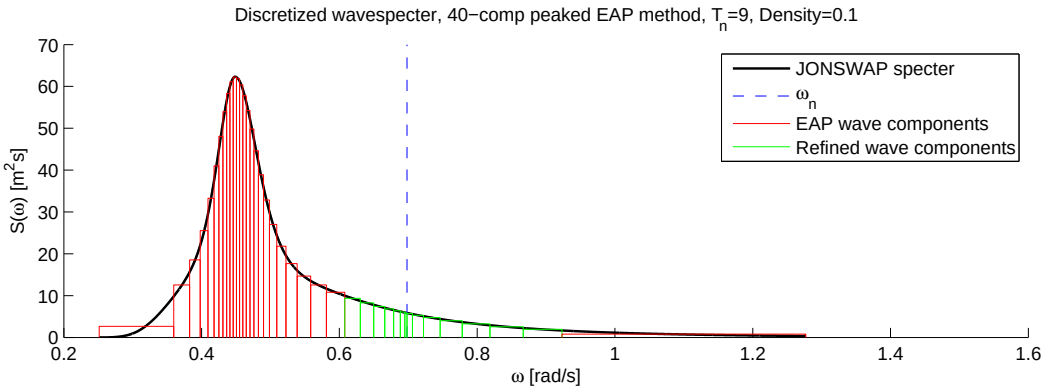

Figure 12: The peaked Equal Area Method, using 40 components

The method suffers from the same problems as the *EAP* with regards to a deterministic/random amplitude generation. As the method has even fewer components in the energy rich parts of the spectrum than a EAP with the same number of components, one would expect less accuracy in the over/under prediction of the extreme value standard deviation. The error must however be verified by testing and comparison with a complete FFT scheme using several thousand components.

4.2 Second order simulation of irregular waves

Simulation of a second order surface process is similar, but far more complex, than simulation of the first order process. The surface of the linear process is corrected by second order wave interaction components:

$$\zeta_2 = \frac{1}{4}\sum_{i=1}^{N}\sum_{j=1}^{N}\zeta_{A1,i}\zeta_{A1,j}\Bigg\{\overbrace{\left(\frac{D_{ij}^{-}-(k_ik_j+R_iR_j)}{\sqrt{R_iR_j}}+(R_i+R_j)\right)cos(\psi_i-\psi_j)}^{difference\ \ frequency} + \underbrace{\left(\frac{D_{ij}^{+}-(k_ik_j-R_iR_j)}{\sqrt{R_iR_j}}+(R_i+R_j)\right)cos(\psi_i+\psi_j)\Bigg\}}_{sum\ \ frequency} \tag{104}$$

Where the R's, D's and ψ's are described in Section 3.4.2. Assuming the first order process is described by N components, there will be N^2 second order correction components. Similarly, there will be N^2 correction terms to the velocity potential, which will need to be found for every step in the time domain analysis. The complexity of the system is significantly increased, and the need of a good representation by few linear components are necessary. The methods described in the previous sections might be valid for a second order process, however more research is needed to draw trustworthy conclusions.

Some additional considerations must be taken when simulating a second order process and calculating kinematics according to this theory. A truncation scheme and/or limiting the interaction terms between waves with very different frequencies, as discussed in Section 3.4.2 must be introduced. It is important to note that the result of the analysis is dependent on the choice of truncation frequency.

Another consideration is to maintain the energy in the wave spectrum. If the first order components are found from a target spectrum, and the second order process is added, the resulting surface process has more variance than the initial spectrum. As the spectrum is set up from a measured surface, the second order contributions (along with even higher order contributions) are incorporated in the wave spectrum. To avoid counting the second order contribution twice, one must first linearise the wave spectrum, i.e. find the underlying linear spectrum which will produce the target spectrum when second order components are added.

An example of the linearisation of a spectrum with a cut-off frequency corresponding to Stansberg's method ($\omega_{cut} = \sqrt{2g/H_s}$) is shown in Figure 13. In the figure a smoothing of the 200 neighbouring values of the second order contribution has been performed for the sake of clarity. The plots presented are for infinite water depth. If one use a finite water depth, there will be significant difference frequency contributions also at the frequencies around zero.

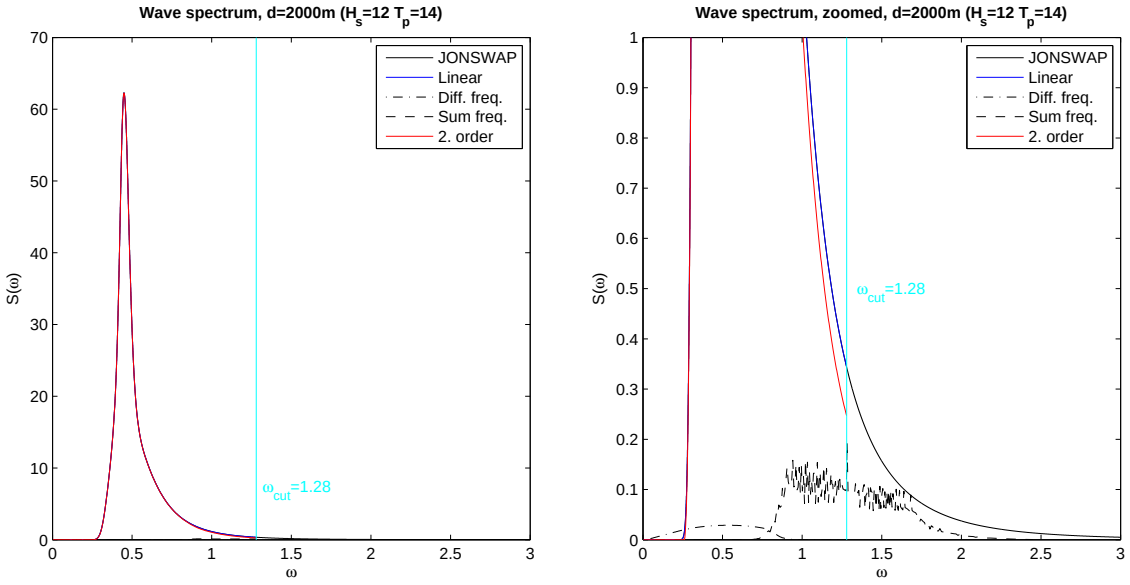

(a) Total (b) Zoomed

Figure 13: Linearised wave spectrum with Stansberg cut off frequency, deep waters

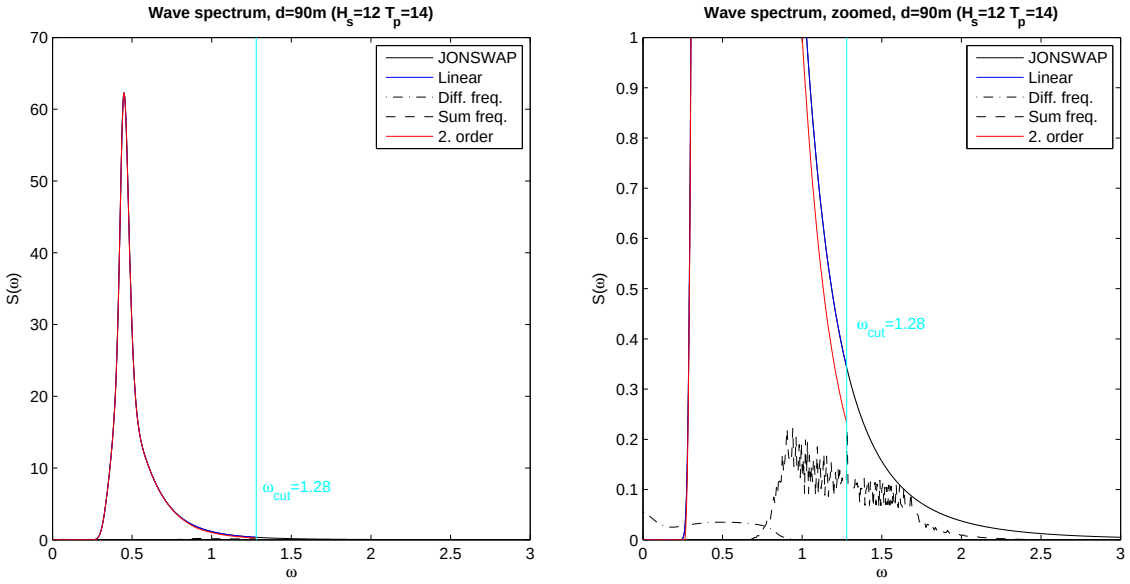

(a) Total (b) Zoomed

Figure 14: Linearised wave spectrum with Stansberg cut off frequency, finite waters, d=90m

4.3 Methods of reducing simulation length

Time domain simulation can be a tedious affair when it comes to time consumption and demand for computer power. A typical first order three hour simulation using the common FFT approach requires several thousand components N in order to satisfy the Gaussian assumption and avoid repetition in the time window. Additionally, when second order seas are to be modelled, N^2 correction terms to the surface elevation and wave kinematics must be introduced. One must therefore consider methods which reduce the length of the simulations.

4.3.1 Spool-to-extreme-wave method

One option of reducing the simulation time is the *spool to extreme wave method*. The time to set up the correct sea elevation is negligible compared to the simulation of force interaction on the structure, and singling out the i'th largest wave in each simulation is possible. One can then perform the analysis only in a certain time-range close to this peak. A significant reduction in the number of response calculations is then achieved. An illustration of the method is shown in Figure 15.

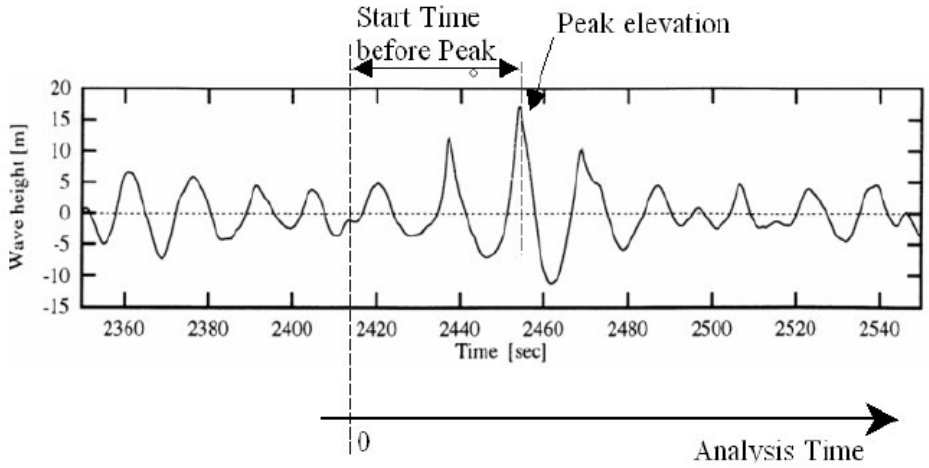

Figure 15: Spool to extreme wave method, Figure from: USFOS hydrodynamic manual [40]

The method should be used with caution, as there are several associated uncertainties. In general the time before the peak must be chosen long enough so that the dynamic behaviour of the structure is similar to when performing the complete time-domain simulation. The necessary set up time must be found through introductory studies of the structure in question, and can be exceeding 4-500 seconds for specific cases.

It is also uncertain if the highest wave will give the largest dynamic response of the structure, as the dynamic amplification factor is dependent on the frequency of the waves, cancellation effects can occur for certain structures at various frequencies, and also the dynamic motions of the structure ($\ddot{r}$, $\dot{r}$, r) will influence the position of the largest waves.

4.3.2 Spool-to-extreme-linear-response method

A slight modification of the spool to extreme wave model might be a possibility when dealing with second order irregular seas. As the degree of complexity of the second order process is N^2 compared to the N of the first order, one can run a full length first order analysis of a given

surface realization, and identify the position of the targeted extreme response. The second order analysis can then be modelled only in a certain area around this peak, by a *spool-to extreme-linear-response* (SELR) approach.

One could also assume that the main dynamic behaviour is properly simulated by the linear solution, and simply impose these on the structure. By doing this the additional second order simulation length might be reduced to, say, 30 seconds around the extreme linear response. The possibility of such methods must be assessed for each separate case. One must also consider whether the largest non linear response is found around the largest linear response. For drag dominated structures which tend to have the extremes at the largest peaks this might be an adequate solution, whilst for mass dominated structures which has maximums around mean water level the validity is questionable.

4.3.3 NewWave method

An alternative to the full random time domain simulation is the NewWave theory described by Tromans et al. [31]. By assuming that the surface elevation follows a Gaussian model, the expected elevation at an extreme event can be theoretically derived. The shape of the surface can further be found by the most probable shape associated with this occurrence, and is expressed in terms of the largest crest elevation c_{max} (found from the Rayleigh model) and the autocorrelation function $R(\tau)$ [31]:

$$\zeta(\tau) = c_{max} \cdot R(\tau) + g(\tau) \tag{105}$$

Where $\tau = t - t_1$, with t_1 the time instant of maximum crest, and g is a non-stationary Gaussian process with zero mean and varying standard deviation. This is 0 at the crest, i.e. at $t = t_1$, and increase to σ_ζ at a distance away from the crest, hence the first term is dominant in the vicinity of the crest, and can be used to calculate surface elevation and kinematics in this area. From the inverse Fourier transform of the autocorrelation function, one can describe the surface elevation around the largest crest as a sum of frequency components (for deep water waves):

$$\zeta(\tau) = \frac{c_{max}}{\sigma_\zeta^2} \sum_{i=1}^{N} |S(\omega_i) d\omega| cos(k_i x - \omega_i t) \tag{106}$$

Due to the linear assumption, the kinematics are known from the superposition of linear surface elevation. The method have proven to show good results against measurements and common random wave modelling for a platform of quasi-static behaviour, refer Elzinga et al. [32]. For dynamic modelling the single crest will not account for the randomness in the sea at which the largest crest is found, and the effect this has on the dynamic response. A possible solution is then to constrain the NewWave profile to a completely random background signal (with statistics decided from the ocean surface), which is discussed and described by Taylor et al. [29]. In this way a time series of a random surface process including the extreme crest will be found, which is similar to the *spool-to-extreme-wave method*, and will reduce the necessary simulation time.

Similar to previous discussions, the methods adequacy depend on whether the structures largest response occur near the extreme crest, and that sufficient set up time for dynamic behaviour is present (if structural motions are important).

5 Case Study

In this report several time domain simulation of a bottom fixed, vertical cylinder subjected to Morrison based wave forces are conducted. The purpose is to investigate simplified methods of simulating a linear and second order random sea with associated kinematics. In order to obtain comparable results from the various studies, the governing structural and environmental parameters must be kept similar, so also the time variables of the simulation. This section described the main features of the simulations, however, some changes had to be done for certain activities, these are discussed in the introductions to the affected studies.

5.1 The Model

The simplified marine structure consists of a single cylinder. The geometrical and material parameters are varied so as to obtain the different natural periods and dominating loads. It is assumed fixed to the seabed, at a depth of 90 m. The total length is set to 120 meter to avoid waves above the column top. The geometrical parameters are presented in Table 1.

Depth	Height	Thickness	Diameter (mass)	Diameter (drag)
90m	120m	0.1m	8m	1m

Table 1: Geometrical parameters of the cylinder

From *USFOS* a graphical interface is given in the *XACT* module, based on the parameters stated in this section. The appearance of the model is given in Figure 16a.

(a) The model

(b) Mesh of cylinder and waves

Figure 16: User interface of USFOS through GUI

The wave loads are an exponential function of wave depth. The largest wave forces, and steepest force-gradients are hence in the area around and above mean water level. It is therefore important to mesh the cylinder so these effects are catched by the model. This is done by dividing the cylinder into elements, with a fine mesh close to the sea surface, and a coarser mesh towards the seabed to save computer time. It is also dedicated more integration points in the elements close to the sea surface for increased accuracy. The cylinder mesh are shown in Figure 16b.

5.1.1 Loads

For this study only wave forces are assumed to act on the cylinders. The wave environment is given by a JONSWAP ocean wave spectrum, with peakedness parameter $\gamma = 3.3$, significant wave height $H_s = 12m$ and spectral peak period $T_p = 14s$. For the initial studies of a Gaussian sea the spectrum is defined in the range $\omega \in [0.251, 2.09](rad/s)$, while for the investigation of second order effects the spectrum is truncated according to the Stansberg cut-frequency, and the lower boundary is set to zero. The linear spectrum is shown in Figure 17.

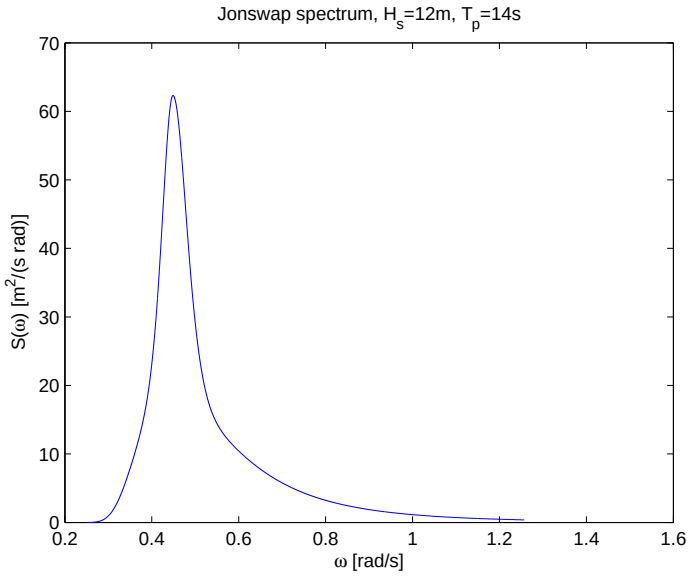

Figure 17: JONSWAP spectrum for use in analysis

In order to investigate the effect steepness have on second order correction terms, a steep hundred year sea state is additionally introduced. The peak period is maintained, while the significant wave height is increased to 16m.

The wave forces are calculated from Morison's equation, 107, with Wheeler extrapolation of the wave-kinematics to the free surface, as discussed in Section 3.3. Two load cases are to be investigated; drag dominated and mass (inertia) dominated:

$$dF = \overbrace{\rho \frac{\pi D^2}{4} C_M a_x dz}^{inertia} + \overbrace{\frac{1}{2}\rho C_D D u|u| dz}^{drag} \tag{107}$$

The dependency of diameter differ between the two load contributions. The cylinder diameter can be varied to adjust the contributions, thus a mass dominated or drag dominated load can be achieved. For a regular wave, the relation between the load terms in Eq. 107 at the mean water level is given by:

$$\frac{dF_{mass}}{dF_{drag}} = \pi \frac{C_M D}{C_D \zeta_A} \tag{108}$$

For simplicity, one can assume that the mass coefficient is twice the drag coefficient. The structure will then have largest drag loads at the mean water level when $\zeta_A/D > 2\pi$, else the mass term is largest. It is however not given that the drag loads are governing when this equality is achieved, as the drag loads decay at a rate of e^{-2kz}, which is the quadrature of the mass

term, e^{-kz}. These equations are not valid for an irregular sea which is made up of many wave components, some of which will constitute largest drag forces, and some mass.

In an irregular sea there will be several wave components with different frequencies and wave heights. If one assume that the largest extreme response occur at largest crest height, one can set up the relation to ensure the dominating loads. The crests of a Gaussian sea is given by the Rayleigh distribution, and becomes $\zeta_{max} \approx 9.6$ when 1000 seconds is used as input, while a suggestion for the period of the extreme wave were given by e.g. Forristall [8] as $\omega = 1.05 \cdot \omega_p$. The following relations holds for the diameters given in Eq. 51:

$$\begin{aligned} Mass: \quad D = 8 \longrightarrow \quad \pi \frac{C_M D}{C_D \zeta_{max}} \quad &\approx \quad \pi \frac{2 \cdot 8}{9.6} = 5.3 > 1 \qquad ok! \\ Drag: \quad D = 1 \longrightarrow \quad \pi \frac{C_M D}{C_D \zeta_{max}} \quad &\approx \quad \pi \frac{2 \cdot 1}{9.6} = 0.65 < 1 \qquad ok! \end{aligned} \tag{109}$$

Additionally, checking if the "small volume" assumption holds for the largest structure, assuming deep waters:

$$\frac{\lambda}{D} \approx \frac{\frac{2\pi g}{\omega^2}}{D} = \frac{\frac{2\pi \cdot 9.81}{(1.05\frac{2\pi}{14})^2}}{8} = 16.25 > 5 \tag{110}$$

Hence the dominating loads are uphold, and the small volume assumption is valid. At specific instances during a simulation, the mass and drag terms can alternate about being the dominant load, and also the extreme value of a specific run might be governed by the "opposite" effect. However, for most of the simulations it is expected that the target load is dominating at the extreme response.

In the above calculations approximations of hydrodynamic coefficients are used for simplification. The following paragraphs deals with a more correct set of coefficients.

Hydrodynamic coefficients

The recommended hydrodynamic coefficients from NORSOK N-003 [23] of slender structures are $C_D = 1.05$ and $C_M = 1.2$ for rough members and $C_D = 0.65$ and $C_M = 1.6$ for smooth members. Whether an 8 meter pipe for an expected extreme crest of 9.6m can be considered slender is questionable, but it is assumed that the coefficients stated above are correct for both cases. It might be more correct to apply a C_M of 2, however as the studies here does not consider absolute extremes, but rather the difference between various methods of simulating the sea spectrum, the important part is suing consistent coefficients.

The roughness is typically decided by whether or not there is marine growth. According to NORSOK one can assume marine growth up to two meters above the surface for marine structures where regular cleaning is not planned. When the sea is realized using the Gaussian, linear, assumption, NORSOK recommends an increase of the drag coefficient to somewhat account for higher order wave effects. The mass coefficient should be taken according to the previous statement. This approximation will be tested in the final study.

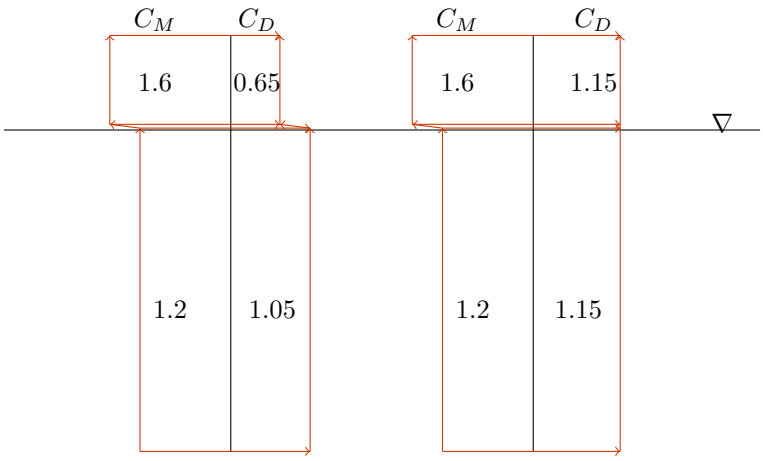

Figure 18: Morrison coefficients over the height of the cylinder for second order simulation (left) and first order simulation (right)

Important: In the previous work the default settings were used in USFOS, which is $C_D = 0.7$ and $C_M = 2$ in the simulations. To be able to compare the results these coefficients are implemented in the first, second and third study in Section 7.

5.2 Response analysis

The structural response is found by solving the equation of motion, as stated in Eq. 111.

$$\boldsymbol{M}\ddot{r} + \boldsymbol{C}\dot{r} + \boldsymbol{K}r = \boldsymbol{R}(t) \tag{111}$$

Here $\boldsymbol{M}$, $\boldsymbol{C}$ and $\boldsymbol{K}$ are the mass, damping and stiffness matrix, respectively, and the $\boldsymbol{R}$ is the load matrix. The left hand side of the equation describes the mechanical properties of the system, while the right hand side correspond to the loads, typically environmental, weights etc. The stiffness and damping will for most structures be of a non-linear nature. As this analysis does not target ultimate loads or limit states of the structure, assuming linear relationships for stiffness and damping is of sufficient accuracy. The problem can then be characterised as a linear mechanical system.

The mass and damping matrices, $\boldsymbol{M}$ and $\boldsymbol{K}$ can be assembled from simple interpolation functions for 3D beams. The mass matrix must, however, include the hydrodynamic added mass. Theoretical description of the process of assembling these matrices can be found in e.g. *USFOS* theory manual, [43]. Some discussions regarding the damping matrix is given later in this chapter.

The responses can be solved for any load history by stepwise numerical integration of the equation of motion. It is of interest to compare the full dynamic simulations versus a simplified static simulation, based on small (negligible) structural responses (r, $\dot{r}$, $\ddot{r}$), and loads without any dynamic amplification($\omega \ll \omega_n$).

5.2.1 Static Analysis

For a static analysis the displacements should be equal to zero. This is achieved by setting the stiffness (Youngs-modulus) equal to a value one hundred times larger than realistic. This yields an eigenfrequency larger than the range of frequencies in the spectrum, and the cylinder can be considered a quasi-static structure. The equation of equilibrium is then simplified to a stiffness relation, given by:

$$\boldsymbol{K}r = \boldsymbol{R} \tag{112}$$

5.2.2 Dynamic Analysis

For a structure exposed to varying environmental loads, inertia and damping forces will appear in addition to the restoring force K. This requires a solution of the complete equation of motion, as given in Eq. 111.

It is of interest to investigate how the FFT, EAP and the peaked EAP interact as the eigenperiod of the structure is varied. It has previously been shown that the EAP gives satisfactory results for marine structures with eigenperiod in the energy rich parts of the wave spectrum, with decreasing accuracy when the eigenperiod is moved towards the tail of the spectrum. Even for eigenperiods in the energy dense parts of the spectrum the dynamic amplification might be significant, and approaches for adequately simulation of these effects must be investigated. This forms the motivation for the *peaked equal area method*, as described in section 4.

In the dynamic analysis the eigenperiods is chosen to be in both the energy rich and the energy dense areas, in both ends of the spectrum. The eigenvalues can be found by solving the *general eigenvalue problem*, found by setting $\boldsymbol{C}$ and $\boldsymbol{R}$ equal to zero in Eq. 111.

$$(\boldsymbol{K} - \omega_n^2 \boldsymbol{M})\varphi_n = 0 \tag{113}$$

where ω_n and φ_n are the eigenvalues and eigenvectors, respectively. The mass term includes added mass, which is dependent on frequency and wave-height. Several eigenvalue analysis are performed in $USFOS$ to set up the wanted eigenperiods by varying the material density and Young's modulus. In order to avoid contamination in the added mass from the waves, the height is set to 0.1 meter for the eigenvalue analysis. In the studies, the following eigenperiods are used

$T_n = 4.5$ The lower part of the wave spectrum

$T_n = 9$ The high transient part right of the peak of the wave spectrum

$T_n = 14$ The high energy part of the wave spectrum

$T_n = 18$ The high transient part left of the peak of the wave spectrum

Figure 19 visualises the placing of the natural periods in the wave spectrum.

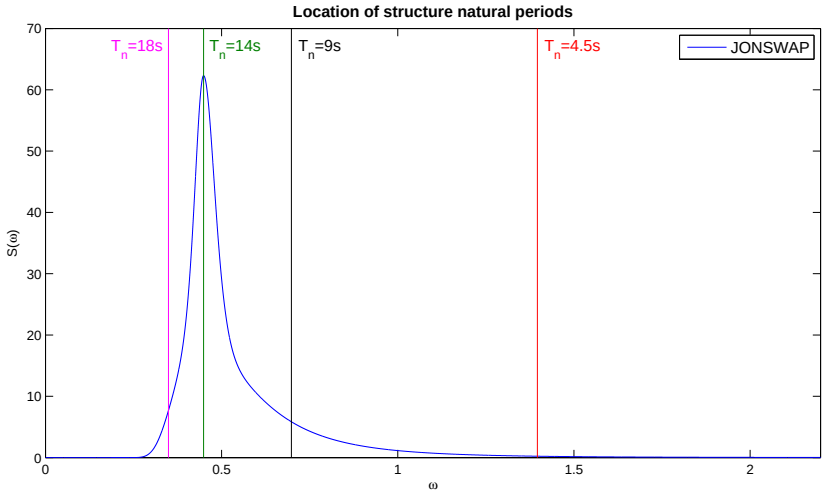

Figure 19: Placing of the cylinder's natural periods

5.2.2.1 Damping effects

The damping is a term describing the structures ability to dissipate kinetic energy, i.e. transform it into other forms of energy (such as waves). In an oscillating system different damping effects are present, and modelling these correctly are not simple. Langen [15] states that simplified methods are shown to give satisfactory solutions in many practical applications. One of these is the *Rayleigh damping*, assuming the damping matrix as proportional to the mass and stiffness matrix, given in Eq. 114.

$$\boldsymbol{C} = \alpha_1 \boldsymbol{M} + \alpha_2 \boldsymbol{K} \tag{114}$$

This is two components in the *Caughy damping series*, using multiplies of $\boldsymbol{M}$, $\boldsymbol{K}$and their inverse to ensure the orthogonality properties of the matrices. It can be readily shown that there is a relationship between the Rayleigh damping coefficients, α_1 and α_2, and the damping ratio λ_i, satisfying the following equation.

$$\lambda_i = \frac{1}{2}\left(\frac{\alpha_1}{\omega_i} + \alpha_2 \omega_i\right) \tag{115}$$

If the damping ratio for two eigenfrequencies in the appropriate range of response are known, α_1 and α_2 can be determined:

$$\alpha_1 = \frac{2\omega_1\omega_2}{\omega_2^2 - \omega_1^2}(\lambda_1\omega_2 - \lambda_2\omega_1) \tag{116}$$

$$\alpha_2 = \frac{2(\lambda_2\omega_2 - \lambda_1\omega_1)}{\omega_2^2 - \omega_1^2} \tag{117}$$

Typical damping ratios for cylinders are in the range of 2-3%. It is therefore assumed a damping ratio of $\lambda = 3\%$ at $\omega_1 = 0.42[rad/s]$, and $\omega_2 = 3.14[rad/s]$, resulting in a uniquely given damping ratio for all frequencys in the wave spectrum, given in Figure 20.

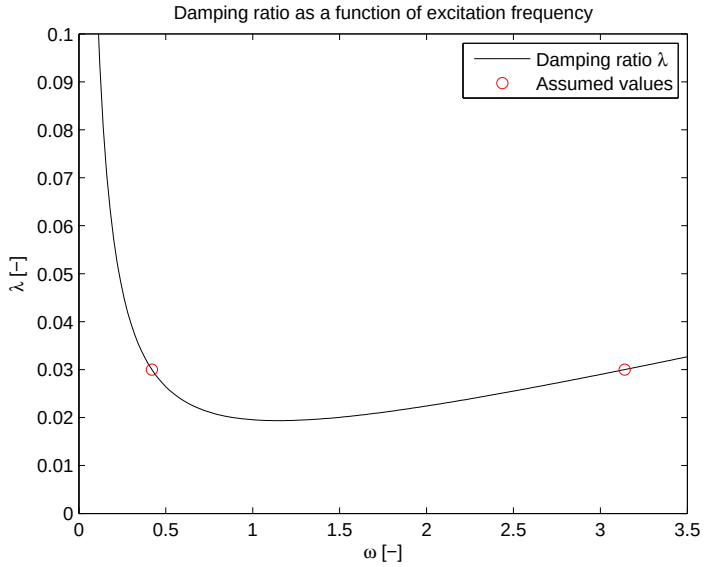

Figure 20: Damping ratios for varying frequencies (Rayleigh damping)

5.2.3 Numerical solution of the equation of motion

Several ways of solving the equation of motion numerically for time-domain simulations exist. The method applied in the computer software *USFOS*, and hence used in the analysis presented in this report, is the $HHT-\alpha$-method. The method, proposed by Hilber et al. [12] employs some sort of time averaging of the damping, stiffness and load term expressed by the α-parameter. The α -parameter introduces artificial damping of higher order vibration modes which is beneficial for the accuracy of the solution. The equilibrium equation reads, ref. *USFOS Theory Manual* [43]:

$$\begin{aligned} \boldsymbol{M}\ddot{r}_{i+1} &= \Big[(1+\alpha)\boldsymbol{R}_{i+1} - \alpha\boldsymbol{R}_i\Big] - \Big[(1+\alpha)\boldsymbol{C}\dot{r}_{i+1} - \alpha\boldsymbol{C}\dot{r}_i + (1+\alpha)\boldsymbol{K}r_{i+1} - \alpha\boldsymbol{K}r_i\Big] \\ r_{i+1} &= r_i + \Delta t\dot{r}_i + \frac{\Delta t^2}{2}(1-2\beta)\ddot{r}_i + \Delta t^2\beta\ddot{r}_{i+1} \\ \dot{r}_{i+1} &= \dot{r}_i + \Delta t(1-\gamma)\ddot{r}_i + \Delta t\gamma\ddot{r}_{i+1} \end{aligned} \tag{118}$$

The factors γ and β are the free parameters of the Newmark-β method which, along with α, determine the stability and accuracy of the quadrature formula. In order to obtain unconditional stability, the following conditions must be satisfied:

$$\begin{aligned} -\frac{1}{3} < \alpha < 0 \\ \gamma = \frac{1}{2}(1-2\alpha) \\ \beta = \frac{1}{4}(1-\alpha)^2 \end{aligned} \tag{119}$$

Note that as α equal zero, the constant average acceleration method appears. Incremental equations are obtained by subtracting the solution at i from the solution at $i+1$, i.e.:

$$\begin{aligned} \boldsymbol{M}(\ddot{r}_{i+1} - \ddot{r}_i) + (1+\alpha)(\boldsymbol{C}\dot{r}_{i+1} - \boldsymbol{C}\dot{r}_i) + (1+\alpha)(\boldsymbol{K}r_{i+1} - \boldsymbol{K}r_i) \\ = (1+\alpha)(\boldsymbol{R}_{i+1} - \boldsymbol{R}_i) + \boldsymbol{R}_i - \boldsymbol{M}\ddot{r}_i - \boldsymbol{C}\dot{r}_i - \boldsymbol{K}r_i \end{aligned} \tag{120}$$

$$\Delta\ddot{r}_{i+1} = \ddot{r}_{i+1} - \ddot{r}_i = \frac{1}{\Delta t^2\beta}\Delta r_{i+1} - \frac{1}{\Delta t\beta}\dot{r}_i - \frac{1}{2\beta}\ddot{r}_i \tag{121}$$

$$\dot{r}_{i+1} = \dot{r}_{i+1} - \dot{r}_i = \frac{\gamma}{\Delta t\beta}\Delta r_{i+1} - \frac{\gamma}{\beta}\dot{r}_i - \Delta t\left(\frac{\gamma}{2\beta} - 1\right)\ddot{r}_i \tag{122}$$

Eqs. 120 through 122 can be combined so that Δr_{i+1} is the only unknown [43]:

$$\begin{aligned} \left[(1+\alpha)\boldsymbol{K} + (1+\alpha)\frac{\gamma}{\Delta t\beta}\boldsymbol{C} + \frac{1}{\Delta t^2\beta}\boldsymbol{M}\right]\Delta r_{i+1} = (1+\alpha)(\boldsymbol{R}_{i+1} - \boldsymbol{R}_i) + \boldsymbol{R}_i - \boldsymbol{M}\ddot{r}_i - \boldsymbol{C}\dot{r}_i - \boldsymbol{K}r_i \\ + \left[\frac{1}{\Delta t\beta}\dot{r}_i + \frac{1}{2\beta}\ddot{r}_i\right]\boldsymbol{M} + \left[(1+\alpha)\left(\frac{\gamma}{\beta}\dot{r}_i + \Delta t\left(\frac{\gamma}{2\beta} - 1\right)\right)\ddot{r}_i\right]\boldsymbol{C} \end{aligned} \tag{123}$$

When Δr_{i+1} is known, the displacement, velocity and acceleration can be found:

$$\begin{aligned} r_{i+1} &= r_i + \Delta r_{i+1} \\ \dot{r}_{i+1} &= \frac{\gamma}{2\beta}\Delta r_{i+1} + \left(1 - \frac{\gamma}{\beta}\right)\dot{r}_i - \Delta t\left(\frac{\gamma}{2\beta} - 1\right)\ddot{r}_i \\ \ddot{r}_{i+1} &= \frac{1}{\Delta t^2\beta}\Delta r_{i+1} - \frac{1}{\Delta t\beta}\dot{r}_i + \left(1 - \frac{1}{2\beta}\right)\ddot{r}_i \end{aligned} \tag{124}$$

5.3 Simulation length and sample numbers

Due to the computational costs of simulating several thousand components for a long period, some simplifications are needed. In this study the length of force recording is 1000 sec. The total length contains an initial phase where the structure experience an unwanted transient response, which should not be included in the records. The necessary simulation time of this phase depend on the structure. A study of the required set up time for the various cylinders is performed, and the results are used in the subsequent studies.

When conducting a time domain simulation of a stochastic processes, it is required to take averages over a number of samples. The accuracy of the results are strongly dependent on the number of samples available. To get reliable results with limited statistical uncertainties and variations one should use a minimum of 20 simulations, but the accuracy is significantly improved by increasing this to 30-40 simulations. For the linear analysis 40 samples are used for the most part, however, due to the increased computational efforts of the second order analysis, only 30 simulations are performed in the final study.

6 Computer tools

This chapter is dedicated to explaining some of the computer tools used in this project. A brief introduction to the use of *USFOS* for time domain simulations, and how to efficiently conduct the analysis through scripting. Furthermore a description of the various *MATLAB* algorithms used in the studys. Particular interest is on the *MATLAB* algorithm for performing a second order sea realization. The scripts are specifically made for the analysis done in this project. To avoid running the complete analysis when specific results are sought, one must edit the source code manually.

6.1 Introduction to *USFOS*

The computer program *USFOS* is used to perform the time domain simulation off the cylinder. *USFOS* is a numerical tool for nonlinear ultimate strength and progressive collapse analysis of frame structures. *USFOS* started out as a program to compute collapse of tubular jacket-like structures, but have since been developed to account for many other effects. This section will describe some of the program's features related to time-domain simulations of irregular waves.

6.1.1 Modules

The *USFOS* analysis system consists of several modules for computation and treatment of results, depending on the problem at hand. The two most important are the *USFOS* analysis module, which performs all numerical calculations and generates the analysis data, and the *Xact* or *USFOS Graphical User Interface* (*GUI*). *GUI* is mainly a post processor, but it also offer help for analysis setup and execution, see e.g. *USFOS- Getting Started* [41].

For time domain simulations the *DYNRES* module is of particular interest. It converts output files from the time-domain analysis (*.dyn*) to .plo files for post processing.

The user may give the input values in several ways. The data can be distributed in up to three .fem files. Most commonly is the control parameters given in a head/control file, and the description of the model in a separate file. The loads can be included in either of these, or given in a separate file. For user defined loads (i.e. wave components) these can be given as .txt files, with correct referring in the load description parameters of the head file. The model itself can be set up in a pre processing software or other analysis software, such as *ABAQUS*, *SESAM* etc. The *STRUMAN* module in *USFOS* is then used to convert the files to input for the analysis.

6.1.2 Hydrodynamic parameters

This is a short summary of the various parameters and possibilities for calculation of hydrodynamic loads in *USFOS*, described in the *USFOS hydrodynamics manual* [40].

USFOS has embedded the following wave theories; Linear Airy with nonlinear stretching/extrapolation, Stokes 5.th order, Dean's stream function. For a simulation of irregular seas *USFOS* allows for usage of standard JONSWAP and PM type wave spectra or user defined wave components. The specified sea state is generated by superposition of regular waves through either EAP or FFT (refer section 4), and consequently linear wave theory is used. The phase angle for the different wave components are randomized, with a uniform density between 0 and 360. The random seed generator needs to be changed between each simulation to obtain different time-series. This is done through the parameter *seed*. The wave kinematics for irregular sea

states are calculated with stretched Airy theory up to the instantaneous sea surface elevation. A stationary current may also be specified. Furthermore, *USFOS* allows for pre calculated kinematics to be inserted as a grid wave. This is of particularly interest in the current project, which use pre calculations of second order wave kinematics for input to *USFOS*.

On the basis of the kinematics, either found in the program or input as grid wave, the loads are calculated according to Morison's equation (for small volume structures). The loads are introduced as a time series with a given time interval. In a dynamical analysis the wave forces have to be introduced gradually, and the wave is ramped up using a user defined envelope. *USFOS* will by default only check the elements that can get influenced by waves for hydrodynamic loads. The command *wetelem* can force *USFOS* to check all elements for hydrodynamic forces in a time-domain simulation.

If the structure exhibits significant displacement, the structure's own motion may start to influence the wave force. In *USFOS* the structure acceleration and velocities are transformed to element local axes, before subtraction from the local wave particle acceleration and velocity. To account for relative velocity is optional in *USFOS*, and is done through the *rel_velo* command. The mass and drag coefficient enter Morison's equation as default values of 0.7 and 2.0 unless otherwise specified.

USFOS allows for specific gravity fields through the command *gravity*. The buoyancy force may be calculated either by determination of the displaced volume or by direct integration of the pressure (hydrostatic and hydrodynamic) over the wet surface. The latter option is achieved by using the command *buoyform panel*. The result of integrating the hydrostatic pressure is the Archimedes buoyancy force for the submersed parts of the elements. The results of integrating the hydrodynamic pressure gives a reduced buoyancy effect during crests and an increase o the buoyancy during a through, compared to static force. The buoyancy forces are added to the load case. By default all elements are buoyant, but using the *flooding* command selected elements can be made non-buoyant.

USFOS allows for modelling of marine growth as a thickness addition to the element diameter, and can be specified by a depth profile. When the pipe is submerged the buoyancy counteracts marine growth, as the density of this is set equal to that of seawater. If the pipe is free of water, the buoyancy disappears and the weight of the marine growth becomes effective.

A method to reduce computational time is by the *SpoolWave* command. The highest crest of the surface profile simulated is located, and only a user-defined interval around this peak is simulated. It is important that the initiation time is sufficient to give similar dynamic behaviour as with a complete time-domain analysis. Refer to section 7.2.

6.1.3 Other Modelling Parameters

For cylindrical beam elements, *USFOS* require a certain aspect ratio (D/h) in order to avoid unwanted errors. This command can be overridden if the structural behaviour is accounted for. It is possible to surpass this requirement by specifying a different element type, namely the *riser* element.

USFOS allows for a separation between a *static* and *dynamic* analysis. The static is used to specify static initialization of a dynamic analysis with all loading controlled through time. This option should only be used for linear response. For the dynamic analysis certain values must be specified. The *rel_velo* for the relative motion between load and structural response as described earlier is one of them. Others are an initial time *ini_time* sufficiently large to avoid transient response from startup of analysis. For the dynamic simulation a damping ratio or Rayleigh damping model can be specified.

For time-domain simulation *Dynres* is a powerful command, allowing for selected parameters to be saved for every incremental time step. The default result file, *.out* saves all data; i.e. structure data, analysis result and restart data for each load step; in one file organized by step number. Post processing based on this file is therefore not possible, and in practice the .out file saving interval is set much higher to save time and unnecessary prints. The Dynres command, along with the DYNRES module allows for easily handled result files.

USFOS follows an updated Lagrange formulation. Accordingly, the load is applied in steps and the system stiffness equations are solved at every step. After each step the structural configurations is updated - element forces, nodal coordinates etcetera and plastic hinges are introduced if necessary. Thus each step constitutes a full linear analysis based on the updated information from all previous analysis steps.

For more detailed explanations and other areas of application it is referred to the various user and theory manuals available on the internet, e.g. [40], [41], [42].

6.1.4 Scripting for efficient use of *USFOS*

In this thesis repeated runs are performed to investigate different load combinations and to perform parametric studies of both realization methods of the surface process and model change. Additionally, when comparing results of stochastic processes, a sizeable number of samples must be available, typically 20-40 samples using different input seeds must be performed. This constitutes a large number of simulations, and the organizations of both input and output results are essential for post processing and presentation. It is therefore used a scripting technique to run many simulations consecutively, and organizing the input and output of each separate analysis in a separate folder. The input are then saved, and one can check that the input are correct for each analysis, and rerun the analysis at a later time to verify results. It also facilities post processing of the output in e.g. *MATLAB*.

USFOS runs in a UNIX environment (even in Windows), therefore an easy way is to use direct terminal, *bash*, scripting. The operations are then the same as applicable directly in the terminal, and will not be discussed further in this section. Some examples of the scripts used are given in the Appendix **??**. In order to apply this technique in Windows, one can use e.g. Cygwin, which creates a Unix-like environment and command line interface, allowing for Unix scripts to be executed in a Windows DOS operating system.

All studies in this report has been performed with some degree of scripting used. In the introduction to each study, a flowchart of the simulations and scripts for that specific study is shown. The scripts are very similar, hence only some selected examples are used for illustration purpose. These are given in Appendix A, and are used for Study 2 and the final study.

6.2 *MATLAB* for pre processing

MATLAB (*Matrix Laboratory*) have been used extensively in this work. It has been used to create the various wave components for input in all linear analysis. The program has furthermore been used extensively to present the output in form of tables and plots. A separate *MATLAB* algorithm is also developed to compute the surface and kinematics of a second order sea. While several scripts have been used in the work, this section will describe the two most pronounced, one to develop wave component input, and the algorithm for calculating kinematics from second order theory. The full scripts can be found in Appendix A.

6.2.1 Creating wave components from various realization of the spectrum

This *MATLAB* algorithm consists of a series of scripts to compute the characteristic wave components for each method of simulating the irregular sea, as described in Section 4. Furthermore, the surfaces are calculated for all methods for n samples, and the statistical parameters are found. The sets of wavecomponents are written to a .txt. for *USFOS* use in time domain simulations. These components are used in Study 1, Study 2 and Study 3 in Section 7.
The flow chart of the algorithm along with output values are given in Figure 21

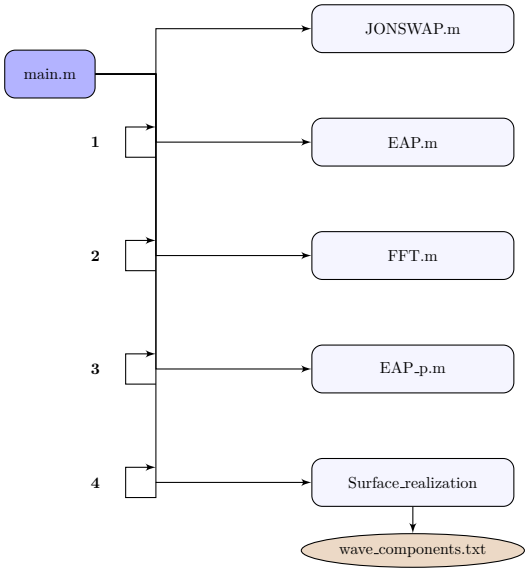

Figure 21: Flowchart for *MATLAB* scripts creating the input files for *USFOS*

Here the loops in (1), (2), and (3) are repeated for the desired number of different spectral resolution, for instance when simulating both with 50, 100 and 150 wave components. This can be set different for EAP and FFT methods. The loop in (4) is repeated for all the above methods, for all n samples, using both the random phase, random amplitude and random frequency as appropriate. The values found in the first functions are the deterministic values of amplitudes and frequencies.

A short description of each function is given in the following. It is referred to the complete *MATLAB* script in Appendix A.

main.m The main function defines important input parameters, executes the various functions, and calculates some theoretical values. This is also the function where all random numbers are generated so as to maintain the same random input in all the phase/frequency/amplitude. Therefore three sets of input seeds are created for all the n different realizations. Furthermore, it opens the files for wave components, and moves them to appropriate directories when written. Additionally, the statistical parameters that are found for each run of *surface_realization.m* for a given case is averaged and printed to the terminal. This enables a quick overview of whether the computed wave components give statistical parameters of the surface as expected, and is in some ways a check of the run.

JONSWAP.m The JONSWAP wave spectrum is set up in this function, according to Eq. 18, with peakedness factor γ of 3.3. 10 million frequency components are used for setting up the spectrum. The reason for using such a high frequency resolution is to avoid errors due to numerical integration when the wave components are assembled. The spectral moments are found for use in theoretical calculations.

EAP.m This function makes a set of wave components based on the equal area method. One can choose to plot a graph to illustrate how the wave components become in comparison with the wave spectrum.

FFT.m This function makes a set of wave components based on the fast Fourier transformation, with a constant $\Delta\omega$. One can choose to plot a graph to illustrate how the wave components become in comparison with the wave spectrum.

EAP_p.m This method sets first up the equal area components based on the total number of components minus those who shall be placed in the proximity to the eigenperiod. Furthermore it locates which wave component the eigenperiod is found, and based on whether this is in the tail region or in the middle of the spectrum, it subdivides the area around it further.

surface_realization.m This function takes in a set of amplitudes, frequencies, seeds frequency ranges and some parameter describing what should be done to these. Given that parameter, it goes on to either create randomly distributed amplitudes, frequencies or both, according to Section 4. Then the surface is set up, and statistical values are found. Furthermore, the wave components in term of amplitudes, periods and seeds are written to a .txt file. Note that as the surface realization here is found using the cosine function, and *USFOS* use sine, a phase shift of 90 degrees is subtracted from all the phases. In this way, the statistical parameters of the surface elevation calculated here will be similar to those found from *USFOS*' surface elevation.

6.3 Wave kinematics for second order irregular seas

An algorithm has been developed for simulation of second order sea. The main function is to calculate the second order surface profile and related *horizontal* kinematics. The theory used are the solution to the second order wave-wave interaction presented in 3.4.2, more precisely Eq.'s 75 through 77. The program find the approximations to the second order kinematics according to Wheeler and Stansberg's methods, and compares these with he Gaussian Wheeler stretching. The linear components can be found through either FFT, EAP or peaked EAP, using either the PM or JONSWAP spectrum. Furthermore, it is possible choose whether to plot time histories and instantaneous profiles of the surface and kinematics, and/or to write the information to files for input to *USFOS*. The flow of the algorithm is presented in Figure 52. The various scripts are executed in a left-to-right fashion, and where there are scripts in vertical direction, only one are executed. This means that *linear_waves.m* are executed before *second_order.m*, and that either a PM or JONSWAP spectrum is created in *PM.m* or *JONSWAP.m*, respectively.

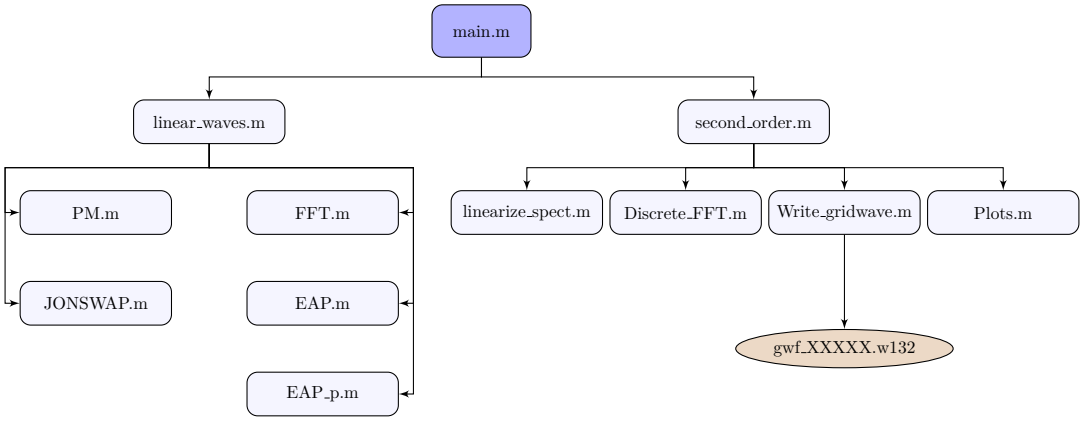

Figure 22: Flow chart for *MATLAB* algorithm to compute second order kinematics

The program is designed specifically to create second order kinematics for an irregular wave, write these to a file, and compare the kinematic profiles against other approximations. The different code are split into various functions that are executed consecutively. This makes the code more orderly, and comprehensible. While this algorithm is made specifically for the task at hand, each of these subroutines can be extracted and easily implemented in other applications.

The main parameters of the simulations, such as information about the sea state, depth, frequency resolution etcetera are defined in *main.m*, and fed to the other functions. Some important variables define which paths the program shall take, i.e.:

- *spect* Decides which of the spectra to be used, 1=PM, 2=JONSWAP.
- *decomp* Decides which of the spectral decompositions to be used, 1=FFT, 2=EAP, 3=peaked EAP. The latter require additionally a *density* and *Tn* variable
- *plott* Decides whether the program shall plot the various kinematics, and/or write the kinematics to files for input to *USFOS* as grid wave. 1=plot only, 2=write only, 3=both. Writing the grid wave files are the most computationally expensive part of the algorithm, and should be excluded if the objective is not find responses, but rather show various effects in kinematics and surface statistics *USFOS*.

The various scripts are given in A with detailed comments. It will in the following paragraphs be given a short description of each script. Note that the scripts *JONSWAP.m*, *FFT.m*, *EAP.m* and *EAP_p.m* are the same as described previously, and will hence not be repeated here.

main.m The main function defines important input parameters and executes the scripts consecutively. Furthermore it calculates the theoretical statistics of surface extremes from the Forristall and Rayleigh distribution (see Section 2), and saves the statistics of each run. When all different seeds are completed, the statistical parameters of the surface are found and printed to terminal. This enables a quick overview of whether the computed wave components give statistical parameters of the surface as expected, and is in some ways a check of the simulation.

linear_waves.m This function is an intermediate stop for generating linear wave components. It assembles the second linear wave spectrum, and finds the linear wave components. Both the spectrum and spectral discretization can be varied.

PM.m This function is an alternative to the JONSWAP spectrum, and sets up the Pierson Moskowitz spectrum as given in Section 2.1.2.

second_order.m The second order corrections are treated in this function. First, the necessary D's R's, k's and ω's as specified in Section 3.4.2 are assembled. Furthermore the script *linearize_spect.txt* is run, which returns the linear and second order surface amplitudes. These are input to *Discrete_FFT.m* which performs a Fourier Transform of the second order surface, and establish a new sets of amplitudes/frequencies/seeds. Furthermore a surface realization is performed, and, depending on the *plot* variable, scripts plotting or writing grid wave files are executed.

linearize_spect.m This function linearises the wave spectrum. It is an iterative procedure, where the linear amplitudes are included as first guess. From these the second order correction terms are found. These are sorted within the frequency ranges given by the linear components. The additional variance from these corrections are summed, and when enforcing similar variance at a given frequency, the original linear components are slightly reduced. The procedure is repeated 3 times, as the convergence was shown in a test case to be quick. At very low frequencies, and frequencies above the truncation, the linear contributions are 0, and hence some additional variance is introduced in the second order simulation.

Discrete_FFT.m In this script a Fourier transform of the second order free surface is conducted to obtain a new set of linear wave components, which will reproduce the second order surface. The complete simulation is performed, and the transformation of these are done using a built-in algorithm in *MATLAB*. A low pass filtering is then conducted, removing all components with frequency higher than $4\omega_p$ as described in Section 3. This means that the resulting wave components will not completely depict the second order sea, but much better than the original linear components.

Write_gridwave.m This function writes the input files for *USFOS* analysis. The mesh of the grid is defined in the top of this script, making it easy to decide on a grid mesh for a particular case. For the current usage, a mesh using only one node in the horizontal plane (xy), and a fine mesh in vertical is conducted, to be optimized for the usage of a cylinder assumed to have small motions. Furthermore, it is chosen to only calculate horizontal velocity and acceleration. One can easily implement pressure and/or kinematics in other directions by adding formulas at their respective places in the code.

Plots.m The final script plots the surface elevation and kinematics in various illustrative ways. Plots of the time history of the surface along with free surface kinematics from various calculation methods are given. Furthermore, plots of the kinematic profiles at the instant of extreme free surface kinematics are done in this script.

7 Introductory studies

This section contains a set of separate studies of various aspects of the simulation of an irregular sea. The objective is to develop a simplified approach to the computationally demanding time domain simulation of a second order sea. First, however, an issue regarding simulations of irregular seas in the computer software *USFOS* were observed in the project work [2], and must be addressed. The following four studies are performed in this section:

(1) A reassessment of the results found in the project work [2], where the deviation from the standard Gaussian process of the simulations might suggest faulty simulations in *USFOS*.

(2) A study of the required time to remove transient behaviour in a spool-wave analysis, in order to optimize the set-up time for second order analysis

(3) A comparitive study of the various methods of representing the sea surface, described in 4, for a linear surface simulation.

(4) Verification and discussions of the *MATLAB* algorithm for calculating second order kinematics on a grid.

Based on the results of the above mentioned studies, a set of short term time domain simulations is to be performed to establish extreme distributions. Different methods of approximating wave kinematics will be performed including Wheeler stretch of a linear and a second order sea, complete second order kinematics from Stansberg method , and a *spool-to-extreme-linear-response* (SELR) approach, as described in 4.3.2. If the results found under item (b) suggest that a simplified approach for realizing the sea spectrum is adequate, this procedure shall also be tested for simulation of a second order process.

The results in this section are found and discussed in terms of statistical parameters of the surface process and extreme value distributions of the extreme load and responses. The latter are assumed to follow a Gumbel extreme value distribution, while the theoretical values for the surface statistics are extensively in Section 2. The dimensions of the cylinder is varied to account for different load effects, as described in the case study.

7.1 Study 1: Project revisited

A project work conducted by the author in the fall of 2013 presented some unexpected results. In this study simplified ways of realizing the sea surface from a wave spectrum were investigated, using similar structures and sea environment as presented in Section 5. The results showed that the commonly accepted FFT procedure gave significantly lower results for extremes as compared to theoretical approximations. It was also shown that the resulting surface statistics of the simulations did not adequately represent a Gaussian process. A further investigation into the potential reasons for this are here conducted. It is referred to the project report in [2] for the complete simulation procedure and results. The statistics of the surface for the FFT simulation is given in Table 2. Here a Gaussian surface, and with Rayleigh/Rice distributed maxima's are used for the theoretical values, which give similar mean and standard deviation of extremes. Due to the individually distributed maxima, and that a limited amount of waves are simulated in 1000 seconds, the theoretical values are expected to be slightly higher than the results from the simulations. In the following table, and the rest of this report, ζ_{max} and $\sigma_{\zeta_{max}}$ is mean and standard deviation of the extreme surface elevation, $\gamma_{2,\zeta}$ and $\gamma_{1,\zeta}$ are the kurtosis and skewness parameters, respectively, while μ_ζ and σ_ζ are the mean and standard deviation of the surface process.

Procedure	$\lvert\zeta_{max}\rvert$	$\sigma_{\zeta_{max}}$	ζ_{max}	ζ_{min}	σ_ζ	$\gamma_{2,\zeta}$	$\gamma_{1,\zeta}$	μ_ζ
Theory	10.2	1.19	9.35	-9.35	3	3	0	0
FFT ($N = 1000$)	9.18	0.8	8.74	-8.95	3.03	2.675	0	0

Table 2: Statistical parameters from Project work [2], 1000 components used in the FFT approach

The theoretical values presented here deviates from the theoretical values presented in [2]. The reason is that the work cited are faulty, in two ways. The first being that the period of which one computes the number of local maxima in a Rician distribution were taken to be the mean zero-up-crossing period (T_{m02}), when one should use the T_{m24}, which is significantly lower, yielding a significantly larger number of peaks, and therefore larger expected extremes. The second error is that the extreme values (which can be both positive and negative) have actually a $2 \cdot N$ number of local maximas, which in turn gives a larger expected extreme. In the further studies one will discuss both the absolute extreme, and the maxima, which occur N times.

7.1.1 Identifying the issue

In the study only 20 samples were used, which is below the lower bound of the NORSOK recommendation (25-40 samples). One can therefore question whether the values found are prone to large statistical uncertainties. To check this 200 new surface realisations were found from the 200 first seeds of *USFOS*. The bulk of time consumption of a time-domain analysis are the step-by step solutions to the equation of motion, and therefore producing 200 new surface realisations from the same wave-spectrum without solving the equation of motion can give a quick check of how the statistical parameters should look. The surface statistics are also compared against a similar results from an analysis of 200 sea surfaces conducted in *MATLAB*, in order to control whether *USFOS* performs errors when simulating the Gaussian process.

The resulting statistics of the surface are presented in Table 3.

Procedure	$\lvert\zeta_{max}\rvert$	$\sigma_{\lvert\zeta_{max}\rvert}$	ζ_{max}	$\sigma_{\zeta_{max}}$	ζ_{min}	σ_ζ	$\gamma_{2,\zeta}$	$\gamma_{1,\zeta}$	μ_ζ
Theory	10.2	1.19	9.58	1.28	-9.58	3	3	0	0
FFT (20 samples, U)	9.18	0.76	8.74	0.6	-8.95	3.03	2.68	0	0
FFT (200 samples, U)	9.1	0.8	8.72	0.77	-8.81	3	2.68	0	0
FFT (200 samples, M)	9.81	1.12	9.33	1.14	-9.27	2.94	2.94	0	0

Table 3: Comparison between surface extremes from *USFOS* (U) and matlab (M)

From Table 3 it is observed that the *USFOS* generated surface elevation process does not converge towards the theoretical value, and one can also see that the kurtosis does not satisfy the Gaussian requirements, even though 200 samples have been used to create the statistics. On the other hand, the *MATLAB* generated surfaces show a much better agreement with the theoretical values, both with regards to kurtosis and extreme value parameters. From Section 2 an expression of the *order of error* of the extreme values were found. Eq. 125 gives an approximation of the error, where N_0 is the total number of zero-up-crossing waves found to be 90 ($N = 1000/T_{m02} = 1000/11.5 \approx 90$).

$$\begin{aligned} e_{|\zeta_{max}|} &= O\left(\sigma_\zeta (ln(2 \cdot n_0)^{-3/2}\right) &= 0.25 \\ e_{\zeta_{max}} &= O\left(\sigma_\zeta (ln(n_0)^{-3/2}\right) &= 0.3 \end{aligned} \tag{125}$$

It seems that the *MATLAB* generated surfaces are significantly more in accordance to the theoretical values and theoretical expected errors. To investigate this further, the seeds (phase angles) used for realizing the surface in *USFOS* were extracted, and run through the *MATLAB* program. Similarly, the *MATLAB* generated phases were run through *USFOS*. Both analysis reproduced the statistical values from the other program in Table 3. As all other parameters were checked to be the same, it is reasonable to assume that any sort of error stems from the generation of the random phase angles.

It is of interest to find out if this error occurs only for the 1000 component FFT approach. Therefore new simulations (only of surface elevation) is conducted, where the number of components are varied from 500 to 5000. 200 simulations were performed with both *USFOS* and *MATLAB* generated phases. The average of the resulting kurtosis and extreme values are shown in Figure 23. The standard deviation of the extremes are included as well.

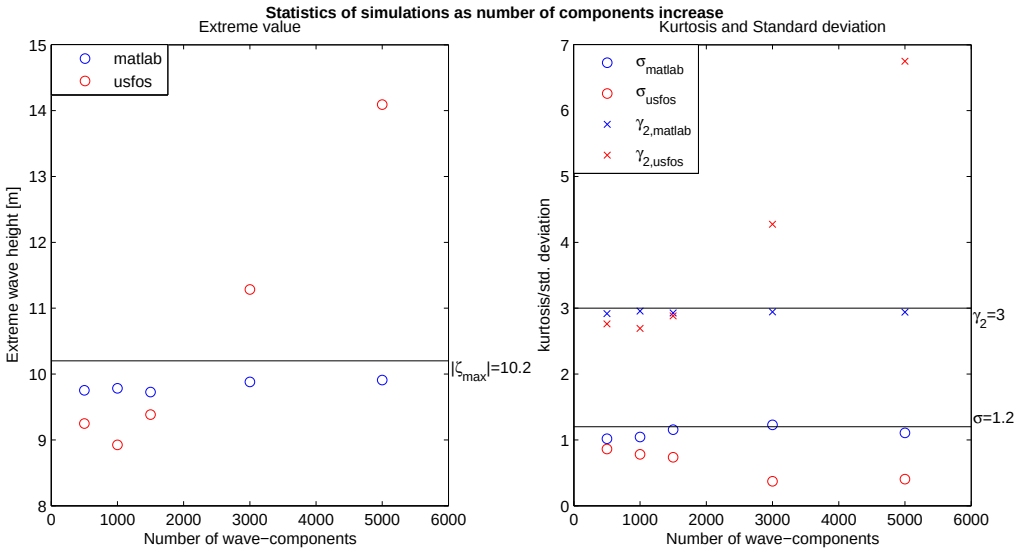

Figure 23: Extreme value (left) and std. dev. and kurtosis (right) plotted against N components

It is observed from Figure 23 that the *MATLAB* results are in accordance with the theoretically expected behaviour, with a good representation even using 500 components, and converging as the number increase. The *USFOS* values shows no such convergence, and the results at the different number of components are scattered, for most cases far from the expected values. The kurtosis and extreme value under estimates the theoretical values at a ”low” number of components, 500-1500, but as the number increase to 3 and 5 thousand, one sees that the extremes and kurtosis increase significantly, far higher than the theoretical. Additionally, one sees that the standard deviation decrease as the number grows. The reason is found when inspecting one of the 5000 component- simulations with both *USFOS* and *MATLAB* phases, presented in Figure 24.

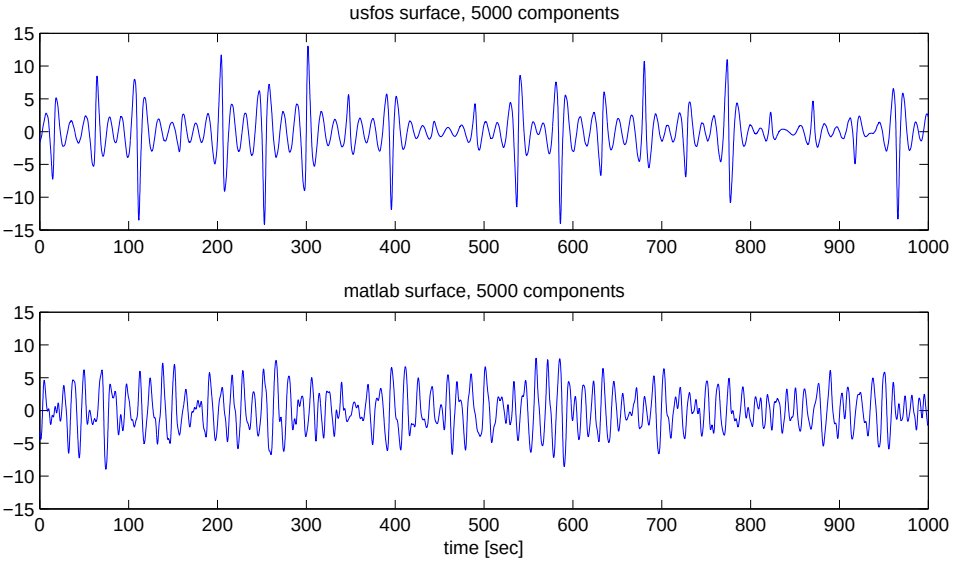

Figure 24: Surface realization with 5000 components, using *USFOS* seed (upper) and *MATLAB* phases (lower)

The lower graph shows a surface process as expected, with a certain groupiness of the waves,

i.e. set of consecutive high waves. The upper graph shows no such things, and has in general a very low surface elevation with some very large single maxima. While the lower illustrates what one typically associate with a time series of surface elevation, the upper figure shows something completely different. The *USFOS* seeds create a process with some very large maxima, giving rise to a large kurtosis and extreme wave height. These maxima are, however, close in size, thus a low standard deviation of the extremes. The graphs presented in Figure 23 are in compliance with the plots in Figure 24.

From the results presented in the previous plots and tables it is clear that the surface realization found by using *USFOS* seeds in combination with the FFT approach is not representing a Gaussian process. From comparisons with *MATLAB*, and the use of *MATLAB* with *USFOS* generated phases, it is clear that something is avry with the phase generation in *USFOS*. It is then possible that an equal area procedure will not suffer the same issues. To investigate this further, the extreme value, standard deviation and kurtosis are compared for the EAP. The 20-sample values are taken from [2], while the 200 sample values are generated using the *MATLAB* script with both *USFOS* and *MATLAB* generated phase angles.

	20 samples-*USFOS*			**200 samples-*USFOS***			**200 samples-*MATLAB***		
	$\lvert\zeta_{max}\rvert$	$\sigma_{\lvert\zeta_{max}\rvert}$	γ_2	$\lvert\zeta_{max}\rvert$	$\sigma_{\lvert\zeta_{max}\rvert}$	γ_2	$\lvert\zeta_{max}\rvert$	$\sigma_{\lvert\zeta_{max}\rvert}$	γ_2
EAP-50	9.97	1.0	2.92	9.97	1.0	2.96	9.88	1.05	2.94
EAP-100	9.7	1.02	2.95	9.95	1.1	2.95	9.86	1.03	2.92
EAP-150	9.4	1.0	2.87	9.86	1.1	2.94	9.83	1.16	2.92
EAP-1000	-	-	-	9.75	1.0	2.87	9.82	1.18	2.94
EAP-3000	-	-	-	10.2	0.94	3.05	9.84	1.15	2.96
EAP-5000	-	-	-	10.54	0.93	3.14	9.95	1.23	2.94

Table 4: Comparison between surface extremes from EAP simulations in *USFOS* and *MATLAB*

It is seen that the errors are less when using the EAP than FFT. The large deviation of the 150 components with the 20 sample seems to be incurred by a lack of sufficient data, i.e. a statistical uncertainty. One observes further that the trend from the FFT simulations of increased kurtosis and extreme value, and decreased standard deviation, as the number of components become very large is present, but far less pronounced. Similarly to the behaviour of the *MATLAB* generated FFT surfaces, the *MATLAB* generated EAP surfaces seems to be converging, and approximates a Gaussian process fairly well for all cases. It is expected that the same behaviour will be shown for the peaked EAP as well.

One have located the error, the random phase angles, and found that the error seems to be less pronounced when the frequencies are not uniformly spaced. The next thing to investigate is therefore these phases, to see if there are significant differences in the phases from *MATLAB* and *USFOS*. A table with the theoretical values, and the mean of the statistical values of the 5000 phases over the 200 different simulations are shown in Table 5. The values are given for phases in degrees.

	Mean	Variance	Skewness	Kurtosis
Theory	180	10800	0	1.8
USFOS phases	179.49	10795	0.00	1.80
MATLAB phases	180.2	10804	0.00	1.80

Table 5: Statistics of the uniformly distributed phases

There are no clear differences in the statistical values. A further check is to plot the cumulative distribution, and see if it lies in a straight line in a probability plot, as done in Figure 25.

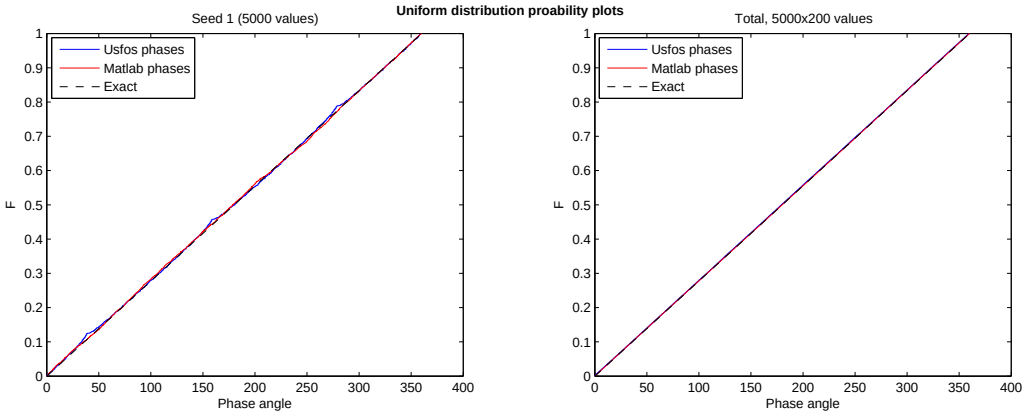

Figure 25: Uniform distribution of phase angles

The plots shows that both *USFOS* and *MATLAB* phases follow a uniform distribution. However, as the wavespectrum is such that almost all energy is found in a very small area of the frequency range, an issue can arise if the phases of these components are correlated. To find out if this is the case, an approach where the phases from *USFOS* are randomly distorted (within each sample, i.e. seed 1 etcetera) are performed. The results of this procedure for 1000, 3000 and 5000 wave components, along with comparison of the *MATLAB* and original *USFOS* results are shown in Table 6.

	Randomly distorted *USFOS*			**Ordinary *USFOS***			***MATLAB***		
	$\lvert\zeta_{max}\rvert$	$\sigma_{\lvert\zeta_{max}\rvert}$	γ_2	$\lvert\zeta_{max}\rvert$	$\sigma_{\lvert\zeta_{max}\rvert}$	γ_2	$\lvert\zeta_{max}\rvert$	$\sigma_{\lvert\zeta_{max}\rvert}$	γ_2
FFT-1000	9.76	1.12	2.91	8.92	0.78	2.69	9.78	1.04	2.96
FFT-3000	9.82	1.04	2.92	11.28	0.37	4.27	9.88	1.23	2.94
FFT-5000	9.82	1.15	2.94	14.09	0.41	6.75	9.901	1.11	2.94

Table 6: Random distortion of *USFOS* phases, compared against previous simulations (200 samples)

The results show that a randomly distortion of the *USFOS* phases makes the statistical properties approach that of the expected Gaussian process. One further finds that the surface elevation now resembles the lower plot in Figure 24. The reason for the low values in the project work seems to be an unfavourable set of randomly generated phases in the *USFOS* seed generator. If the main energy contributions of the wave spectrum (around the spectral peak period) had a set of correlated phases, this would explain the results. When this occur for all of the 200 seeds, one can conclude that something is wrong with the generation, and *USFOS*-generated phases should not be used. However, as the loads and responses are the values sought for, it is of interest to investigate how these are inflicted.

7.1.2 Impact on the extreme forces

The goal of a time domain simulation is most often to investigate how a structure behaves in a given seastate. Important quantities are therefore the most extreme forces, moments, motions (..etc.) that the structure will experience. One can expect some of the same issues as found for the extreme surface elevation, but it is of interest to find out more about how these quantities are affected directly. As it is required a full solution of the equation of motion to assemble these values, one compares the original result (20 *USFOS* seeds) versus 20, and 40 *MATLAB* generated seeds. Additionally, as it was found that the EAP (and peaked EAP) did not seem to suffer as much from the phase-error in *USFOS* one includes the results of the 100 wave component EAP and peaked EAP (0.1 density). The peaked EAP is included for the structure with natural period in the low energy parts, and the common EAP for a situation where the period is in the energy rich parts.. The reason for this is the EAP's inability to account for dynamics at energy dense areas of the wave spectrum, discussed in e.g. Binner [1]. That phenomena is illustrated and discussed extensively in Section 7.3 (Study 3), but is not the area of interest in this particular activity.

Note that the *MATLAB* generated seeds are run through *USFOS* to obtain the load and response histories. This is done for both mass and drag dominated structures, with eigenperiods in an energy rich (14s) and dense (4.5s) parts of the wave spectrum. The reaction overturning moment (ROM) will be representing the extreme forces and moments here.

			$T_n = 4.5$				$T_n = 14$			
Method (samples)	**Surface**		**Wave load**		**Moment**		**Wave load**		**Moment**	
	$\mu_{\zeta_{max}}$	$\sigma_{\zeta_{max}}$	μ_x	σ_X	μ_x	σ_X	μ_x	σ_X	μ_x	σ_X
MASS DOM										
FFT-*USFOS* (20)	9.18	0.76	8.85	0.53	1.25	0.11	8.85	0.53	4.46	0.46
EAP-*USFOS* (20)	9.68	1.08	-	-	-	-	9.51	0.93	4.56	0.73
EAP-p-*USFOS* (20)	9.87	1.00	9.50	1.10	1.34	0.12	-	-	-	-
FFT-*MATLAB* (20)	9.50	0.94	9.02	0.84	1.30	0.14	9.02	0.83	4.15	0.69
FFT-*MATLAB* (40)	9.70	1.08	9.34	1.08	1.34	0.14	9.34	1.08	4.33	0.69
DRAG DOM										
FFT-*USFOS* (20)	9.18	0.76	1.95	0.19	2.06	0.11	1.72	0.18	7.49	0.82
EAP-*USFOS* (20)	9.68	1.08	-	-	-	-	1.79	0.38	7.59	1.40
EAP-p-*USFOS* (20)	9.87	1.00	2.26	0.40	2.44	0.40	-	-	-	-
FFT-*MATLAB* (20)	9.50	0.95	2.07	0.39	2.31	0.31	1.80	0.28	7.03	1.25
FFT-*MATLAB* (40)	9.70	1.08	2.21	0.45	2.34	0.34	1.89	0.37	7.40	1.31

Table 7: Comparison of extreme load, responses and standard deviation found using *USFOS* and *MATLAB* random phases. The mass loads/moments are given in $[MN]/[GNm]$ while the drag are $0.1[MN]/0.01[GNm]$

The FFT-*MATLAB* (20) values are the 20 first samples of the total 40 simulated *MATLAB* values. Taking the extremes of the 20 latter would lead to larger mean and standard deviation than the total 40, the reason for showing the 20 is to illustrate some of the uncertainty when operating with 20 samples.

Some very interesting observations are made from Table 7. In the surface columns, one sees a remarkable better fit from the EAP methods than the FFT method with seeds from *USFOS*.

As the wave loads are correlated to the surface maxima, one finds that the *USFOS* EAP and peaked EAP are more in compliance with the "exact results" from the *MATLAB* phases. The FFT seems to give low mean of the extreme loads and, in particular, the standard deviation of the extreme loads. This was an issue of discussion in the project work, and based on the results presented it seems that the *USFOS* FFT approach underestimated the standard deviation to around 30-80% of the correct value.

The results of the reaction forces are more unclear. For the eigenperiod in the low energy part (4.5s), which is expected to have a low degree of dynamic behaviour, the reaction moments are slightly lower with the *USFOS* FFT method, around the same percentage as the loads, and the *USFOS* EAP methods gives a better approximation than the *USFOS* FFT both in terms of standard deviation and mean of extreme reaction moment.

When the eigenperiod is 14 sec, one finds that while the wave loads shows a large underestimation of the extremes, the reaction overturning moment is more in complience with the *MATLAB* results. The reason for this can simply be that the dynamic effects are very dominant and the surface elevation is only of secondary importance. The statistical uncertainties with 20 samples will therefore make the resulting mean somewhere in the proximity of the 40-sample results, but whether it is higher or lower is uncertain. However, even though the mean is reasonable described, the standard deviation is not so, and underpredicted by around one third. The *USFOS*-EAP seems to give a better result for this case also, especially in terms of the extreme standard deviation.

7.1.2.1 Effect on extreme response distribution

When using the time domain simulation in a design phase, what one typically is interested in is the extreme response distribution for the given short term statistics (H_s, T_p, etc). Assuming that the extreme response follows a Gumbel model, which is a fair assumption for long simulations, the distribution parameters are found from the mean and standard deviation of the different cases presented in Table 7 through the estimators presented in Section 2.1.5:

$$\beta = \frac{\sigma_X \sqrt{6}}{\pi} \quad \alpha = \mu_X - 0.5772 \cdot \beta \tag{126}$$

The extreme value distributions for two cases are fit to the model, the mass dominated loads with an eigenperiod of 14 s, and drag dominated loads where the eigenperiod is 4.5 sec. These are shown in Figures 26 and 27. Similar plots can be assembled for the other cases, but the trends are the same and the given plots are found sufficient.

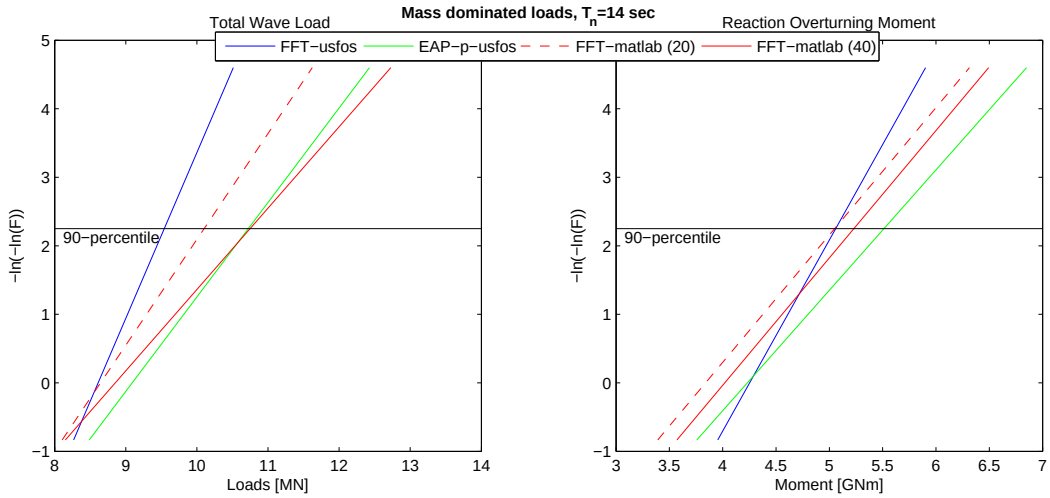

Figure 26: Example of Gumbel extreme value distributions from the discussed method, mass dominated loads, $T_n = 14s$

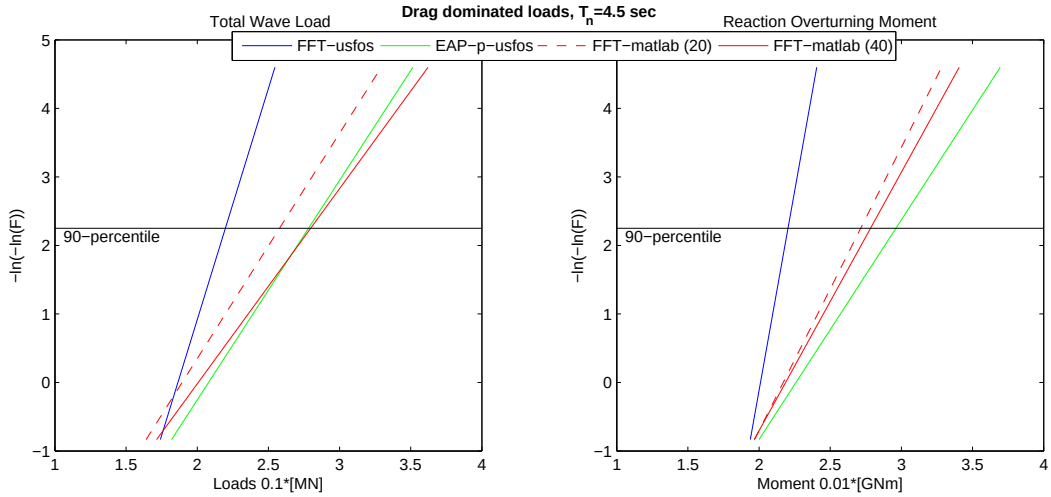

Figure 27: Example of Gumbel extreme value distributions from the discussed method, drag dominated loads, $T_n = 4.5s$

From the extreme value distributions one clearly sees that the equal area method, or peaked equal area method fits much better with the FFT from *MATLAB* generated phases. The blue line, illustrating the *USFOS* FFT deviates a lot from this, and are on the non-conservative side. For instance, the 90 percentile is used in a lot of design situations where the contour line method is applied. Using the FFT with *USFOS* generated seeds will then give much lower loads and moments, for all the cases presented, and especially for the reaction moment for the drag dominated case, where the value found at the 90 percentile is half of what the 40 sample *MATLAB* procedure give. Significant errors in the design responses are therefore incurred.

Another interesting observations is the spreading in the 40 sample FFT and the 20 sample FFT, both with *MATLAB* generated seeds. The difference in these are due to statistical uncertainties when using few samples.

7.1.3 Conclusion

From the discussions above it is clear that the *USFOS* generated seeds in an FFT approach will lead to a significant underestimation of the mean and extreme of surface elevation, and also for the loads and reaction moments. The reason seems to be that the phase angles produced in *USFOS* are in some way correlated, as a random distortion of these produce a surface elevation more in line with theory.

The errors are limited when using the equal area principle with *USFOS* seeds, and it is believed this is because the non-constant frequency separation of the wave components. However the trend seems to be that as the number of EAP components increase, an error is introduced. An alternative is to use *MATLAB* (or other software) to generate the phases, amplitudes and frequencies of the irregular sea, and input these to *USFOS*. This approach is applied in the subsequent studies

7.2 Study 2: Spool-to-extreme wave

A structures response under a given loading is significantly affected by the dynamic motions of the structure itself. When a time-domain simulation is performed on a structure with no initial motions, the transient response is an unwanted behaviour. One must remove this initial phase from the resulting force history. Similarly, if one shall conduct a *spool-to-extreme-wave* (or response) analysis, one must use a sufficient set up to remove all transient behaviour. The required initiation-time is suggested to be governed by the degree of dynamics and the shape of the structure. In the project work, and also in the previous activity, this was assumed to be 500 seconds for all the simulated cylinders. This might be overly much for some, and maybe not enough for others, therefore a more thorough study of these effects is required.

In this study the *time before peak* (TBP) in the spooling process have been varied to identify at which simulation length before an extreme peak the dynamic forces and moments at that peak is reproduced to a satisfactory degree. The loads investigated have been both mass and drag dominated, and analysis with all 4 eigenperiods discussed in 5 have been performed. Both dynamic and static simulations were conducted. This study does not say anything about whether the largest response occur at the largest peak, but aims to identify the time it takes to set up the correct response at and around the largest peak. To avoid contamination of an extreme response not at the intended peak, the response is found within a 10 second interval around the target peak.

Two methods investigated, the peaked EAP and the common FFT, both with Rayleigh distributed amplitudes. The reason for not including more methods of decomposing the spectrum is the vast amount of simulations needed. It is further assumed that the "few-component-schemes" experience similar behaviour with respect to required set up time, and a peaked EAP approach with 50 100 and 150 components did not show any ill-representation of dynamic effects such as the EAP in the project work [2]. The length of the sea state is set to 3 hour (10800 sec), and in order to avoid repetition of the wave history for the FFT approach, 3200 components are used (along with the spectrum limits given in the case study, this will ensure a non repetitive history).

The response is measured using a spool-time of 1000, 400, 300, 200, 150, 100, 50 and 25 seconds. It is assumed that 1000 seconds are enough to completely describe any dynamic behaviour. The two largest peaks are investigated by the spool wave command in *USFOS*, in order to check if there are any differences between these. It will also produce more statistical data for drawing trustworthy conclusions. This is repeated for 40 samples, for all 4 surface realizations (FFT-3200, EAP-p-50, EAP-p-100, EAP-p-150), for all 4 eigenperiods of the structure and also a quasi static simulation. An outline of the simulations are shown in Figure 28.

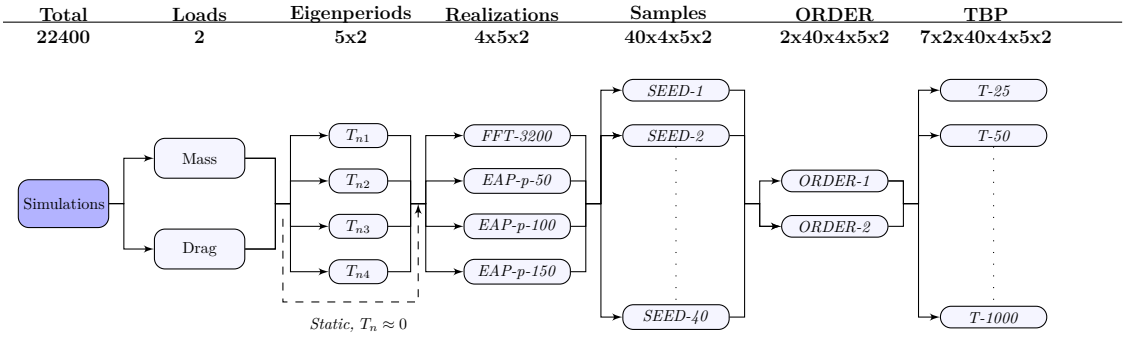

Figure 28: Overview Spool-Wave analysis, TBP=Time Before Peak and ORDER which i'th highest wave to spool to

In the post processing of the simulations, the largest extreme response in a 10 second interval around the peak wave are extracted. If the largest or second largest peak occur before 1000 seconds have passed, that sample is nulled, as one will no longer have a 1000-second result to compare against (it would be for instance 600 if the peak occur after 600 of the 10800 seconds). The three-hour simulation window was set to avoid too many nulled values. This simulation length enforced the 3200 FFT components, thus inducing large computational costs.

For each case, i.e. a set of 40 seeds x 7 TBP's, the root mean square error of the standardized response (divided by the "1000 sec exact") is found and summed, according to:

$$RMSE = \sqrt{\frac{\sum_i^N (\frac{x_i - X_i}{X_i})^2}{N}} \tag{127}$$

In this work, the requirement of a TBP to be accepted is that the RMSE is less than 1%. Furthermore the single maximum error of the 40 seeds (for each TBP) is found and standardized. For the smallest TBP which satisfies a 1% RMSE the largest error is checked to make sure that the maximum error is less than 2-3 %. If these two criteria are fulfilled, the TBP are accepted for that eigenperiod/governing load combination.

In order to verify that the analysis have run as expected, with no repetition of the surface, the extreme surface statistics are first found and compared against the theoretical values. In the following sections the main findings in the results is presented and discussed. The complete set of numerical results can be found in Appendix C.1 and C.1.

7.2.1 Discussion around surface elevation

A comparison between the extremes of the waves and the theoretical maximum is presented in Table 8. Only the case of $T_n = 4.5$ sec is included for the peaked EAP.

Procedure	ζ_{max}	$\sigma_{\zeta_{max}}$
Theory	11.6	1.0
FFT ($N = 3200$)	11.2	0.9
EAP-p ($N = 50$)	11.4	1.2
EAP-p ($N = 100$)	11.3	1.3
EAP-p ($N = 150$)	11.2	1.1

Table 8: Inspection of extremes from spool-wave analysis

The extreme values of the surface process are quite close to the theoretical, which verifies that the simulations have run as expected, and that there seems to have been no repetition of the wave history. Another test is, as the simulations have been done for both the highest and second highest peaks in each run, to look into each pair of extreme values (same seed, different order). If these are identical, then repetition might very well have occurred. For instance, a simulation of 1000 seconds with 100 FFT frequency components, would give identical first, second and third order waves. From the comparison of the two largest waves of every run one finds that no repetition has occurred for any of the methods.

It is found that some of the peaks occur before 1000 seconds have passed. The number varies between 3-8 for the different methods. It is here assumed that 32-37 samples are enough to describe the governing behaviour with respect to necessary set-up time.

7.2.2 Results from static simulations

The results from the static simulations are presented as a plot of the RMSE vs. the TBP, presented in Figure 29

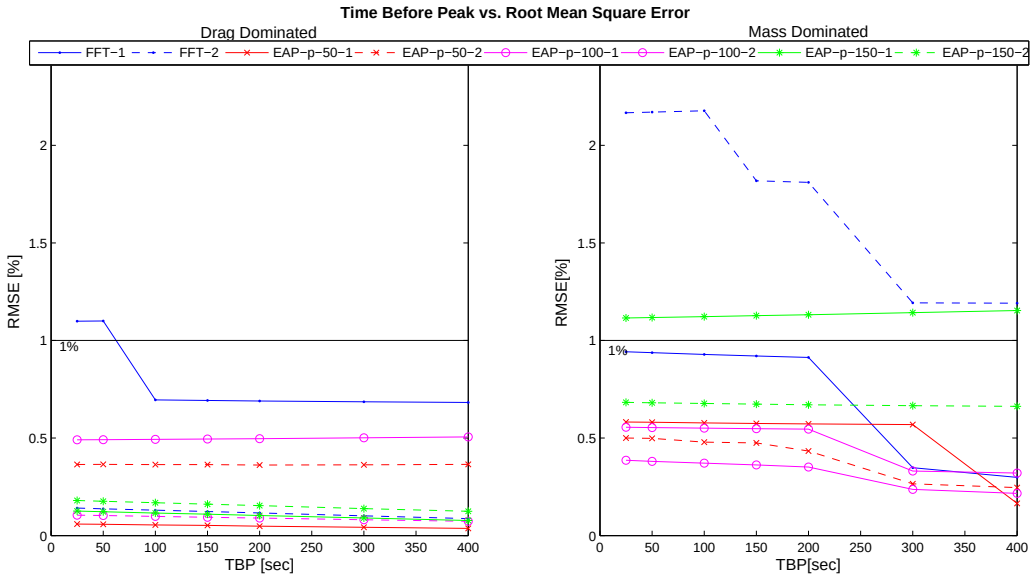

Figure 29: RMSE vs. TBP for all static runs, drag dominated loads (left) and mass dominated loads (right)

7.2.3 Discussions of static simulations

From the graphs one can see that for the drag dominated structure, the error is within the required RMSE for most cases, even at 25 second TBP. This is expected from a static simulation, as the structural motions are (close to) zero. There are no significant differences between the various peaked EAP and FFT, or whether one spools to the largest or second largest wave amplitude.

For the mass dominated load case several issues are found. Firstly, it is observed that two cases does not reach the required RMSE level, even at 400 seconds. It is also observed that one of the cases, the 150 component 1 order peaked EAP (EAP-150-1) diverges as TBP increase. When inspecting the maximum error for each case, one finds that the results varies even more, up to 5-6%, and diverges for some cases within both drag and mass dominated simulations. These results goes against any theoretical knowledge, and are due to faulty simulations.

Through an inspection of the simulated time histories of the static cases (raw data), it is found that the decimal points at which the loads are calculated and found, differ depending on the TBP used.

Time Before Peak	Actual time peak occur in *USFOS*
25	25.00025
50	50.0005
100	100.001
150	100.0015
200	200.002
400	400.004
1000	1000.01

Table 9: Target vs. Actual peak occurrence

As the loads are found at intervals of 0.1, this inflicts an error of max 10% of the load step. Therefore the structure that is simulated 1000 seconds will not have experienced the same load history as the one simulated 400 seconds, or 300 seconds or so on. So why does this not incur errors in all of the graphs in Figure 29? The surface process is generally slowly varying, thus the major behaviour is caught by all the simulations. One would also expect some sort of convergence in general, as .004 (400 sec) is closer to the values at .01 (1000 sec) than .00025 (25 sec) etcetera.

The issue is then, where does the divergence as TBP increase come for specific simulations? Consider the rapidly fluctuating response (base shear). One of the single simulations that showed divergence have been plotted in Figure 30, for base shear response.

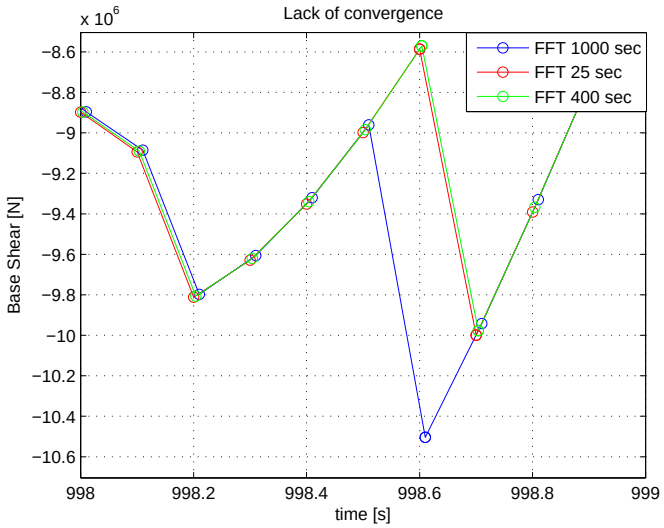

Figure 30: Lack of convergence, static analysis, 25 400 and 1000 second TBP

The graphs of both the 25, 400 and 1000 sec simulations are similar for the main part of the problem, but deviates significantly at one point, i.e. the time 998.6. The divergence becomes clear, as the red point at 998.7 are closer to the previous blue than the green, and will therefore give a better prediction of the previous blue point. One have the reverse effect of that mentioned above, i.e. 998.70025 is closer to 998.61 than 998.704.

The issue is that one have no information about how the response acts between each point when this step-by-step numerical procedure is performed. The lines are drawn directly from point to point, but there is no information suggesting that, for instance, the blue line should not follow the green and red to the 998.6, then have a rapid decrease down to the minimum value (at 998.61). Neither can one be sure the green and red should not have a rapid decrease to (around)

the blue minima at the instant 998.61, before rising again to 998.7. The problem is that the time intervals are set at 0.1, which is to high to catch these incidents, especially when the placing of the points are 10% different within the interval. As just some of the plots shows this behaviour, one can assume that this is not a significant issue, and only relevant for the cases with extreme gradients of the surface (very steep waves) which incur very steep response histories.

It is concluded that although the values varies, this is mainly due to an approximation to the significant digits used, and are consequently not wrong, only different, the same way one would find slightly different results if the complete time series were offset by 0.05 seconds. Therefore the required TBP is set to 25 seconds for the case of a static simulation.

7.2.4 Results from dynamic simulations

The results of the dynamic spoolwave analysis are presented through a set of graphs for each load/eigenperiod case. Note that the y-axis is logarithmic, to better the visibility of the plots which show larger deviations than the static case.

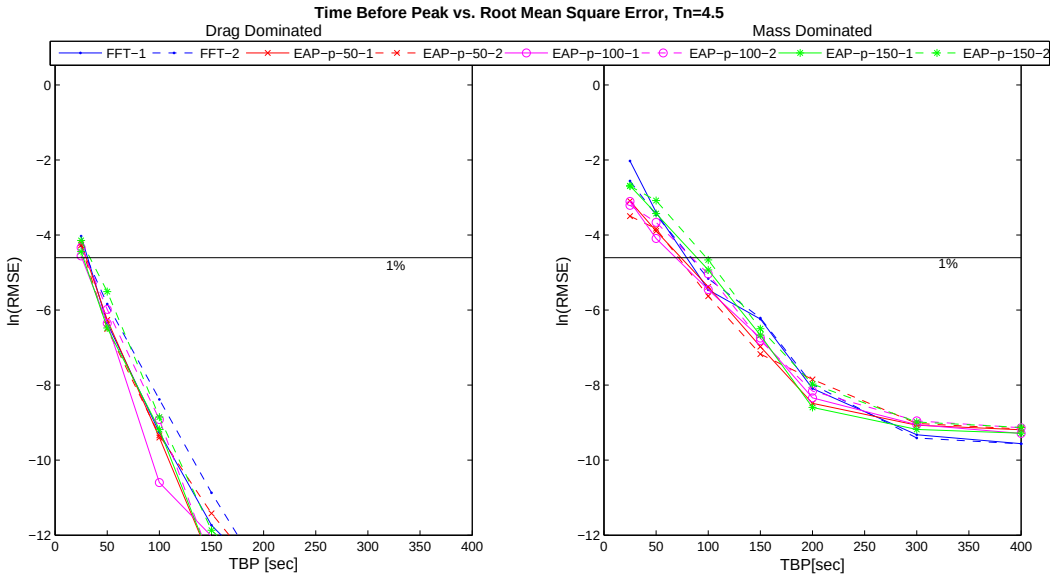

Figure 31: Required time before peak for cylinder with $T_n = 4.5$ s

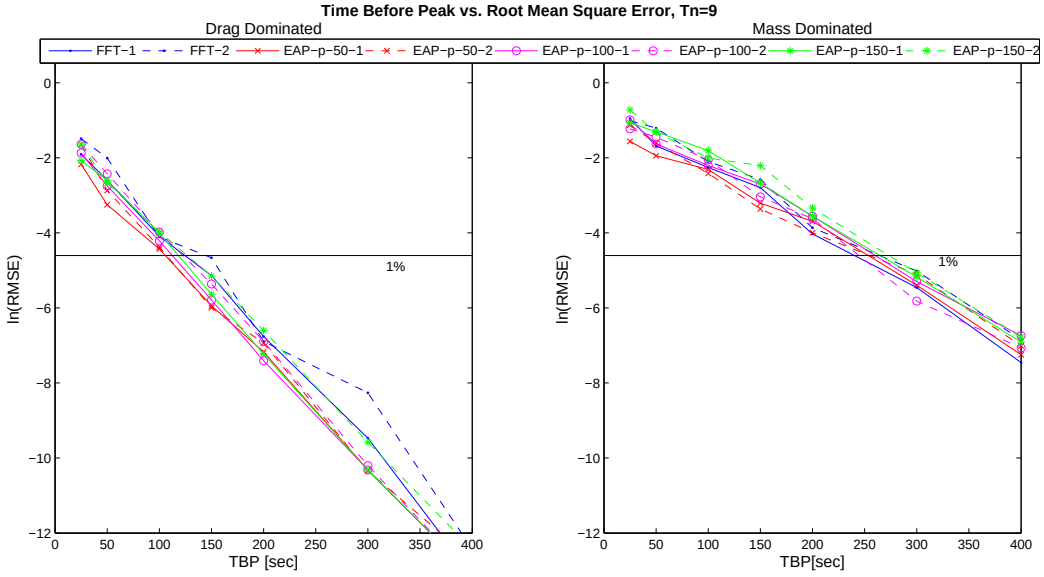

Figure 32: Required time before peak for cylinder with $T_n = 9$ s

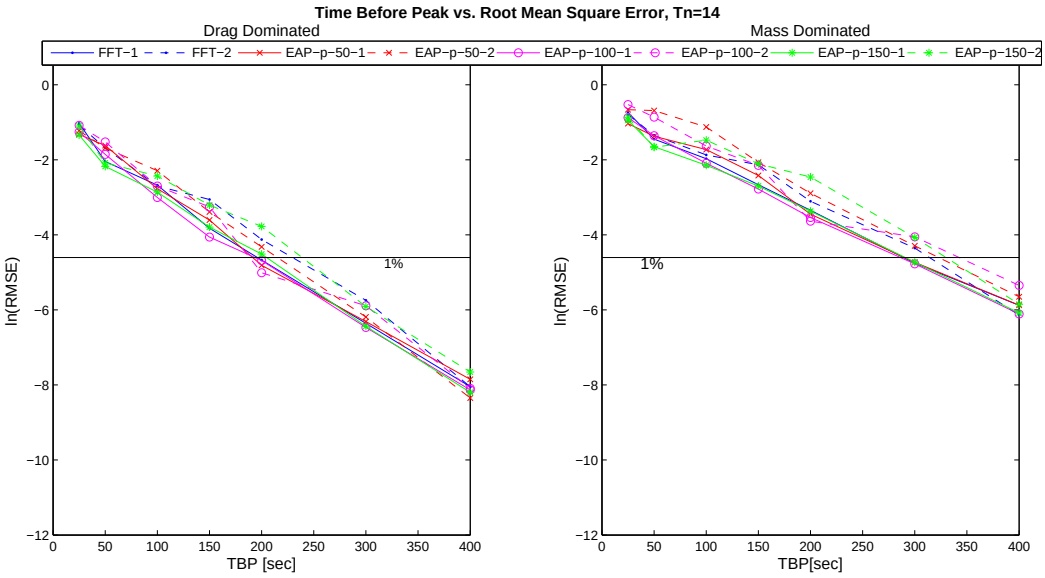

Figure 33: Required time before peak for cylinder with $T_n = 14$ s

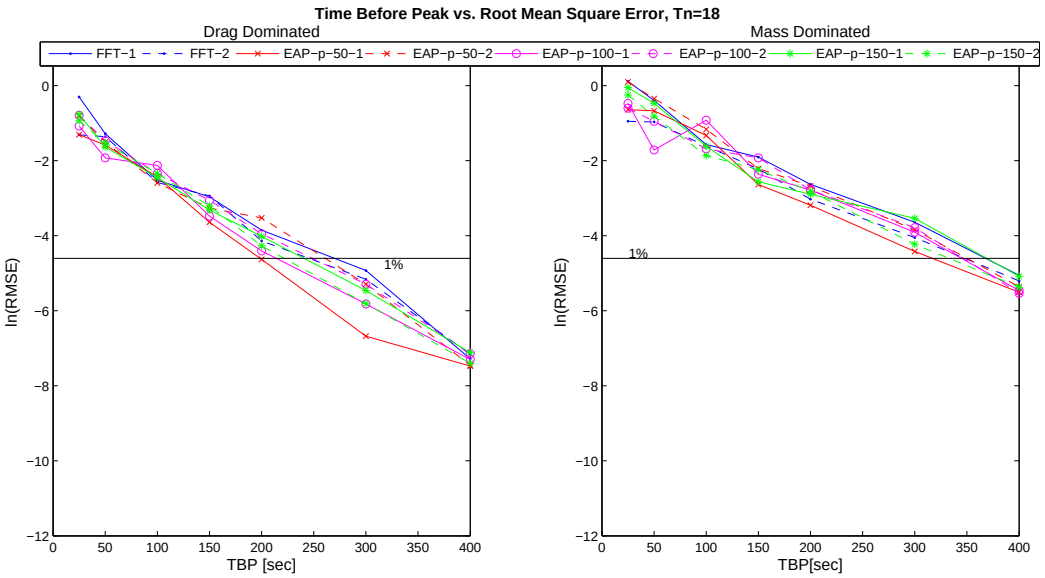

Figure 34: Required time before peak for cylinder with $T_n = 18$ s

7.2.5 Discussions of the dynamic simulation

From the graphs in Figure 31 through 34 it is evident that the required time before peak to set up the dynamic behaviour is strongly governed by both the structures eigenperiod, and the governing loads. The results show, however, no clear differences between the peaked EAP and FFT methods of simulation. Both follow the approximate same curve, and fluctuates about being the one with largest and least RMSE for a given TBP. Furthermore there seems not to be any difference in whether the spoolwave command is used to the highest or second highest peak. A result of this is that one can assume the same TBP for all procedures, and set the requirement equal to the most conservative of the methods for a given load/eigenperiod combination.

No issues regarding lack of convergence is experienced, as the dynamic simulations use the same time instant with an accuracy of 8 digits (compared to the 2 digits for the static case). An interesting observation is the seemingly logarithmic relation between RMSE and TBP for all the cases. If similar behaviour is observed for other structures, one could use this relation to avoid numerous simulations, and rather extrapolate from some few runs. For the current case one could use this information to extrapolate the results to find for instance the TBP needed for a different RMSE requirement, or to find the expected RMSE for a long simulation.

In the following paragraphs the reason for the change in required TBP for different loads and eigenperiod are discussed.

7.2.5.1 Effect of eigenperiod

The eigenperiod affect the result by influencing the dynamic amplification factor. When the eigenperiod is in the proximity of the excitation period, the dynamic amplification is large, leading to increased forces and therefore motions of the structure. If the eigenperiod is far from the excitation, the forces and motions of the structure are smaller. By looking at a simplified one degree of freedom system, with an excitation load oscillating with the mean zero-up-crossing period (≈ 11.6) one can illustrate how this affects the required time before peak.

The cases of T_n of 14 and 4.5 seconds are investigated, the mass is set to 5, the stiffness found to uphold the eigenperiod ($k = m\omega_n^2$), and the damping set to 3% of critical. The system is subjected to a harmonic load oscillating at a period of T_{m02}, with an amplitude of 1. It is interesting to see how long time it takes for the two simplified structures to dampen out the transient response in terms of velocity and acceleration, and obtain the harmonic motions. For this simplified system, it is assumed that the structure's motions does not influence the loads. Figure 35 shows the results in terms of acceleration and velocity, and the displacement can be expected to follow the same behaviour.

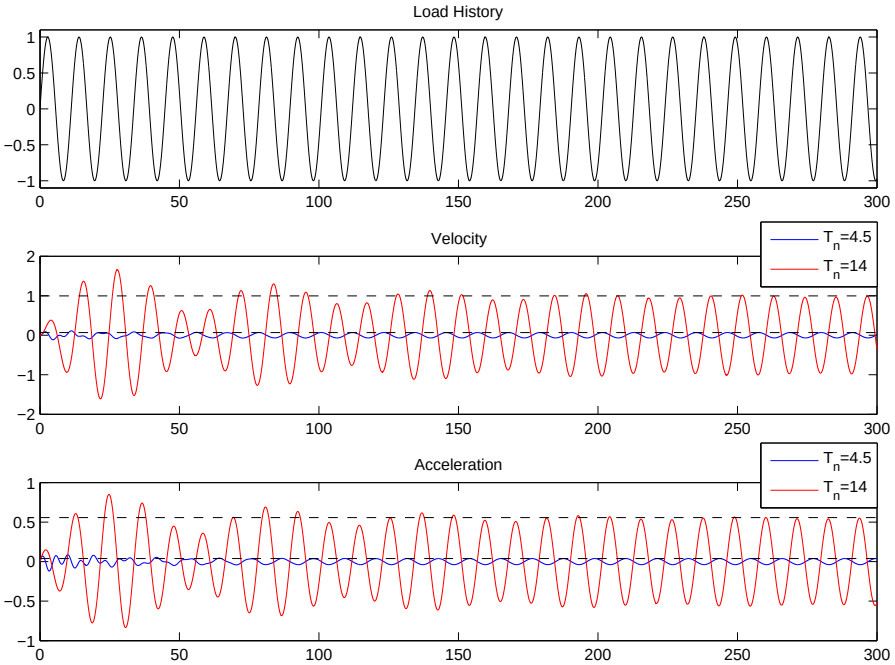

Figure 35: Damping of transient response for a 1-dof system, M=5, dampingratio=3%. Horizontal line is homogeneous response

It is obvious that the structure with an eigenperiod close to the excitation period experience a lot more dynamic effects in terms of larger motions, as the red line has far larger amplitudes. It is observed that while the low eigenperiod reaches harmonic state for both velocity and acceleration at around 50-100 seconds, the higher eigenperiod reaches it at around 250-300 seconds. This is similar to the required values observed in the actual simulation of the cylinder. Additionally, the kinematics of the structure will affect the loads, as it is the relative acceleration and velocity that enters into the equation. It is therefore expected that this simplified system under predicts the required time before peak.

7.2.5.2 Effect of governing loads

It is also found that the governing loads influence the required time before peak. As the mass and drag governed loads are functions of acceleration and velocity, respectively, a reason for the differences could be that the time to dampen the transient response was different for the structures acceleration and velocity terms. However, Figure 35 shows that the acceleration and velocity terms approach the homogeneous state at approximately the same time instant, and with similar behaviour of the transient response. Other than being shifted by $\pi/2$, the two red and the two blue lines behaves quite similar. In order to find possible reasons, one of the load histories of the simulations are assessed. Figure 37 shows the surface elevation, load history (both mass and drag), reaction moment and the target structures velocity/acceleration for a structure with an eigenperiod of 9 seconds. The surface for this particular simulation is presented in Figure 36.

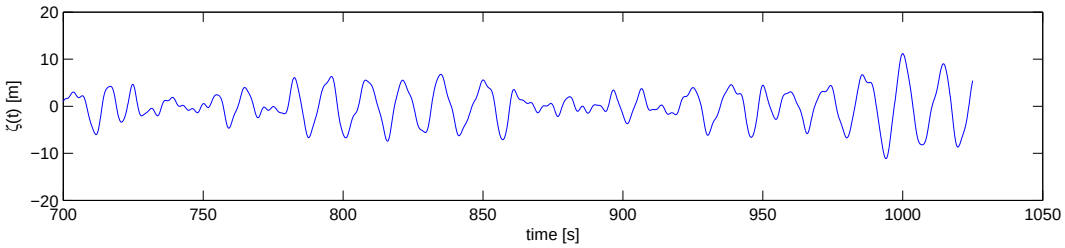

Figure 36: Example surface elevation (FFT)

The loads and responses are presented in Figure 37 for both drag and mass dominated loads. The last 300 seconds of the 1000 second simulation is included (blue), and compared against a simulation starting at 900 sec (red).

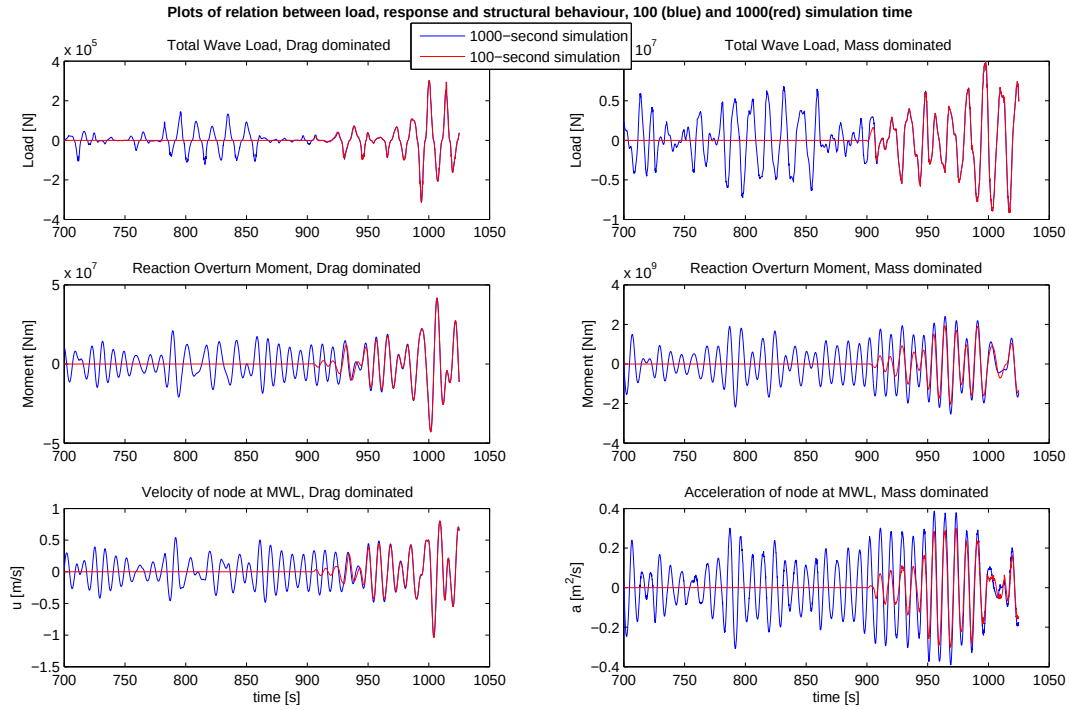

Figure 37: Example of loads, responses and structure motions from a spool-wave analysis (FFT)

While both mass and drag dominated structures have a decently represented wave load, as this is mainly governed by the wave kinematics, the reaction moment and structure motions are varying. The drag dominated loads (left) are very small in the main part, and dominated totally by the actions around the largest amplitude, resulting in small motions for the major part, and therefore also limited need of simulation time to set up the dynamic behaviour. The mass dominated loads (right) have a larger consistent load level and are not dominated in the same way by the action around the largest wave. As the response are large in the major part of the simulation, a longer simulation time is required to set up the proper dynamic behaviour. Furthermore it is observed that the extreme moment in the mass dominated simulations does not occur at the end of the simulation, but rather some few seconds before. The largest moment will not be included in the calculation, as this is outside of the 10 second interval around the largest surface peak (at 1000 sec). As the errors are similar both at the largest moment (950 sec) and at 1000 sec, it is not expected to incur any additional errors.

One can clearly see from the second plots that while the 100 second simulation of the drag dominated structure will be accepted, the 100 second simulation of the mass dominated structure will be rejected as the red line are not equal to the blue line for the reaction overturning moment. These results are used to illustrate the general trends and other simulations might show slightly different results.

The error stems from a more constant high load for the mass term. To explain this behaviour, one can investigate the different load terms from Morison, Eq. 107. The mass term is a function of the relative acceleration, while the drag term is dependent on the relative velocity squared. To illustrate the difference this introduce, an example of an irregular sea (no spool-wave involved) is shown in Figure 38. The kinematics presented are those present at the mean water level at all times, i.e. no stretching or extrapolation to crests, and no reduction in troughs. The kinematics are shown as they enter Morison's equation ($u \cdot |u|$ and a). The effect of the structures motion is not accounted for in this example.

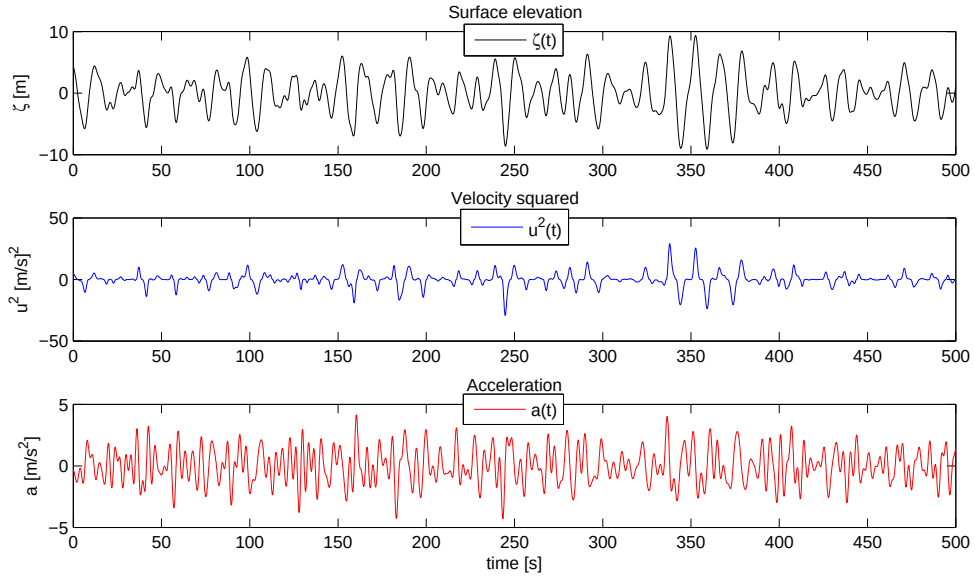

Figure 38: Example of irregular surface process with wave kinematics as they enter Morrison's equation

The same trends as for the loads are observed. The $u|u|$ term is low, and spikes around the largest surface elevations. The result is that the drag load term will be low for the most part, and have spikes around the largest peaks, i.e. exactly what was experienced in Figure 37. The acceleration are shown to fluctuate more with larger amplitudes over the whole simulation, and are thus not as dominated by the action around the peaks. This supports the observation of a more consistently high loading for the mass dominated structure, and can therefore explain some of the reason why a longer simulation time is needed to properly account for the mass dominated loads.

7.2.6 Conclusion

In conclusion, the necessary time before peak to properly account for the dynamic effects are strongly dependent on the eigenperiod and loads. The recommended values for the bottom fixed cylinder, for any spectrum realization procedure, are given in Table 10 and plotted in Figure 39. The RMSE and largest individual error at this level is also included in the table, to show what degree of error is inflicted. These are taken as the largest (most conservative) of all the different simulation procedures and peaks.

Dominating Load	Eigenperiod	TBP [s]	RMSE [%]	Largest error [%]
Drag	4.5	50	0.4	1
	9	150	0.9	2.6
	14	300	0.3	0.5
	18	300	0.7	1.7
Mass	4.5	100	0.9	2.5
	9	300	0.7	2.3
	14	400	0.5	1.3
	18	400	0.6	1.9

Table 10: ULS and ALS design response

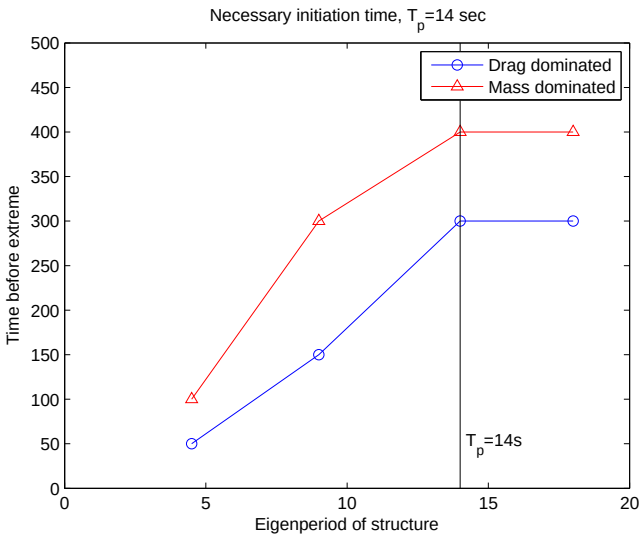

Figure 39: Plot of required time to establish dynamic behaviour

7.3 Study 3: Simplified procedures of simulating a Gaussian sea

The results form Study 1 shows significant uncertainties related to the conclusions drawn in the project work [2]. It is therefore chosen to re-run all analysis in the current work, where all the data of the different wave components are generated from a *MATLAB* script. Additionally, one wants to test other ways of realizing the surface process, as described in Section 4, in order to identify if any of these are can be used in a simplified second order realization. The following methods are therefore compared for a linear realization of the sea spectrum:

Identifier	# components	Description
FFT-0	1000	FFT with random phase scheme (common)
FFT-1	1000	FFT with random coefficient scheme (recommended)
FFT-2	[50 100 150]	FFT with random frequency scheme (non-repetitive)
FFT-3	[50 100 150]	FFT with random frequency and random coefficient
EAP-0	[50 100 150]	EAP with random phase scheme
EAP-1	[50 100 150]	EAP with random coefficient scheme
EAP-p-0	[50 100 150]	peaked EAP with random phase scheme
EAP-p-1	[50 100 150]	peaked EAP with random coefficient scheme

Table 11: Methods to be investigated

To limit the amount of statistical uncertainties, 40 samples are simulated for each method/-case. 40 seeds, i.e. sets of random numbers for finding phases, frequencies and amplitudes are stored and used for each method. All methods will hence have the same random input, (however using a 50 component scheme will only use the 50 first random numbers). By this procedure, one can compare the direct effect of each change, i.e. one will have the same phase angles for each simulation of FFT-2-100 and FFT-3-100, and the effect of introducing a random amplitude in FFT-3-100 can be compared directly against the result of a deterministic approach.

Both mass dominated and drag dominated structures are investigated, using cylinders with four different eigenperiods. The outline of the analysis performed are presented in Figure 40.

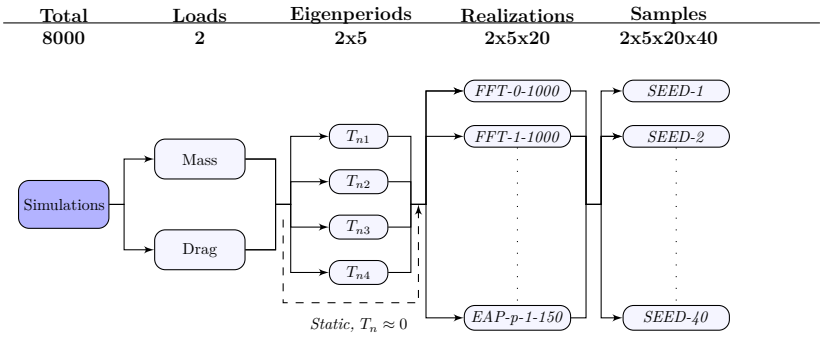

Figure 40: Overview of simulations to be run to investigate simplified procedures

The adequacy of the various methods will be discussed in terms of how well the method describes the (theoretical) statistics of the surface elevation, and how the extreme value distribution of wave loads and reaction moments compare with the random-coefficient FFT method, assumed to be correct. From Study 2 it was found that the required set up time before force recording should be performed varied. However, it is wanted to record the response under a similar surface elevation history for all the various structures. As the highest necessary TBP was found to be

400 second for the cylinders in Study 2, it is here chosen to assume an additional safety, and apply an initiation time of 500 seconds. The forces are therefore recorded from 500 to 1500 seconds for both dynamic and static analysis, and for all the various cylinders.

The peaked equal area principle finds a different sea spectrum realization for all the 4 different eigenperiods. These are, however, not very different, and are expected to show similar effects in terms of surface Statistics and static loads. It is therefore chosen to only include the *most unfavourable* of these, which is the one focusing on an eigenperiod at 4.5s. This is the one expected to have largest errors in surface statistics and static load levels, as the focus is furthest from the spectral peaks.

7.3.1 Results - Surface profile

From the time history of the surface elevation, a number of statistical parameters are calculated and tabulated in Table 12. The theoretical values are found from the Rayleigh distribution, see Section 2. An additional parameter is included, the variance of the variance of the spectrum, σ^2_{m0}. The theoretical value is found from Eq. 99, Section 4, and is included to better explain the behaviour of the few-component schemes. The mean and standard deviation of the 1000-second extremes are compared against the FFT-1-1000 (random amplitude and phase), in bold.

	$\lvert\zeta_{max}\rvert$		$\sigma_{\lvert\zeta_{max}\rvert}$		ζ_{max}	ζ_{min}	σ^2_ζ	σ^2_{m0}	$\gamma_{2,\zeta}$	$\gamma_{1,\zeta}$	μ_ζ
Theory	10.2	-	1.19	-	9.58	-9.58	9	1.71	3	0	0
FFT-1-1000	9.70	**1.00**	1.28	**1.00**	9.30	-9.22	8.89	1.94	2.90	-0.01	0.00
FFT-0-1000	9.70	**1.00**	1.08	**0.84**	9.48	-9.14	8.97	1.05	2.90	0.01	0.00
FFT-2-50	9.42	**0.97**	0.77	**0.60**	8.98	-8.98	9.02	0.08	2.80	-0.01	0.00
FFT-2-100	9.72	**1.00**	0.84	**0.66**	9.19	-9.45	9.14	0.37	2.95	-0.01	0.00
FFT-2-150	10.04	**1.04**	0.90	**0.70**	9.78	-9.38	9.06	0.40	2.98	0.01	0.00
FFT-3-50	9.29	**0.96**	1.46	**1.14**	8.82	-8.85	9.08	6.56	2.72	0.00	0.00
FFT-3-100	9.58	**0.99**	1.44	**1.12**	9.12	-9.17	9.42	6.43	2.85	0.00	0.00
FFT-3-150	9.94	**1.02**	1.41	**1.10**	9.52	-9.22	9.03	3.71	2.91	0.01	0.00
EAP-0-50	9.68	**1.00**	0.97	**0.76**	9.24	-9.12	8.98	0.59	2.90	0.00	0.00
EAP-0-100	9.98	**1.03**	1.05	**0.82**	9.28	-9.73	9.04	0.75	2.93	-0.01	0.00
EAP-0-150	9.65	**0.99**	1.12	**0.87**	9.18	-9.29	8.96	1.33	2.93	0.01	0.00
EAP-1-50	9.91	**1.02**	1.43	**1.12**	9.47	-9.47	9.35	3.03	2.90	0.01	0.00
EAP-1-100	9.68	**1.00**	1.34	**1.05**	9.21	-9.41	9.22	1.90	2.89	-0.01	0.00
EAP-1-150	10.05	**1.04**	1.32	**1.03**	9.50	-9.62	9.26	2.34	2.99	0.01	0.00
EAP-p-0-50	9.97	**1.03**	0.99	**0.77**	9.43	-9.41	8.93	0.55	2.94	-0.02	0.00
EAP-p-0-100	9.90	**1.02**	1.01	**0.79**	9.49	-9.32	9.03	0.79	2.93	0.01	0.00
EAP-p-0-150	10.14	**1.05**	1.13	**0.88**	9.60	-9.77	9.30	1.84	3.01	0.00	0.00
EAP-p-1-50	9.93	**1.02**	1.58	**1.23**	9.41	-9.45	8.93	3.45	2.94	-0.01	0.00
EAP-p-1-100	9.90	**1.02**	1.37	**1.07**	9.41	-9.45	9.20	2.12	2.91	0.00	0.00
EAP-p-1-150	9.89	**1.02**	1.24	**0.97**	9.46	-9.58	9.33	1.93	2.95	-0.01	0.00

Table 12: Statistics of the surface elevation

A method frequently used to check if a set of data follow a specific probability model, and to check if two set of data follow the same model, is to plot these in a probability model. Here one expect the largest extremes to follow a Gumbel model, with parameters as described in Section 2.1.5. In Figure 41 the fitted Gumbel models with sample population are plotted in a Gumbel probability paper. In the top plot the two 1000 FFT methods are plotted, while in the rest both the 50, 100 and 150 component schemes of the carious methods are plotted and compared against the FFT-1-1000, which is the red line in all plots. The colour code is given in the top of the figure.

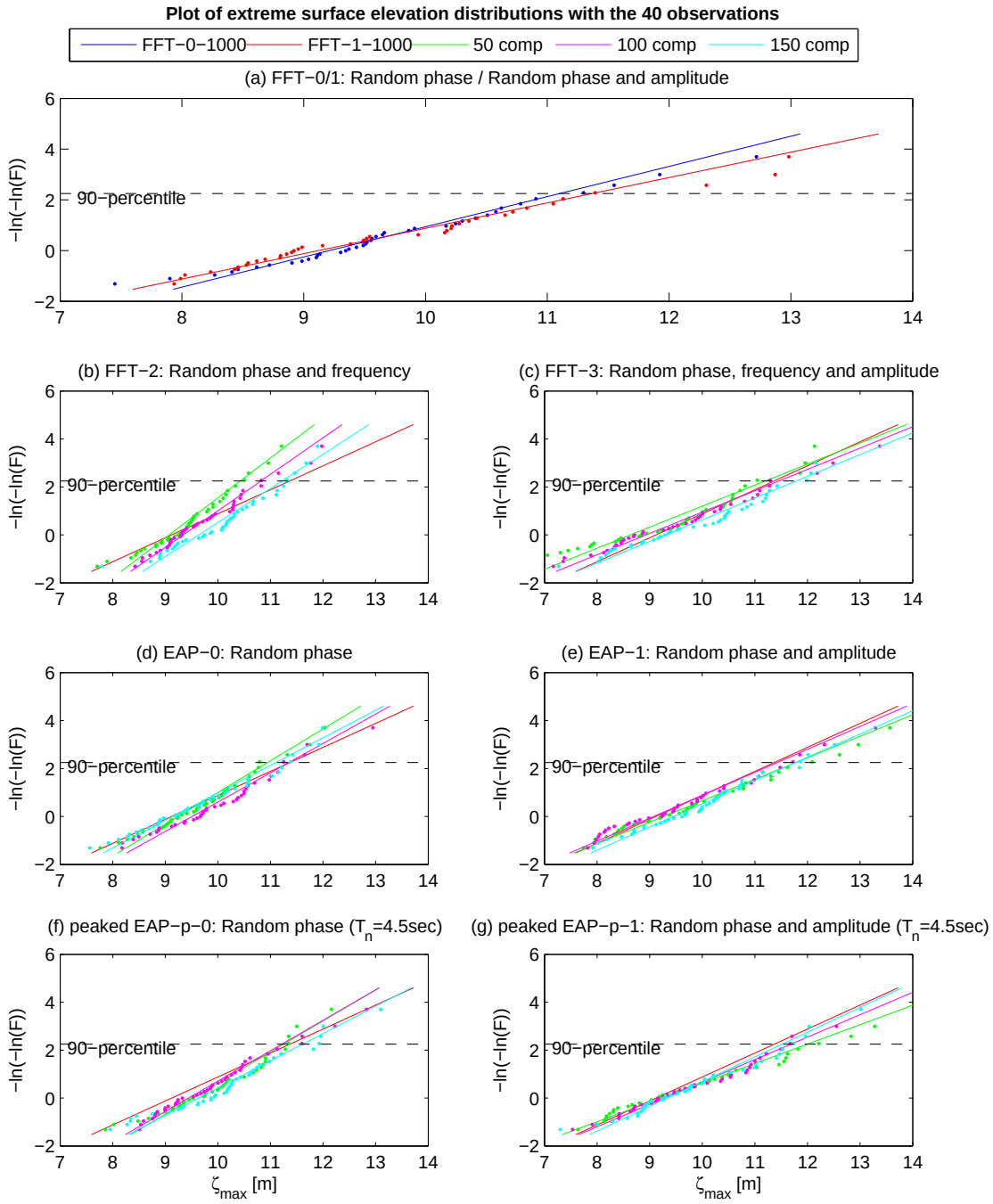

Figure 41: The extreme surface elevation distributions for the various methods, along with observations

7.3.2 Discussions - Surface profile

The Gaussian assumption requires zero mean (μ_ζ), zero skewness ($\gamma_{1,\zeta}$) and a kurtosis ($\gamma_{2,\zeta}$) of three. Additionally the variance of the surface should equal the variance of the wave spectrum, i.e. $\sigma_\zeta^2 = (H_s/4).^2 = 3$. It is found from the 5.th and three last columns in Table 12 that for most of the simulations, these are all within an acceptable range (i.e. $\approx 5\%$ deviation). The kurtosis is the one which errs the most for all the simualtions, as it tends to be too low by a few percent. For some cases, such as the FFT-2-50 and the FFT-3-50 the error in the kurtosis is significant, around 10%, and the result (or reason) of this can be seen in a lower mean of the maxima. Furthermore one sees that the mean of the maxima, minima, and absolute maxima are similar for most cases, and slightly below the theoretical value. This is to be expected as the assumption of individually Rayleigh distributed waves are somewhat conservative, and an error is introduced when the number of waves in the simulations is low (here 90).

There is, however, some rather large differences in the standard deviation of the extremes, the variance of the variance of the seastates (σ_{m0}^2) and also in the extreme values themselves. As the Gumbel plots in Figure 41 are directly related to the mean and standard deviation of the extremes, some difference is introduced in these as well. The plots show that for all cases the fitted distributions (lines) fit reasonably well with the population (dots), but all distributions does not show satisfactory agreement with the "correct" FFT-1-1000. These discrepancies will be discussed in the following paragraphs.

7.3.2.1 Standard deviation of sample maxima

To explain the fluctuating standard deviaton of the maxima, one can begin by looking at the variance of the variance of the sea state. The variance of the sea is an important part in the theoretical expression of the expected largest waveheight. When the variance varies in each seastate, the expected largest varies. Therefore there is a larger possibility that especially large and small simulation maxima are found. This will consequently increase the standard deviation of the maxima, while the mean might not be influenced much. This relation is clearly visible in Table 12, by comparing the σ_{m0}^2 with the $\sigma_{|\zeta_{max}|}$. One finds that the common FFT-0-1000 procedure underestimates the variance of the variance, and therefore also the variance of the maxima, however it does not change the mean of the maximum. The error to the standard deviation is not very large, as an 1000 components approximates the asymptotic limit quite well. However, when one introduce a scheme that require fewer components, such as the FFT-2 random frequency, the infinity limit is far from reached. The variance of the variance is grossly underestimated, leading to a large underestimation of the standard deviation of the extremes (30-40%). The solutions converge towards the FFT-1-1000 as the number of components increase, which can be seen in Figure 41b.

The other possible way of simplifying the FFT is to use the random amplitude scheme along with the random phase/frequency scheme, i.e. FFT-3. For these cases, the variance of the variance is heavily over estimated, leading to a high standard deviation of the extremes (10-15%). While this is on the conservative side, one would want to reduce this error. Increasing the number of components even further would be expected to better the goodness of the method, with the additional cost of simulating more components.

The various methods with the equal area principle shows a better fit with the theory and 1000 component FFT methods. The degree of error both in terms of σ_{m0}^2 and $\sigma_{|\zeta_{max}|}$ are significantly lower than the FFT with the same amount of components. The reason for this was discussed by

Elgar et al. [6], who compared the random phase and random amplitude methods using both a narrowband and broadband spectrum, and found that the required number of components to represent the process satisfactory differed much between the spectra. It lead to the conclusion that:

> *"The differences between the broad and narrow spectra suggest that it is more appropriate to consider the effective number of spectral coefficients to be those within the energetic parts of the spectrum, and not the total number of coefficients"* [6]

The EAP method is based on exactly this principle, that the most energetic parts of the spectrum carry most importance. For the JONSWAP spectrum used in this study, one finds that around 75% of the energy of the spectrum lies within a small frequency range, (0.4-0.65) [rad/s]. The representation in this area is therefore vital to correctly simulate the Gaussian process. In Figure 42 the discretization in this energetic part of the spectrum is shown for both an EAP and FFT procedure, with a total of 50 components.

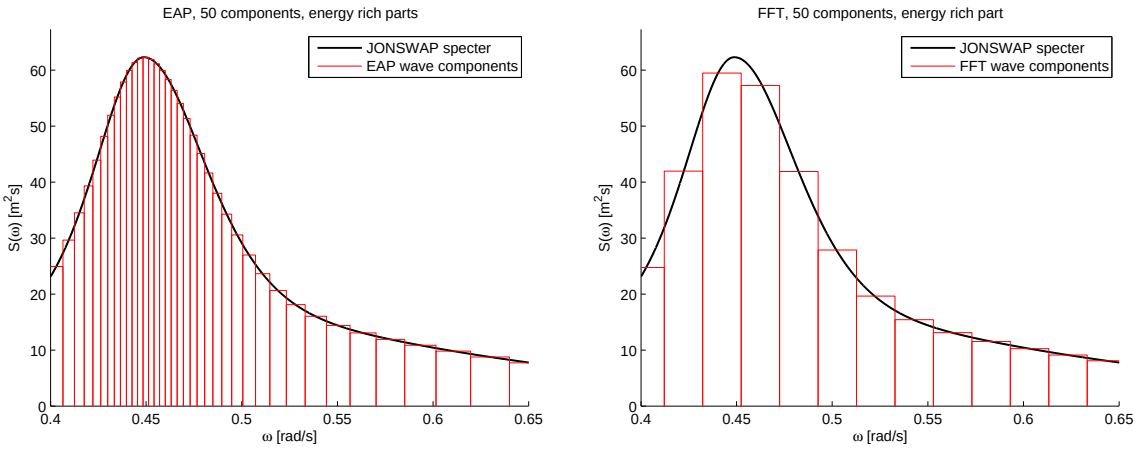

(a) EAP (b) FFT

Figure 42: Discretization of the wave spectrum in the energetic parts

Including all components which are parts of these figures, the effective number of spectral components is 38 for the EAP and 13 for the FFT. In the energy rich parts, the EAP will approximate a Gaussian surface adequately, while the errors introduced in the energy dense parts is of secondary importance. The spikes of the variance of variance found when using a random amplitude for the random frequency FFT method is not experienced in the same degree for the EAP either. The reason is the same as described above, the EAP simulates better a Gaussian surface. However, some errors are expected for the cases of fewest components. The reason is a too large impact of each randomly generated amplitude, thus introducing too much randomness to the system, as described in Section 4.1.1.3.

The peaked EAP has variations somewhere in between of the EAP's and the simplified FFT's. The reason is simple, while the main bulk of the components are EAP, some components are dedicated around the spectral peak period, and consequently the energetic parts are less represented than the EAP, but more than the FFT.

7.3.2.2 Mean of sample maxima

The mean of 40 sample are found to be slightly conservative for the bulk of the EAP cases, and slightly non conservative for the random frequency schemes. The effect of σ_{m0}^2 on the mean run length of wave groups, i.e. a set of consecutive high waves, were suggested by Tucker et al. [34], and discussed extensively by Elgar et al. [6], leading to the previously described definition of the effective number of components. In this study, Elgar et al. showed that for a sufficient amount of components, the effect of the run length of wave groups were small. However, it was also found that some error were introduced for a narrow band spectrum when the number of components were low. For instance, a 12% difference in run length were found for 66 random phase Fourier components using the random phase scheme. The JONSWAP spectrum is a somewhat peaked and narrowband spectrum, and one would therefore expect some similar effects in the results. This will also create the low kurtosis as experienced by FFT-2-50 and FFT-3-50 in Table 12.

7.3.2.3 Extreme value distributions

From the extreme value distributions in Figure 41 one sees the effect of mean and standard deviation of sample maxima. For instance, in Figure 41b, the Gumbel model of the 50 component model (green) is far from the target 1000 component FFT model (red), while the model converges as number of components increase. The vertical line is the 90-percentile, a much used value for design considerations. If one used the green (50 component) model, the error would be 1-2 meters, on the non-conservative side. The rest of the plots, and in particular all EAP and peaked EAP models, fit well with the 1000 component FFT model.

From the results and discussions presented in this sections, it is clear that the equal area principle is a more adequate way of *generating the sea surface* when the number of components is limited. However, some errors are introduced in the form of a lack or excess of standard deviation of extreme values.

There are, however, uncertainties related to the statistical values when performing 40 simulations. To illustrate these, a test were performed with 1000 surface realizations for selected methods. Table 13 presents the results. One sees clearly that the average over 1000 simulations are not completely in line with those produced by 40 simulations, however the general trends are there. Note that one have here used 100 components in the simplified procedures, and it seems that this is sufficient to create a good mean of surface extreme, but a varying standard deviation.

	$\lvert\zeta_{max}\rvert$		$\sigma^2_{\lvert\zeta_{max}\rvert}$	
Method	1000	40	1000	40
FFT-1-1000	9.91	9.70	1.20	1.28
FFT-0-1000	9.91	9.696	1.14	1.08
FFT-2-100	9.73	9.72	0.84	0.66
FFT-3-100	9.55	9.58	1.35	1.44
EAP-0-100	9.92	9.98	1.12	1.05
EAP-1-100	9.87	9.68	1.28	1.34
EAP-p-0-100	9.92	9.89	1.12	1.01
EAP-p-1-100	9.87	9.90	1.28	1.37

Table 13: Methods to be investigated

7.3.3 Results from Static simulation

The first simulations are done neglecting the mass and damping terms of the equation of moment. Additionally the E-module is increased in order to avoid structural motions. The results are presented in Tables 14 and 15 for mass and drag dominated loads respectively. The mean of the maximum wave load and reaction moment, along with the standard deviation of these values, are presented and compared against the FFT-1-1000. In order to identify any correlations with the surface maxima, the ratio of the surface maxima and standard deviation relative to the FFT-1-1000 is given in the two last columns, in both tables. The total wave load (LOAD) and reaction overturn moment (ROM) are here presented to represent the forces. For a static analysis, the reaction base shear will be identical to the total wave load.

The ratios of the standard deviations are given in *italic*, while the ratio of extreme values are presented in **bold**.

MASS DOMINATED LOADS										
	Wave Load $10^6[N]$				ROM $10^8[Nm]$				Surface Extreme	
	Maxima		Std. dev.		Maxima		Std. dev.		$\lvert\zeta_{max}\rvert$	$\sigma_{\lvert\zeta_{max}\rvert}]$
FFT-1-1000	9.13	**1.00**	1.18	*1.00*	6.21	**1.00**	0.87	*1.00*	**1.00**	*1.00*
FFT-0-1000	9.35	**1.03**	1.08	*0.91*	6.36	**1.03**	0.73	*0.84*	**1.00**	*0.84*
FFT-2-50	9.16	**1.00**	0.71	*0.60*	6.21	**1.00**	0.50	*0.58*	**0.97**	*0.60*
FFT-2-100	9.42	**1.03**	0.93	*0.79*	6.36	**1.02**	0.67	*0.77*	**1.00**	*0.66*
FFT-2-150	9.77	**1.07**	1.19	*1.01*	6.63	**1.07**	0.85	*0.98*	**1.04**	*0.70*
FFT-3-50	8.82	**0.97**	1.34	*1.13*	6.05	**0.97**	0.89	*1.02*	**0.96**	*1.14*
FFT-3-100	9.45	**1.04**	1.42	*1.20*	6.41	**1.03**	0.96	*1.11*	**0.99**	*1.12*
FFT-3-150	9.32	**1.02**	1.34	*1.14*	6.36	**1.03**	0.92	*1.06*	**1.02**	*1.10*
EAP-0-50	9.40	**1.03**	1.01	*0.85*	6.40	**1.03**	0.68	*0.78*	**1.00**	*0.76*
EAP-0-100	9.62	**1.05**	1.09	*0.93*	6.48	**1.04**	0.74	*0.85*	**1.03**	*0.82*
EAP-0-150	9.48	**1.04**	1.14	*0.96*	6.44	**1.04**	0.75	*0.86*	**0.99**	*0.87*
EAP-1-50	9.46	**1.04**	1.32	*1.11*	6.34	**1.02**	0.88	*1.02*	**1.02**	*1.12*
EAP-1-100	9.32	**1.02**	1.28	*1.09*	6.33	**1.02**	0.92	*1.05*	**1.00**	*1.05*
EAP-1-150	9.88	**1.08**	1.48	*1.25*	6.65	**1.07**	1.00	*1.14*	**1.04**	*1.03*
EAP-p-0-50	9.48	**1.04**	0.98	*0.83*	6.35	**1.02**	0.67	*0.77*	**1.03**	*0.77*
EAP-p-0-100	9.47	**1.04**	1.04	*0.88*	6.39	**1.03**	0.68	*0.78*	**1.02**	*0.79*
EAP-p-0-150	9.83	**1.08**	1.12	*0.95*	6.57	**1.06**	0.80	*0.92*	**1.05**	*0.88*
EAP-p-1-50	9.55	**1.05**	1.57	*1.33*	6.39	**1.03**	1.09	*1.25*	**1.02**	*1.23*
EAP-p-1-100	9.50	**1.04**	1.25	*1.06*	6.40	**1.03**	0.84	*0.96*	**1.02**	*1.07*
EAP-p-1-150	9.56	**1.05**	1.12	*0.95*	6.46	**1.04**	0.80	*0.92*	**1.02**	*0.97*

Table 14: Static simulations, mass dominated forces

DRAG DOMINATED LOADS										
	Wave Load $10^5[N]$				ROM $10^7[Nm]$				Surface Extreme	
	Maxima		Std. dev.		Maxima		Std. dev.		$\lvert\zeta_{max}\rvert$	$\sigma_{\lvert\zeta_{max}\rvert}$
FFT-1-1000	2.18	**1.00**	0.59	*1.00*	1.66	**1.00**	0.52	*1.00*	**1.00**	*1.00*
FFT-0-1000	2.22	**1.02**	0.49	*0.84*	1.70	**1.03**	0.42	*0.81*	**1.00**	*0.84*
FFT-2-50	2.07	**0.95**	0.32	*0.55*	1.55	**0.94**	0.29	*0.56*	**0.97**	*0.60*
FFT-2-100	2.13	**0.98**	0.37	*0.63*	1.59	**0.96**	0.32	*0.61*	**1.00**	*0.66*
FFT-2-150	2.39	**1.10**	0.42	*0.72*	1.84	**1.11**	0.35	*0.68*	**1.04**	*0.70*
FFT-3-50	2.04	**0.94**	0.56	*0.96*	1.55	**0.93**	0.48	*0.92*	**0.96**	*1.14*
FFT-3-100	2.15	**0.99**	0.58	*0.98*	1.65	**0.99**	0.49	*0.94*	**0.99**	*1.12*
FFT-3-150	2.29	**1.05**	0.64	*1.09*	1.74	**1.05**	0.56	*1.07*	**1.02**	*1.10*
EAP-0-50	2.20	**1.01**	0.40	*0.68*	1.66	**1.00**	0.36	*0.70*	**1.00**	*0.76*
EAP-0-100	2.20	**1.01**	0.47	*0.80*	1.64	**0.99**	0.42	*0.81*	**1.03**	*0.82*
EAP-0-150	2.15	**0.99**	0.42	*0.71*	1.62	**0.98**	0.33	*0.64*	**0.99**	*0.87*
EAP-1-50	2.28	**1.05**	0.58	*0.99*	1.73	**1.04**	0.46	*0.89*	**1.02**	*1.12*
EAP-1-100	2.17	**0.99**	0.56	*0.96*	1.63	**0.98**	0.48	*0.93*	**1.00**	*1.05*
EAP-1-150	2.32	**1.06**	0.59	*1.00*	1.74	**1.05**	0.48	*0.93*	**1.04**	*1.03*
EAP-p-0-50	2.25	**1.03**	0.41	*0.69*	1.69	**1.02**	0.37	*0.71*	**1.03**	*0.77*
EAP-p-0-100	2.25	**1.03**	0.48	*0.81*	1.71	**1.03**	0.43	*0.82*	**1.02**	*0.79*
EAP-p-0-150	2.34	**1.07**	0.49	*0.84*	1.76	**1.06**	0.42	*0.80*	**1.05**	*0.88*
EAP-p-1-50	2.28	**1.05**	0.68	*1.15*	1.72	**1.04**	0.58	*1.12*	**1.02**	*1.23*
EAP-p-1-100	2.24	**1.03**	0.54	*0.92*	1.67	**1.01**	0.46	*0.90*	**1.02**	*1.07*
EAP-p-1-150	2.25	**1.03**	0.54	*0.91*	1.70	**1.03**	0.47	*0.91*	**1.02**	*0.97*

Table 15: Static simulations, drag dominated forces

7.3.3.1 Discussion of results from Static simulations

The general impression from Table 14 and 15 is that the mean of the maxima for both wave load and overturning moment, for both drag and mass dominated load cases, compares well with the FFT-1-1000 method. The largest deviation in mass loads are, for all of the methods, found to be around 7-8%, while the drag has a slightly higher deviation of 10-11 percent for both wave loads and moments. The largest deviations present themselves for the same simulation methods for both drag and mass dominated structures (FFT-2-150, EAP-1-150 and EAP-p-0-150), and these are also the cases with largest deviation in mean of the surface maxima. More importantly, it is seen that the 50 component FFT schemes are on the non-conservative side regarding static loading, in particular for drag dominated structure. The drag term shows larger errors because the differences introduced in the surface elevation is squared in the drag term of Morison's equation. In a static simulation, the wave amplitudes are dominating the response picture, and the trends of the surface extremes are evident in the loads and responses.

Similar observations are made for the ratio of the standard deviation. One sees that the cases where the standard deviation of the surface maxima are too low tend to give a too low standard deviation of response and moment. For the drag dominated case, most of the cases produce a too low standard deviation even though the surface maxima's standard deviation are high. Other cases, such as the EAP-1-150 the standard deviation is significantly over predicted despite of a good approximation of the surface maxima's.

For the simulations that are not significantly affected by the few-component errors described in the previous section, the maximum loads and moments are on the conservative side. The

standard deviation are varying both as conservative and non-conservative, but follows the same trends as that of the surface maxima. Most of the static behaviour can therefore be explained by the same arguments as for the surface elevation, and will not be repeated here.

7.3.4 Results and Discussions from Dynamic simulations

The results from the dynamic simulations are split in the results with mass and drag dominating loads. The results are presented as tables including the mean of the extremes and the standard deviation of the extremes, and a comparison relative to the extreme of the FFT-1-1000 method. Ratio's of mean of extremes are given in **bold** and *itallic* for the standard deviation.

7.3.4.1 Results - Mass dominated loads

The extreme value statistics of wave load and reaction moment for the simulations of a mass dominated structure are given in Table 16. Note that while the same wave-component set is used for all the different eigenperiods for FFT and EAP procedures, the peaked EAP have been performed with the refinement around the eigenperiod and is therefore not the same for all the columns.

MASS DOMINATED LOADS																
	$T_n = 4.5[sec]$				$T_n = 9[sec]$				$T_n = 14[sec]$				$T_n = 18[sec]$			
	μ_X		σ_X		μ_X		σ_X		μ_X		σ_X		μ_X		σ_X	
LOAD [MN]																
FFT-1-1000	9.09	**1.00**	1.14	*1.00*	9.12	**1.00**	1.18	*1.00*	9.12	**1.00**	1.16	*1.00*	9.17	**1.00**	1.15	*1.00*
FFT-0-1000	9.34	**1.03**	1.08	*0.95*	9.33	**1.02**	1.09	*0.92*	9.34	**1.02**	1.08	*0.93*	9.39	**1.02**	1.06	*0.93*
FFT-2-50	9.13	**1.00**	0.73	*0.64*	9.13	**1.00**	0.72	*0.61*	9.11	**1.00**	0.70	*0.61*	9.12	**0.99**	0.69	*0.60*
FFT-2-100	9.40	**1.03**	0.93	*0.81*	9.38	**1.03**	0.92	*0.78*	9.40	**1.03**	0.88	*0.76*	9.43	**1.03**	0.90	*0.79*
FFT-2-150	9.73	**1.07**	1.22	*1.07*	9.74	**1.07**	1.21	*1.03*	9.73	**1.07**	1.22	*1.05*	9.75	**1.06**	1.20	*1.05*
FFT-3-50	8.78	**0.97**	1.34	*1.18*	8.80	**0.97**	1.36	*1.15*	8.83	**0.97**	1.36	*1.18*	8.84	**0.96**	1.37	*1.20*
FFT-3-100	9.42	**1.04**	1.39	*1.22*	9.42	**1.03**	1.39	*1.17*	9.42	**1.03**	1.41	*1.22*	9.44	**1.03**	1.40	*1.22*
FFT-3-150	9.29	**1.02**	1.34	*1.18*	9.29	**1.02**	1.32	*1.12*	9.29	**1.02**	1.32	*1.15*	9.34	**1.02**	1.38	*1.20*
EAP-0-50	9.40	**1.03**	1.00	*0.88*	9.41	**1.03**	1.03	*0.87*	9.39	**1.03**	1.00	*0.86*	9.43	**1.03**	1.05	*0.91*
EAP-0-100	9.58	**1.05**	1.07	*0.93*	9.58	**1.05**	1.09	*0.92*	9.60	**1.05**	1.09	*0.94*	9.62	**1.05**	1.06	*0.93*
EAP-0-150	9.50	**1.04**	1.14	*1.00*	9.48	**1.04**	1.16	*0.98*	9.49	**1.04**	1.17	*1.01*	9.51	**1.04**	1.19	*1.04*
EAP-1-50	9.44	**1.04**	1.29	*1.12*	9.43	**1.03**	1.30	*1.10*	9.42	**1.03**	1.30	*1.12*	9.46	**1.03**	1.29	*1.13*
EAP-1-100	9.33	**1.03**	1.28	*1.12*	9.28	**1.02**	1.25	*1.05*	9.29	**1.02**	1.30	*1.12*	9.34	**1.02**	1.31	*1.15*
EAP-1-150	9.89	**1.09**	1.51	*1.32*	9.86	**1.08**	1.49	*1.26*	9.83	**1.08**	1.46	*1.27*	9.87	**1.08**	1.45	*1.26*
EAP-p-0-50	9.47	**1.04**	0.99	*0.87*	9.63	**1.06**	0.97	*0.82*	9.10	**1.00**	0.84	*0.72*	9.45	**1.03**	1.10	*0.96*
EAP-p-0-100	9.43	**1.04**	1.04	*0.91*	9.83	**1.08**	1.08	*0.91*	9.57	**1.05**	1.39	*1.21*	9.50	**1.04**	1.01	*0.88*
EAP-p-0-150	9.81	**1.08**	1.12	*0.98*	9.35	**1.03**	0.85	*0.72*	9.29	**1.02**	1.07	*0.93*	9.72	**1.06**	1.10	*0.96*
EAP-p-1-50	9.52	**1.05**	1.51	*1.32*	9.66	**1.06**	1.62	*1.37*	8.93	**0.98**	1.24	*1.07*	9.49	**1.03**	1.23	*1.07*
EAP-p-1-100	9.46	**1.04**	1.24	*1.09*	9.39	**1.03**	1.40	*1.18*	9.45	**1.04**	1.13	*0.98*	9.55	**1.04**	1.40	*1.22*
EAP-p-1-150	9.53	**1.05**	1.07	*0.94*	9.48	**1.04**	1.13	*0.96*	9.45	**1.04**	1.03	*0.89*	9.42	**1.03**	1.12	*0.97*
ROM [GNm]																
FFT-1-1000	1.35	**1.00**	0.14	*1.00*	2.79	**1.00**	0.37	*1.00*	4.31	**1.00**	0.76	*1.00*	1.67	**1.00**	0.23	*1.00*
FFT-0-1000	1.34	**0.99**	0.14	*1.00*	2.83	**1.01**	0.36	*0.98*	4.33	**1.00**	0.69	*0.91*	1.74	**1.04**	0.22	*0.97*
FFT-2-50	1.32	**0.98**	0.11	*0.82*	2.64	**0.95**	0.27	*0.74*	3.59	**0.83**	0.35	*0.46*	1.48	**0.89**	0.23	*1.03*
FFT-2-100	1.34	**0.99**	0.14	*1.04*	2.82	**1.01**	0.23	*0.63*	4.17	**0.97**	0.42	*0.56*	1.69	**1.01**	0.14	*0.61*
FFT-2-150	1.36	**1.01**	0.15	*1.05*	2.82	**1.01**	0.31	*0.84*	4.29	**1.00**	0.49	*0.65*	1.67	**1.00**	0.24	*1.05*
FFT-3-50	1.29	**0.96**	0.21	*1.53*	2.51	**0.90**	0.65	*1.74*	3.30	**0.77**	1.04	*1.37*	1.40	**0.84**	0.31	*1.35*
FFT-3-100	1.35	**1.00**	0.20	*1.43*	2.75	**0.99**	0.41	*1.10*	3.86	**0.90**	1.00	*1.32*	1.59	**0.96**	0.32	*1.41*
FFT-3-150	1.33	**0.99**	0.16	*1.19*	2.80	**1.00**	0.48	*1.29*	4.09	**0.95**	0.87	*1.14*	1.65	**0.99**	0.31	*1.35*
EAP-0-50	0.98	**0.73**	0.13	*0.91*	2.66	**0.95**	0.21	*0.58*	4.29	**1.00**	0.68	*0.90*	1.55	**0.93**	0.19	*0.82*
EAP-0-100	1.00	**0.74**	0.13	*0.94*	2.69	**0.96**	0.28	*0.76*	4.26	**0.99**	0.59	*0.77*	1.70	**1.02**	0.21	*0.91*
EAP-0-150	1.08	**0.80**	0.12	*0.87*	2.85	**1.02**	0.36	*0.97*	4.22	**0.98**	0.80	*1.05*	1.67	**1.00**	0.23	*1.01*
EAP-1-50	0.98	**0.73**	0.14	*1.02*	2.59	**0.93**	0.64	*1.73*	4.23	**0.98**	0.80	*1.05*	1.55	**0.93**	0.40	*1.78*
EAP-1-100	1.00	**0.74**	0.15	*1.07*	2.61	**0.93**	0.49	*1.32*	4.43	**1.03**	0.80	*1.06*	1.65	**0.99**	0.33	*1.44*
EAP-1-150	1.08	**0.80**	0.19	*1.41*	2.83	**1.01**	0.41	*1.10*	4.29	**1.00**	0.92	*1.21*	1.69	**1.01**	0.32	*1.41*
EAP-p-0-50	1.18	**0.88**	0.10	*0.70*	2.87	**1.03**	0.30	*0.82*	4.20	**0.98**	0.64	*0.84*	1.72	**1.03**	0.21	*0.92*
EAP-p-0-100	1.34	**0.99**	0.13	*0.92*	2.82	**1.01**	0.30	*0.80*	4.49	**1.04**	0.87	*1.15*	1.73	**1.04**	0.27	*1.17*
EAP-p-0-150	1.37	**1.02**	0.15	*1.08*	2.91	**1.04**	0.37	*1.00*	4.30	**1.00**	0.65	*0.85*	1.69	**1.01**	0.26	*1.13*
EAP-p-1-50	1.17	**0.87**	0.19	*1.40*	2.77	**0.99**	0.47	*1.26*	4.16	**0.97**	0.81	*1.07*	1.69	**1.01**	0.22	*0.95*
EAP-p-1-100	1.32	**0.98**	0.14	*1.03*	2.73	**0.98**	0.38	*1.03*	4.46	**1.04**	0.83	*1.09*	1.66	**1.00**	0.23	*0.99*
EAP-p-1-150	1.33	**0.99**	0.17	*1.24*	2.89	**1.03**	0.45	*1.21*	4.35	**1.01**	0.68	*0.90*	1.61	**0.97**	0.27	*1.17*

Table 16: Extreme value statistics from dynamic simulation, mass dominated forces

To visualize the results, and show how the different discrepancies appear in the extreme distributions, Gumbel models for extreme moment have been fitted. The most important quantity for the engineer is the reaction forces, here represented by the reaction moment, therefore only this quantity is plotted. An argument can also be made that the extreme wave loads are behaving very similar to the surface elevation in terms of extreme statistics, and does not variate overly much with structure eigenperiod.

The outer points in terms of wave energy around the eigenperiod is shown in Figure 43 and 44, that is, $T_n = 4.5$ sec and $T_n = 14$ sec. The two other cases shares many similarities with the ones presented here, albeit with a less pronounced effect, and can be found in Appendix C.2. The simplified methods are compared against the FFT-1-1000 (thick red line) to show whether the models are in agreement.

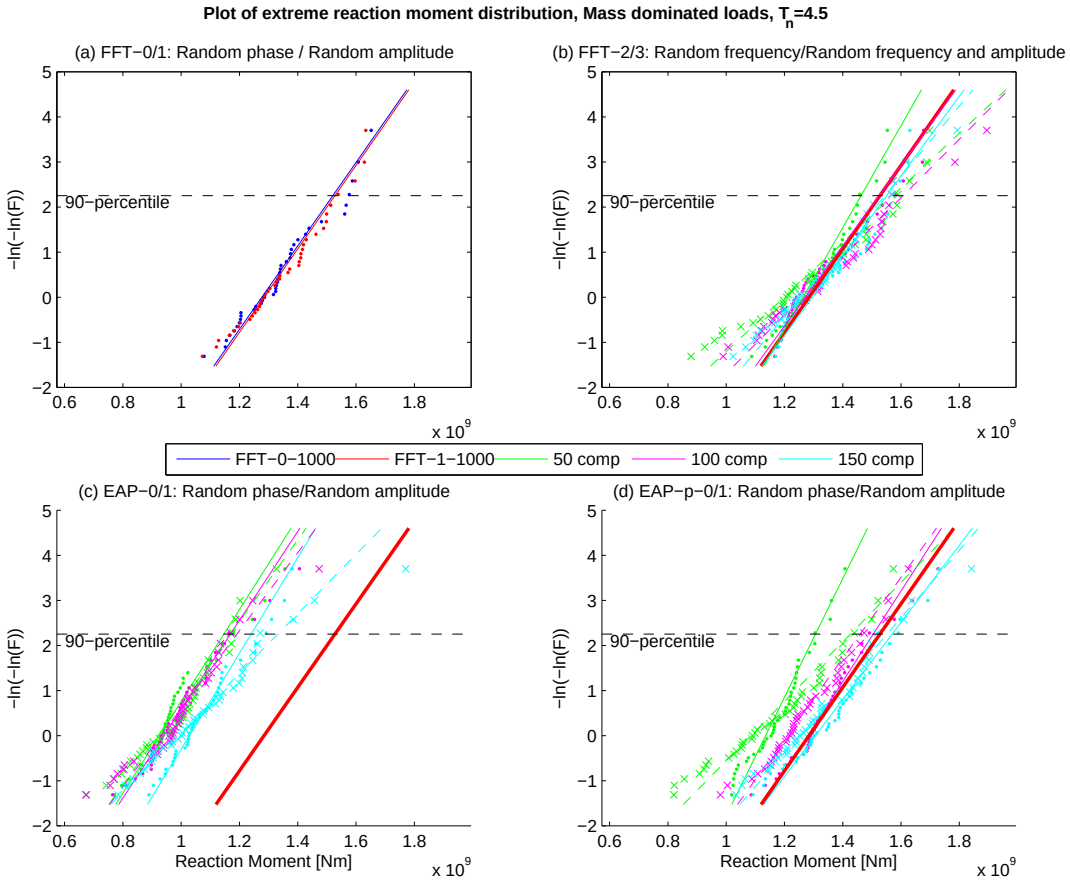

Figure 43: The distributions of extreme reaction moment for mass dominated loads, with $T_n = 4.5$ sec. Solid lines and dots (.) in Figures (b)-(d) represent the case of deterministic amplitudes, while dashed lines and x's are from simulations with random amplitudes

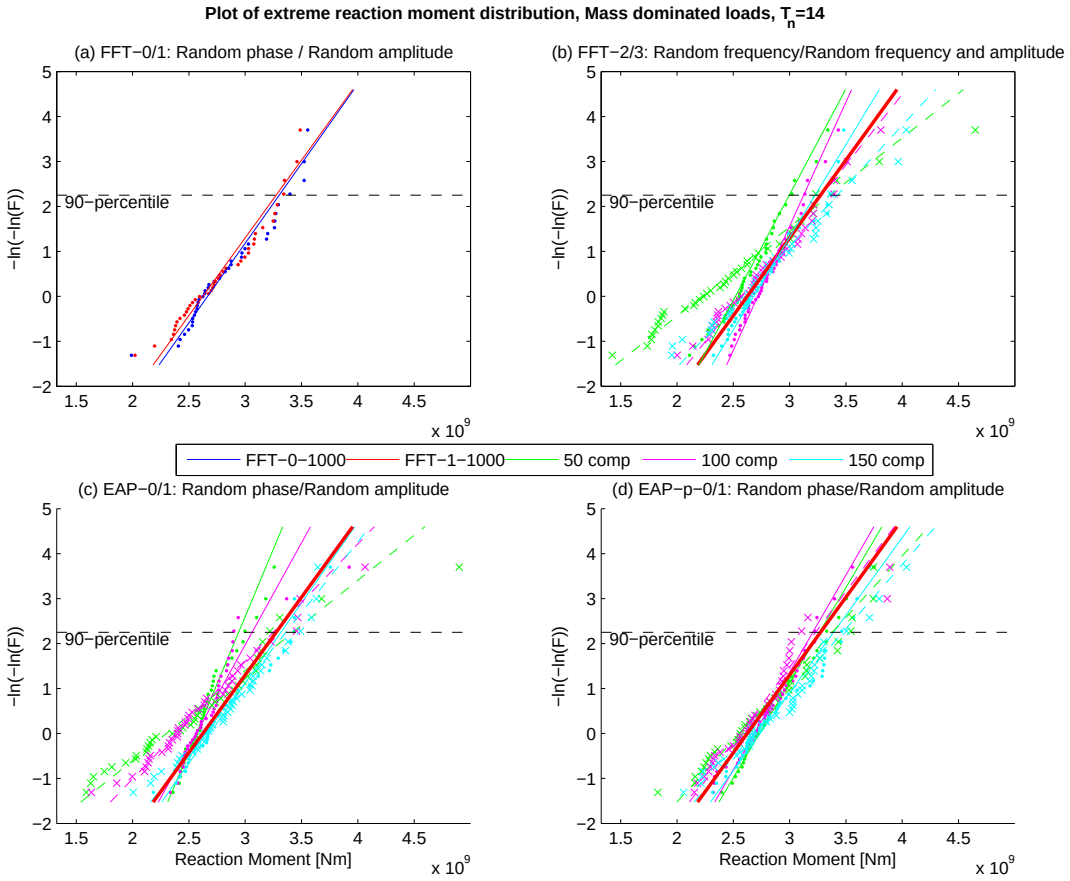

Figure 44: Plot of distributions of extreme reaction moment for mass dominated loads, with $T_n = 14$ sec. Solid lines and dots (.) in Figures (b)-(d) represent the case of deterministic amplitudes, while dashed lines and x's are from simulations with random amplitudes

7.3.5 Discussions - Mass dominated loads

Overall a good fit between the various methods compared to the FFT-1-1000 procedure is observed in terms of extreme wave loads. Furthermore one observe that the wave loads does not change much with the degree of dynamics (various eigenperiods), and the values are quite similar to those obtained from the static results in Table 14. This indicates that the motions of the structure is small, in particular the structures acceleration, which enters the wave load calculation for mass forces. Furthermore, one can see the same variations in terms of the standard deviation of extremes as discussed previously. However, when it comes to the reaction overturning moments, large discrepancies are observed. The further discussion of these are divided in errors in the mean of maxima, and errors in the standard deviation of maxima.

7.3.5.1 Discrepancies in the extreme value ROM

While the commonly used FFT-0-1000 gives very good description of the extreme statistics of both wave loads and reaction moment compared to the "exact" FFT-1-1000, several of the simplified methods show large deviations. Non-conservative deviations are found in the overturning moments presented in Table 16, however they foes not occur for the same eigenperiod. The few-component FFT approaches experience an under prediction of the reaction moment by 5-23% for a structure with eigenperiod 14 sec, and do also show trends to under predict at 9 sec and 18 sec. The EAP methods underestimates the response for eigenperiods at 4.5, 9, and 18 sec, with the strongest disagreement at 4.5 sec. The error here is 27% for the 50 component EAP scheme. The results get somewhat better with increasing components, and for instance, the 150 component methods is not does not experience an error for an eigenperiod at 9 or 18 sec. The peaked equal area principle methods are the least affected by these errors. However, the 50 component EAP-p-0 and EAP-p-1 methods experience a 12-13% under prediction at $T_n = 4.5$ sec, albeit much less than the corresponding EAP method.

The deviations of the mean of extremes in the tables are clearly visible in the extreme distributions presented in Figure 43 and 44. Figure 43 (c) shows a left side shift of the EAP relative to the FFT-1-1000, indicating a lower mean, corresponding to the under prediction at $T_n = 4.5$. Plot (b) and (d) in the same figure show some of the same results for the 50-component simulations (green lines), while the 100 and 150 component simulations are in agreement with the FFT-1-1000. In Figure 44 the EAP and EAP-p in plot (c) and (d) are similar to the FFT-1-1000, while i.e. the few component FFT's in (b) show a large spreading.

The deviation of the EAP was expected beforehand, and supports the findings of Binner [1]. However, the deviation in peaked and simplified FFT approaches was not suspected. The reason for all these discrepancies might be found when examining the frequency resolution in the different areas. In Figure 45 the spectrum discretization in the tail region, along with the position of the eigenperiod at 4.5sec are shown. The plots are given for the 50 component simplified procedures, as these show the most discrepancies.

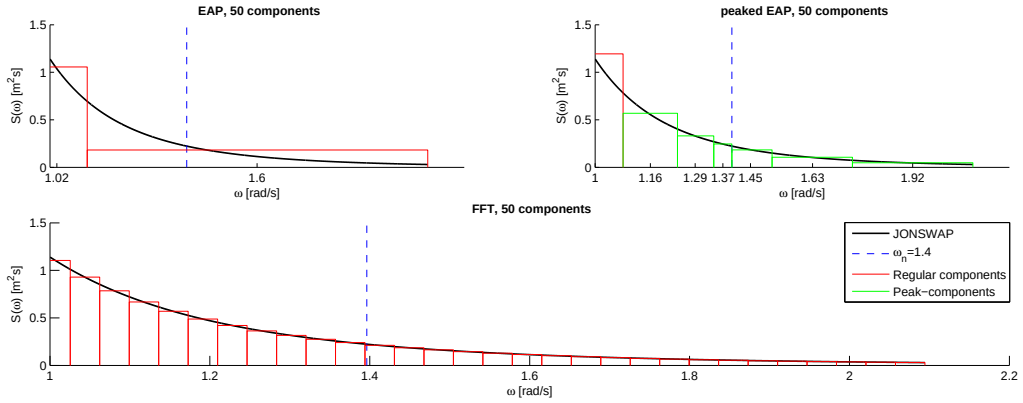

Figure 45: Frequency resolution in the tail region for FFT, EAP and peaked EAP approaches

It is observed that the tail region is ill represented in the EAP, somewhat better in the peaked EAP, and much better in the FFT (50 components for all). In particular, the very large end-block in the EAP method has a frequency far from the eigenfrequency. For low dynamics, when the eigenfrequency is far from the wave component, the behaviour of the *dynamic amplification factor* (DAF) is approximately linear, and very little error is introduced when one assumes the average frequency over the block. However, when the excitation frequency is close to the eigenfrequency, the DAF have nonlinear behaviour. To illustrate this, the dynamic amplification factor for the various wave components in Figure 45 is found from Eq. 128, and plotted in Figure 46. The frequencies of the FFT is here assumed as the mean in the interval, while in the simulations they were taken as uniformly distributed within each interval, to avoid repetition of the sea spectrum.

$$DAF = \frac{1}{\left[\left(1-\left(\frac{\omega}{\omega_n}\right)^2\right)^2 + \left(2\lambda\frac{\omega}{\omega_n}\right)^2\right]^{1/2}} \tag{128}$$

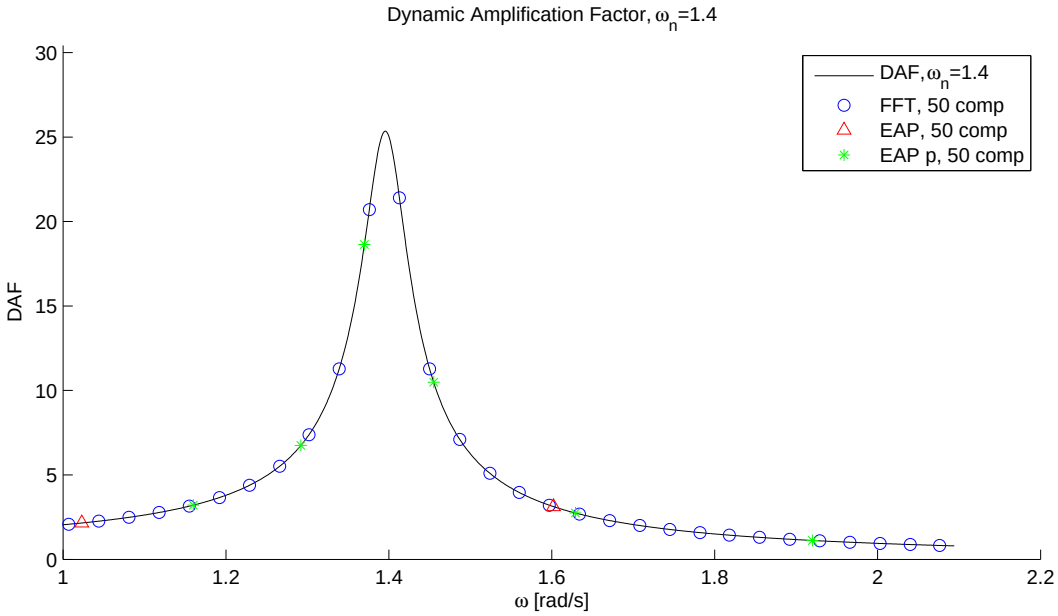

Figure 46: Dynamic amplification factor for the harmonic components in the tail region, $T_n = 4.5$ sec

From Figure 46 it is seen that the common EAP completely misses the peak in the dynamic amplification. The dynamic amplification which should have been here is neglected, and when all contributions are superimposed, the total load will too low. It is also believed that if the discretization/natural period were so that the frequency of a single harmonic component hit very close to the natural period, there would be a significant over estimation. The peaked EAP describes the behaviour around the peak somewhat better, but one should consider using even more components in this area. The peaked EAP use 10% of the components around the peak, which is 5 for the 50 component version, and it is seen that by increasing this number to 10 (100 component peaked EAP), the results improve significantly. The 50 component FFT gives the best description of the DAF of the illustrated methods. However, with these 50 components, the FFT miss the absolute peak, which is seen in a few percent lower result of the extreme in Table 16. Clearly, when increasing the total number of components, all three methods would get a somewhat better description of the DAF behaviour, which is also observed in the results.

The second issue, the deviation of extreme ROM found from the 50 (and 100) component FFT at 9, 14 and 18 sec can be explained in similar ways. It is seen in Figure 46 that the 50 coponent miss the absolute peak of the DAF. For the low energy parts of the spectrum this might not be too large an issue, however, for parts with more energy, the loss of the DAF peak become apparent. In these areas, the EAP and peaked EAP will give better results, as these are focused more on the energetic parts of the wave spectrum. An illustration of this effect for the $T_n = 14$ sec is shown in the Figures 47 and 48, here the 1000 components FFT is showed additionally. Note that the illustration spans over a much smaller frequency range, 0.4-0.5 rad/s.

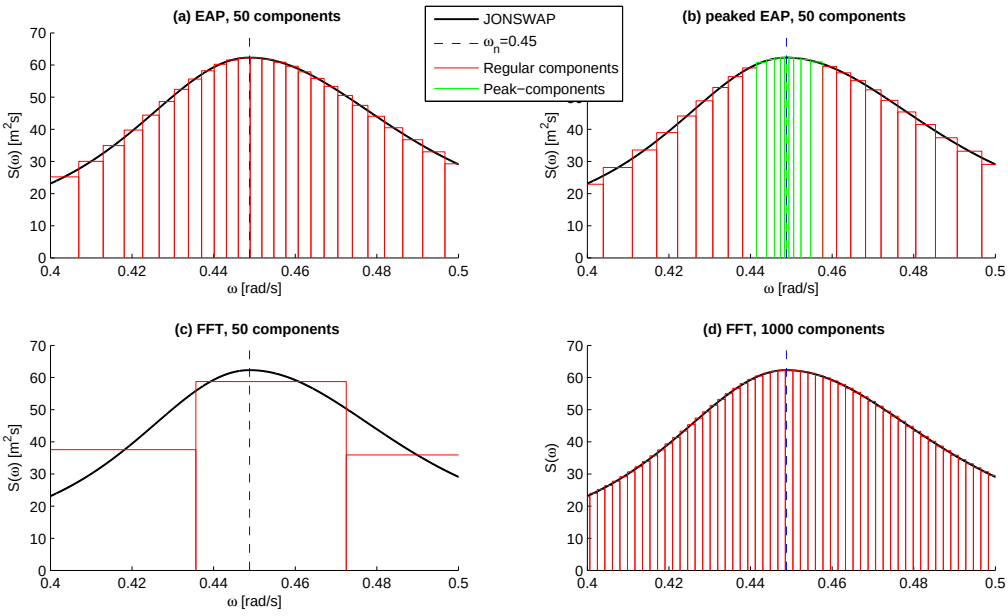

Figure 47: Frequency resolution in the peak regime for FFT, EAP and peaked EAP approaches

As the FFT use a constant frequency span, the spectral peak is not properly handled when the number of components becomes too low. This was observed with a deviation in the Gaussian surface process. Here it is illustrated by the unability to handle dynamic effects properly. Note that this error is also present for the other eigenperiods for few component FFT's, however the total load picture is not as dominated by the actions around the eigenperiod when this is in an energy dense area.

Both EAP and peaked EAP will on the other hand give good representation of the peak area of the spectrum, and hence the effect of the dynamics in this area. In Figure 48 the 50 component FFT have only three components, which is not enough to describe the DAF satisfactory. It seems as the 1000 component FFT has small enough intervals to describe the peak satisfactory. However, one should consider using an even finer mesh in the absolute proximity of the eigenfrequency, as the EAP and peaked EAP follows the peak of the DAF in Figure 48 better.

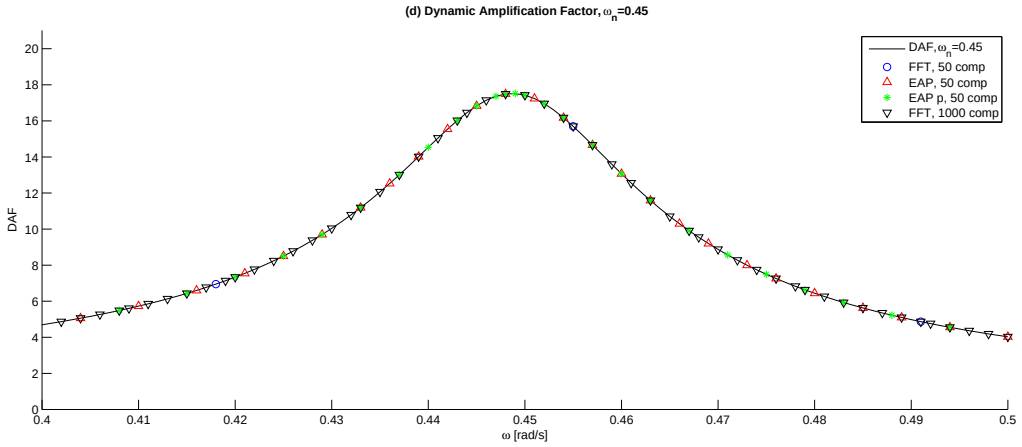

Figure 48: Dynamic amplification factor for the harmonic components in the peak region, $T_n = 14$ sec

To sum up, the results show that one can not use less than 100 components for any of the simplified methods. Otherwise, all methods give reasonably accurate mean of extreme values for certain structural eigenperiods. The EAP should not be used in combination with a mass dominated structure when the eigenperiod lies in the less energetic parts of the spectrum, while the random frequency FFT should not be exercised when the eigenperiod is in the energetic parts. The peaked EAP seems to give good results for all the mass dominated simulations, provided that a minimum of 100 components are used.

7.3.5.2 Discrepancies in the standard deviation of the extreme ROM

The standard deviation of the extreme ROM experience some of the same behaviour as observed from the static force, and surface extremes in the previous sections. However, there is a trend that the random amplitude (dashed lines in Figure 43 and 44) results in even larger standard deviation relative to the FFT-1-1000 than was found from the static simulations. To discuss this, one can focus on the standard deviations given in Table 16 for an eigenperiod of 9 seconds. A comparison between standard deviation (ratios to FFT-1-1000) of extreme surface elevation, static extreme ROM and dynamic extreme ROM for $T_n = 9$ sec is given in Table 17.

	$\sigma_{\lvert\zeta_{max}\rvert}$	$\sigma_{X,\,static}$	$\sigma_{X,\,T_n=9}$
FFT-2-50	0.6	0.55	0.74
FFT-3-50	1.14	0.9	1.74
EAP-0-50	0.76	0.7	0.58
EAP-1-50	1.12	0.89	1.73
EAP-p-0-50	0.77	0.71	0.82
EAP-p-1-50	1.23	1.12	1.26

Table 17: Standard deviation of extremes, relative to FFT-1-1000

When the amplitude is deterministic (first, third and fifth row in Table 17) the fit between static, dynamic and surface is good. For the case of a random amplitude, the dynamic result do not agree with the static or surface elevation. The explanation is again the resolution of the wavespecter around the eigenfrequency. The effect is similar to that discussed for the variance of the surface variance. When a few components carry most of the effect of dynamics, and these are found through a random Rayleigh distribution, the effect might be extremely high in some runs, and extremely low in other. The result is an approximate mean, and a too large variation, when random amplitudes are used. The effect is though not as present for the peaked EAP, as the dynamics around the eigenperiod are carried by more components (i.e. they average out).

While the above presented reason explain some of the behaviour, there are in general a lot of variations in the simulated results. The general observation is that the standard deviations seems to be low for the deterministic amplitude methods, and high for the random amplitude methods. One should therefore exercise caution when applying any of these methods to a simulation of mass dominated loads.

7.3.6 Results - Drag dominated loads

The extreme value statistics of wave loads and reaction overturning moments for a drag dominated cylinder are presented in Table 18.

DRAG DOMINATED LOADS																
	$T_n = 4.5[sec]$				$T_n = 9[sec]$				$T_n = 14[sec]$				$T_n = 18[sec]$			
	μ_X		σ_X		μ_X		σ_X		μ_X		σ_X		μ_X		σ_X	
Loads 0.1[MN]																
FFT-1-1000	2.19	**1.00**	0.52	*1.00*	2.09	**1.00**	0.52	*1.00*	1.88	**1.00**	0.44	*1.00*	2.05	**1.00**	0.52	*1.00*
FFT-0-1000	2.21	**1.01**	0.45	*0.86*	2.09	**1.00**	0.41	*0.79*	1.89	**1.00**	0.37	*0.83*	2.07	**1.01**	0.43	*0.82*
FFT-2-50	2.10	**0.96**	0.33	*0.63*	1.97	**0.94**	0.27	*0.53*	1.81	**0.96**	0.26	*0.58*	1.94	**0.95**	0.28	*0.54*
FFT-2-100	2.16	**0.99**	0.39	*0.75*	2.08	**0.99**	0.33	*0.63*	1.86	**0.99**	0.26	*0.60*	1.98	**0.97**	0.34	*0.66*
FFT-2-150	2.40	**1.10**	0.43	*0.83*	2.30	**1.10**	0.42	*0.81*	2.01	**1.07**	0.33	*0.75*	2.23	**1.09**	0.38	*0.73*
FFT-3-50	2.05	**0.93**	0.55	*1.06*	1.92	**0.92**	0.52	*1.00*	1.82	**0.97**	0.45	*1.01*	1.88	**0.92**	0.47	*0.90*
FFT-3-100	2.19	**1.00**	0.57	*1.10*	2.08	**0.99**	0.54	*1.03*	1.87	**1.00**	0.44	*0.99*	1.99	**0.97**	0.50	*0.97*
FFT-3-150	2.26	**1.03**	0.56	*1.07*	2.15	**1.03**	0.60	*1.15*	1.97	**1.05**	0.49	*1.09*	2.12	**1.03**	0.55	*1.07*
EAP-0-50	2.22	**1.01**	0.39	*0.75*	2.05	**0.98**	0.40	*0.77*	1.93	**1.03**	0.35	*0.79*	2.04	**0.99**	0.36	*0.69*
EAP-0-100	2.24	**1.02**	0.45	*0.86*	2.10	**1.00**	0.41	*0.78*	1.91	**1.02**	0.33	*0.75*	2.05	**1.00**	0.41	*0.80*
EAP-0-150	2.21	**1.01**	0.47	*0.90*	2.10	**1.01**	0.42	*0.80*	1.84	**0.98**	0.30	*0.68*	2.02	**0.98**	0.39	*0.74*
EAP-1-50	2.33	**1.06**	0.55	*1.05*	2.19	**1.05**	0.54	*1.03*	1.98	**1.05**	0.49	*1.11*	2.12	**1.03**	0.50	*0.96*
EAP-1-100	2.19	**1.00**	0.53	*1.01*	2.08	**0.99**	0.49	*0.95*	1.84	**0.98**	0.37	*0.84*	2.02	**0.99**	0.49	*0.93*
EAP-1-150	2.36	**1.08**	0.58	*1.11*	2.22	**1.06**	0.53	*1.03*	2.00	**1.06**	0.41	*0.93*	2.17	**1.06**	0.52	*1.01*
EAP-p-0-50	2.27	**1.04**	0.38	*0.73*	2.18	**1.04**	0.33	*0.62*	1.85	**0.98**	0.31	*0.70*	2.03	**0.99**	0.42	*0.80*
EAP-p-0-100	2.29	**1.04**	0.43	*0.83*	2.11	**1.01**	0.35	*0.67*	1.83	**0.97**	0.35	*0.78*	2.16	**1.06**	0.41	*0.78*
EAP-p-0-150	2.35	**1.07**	0.46	*0.88*	2.10	**1.00**	0.36	*0.69*	1.88	**1.00**	0.35	*0.80*	2.14	**1.04**	0.37	*0.71*
EAP-p-1-50	2.35	**1.07**	0.66	*1.28*	2.24	**1.07**	0.58	*1.11*	1.84	**0.98**	0.41	*0.92*	2.01	**0.98**	0.47	*0.91*
EAP-p-1-100	2.27	**1.03**	0.54	*1.03*	2.12	**1.01**	0.57	*1.09*	1.86	**0.99**	0.33	*0.74*	2.17	**1.06**	0.52	*1.01*
EAP-p-1-150	2.30	**1.05**	0.46	*0.89*	2.15	**1.03**	0.49	*0.94*	1.85	**0.99**	0.33	*0.74*	2.08	**1.02**	0.46	*0.88*
ROM 0.01[GNm]																
FFT-1-1000	2.32	**1.00**	0.42	*1.00*	4.14	**1.00**	0.55	*1.00*	7.25	**1.00**	1.28	*1.00*	3.44	**1.00**	0.58	*1.00*
FFT-0-1000	2.34	**1.01**	0.34	*0.81*	4.19	**1.01**	0.58	*1.04*	7.39	**1.02**	1.31	*1.02*	3.60	**1.05**	0.60	*1.03*
FFT-2-50	2.20	**0.95**	0.24	*0.58*	4.08	**0.98**	0.35	*0.63*	6.22	**0.86**	0.54	*0.42*	3.15	**0.92**	0.46	*0.78*
FFT-2-100	2.35	**1.01**	0.36	*0.86*	4.28	**1.03**	0.50	*0.89*	7.29	**1.01**	0.85	*0.67*	3.55	**1.03**	0.47	*0.80*
FFT-2-150	2.41	**1.04**	0.32	*0.76*	4.27	**1.03**	0.47	*0.85*	7.34	**1.01**	1.02	*0.80*	3.53	**1.03**	0.71	*1.22*
FFT-3-50	2.22	**0.96**	0.42	*0.99*	3.99	**0.96**	0.81	*1.46*	5.71	**0.79**	1.76	*1.37*	3.03	**0.88**	0.75	*1.28*
FFT-3-100	2.37	**1.02**	0.48	*1.15*	4.20	**1.02**	0.66	*1.20*	6.74	**0.93**	1.82	*1.42*	3.40	**0.99**	0.80	*1.38*
FFT-3-150	2.40	**1.03**	0.51	*1.21*	4.30	**1.04**	0.73	*1.32*	7.01	**0.97**	1.59	*1.24*	3.55	**1.03**	0.83	*1.43*
EAP-0-50	2.21	**0.95**	0.35	*0.83*	4.13	**1.00**	0.46	*0.83*	7.24	**1.00**	1.22	*0.95*	3.33	**0.97**	0.62	*1.07*
EAP-0-100	2.30	**0.99**	0.43	*1.02*	4.20	**1.01**	0.49	*0.88*	7.12	**0.98**	0.96	*0.75*	3.55	**1.03**	0.64	*1.09*
EAP-0-150	2.23	**0.96**	0.31	*0.74*	4.25	**1.03**	0.55	*1.00*	7.25	**1.00**	1.49	*1.16*	3.47	**1.01**	0.68	*1.17*
EAP-1-50	2.27	**0.98**	0.44	*1.05*	4.14	**1.00**	0.86	*1.55*	7.31	**1.01**	1.51	*1.18*	3.42	**0.99**	1.01	*1.73*
EAP-1-100	2.25	**0.97**	0.53	*1.28*	4.11	**0.99**	0.77	*1.38*	7.50	**1.03**	1.43	*1.12*	3.48	**1.01**	0.81	*1.39*
EAP-1-150	2.40	**1.03**	0.50	*1.21*	4.33	**1.05**	0.79	*1.42*	7.49	**1.03**	1.66	*1.30*	3.69	**1.07**	0.88	*1.51*
EAP-p-0-50	2.37	**1.02**	0.35	*0.85*	4.24	**1.02**	0.60	*1.09*	7.26	**1.00**	1.25	*0.97*	3.53	**1.03**	0.56	*0.95*
EAP-p-0-100	2.44	**1.05**	0.43	*1.04*	4.31	**1.04**	0.50	*0.90*	7.61	**1.05**	1.58	*1.23*	3.64	**1.06**	0.79	*1.36*
EAP-p-0-150	2.46	**1.06**	0.45	*1.07*	4.28	**1.03**	0.48	*0.87*	7.25	**1.00**	1.10	*0.86*	3.50	**1.02**	0.67	*1.15*
EAP-p-1-50	2.40	**1.03**	0.51	*1.23*	4.32	**1.04**	0.68	*1.23*	7.21	**0.99**	1.54	*1.20*	3.56	**1.04**	0.60	*1.02*
EAP-p-1-100	2.41	**1.04**	0.42	*1.01*	4.18	**1.01**	0.60	*1.09*	7.44	**1.03**	1.47	*1.15*	3.55	**1.03**	0.75	*1.29*
EAP-p-1-150	2.41	**1.04**	0.45	*1.08*	4.28	**1.03**	0.64	*1.15*	7.43	**1.02**	1.15	*0.90*	3.34	**0.97**	0.75	*1.29*

Table 18: Extreme value statistics from dynamic simulation, drag dominated forces

Similar as for the mass dominating forces, Gumbel models have been established for the extreme ROM distributions. Figure 43 and 44, shows the cases where T_n is 4.5 and 14 sec. Plots showing the cases where the eigenperiod is 9 and 18 sec can be found in Appendix C.2. The simplified methods are compared against the FFT-1-1000 (thick red line) to illustrate the agreement of the simplified methods.

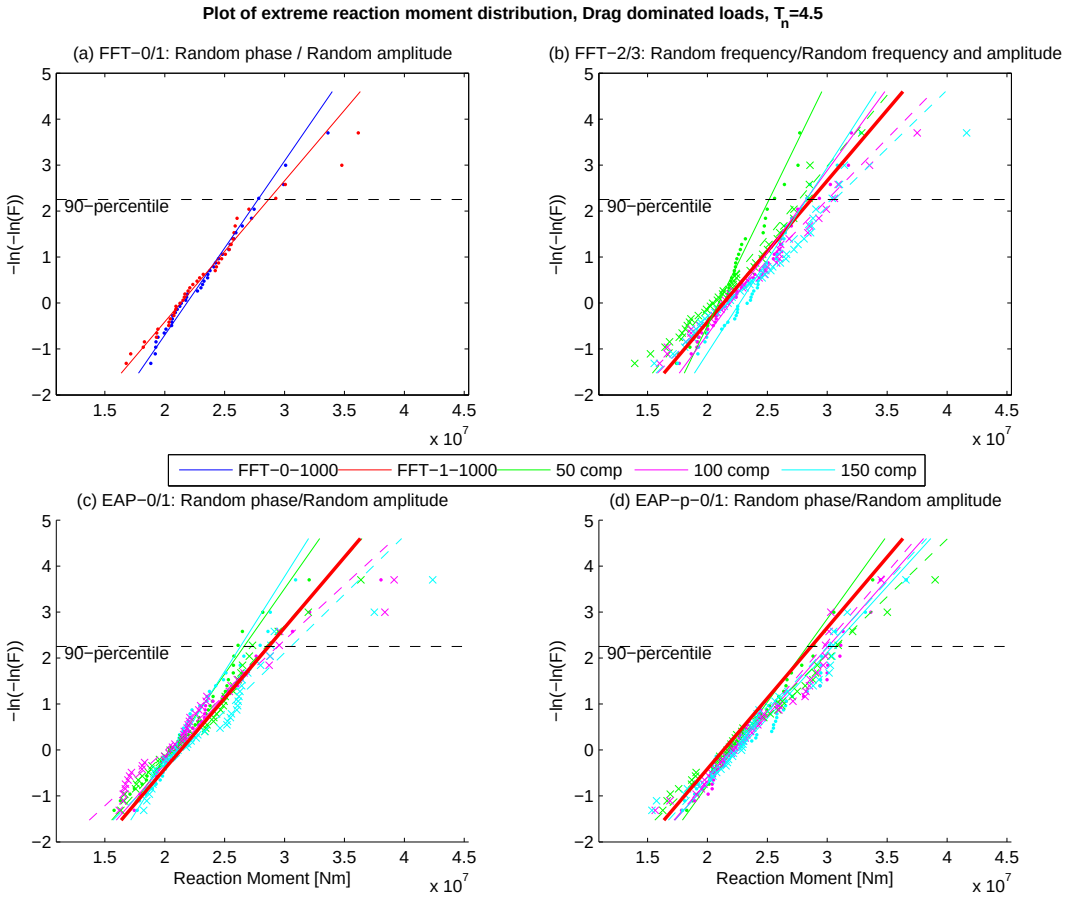

Figure 49: The distributions of extreme reaction moment for mass dominated loads, with $T_n = 4.5$ sec. Solid lines and dots (.) in Figures (b)-(d) represent the case of deterministic amplitudes, while dashed lines and x's are from simulations with random amplitudes

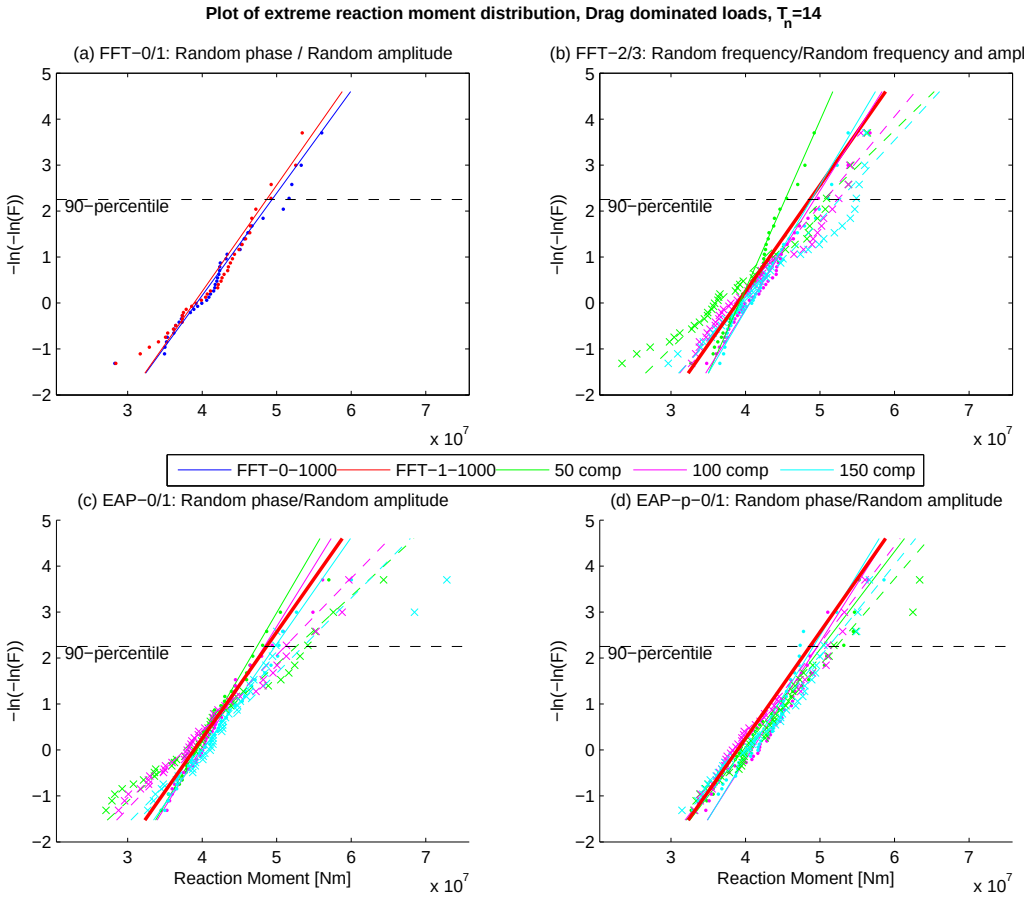

Figure 50: Plot of distributions of extreme reaction moment for mass dominated loads, with $T_n = 14$ sec.Solid lines and dots (.) in Figures (b)-(d) represent the case of deterministic amplitudes, while dashed lines and x's are from simulations with random amplitudes

7.3.7 Discussions - Drag dominated loads

The simplified methods perform significantly better when the drag term in Morison's equation is governing. With exception of the 50-component FFT approaches, the largest deviation from FFT-1-1000 is found to be 5-7% for the mean of the extreme values, and mostly on the conservative side. The issue with the mass dominated forces are only visible for the mentioned FFT-50 approaches, and somewhat also for the EAP method when the eigenperiod is 4.5 sec, but the errors are less than 5 % here. The analogy of the DLF can not be used directly, as it constitutes a linear relationship between load and response. The drag term is a function of the squared value of the wave kinematics, and are hence non linear. However, errors related to a too low resolution around the eigenperiod is still present, as the FFT-50 underestimates significantly when the eigenperiod is at the peak of the wave spectrum (14 sec).

The seemingly better fit for the drag dominated structure can be explained in terms of a Fourier series of the non linear load term, which for the i'th harmonic component can be expressed as:

$$F_i(t) = F_{0,i}\left(\frac{8}{3\pi}sin(\omega_i t) - \frac{8}{15\pi}sin(3\omega_i t) - \frac{8}{105\pi}sin(5\omega_i t) + ...\right) \tag{129}$$

Where $F_i(t)$ is the total force from wave component i, $F_{0,i}$ is given as $F_{0,i} = \frac{1}{2}\rho C_D D dz \cdot u_{0,i}^2$ and $u_{0,i}$ is the velocity amplitude of the i'th component. It is seen that the load component with frequency ω_i will excite forces on all odd multiples of its own frequency. If current is involved, forces will be excited on the even multiples of the frequency additionally. The amplitude of the terms decay rapidly, but the second and third term contains substantial forces, 17 % and 2 %. These can create large load contributions on a higher frequency. A result of this is, using the DAF analogy used previously, that significant dynamics will be created by wave components not in the immediate proximity of the eigenperiod. Figure 51 illustrates the dynamic amplifications these additional components will constitute on the structure with $T_n = 4.5$ sec for the 50 component FFT and EAP procedure.

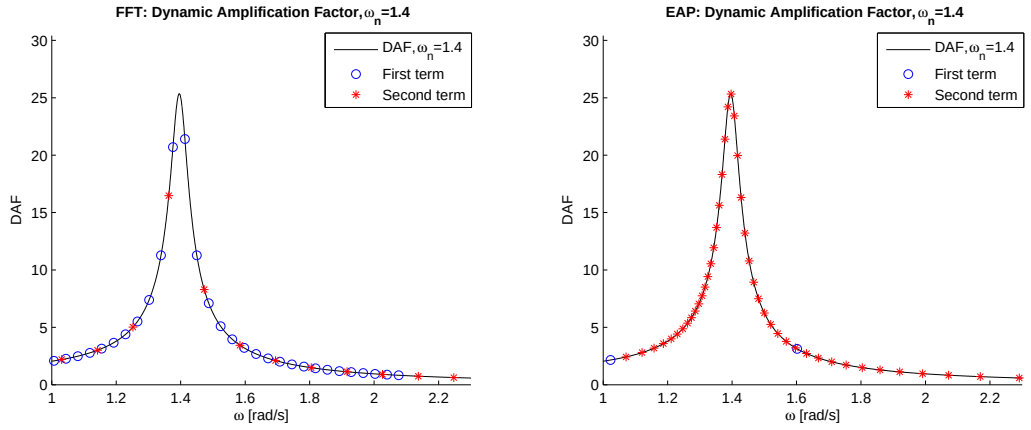

Figure 51: Plot of dynamic amplification for first and second order contributions of drag loads

The EAP will get significant contributions from several of the wave components, as the peak of the wave spectrum lies around 3 times the eigenperiod of the structure. Each of these EAP terms will have a force of 17% of the force amplitude $F_{0,i}$, which is proportional to $(\omega_i \zeta_{A,i})^2$, $\zeta_{A,i}$ being identical for all EAP components. For the FFT approach, the amplitudes will be larger, but there are fewer components. The consequence of these second order terms is that more of the harmonic components will constitute large dynamic effects around a low eigenperiod (large

eigenfrequency), hence the error of too low resolution will be lower.

As the limit of wave components is set at 25 seconds, the lowest period at which such odd-frequency multiples will be experienced is 8.3 (25/3). For the FFT approach, the amplitudes here will be very small, while for the EAP, the component with largest period is 20 sec. This would mean that the results at higher eigenperiods should not experience this correction effect. The results at 9 seconds shows however an increased accuracy compared to the mass results, while the results of the simplified FFT approach at 14 or 18 sec eigenperiod shows similar errors as for the mass dominated structures. The reason for this might simply be that the first order term contain only 84% of the total load amplitude, and hence more of the real response picture is moved away from the eigenperiod (as no second order term will excite this frequency). If the structure is supposed to experience less dynamics, the relative error of neglecting some of it becomes smaller.

Another possible explanation can be found in the load histories. Drag loads tend to have small fluctuations in the load history, until the load spikes around some extreme surface elevation, while the mass term have a more consistent large fluctuations. This could mean that the response in terms structural motions (which enters the drag force calculations through *relative* velocity squared) is not significantly under predicted for the drag loads, as these are typically low, while the lack of dynamic motions might give very wrong structural motions, and hence also loads.

In terms of standard deviation of the extremes, the same observations as before is made from the results (Table and plots). The methods using a random amplitude tend to be high, while the deterministic amplitude approaches underestimates. Some discrepancies are found, but the trend is quite clear, and comparable with the results for the individual amplitudes and static solutions.

7.3.8 Conclusion

In this study various simplified approaches of realizing the sea surface for time-domain simulation of a bottom fixed vertical cylinder have been assessed. Another purpose have been to identify any errors incurred by applying a deterministic amplitude rather than using Rayleigh distribution, when the number of components are 1000.

It is found that at 1000 components, the approximation of a deterministic amplitude performs satisfactory, with comparative results in term of extreme value statistics. One should, however, consider a safety factor on the standard deviation of surface and response extremes, as these were non-conservative for some of the simulated cases (by a $\approx 10 - 15\%$).

Furthermore, two main sources of error are found from the simplified few component methods. The first error stems from a lack of *effective components* to properly represent the peaked JONSWAP spectrum. The error is very visible for the few-component FFT schemes, as these have very few effective components, and materialize as either low or high standard deviation of extreme surface elevation, dependent on whether a deterministic or random amplitude is used. For the 50 component schemes, the mean of extremes are also on the non conservative side. The EAP and peaked EAP experience better results, as most of the components in these methods are in the energetic part, however also these suffer from large variations in the standard deviation of extreme surface elevation,. From the simulation of the Gaussian sea it is seen that the EAP produces the most accurate description of the sea in terms of statistical parameters.

The second error occurs when the method have low resolution in the proximity of the eigenperiod of the structure. It is further observed that there is larger demand of the resolution when the eigenperiod lies in the energetic parts of the spectrum. It is shown that both EAP and simplified FFT makes large errors for mass dominated loads, and some errors for the drag dominated loads. The peaked EAP does not suffer significantly from this error when a minimum of 100 components are used.

In general, using a random amplitude in connection with few components results in a process with too much standard deviation, which results in too large standard deviation of surface and response extremes. Using a deterministic amplitude with few components resulted in low values for the standard deviation of the extremes, and for some cases also an under prediction of the surface extremes. One should therefore use a random amplitude to maintain conservatism for all few-component schemes.

All the simplified methods are applicable for certain load/eigenperiod combinations. However, the method which showed best results overall was the peaked EAP with random amplitudes and at least 100 components, which had at most 3% deviation in mean of extreme force/moment. The peaked EAP will therefore be used in combination with the second order seas in the final study.

7.4 Study 4: Verification of second order algorithm, and illustration of second order effects

A *MATLAB* algorithm to compute a second order irregular surface and its associated kinematics have been made in the present report. The purpose of this study is to verify the program by comparison with theoretical models of the surface statistics and by comparison with expected behaviour of kinematics and loads relative to linear behaviour.

To compare the statistical behaviour of the surface, a significant amount of different simulations must be performed. As this is the least expensive computational operation (as compared to generate kinematics at every time step), 200 simulations is executed to establish proper statistical parameters. Two different sea states are investigated, the previously used H_s/T_p combination, i.e. 12m/14s, and a steep 100 year sea state, assumed given by $H_s/T_p = 16m/14s$. The JONSWAP spectrum is used for both cases. The depth is additionally varied between deep (1000m), finite (90m) and shallow (50m).

For illustration of kinematics a single test simulation for each sea state are used, as the time consumption is severe. The forces are calculated using the previously described cylinder, hence only horizontal velocity and acceleration are of importance. Note that one neglects the angle change, and hence change in normal vector, caused by the motion of the cylinder in the calculation of forces. As the T_p is kept constant, it is assumed that the required Time Before Peak found in 7.2 are approximately correct. The cylinder in question have been both mass and drag dominated, with a natural period of 9 sec, and hence a 300 sec start-up time is used before the measurements of forces are conducted. A total of 1300 seconds is simulated, hence 1000 seconds of surface elevation and force histories are recorded.

For each of the sea states, the wave spectrum is linearised and truncated according to Stansberg's method, in order to maintain sea variance, and avoid issues regarding wave-wave interaction for continuous spectra as discussed in Section 3.4.1.

In the present study, 500 random amplitude wave components are used in combination with the FFT method. The reason is unaffordable computational demands with 1000 components. On the positive side, introducing the Stansberg cut-off, 500 components will repeat first after $\approx$ 2000 sec, well away from the herein used 1300 sec. Admittedly, there is some uncertainty in whether 500 components is sufficient to describe the sea spectrum. To somewhat check if an error is introduced (in the spectrum realization) 200 simulations using the 1000 component FFT to generate linear and second order sea surface for a depth of 90 meter is done (for both sea states). This will show if issue (1) from Study 3 is present.

Figure 52 shows the outline of the simulations conducted.

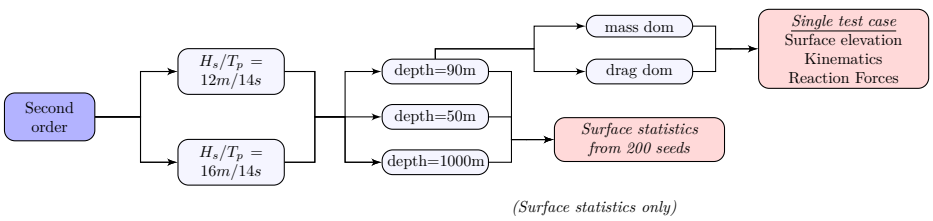

Figure 52: Overview of studies of second order effects

7.4.1 Second order Surface profile

In this study the surface elevation is assessed, in order to verify that the surface elevation is properly found in the algorithm, as compared to theoretical models. 200 different seed variations of phase angles/random amplitude percentages are used to create the statistical values. The same sets are used for all the different depths, to investigate the effects of the depth itself.

7.4.1.1 Results

The results of the constant $d\omega$ FFT are presented in Table 19, for varying water depths. The second order surface statistics are compared with the Forristall crest height model, described in Section 2.1.4. The linear model is compared against the Rayleigh crest height.

	$H_s/T_p = 12m/14s$						$H_s/T_p = 16m/14s$					
Procedure (comp)	ζ_{max}	$\sigma_{\zeta_{max}}$	σ_ζ	$\gamma_{1,\zeta}$	$\gamma_{2,\zeta}$	μ_ζ	ζ_{max}	$\sigma_{\zeta_{max}}$	σ_ζ	$\gamma_{1,\zeta}$	$\gamma_{2,\zeta}$	μ_ζ
1. order - Any d												
Theory	9.59	1.28	3.0	0	3	0	12.78	1.71	4	0	3	0
FFT (1000)	9.34	1.30	2.98	0	2.90	0	-	-	-	-	-	-
FFT (500)	9.3	1.23	2.99	0	2.98	0	12.35	1.66	3.95	0	2.96	0
2. order - 1000m												
Theory	10.57	1.49	3.0	-	-	-	14.58	2.11	4.0	-	-	-
FFT (500)	10.27	1.43	3.0	0.18	2.97	0	14.13	2.13	3.97	0.23	3.04	0
2. order - 90m												
Theory	10.63	1.51	3.0	-	-	-	14.68	2.12	4.0	-	-	-
FFT (1000)	10.35	1.56	3.0	0.16	2.99	0	14.13	2.14	4.01	0.0.20	3.00	0
FFT (500)	10.28	1.45	3.0	0.16	2.97	0	14.13	2.09	3.97	0.21	3.03	0
2. order - 50m												
Theory	10.85	1.53	3.0	-	-	-	15.09	2.15	4.0	-	-	-
FFT (500)	10.3	1.45	3.0	0.15	2.97	0	14.19	2.06	4.01	0.18	3.04	0

Table 19: Statistical values of second order surface process for various depth and H_s, 200 different seeds

In Figure 53 an example of the surface elevation around the largest peak is shown, for both sea states, illustrating the various contributions. Note that both the examples presented are quite large for their respective sea state, with similar shape (albeit at different time steps).

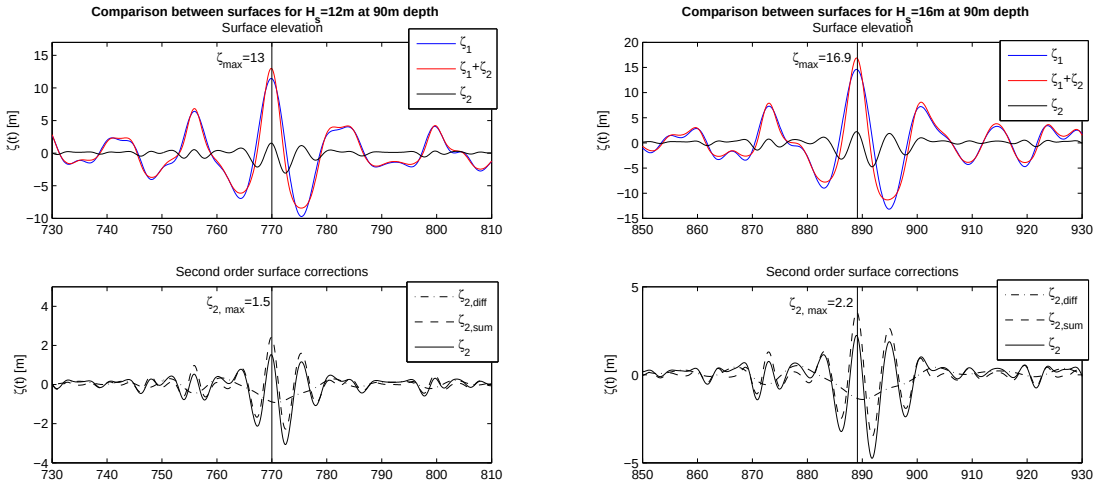

(a) $H_s/T_p = 12m/14s$ (b) $H_s/T_p = 16m/14s$

Figure 53: Contributions to the second order surface, using equal $d\omega$ FFT wave components

7.4.1.2 Discussions

The statistical parameters in Table 19 compare well with each other. There is a difference of less than 1% in mean of surface extreme between 500 and 1000 components, and less than 10 % in standard deviation of extremes. Compared to theoretical values, one sees the same slightly low values as found in Study 3, which is assumed to be due to too few waves, i.e. too short simulation length for the extremes to assume the asymptotic Gumbel model.

The example plots show the effect of the second order contributions around the largest crest. It is seen that all the surface crests get a positive contribution from the second order sum frequency term. The sum frequency contribution oscillates at twice the frequency of the surface process, giving positive corrections in both troughs and crests. That is, increase the crest height and make the troughs shallower. Furthermore, by oscillating at twice the frequency it creates a negative contribution midway between crest and trough, creating rounded troughs and steep crests. These effects can be observed in both sea states, in Figure 53.

The difference frequency term is a slowly varying term which gives a negative correction in the area around the largest crest. Furthermore it is observed that the correction terms are larger for the steeper sea state, both in terms of absolute value and relative to the complete second order surface. For the 16m H_s sea state, the second order contribution makes up 14%, while for the 12 m H_s it is around 11%. Similar behaviour are observed in all the simulated cases, albeit generally of a lower magnitude. As the events presented here are significantly larger than the mean, it is expected that the average will be lower for both sea states. The non linearities are therefore more pronounced in steeper seas.

An interesting observation is that the skewness parameter, $\gamma_{1,\zeta}$, is no longer zero, as the second order surface process has steeper crests and shallower troughs. It is here not done any theoretical deviation of the skewness or kurtosis of the Forristall distribution, however, one notes that the skewness is in an area similar to that reported by e.g. Goda [9], around $[0,\ 0.2]$.

An increase in extreme crests when the depth grows shallower are seen for both sea states in Table 19. From the Forristall formula the decrease in depth makes the Ursell parameter grow, hence altering the Forristall parameters, and increasing the extreme values. The simulations show somewhat similar behaviour, and the reason for that can be found by looking at the correction terms in 3.4.2. If one disregards the linearising of the spectrum, the linear contributions remain the same for any depth, and the changes are due to changes in ζ_{sum} and ζ_{diff}. For shallow waters $k_i > R_i$, and as the depth increase $k_i = \lim_{d\to\infty} R_i$. Additionally, the $D_{ij}^{+} = 0$ at deep waters, and increase more rapidly than the D_{ij}^{-} when the depth decrease. Both these effects leads to a lower difference frequency contribution relative to the sum frequency contribution, and hence a larger crest height at shallow waters.

A larger increase is seen in the theoretical extremes than observed values as depth decrease (3-4% low at 1000 m versus 5-7% low at 50m). After a thorough investigation of the code no errors were found, but caution must be used when simulating at shallow waters. It is possible that the perturbation scheme of wave-wave interaction fails similarly to the regular wave perturbation scheme when the depth becomes too low compared to the period and wave height.

7.4.2 Kinematic profiles

The examples discussed in the previous section are further studied in terms of kinematics and responses. The figures presented in this section is of the sea state where $H_s = 16m$, as the second order effects are more pronounced and hence more easily observed. Similar plots for the sea state $H_s = 12m$ can be found in Appendix C.3.

Three different approximations of the wave kinematics are compared:

1. Wheeler stretching of linear components from *first order sea* to first order free surface.
2. Wheeler stretching of linear components from *second order sea* to second order free surface.
3. Stansberg linear extrapolation to second order free surface (second order kinematics).

7.4.2.1 Results

For the same simulation as given in Figure 53b, the last 300 seconds of the recorded time history of surface elevation and *free surface kinematics* are given in Figure 54. The cyan coloured line follows the red at every instant for the surface elevation.

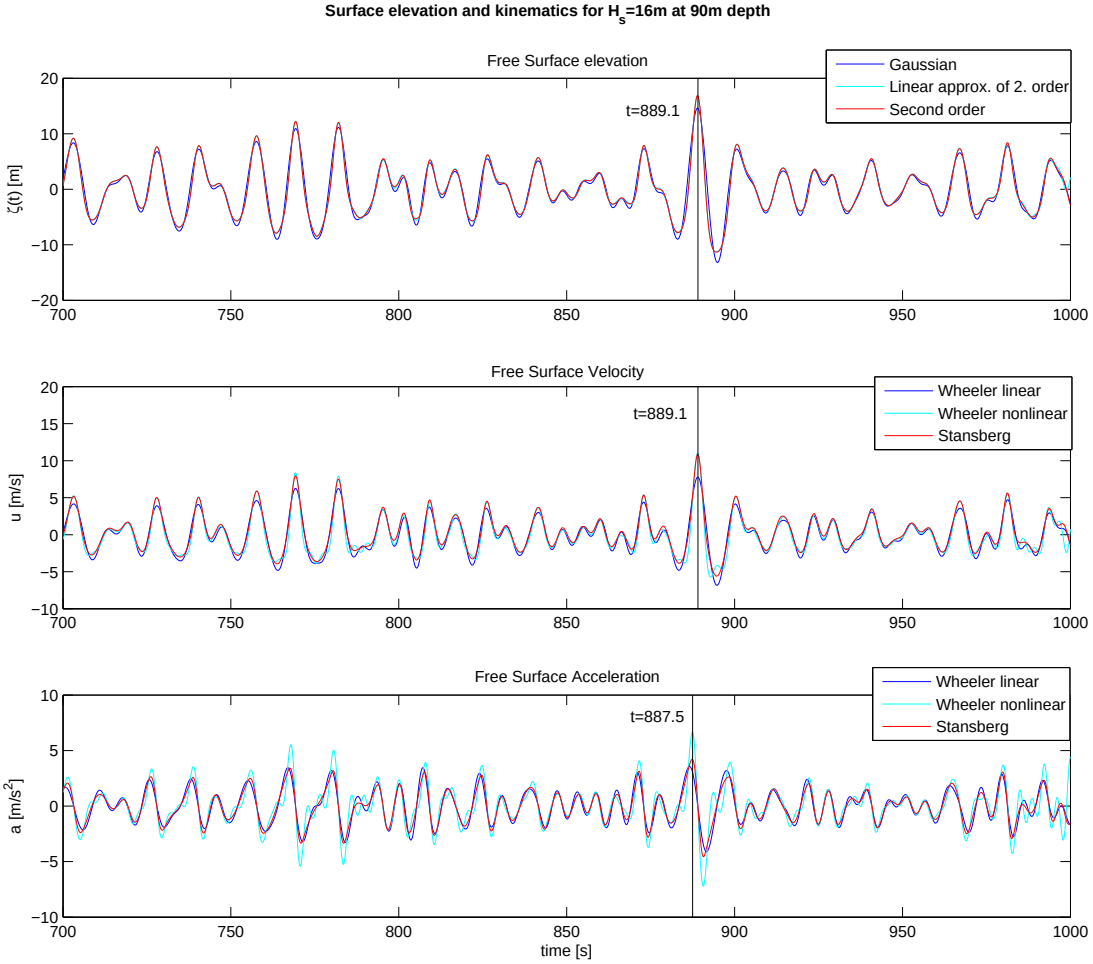

Figure 54: Surface profiles and free surface kinematics from various methods

Figure 55 consider the kinematic profiles at the instantaneous events marked out in Figure 54. The dashed lines illustrates the underlying contributions, while the solid lines are the profiles used in the load calculations. The dashed black lines along with the dashed blue makes up the second order velocity, given by dashed red. However, due to issues related to the decay rate of spectral tail etc. the linear extrapolation is used, i.e. the solid red line has the same gradient as the solid black for $z > 0$. The blue and cyan coloured graphs are the Wheeler stretched versions of their respective dashed velocities.

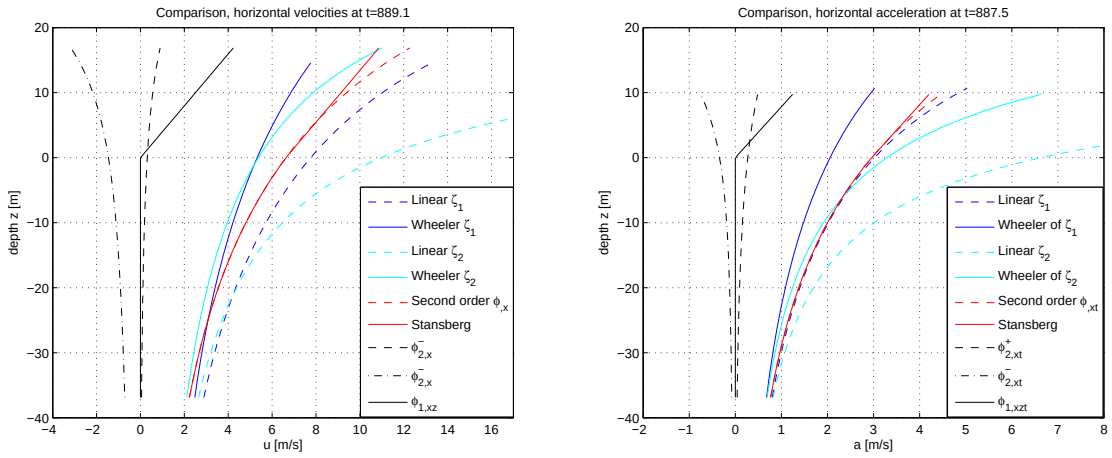

(a) Horizontal velocity profile at t=889.1 s (b) Horizontal acceleration profile at t=889.1 s

Figure 55: Kinematic depth profiles at largest maximum

To verify the kinematic profiles from the second order approximation, a Stokes V wave are fit to the extreme wave (At t=889.1s), and the surface and kinematic profiles are found and plotted against the different solid lines given in the previous figure. Note that the Stokes' kinematics are not the exact solution, but should provide kinematic profiles comparable to the irregular sea if the fit of the wave is good.

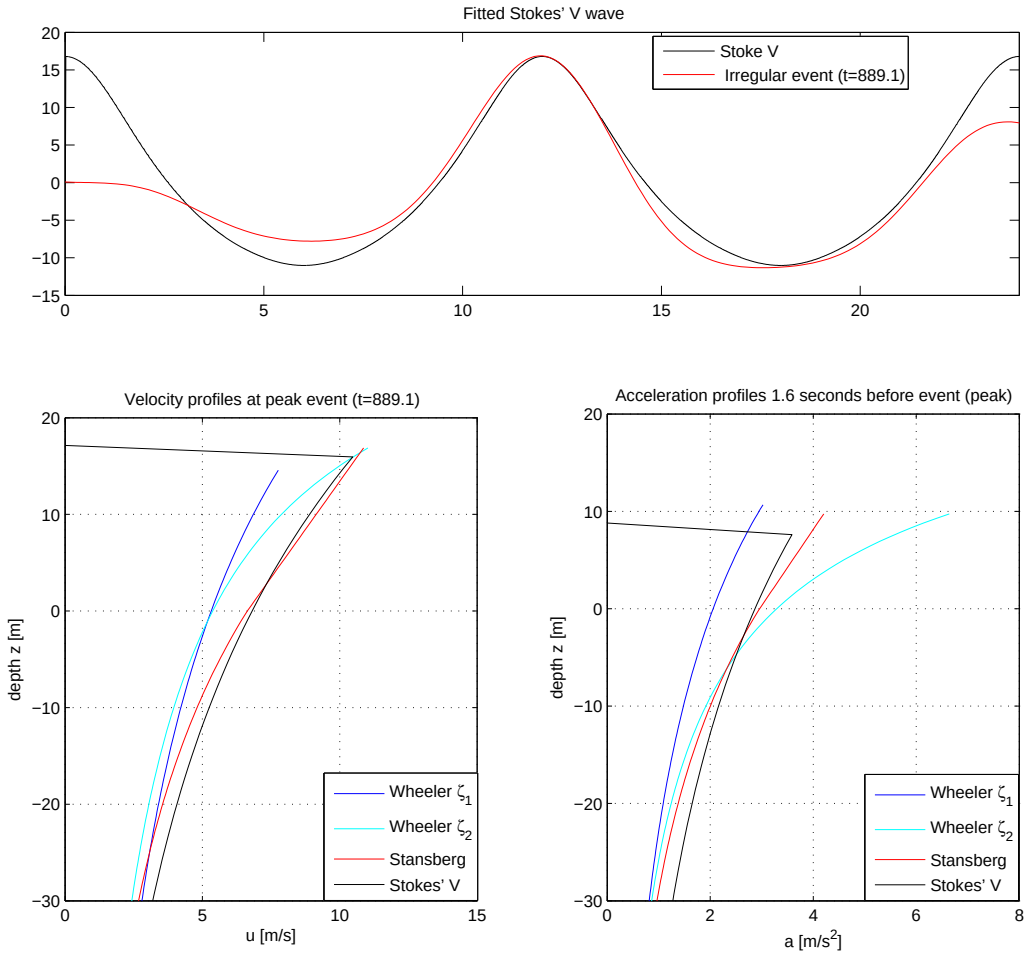

Figure 56: Comparisons with fitted Stokes V wave, H=27.85m and T=12s

7.4.2.2 Discussions

The issues regarding Wheeler stretching of components from both linear and nonlinear surface profiles are well known, and briefly explained in Section 3.6. Basically Wheeler stretching of a nonlinear surface gives a good representation around the surface, but underestimates the profile, while Wheeler of linear components will underestimate at the free surface additionally. This behaviour, compared to the Stansberg second order velocity approximation, are found in Figures 54 and 55. Additionally, a comparison with the fitted Stokes' wave gives good reason to believe that the velocity estimates in the program are correct. These are, however, approximations due to the truncation implemented for the wave spectrum, and the linear extrapolation of kinematics above mean water level.

The largest acceleration are expected to be fairly unchanged from linear to second order. The acceleration tends to have a maximum around $z = 0$, and thus the stretching procedure will not lead to an "overly stretched" kinematic profile as observed for horizontal velocity stretched to the crest. In Figure 54 this is illustrated, as the red and blue line are quite similar, but with a phase shift. The shift occurs because the second order corrections to the acceleration are zero where the linear acceleration has its peak. A plot showing the difference between velocity and acceleration is given in Figure 57. Note that both sum and difference frequency effects, and the linear extrapolation to the free surface is included in "Corrections".

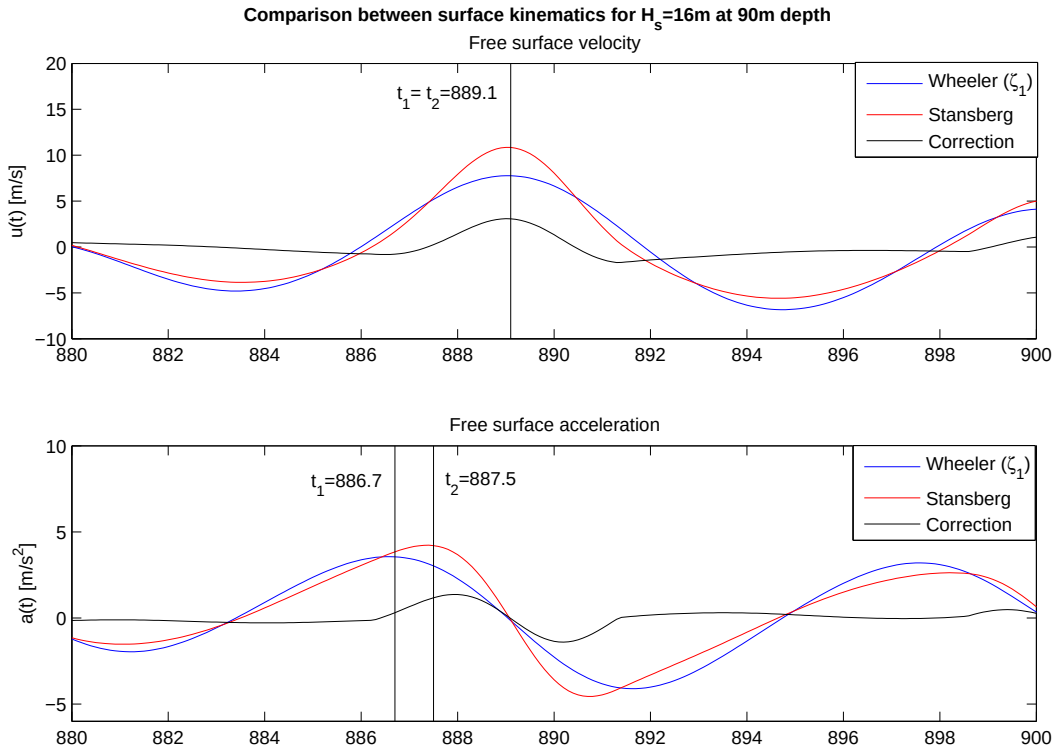

Figure 57: Comparison of the time history of the kinematics under largest crest

The before mentioned shift is the main reason why the **acceleration plots** in Figure 55 and 56 show large discrepancies for the blue line, as the time instant these are found is not the instant of largest linear acceleration. Figure 58 shows the resulting acceleration profiles if one use the time steps marked in the previous figure. The main difference in this figure is the height of

the profile, which is partly because the second order corrections make the acceleration maxima climb up the back of the wave, i.e. a larger surface elevation.

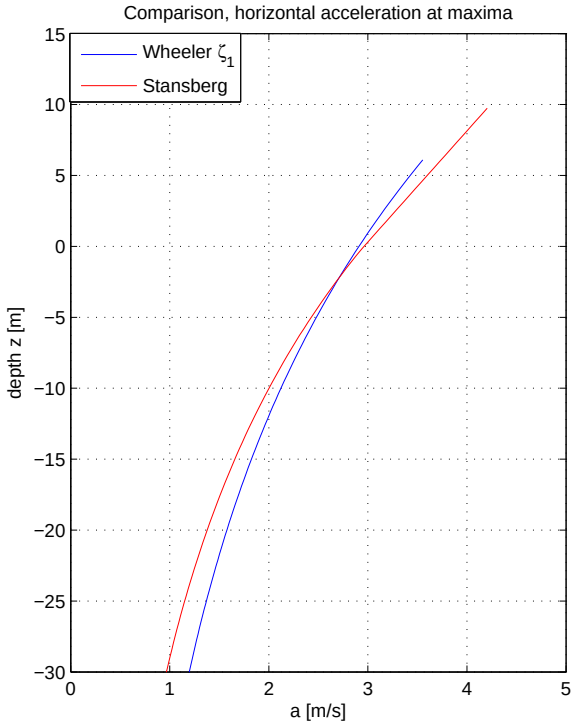

Figure 58: Vertical acceleration profiles for instant of largest surface acceleration (Not the same time).

A large discrepancy is found in the Wheeler stretching of acceleration from second order surface. This over estimates the acceleration significantly both at crest and trough compared to the two other methods, and the Stokes' wave. A possible reason for this is the low pass filter frequency used by Wheeler, i.e. $\omega_{cut} = 4\omega_p = 1.8$. This is significantly higher than the cut off frequency used here for second order kinematics, $\omega_{max} = \sqrt{2g/H_s} = 1.1$. In general the cut-frequency will influence the kinematics of the sea state, and it is introduced to avoid contamination. While Wheeler stretching gives good accuracy for the velocity, the acceleration is the derivative of velocity, and some errors might be magnified. Assuming deep waters for these high frequency components, the decay rate will be $\approx e^{\omega^2/g \cdot z}$, which will have a rapid decay rate in the water column, hence these errors are only affecting the acceleration in a limited area below the free surface. This is also observed in the figures, as the cyan coloured line converges towards the Stokes' V and Stansberg acceleration in Figure 56 fast (in vertical direction).

In general the figures presented here show the issues with linear approximations to the second order surface. All graphs fit well with expectations and theoretical arguments and is therefore somewhat a verification of the algorithm for calculating second order kinematics. Similar results as presented here, can be found for the less extreme sea state in Appendix C.3. The discussions made in this section is just as valid for those plots, however, the degree of error/variation is less as the sea is less steep.

7.4.3 Loads

The structural behaviour in terms of quasi static and dynamic base shear and overturning moment are found from simulations in *USFOS*. The purpose is to illustrate how the various approximations of wave kinematics influence the load level on the cylinder. It is of interest to divide the load in the two terms in Morison's equation, mass and drag, and investigate the effect of different kinematics for each of these. Therefore the cylinder diameter is varied, and additionally, the hydrodynamic coefficients are varied so as to remove the contribution of the other load term (set to 0.1). The hydrodynamic coefficients of the investigated load term is set according to NORSOK recommendations as described in Section 5.

In addition to the three ways of approximating the kinematic profiles described in the previous section, it is wanted to test some possible simplification of the second order corrections. One of these is a combination procedure where a linear sea and Wheeler stretched kinematics is used until 15 seconds before the linear extreme overturning moment, and thereafter 30 seconds of second order kinematics from the Stansberg method. This method is hereafter referred to as the *Spool-to-Extreme-Linear-Response* (SELR). Furthermore the effect of changing C_D to 1.15 for a drag dominated structure in a linear sea will be demonstrated.

In this section the results from both sea states described above will be presented in tables, however only plots and illustrations of the most severe sea are included. Similar plots can be found in Appendix C.3 for the sea state where H_s is 12m.

7.4.3.1 Results and discussions, quasi static loading

The quasi static load and moments for a mass and drag dominated cylinder are here investigated. To verify the load level the quasi-static response of the cylinder exhibited to the Stokes' V wave profile shown previously is found. The results are presented and compared against Stansberg's method in Tables 20 and 21.

Drag dominated	$H_s/T_p = 12m/14s$				$H_s/T_p = 16m/14s$			
	BSH $\times 10^5$	Ratio	OTM $\times 10^6$	Ratio	BSH $\times 10^5$	Ratio	OTM$\times 10^6$	Ratio
(1) Stansberg	4.72	**1.00**	42.6	**1.00**	8.50	**1.00**	78.6	**1.00**
(2) Wheeler (ζ_1)	3.43	**0.73**	28.9	**0.68**	5.79	**0.68**	48.7	**0.62**
(3) Wheeler (ζ_2)	3.79	**0.80**	33.9	**0.80**	6.63	**0.78**	60.7	**0.77**
(4) Combo (1+2)	4.71	**1.00**	42.6	**1.00**	8.52	**1.00**	78.8	**1.00**
(5) Increased C_D	4.42	**0.94**	38.6	**0.91**	7.57	**0.89**	66.3	**0.84**
(6) Stokes' V	5.20	**1.10**	43.9	**1.03**	9.20	**1.08**	78.5	**1.00**

Table 20: Quasi-static base shear (BSH) and overturn moment (OTM) for drag dominated cylinder ($C_D = 0.65/1.05$, $C_M = 0.1$)

Mass dominated	$H_s/T_p = 12m/14s$				$H_s/T_p = 16m/14s$			
	BSH $\times 10^6$	Ratio	OTM $\times 10^8$	Ratio	BSH $\times 10^6$	Ratio	OTM $\times 10^8$	Ratio
(1) Stansberg	6.60	**1.00**	4.72	**1.00**	8.93	**1.00**	6.47	**1.00**
(2) Wheeler (ζ_1)	6.49	**0.98**	4.47	**0.95**	8.34	**0.93**	5.71	**0.88**
(3) Wheeler (ζ_2)	7.39	**1.11**	5.55	**1.17**	9.80	**1.09**	7.34	**1.13**
(4) Combo (1+2)	6.59	**1.00**	4.72	**1.00**	8.94	**1.00**	6.48	**1.00**
(6) Stokes' V	6.50	**0.98**	4.51	**0.96**	8.17	**0.98**	6.12	**0.95**

Table 21: Quasi-static base shear (BSH) and overturn moment (OTM) for mass dominated cylinder ($C_D = 0.1$, $C_M = 1.2/1.6$)

The results from the quasi static analysis can be seen directly in comparison with the kinematic plots in Figure 56 and Appendix C.3. As the structure acts static, all loads must be taken as shear forces, and hence the largest shear is equal to the total wave load. The reaction force and moments can then be given directly by the integration of Morrison's equation:

$$\begin{aligned} dF =& \overbrace{\rho\frac{\pi D^2}{4}\int_{-d}^{\zeta} C_M a_x dz}^{inertia} && + \overbrace{\frac{1}{2}D\int_{-d}^{\zeta} C_D u|u|dz}^{drag} \\ dM =& \rho\frac{\pi D^2}{4}\int_{-d}^{\zeta} C_M(z+h)a_x dz && + \frac{1}{2}\rho D\int_{-d}^{\zeta} C_D(z+h)u|u|dz \end{aligned} \tag{130}$$

One can clearly see from Figure 56 that the horizontal velocity of the various Wheeler methods has an ill fit at the mean water level, compared to the second order and Stokes' V wave. The velocity enters quadratic in the drag forces, thus the error is squared. At mean water level the velocity profile of the Wheeler methods are practically the same (for this example), and so are Stansberg and Stokes velocity profiles. The quadratic velocity at this level are:

$u^2_{st....}$	$7^2 = 49m/s$
$u^2_{wheeler}$	$5^2 = 26m/s$
Ratio	2

The consequence is that the drag force level is twice as high for the extrapolated second order theory at z=0. The total error done for the Wheeler stretched methods is significantly lower, as the error decreases further down in the water column. Wheeler of second order theory provides relatively good surface velocities, and the linear sea has lower crests, i.e. a lower upper integration limit of the force equation. The combined effect is a slightly more accurate force level for the second order approximation of Wheeler stretching. The SELR simulation (4) compares well with full second order loads, as no dynamic motions are included in this quasi static simulation. Furthermore, increasing the drag coefficient tends to decrease this error, yet do not remove it completely. Introducing a constant scale parameter will not be able to describe the necessary correction for an arbitrary sea, as this is strongly dependent on the steepness.

The mass dominated loads tells a different story, but the answers can still be found in the kinematic profiles. The linear Wheeler stretching compares well with the second order theory, which is also expected. From the discussions around the accelerations in the previous section one found that these were practically the same, with a shift in time, and thus the inertia load will be the same, yet at a shift in time. The Wheeler stretching of second order kinematics grossly overestimates the largest accelerations at free surface, and the reason is thought to be some kind of high frequency contamination. This leads to a larger force, and specifically a larger force around the surface, hence even larger moments. As this is much larger than both second order, linear and Stoke's V, it is believed this is in fact an inherent error in either the method (Wheeler stretching of second order surface), or the algorithm made.

It is furthermore clear that the non-linear effects in terms of quasi static drag reaction force and moment become more pronounced in the steeper sea. Similar effect is observed for the acceleration of Gaussian sea, this is thought to be because the time shift will mean that the largest acceleration occur at an instant with larger crest elevation, and the integration will hence produce larger forces. The various ratios of the Stokes waves loads and moments can similarly be argued from the kinematic profiles. However, these are not supposed to be correct, as fitting the Stokes' wave is an approximate method to see whether kinematics and the quasi static load level is within the expected area. A more optimized fit of the Stokes wave profile to the irregular

surface would probably show better comparison with Stansberg's forces, but this is not dealt with here.

7.4.3.2 Results and discussions, dynamic loads

A dynamic analysis of the test cases are conducted. The forces and moments are presented numerically in Tables 20 and 21, and graphically in Figures 59 and 60.

Drag dominated	$H_s/T_p = 12m/14s$				$H_s/T_p = 16m/14s$			
	BSH $\times 10^5$	Ratio	OTM $\times 10^6$	Ratio	BSH $\times 10^5$	Ratio	OTM$\times 10^6$	Ratio
(1) Stansberg	5.54	**1.00**	53.4	**1.00**	9.06	**1.00**	84.5	**1.00**
(2) Wheeler (ζ_1)	5.09	**0.92**	48.8	**0.91**	7.64	**0.84**	70.6	**0.83**
(3) Wheeler (ζ_2)	5.17	**0.93**	49.6	**0.93**	8.50	**0.94**	78.24	**0.93**
(4) Combo (1+2)	5.52	**1.00**	53.3	**1.00**	9.08	**1.00**	84.7	**1.00**
(5) Increased C_D	5.87	**1.06**	56.7	**1.06**	8.84	**0.98**	82.5	**0.98**

Table 22: Dynamic base shear (BSH) and overturn moment (OTM) for drag dominated cylinder ($C_D = 0.65/1.05$, $C_M = 0.1$)

A plot of the dynamic reaction overturning moment for the steeper sea state is given in Figure 59. Plots of the other sea states and reaction forces could also have been assembled, but would provide no other information and less pronounced effects. Note that the increased drag coefficient correction is not included in the figure, as more lines would only confuse the main observations.

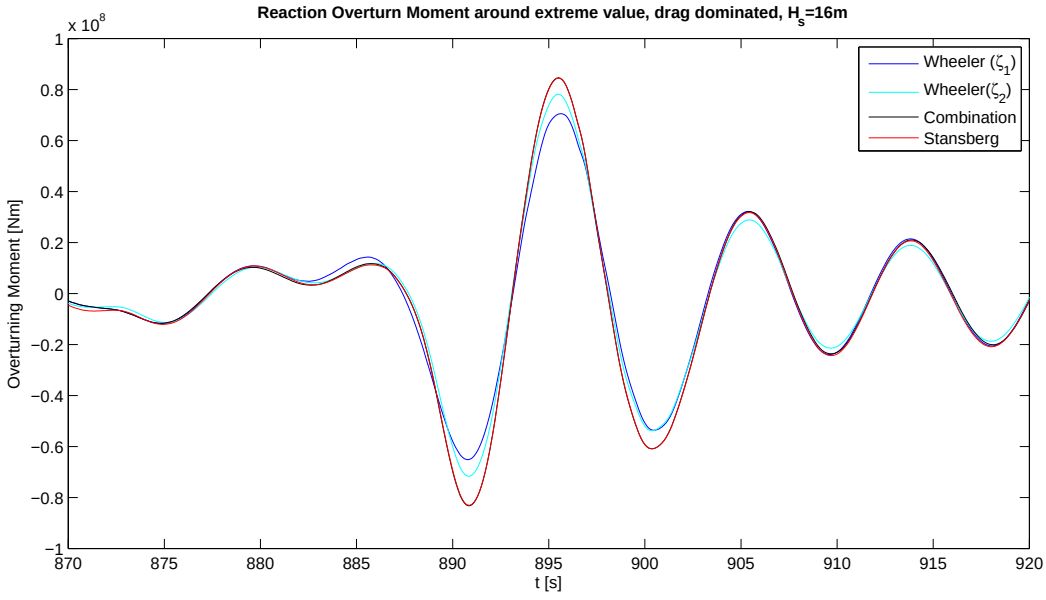

Figure 59: Reaction Overturn Moment around extreme, drag dominated loads

For the cylinder with very low drag coefficient, and large diameter, the forces and moments were found to be:

Mass dominated	$H_s/T_p = 12m/14s$				$H_s/T_p = 16m/14s$			
	BSH $\times 10^6$	Ratio	OTM $\times 10^8$	Ratio	BSH $\times 10^6$	Ratio	OTM $\times 10^8$	Ratio
(1) Stansberg	12.7	**1.00**	1.34	**1.00**	22.8	**1.00**	2.27	**1.00**
(2) Wheeler (ζ_1)	13.3	**1.04**	1.41	**1.05**	22.8	**1.00**	2.27	**1.00**
(3) Wheeler (ζ_2)	13.0	**1.05**	1.36	**0.99**	23.3	**1.02**	2.32	**1.02**
(4) Combo (1+2)	12.7	**1.00**	1.34	**1.00**	22.77	**1.00**	2.26	**1.00**

Table 23: Dynamic base shear (BSH) and overturn moment (ROTM) for mass dominated cylinder ($C_D = 0.1$, $C_M = 1.2/1.6$)

The reaction overturning moment around the largest extreme value is plotted in the following. One can also note the difference in the mass load-history and drag history in Figure 59, which is similar to the observations and discussions in Study 2. For these specific test cases the extreme values were found in the vicinity of the largest crest height, which will not hallways be the case.

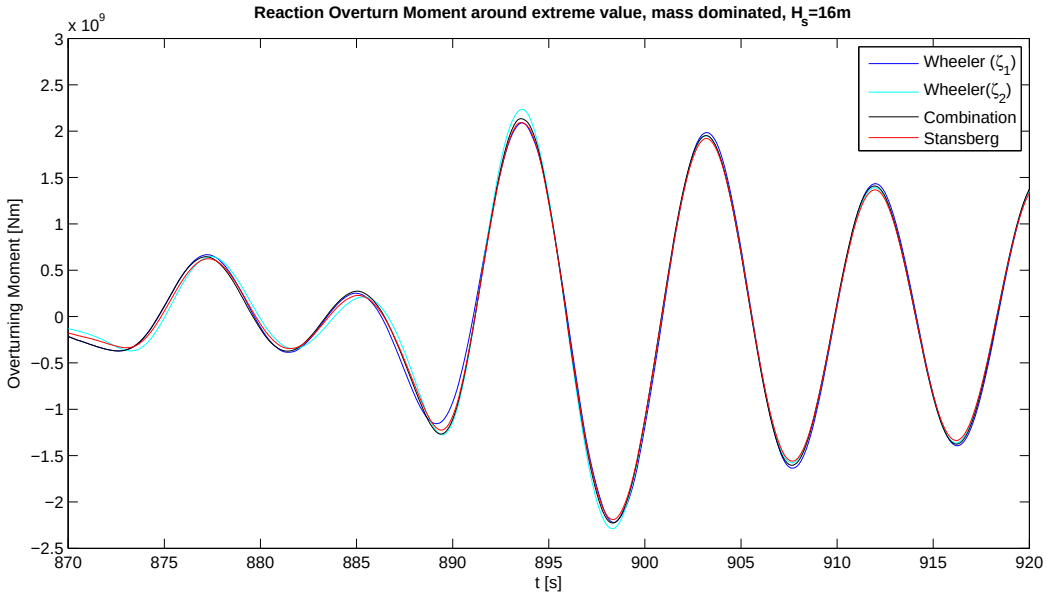

Figure 60: Reaction Overturn Moment around extreme, mass dominated loads

For the dynamic simulations one observes that similar effects as from the quasi-static simulations, albeit to a lower degree, are present. The reason for this is that a dynamic amplification factor is included, and thus the kinematic profiles will not be directly linked with the force level. In order to illustrate the difference when including dynamics, a plot comparing the energy, dynamic amplification and cut off frequencies applied in Figure 61.

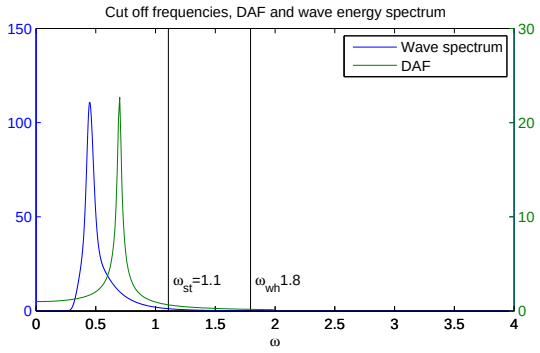

Figure 61: Comparison between wave energy, dynamic amplification and cut frequencies

There are two main observations. Firstly, the dynamic amplification is very large in a small area, at frequencies where the linearisation of the wave spectrum enforce similar energy levels for both linear and second order theory. This means that a selected few components of the total number which makes out the total force level is picked out, and the force these create is enlarged. These components and enlargements will be approximately the same for both linear and non linear terms, and thus more focus is given to the parts of the kinematic profiles which are equal in linear for both linear and second order methods. The percentage error will thus be reduced. This is easily observed when comparing, for instance, the 16m sea state in Table 22 with Table 20, where the ratio of overturning moment increase from 0.61 to 0.84 for the Wheeler stretching of a linear sea (and 0.68 to 0.88 for base shear).

Another observation from Figure 61 is that the dynamic amplification becomes lower than 1 when the frequency becomes larger than one, and decays with increasing frequency. Therefore most of the frequencies which makes up the large spike of the second order Wheeler stretched acceleration in the top of the profile plot in Figure 55 will have a dynamic reduction. From the same argument as made in the above paragraph, the forces and moments will hence be less, and the error compared to Stansbergs method will be less.

The plots of the response histories shows a similar behaviour in a large parts of the time, and a rather large deviation around the largest responses, particularly the plot from drag loads. The reason for this is that second order theory is not necessary for small waves, and only constitute large effects around the extremes. Of particular interest in these plots are the way the SELR method (black line) initially follows the blue line, then splits off from it around 880 sec, and use some seconds to converge towards the red, which it follows pretty good around the largest oscillations. This behaviour illustrates that it might very well be sufficient to use the computationally demanding second order theory only in the area around the largest linear extreme.

While the results here show that the second order correction is increasingly important with severity of seas, and only for drag dominated structures, it is important to note that the values presented here are those of a single test case run in order to verify the program and familiarize oneself with second order kinematics. In Section 8 a thorough analysis using 30 different seed variations are performed.

7.5 Summary of findings in the introductory studies

A summary of the studies performed in this section is here given

Study 1

It is found that the phase angles generated in *USFOS* are not random, and will lead to an error if used to realize the Gaussian surface. This error is removed by using another random seed generator, such as the rand function in *MATLAB*, and input these in *USFOS*. While the error source is not completely identified, it is seen that a random distortion of the phases from *USFOS* will suffice to remove the issue, hence some sort of repetitiveness that was not caught in typical test of probabilistic models is thought to be the issue.

Study 2

A study of the required time to remove transient behaviour of a cylinder with varying shape and degree of dynamics was performed in Study 2. It is shown that there is a difference both in terms of wave energy around the structural eigenperiod and dominating loads. In general, the mass dominated cylinder demanded a longer time to obtain the target accuracy. The largest time was found to be 400 seconds, which applied to a mass dominated cylinder with an eigenperiod of 14 or 18 sec. In particular, the studies of second order effects are performed with a cylinder which have an eigenperiod of 9 second. The required set-up time is then 150 seconds for a drag dominated structure, and 300 for a mass dominated structure.

Study 3

Furthermore a test of simplified approaches of subdividing the wave spectrum for time domain simulations were performed, which showed that all proposed methods had uses in certain circumstances. It was, however, observed that using fewer than 100 components would result in some kind of erroneous behaviour for all methods. All simplified methods showed a lack of standard deviation of extreme value if a deterministic amplitude was found from the wave spectrum, and hence the amplitude should be taken as a Rayleigh distributed variable, if simplified approaches are performed. For the 1000 component procedure, there was shown no significant error with a deterministic amplitude.

The ability of the methods to produce correct statistical parameters for the Gaussian sea elevation was found to be governed by the number of *effective components* in a small frequency range around the peak of the spectrum. Hence, the equal area principle and peaked equal area principle showed best results in terms of statistical parameters of the Gaussian sea. The ability to produce correct dynamic loads were seen to be determined by both the above mentioned issue, and the number of components in the vicinity of the structures natural period *relative to the density of the wave spectrum at this point.* Hence, the equal area principle gave low force levels for natural periods not in the peak of the spectrum, and the simplified random $d\omega$ FFT approach gave low values for periods in the peak of the spectrum. It was also observed that these issues were most pronounced for the mass dominated load case. The main reason for the reduced error for drag loads is that the super-harmonic loading excite forces at odd frequency multiples, which, for structures with low natural periods, will catch some of the dynamic behaviour.

The equal area principle with increased focus around the natural frequency of the cylinder showed best results in terms of modelling the sea and dynamic forces for an arbitrary structural eigenperiod, and is therefore the recommended practice. The error found were at most 3% in mean of extremes, and 10% in standard deviation of extremes. This method will be tested in a second order realization in next chapter.

Study 4

A test simulation of second order kinematics is lastly performed, which showed results as theoretically expected. A comparison of surface profile with theoretical models, velocity profiles with various well known methods and additionally a Stokes V wave give reason to believe the program assembles the correct kinematics. Furthermore the issues of Wheeler stretching of Gaussian and non linear sea was demonstrated by a test case.

From these studies it is decided to proceed with establishing the extreme force distributions from 30 seed variations. The simplified approaches of Wheeler stretching of second and linear sea, the combination method (SELR), and full second order theory from the peaked EAP will be compared against the, here taken as exact, 500 component FFT. The highest estimate of required time before peak for the cylinder with an eigenperiod of 9 sec was found to be 300 sec in Study 2, hence this will be used as the initiation time for force record.

8 Second order simulation of irregular seas

8.1 Introduction

In this activity the object is to investigate the quasi-static and dynamic extreme value distributions for the bottom fixed cylinder described in the case study. The necessity of applying second order kinematics to establish proper structural reaction forces and moments are investigated for two different sea states, and for both a mass and a drag dominated cylinder. Additionally, simplified approaches of estimating kinematics for load calculations in the time domain simulation are performed, and the accuracy of these, along with the computational savings are discussed.

30 seed variations of each separate method is performed in order to avoid large statistical uncertainties. Due to an overly large workload using 1300 sec simulations in the test study, only 1100 seconds were used for these 30 seed variations, and only the cylinder with a natural period period of 9 sec were studied. This means a total of 800 second record of forces when the initial 300 sec set up time to dampen transient response are removed, according to Study 2 in Section 7.

Furthermore the equal area principle with increased focus around the natural period, the peaked EAP, have been used as the simplified method of realising the sea spectrum, as it showed the greatest prowess in Study 3. It is used 100 harmonic components when the sea surface is realised through the peaked EAP, and 500 components when the discrete Fourier components with equal frequency spacing are used. Both these methods showed good comparisons of surface parameters to the 1000 component FFT method in Study 4.

The following methods are compared in the following pages:

(1) FFT: Complete second order kinematics model, using the Stansberg method

(2) FFT: Wheeler stretching of linear components from linear surface

(3) FFT: Wheeler stretching of linear components from second order surface

(4) FFT: Combination of linear method with second order theory in a 30 second interval around the largest linear response (Spool-to-Extreme-Linear-Response SELR)

(5) FFT: Effect of increasing C_D for drag dominated structures

(6) EAP-p: Complete second order kinematics model, using the Stansberg method

(7) EAP-p: Wheeler stretching of linear components from linear surface

A schematic outline of the simulations are given in Figure 62. The *MATLAB* algorithm sets up the wave kinematics for each time-step, while the actual solution of the equation of motion is performed in *USFOS*. The kinematics are given to *USFOS* through grid wave files, see e.g. the *USFOS* hydrodynamics manual, [40], for detailed information regarding this procedure.

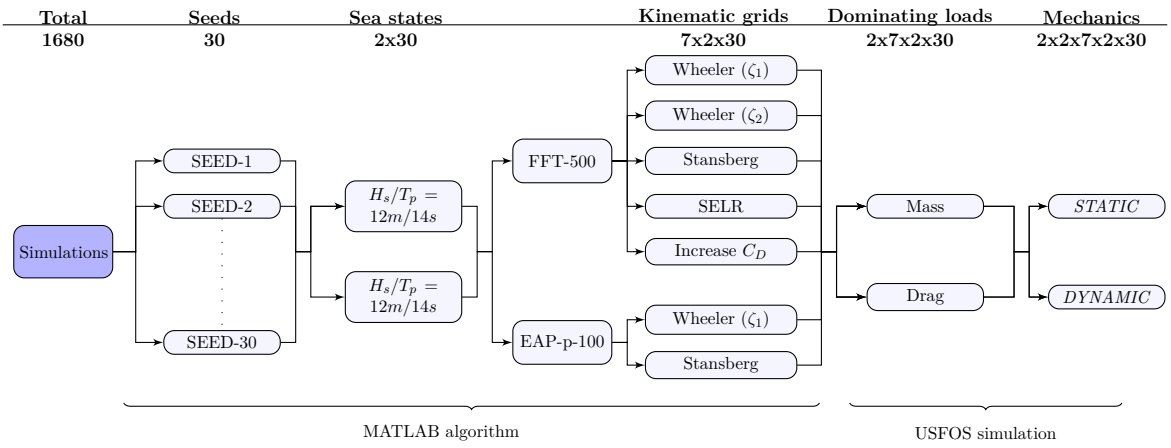

Figure 62: Overview of simulations performed in the current study

The results are discussed in terms of statistical parameters of surface elevation, and extreme value statistics of quasi static and dynamic extreme response. Special interest is on the deviation at the high percentile levels as these are the values used for design considerations in for instance the contour line method. This is illustrated by Gumbel fit model for bot surface extremes, and quasi static and dynamic extreme response. Most of the discussions in this section will refer to Study 4 where a single test case is thoroughly examined.

8.2 Surface elevation

The first measure of the adequacy of simplified methods is found by comparing statistical values of the surface elevation and in particular, the extreme values of these. In Study 4 it was shown that the 500 component FFT approach showed good comparison with theoretical values. Here it will be shown how this subset (30 seeds) compare, and also how the peaked EAP generated sea for a second order theory compare. It is also of interest to see how well the sea is depicted when the second order realization is done, and a fast Fourier transform (with frequency cut-off $4\omega_p$) are conducted to establish new linear components.

The expected theoretical values will not be the same for this study as those found in Study 4, as the recorded simulation length is here reduced to 800 sec.

8.2.1 Results

The statistical values are presented in Table 24, while the extreme value distributions are plotted against observations in Figure 63. Note that the cases (4) and (5) are not included, as (4) will be a combination of (1) and (3), and (5) will have equal surface as (2). The theoretical values for a Forristall second order model is also given in the table. These values are for the 800 seconds recorded out of the total 1100 seconds simulated.

	$H_s/T_p = 12m/14s$						$H_s/T_p = 16m/14s$					
Procedure	ζ_{max}	$\sigma_{\zeta_{max}}$	σ_ζ	$\gamma_{1,\zeta}$	$\gamma_{2,\zeta}$	μ_ζ	ζ_{max}	$\sigma_{\zeta_{max}}$	σ_ζ	$\gamma_{1,\zeta}$	$\gamma_{2,\zeta}$	μ_ζ
Theory, Forristall	10.38	1.54	3.00	-	-	0	14.3	2.17	4.00	-	-	0
(1) Second order, FFT	10.15	1.58	2.96	2.96	0.16	0	14.23	2.23	3.99	3.04	0.22	0
(2) Linear (ζ_1), FFT	9.18	1.32	2.95	2.92	0.00	0	12.51	1.82	3.96	2.97	0.00	0
(3) Linear (ζ_2), FFT	10.08	1.57	2.95	2.96	0.16	0	14.20	2.25	3.99	3.04	0.21	0
(6) Second order, EAP-p	10.09	1.58	2.94	3.02	0.18	0	14.08	2.04	3.93	3.09	0.18	0
(7) Linear (ζ_1), EAP-p	9.14	1.30	2.93	2.97	0.02	0	12.31	1.63	3.90	3.04	-0.03	0

Table 24: Statistical values for the various surface realizations, 30 samples

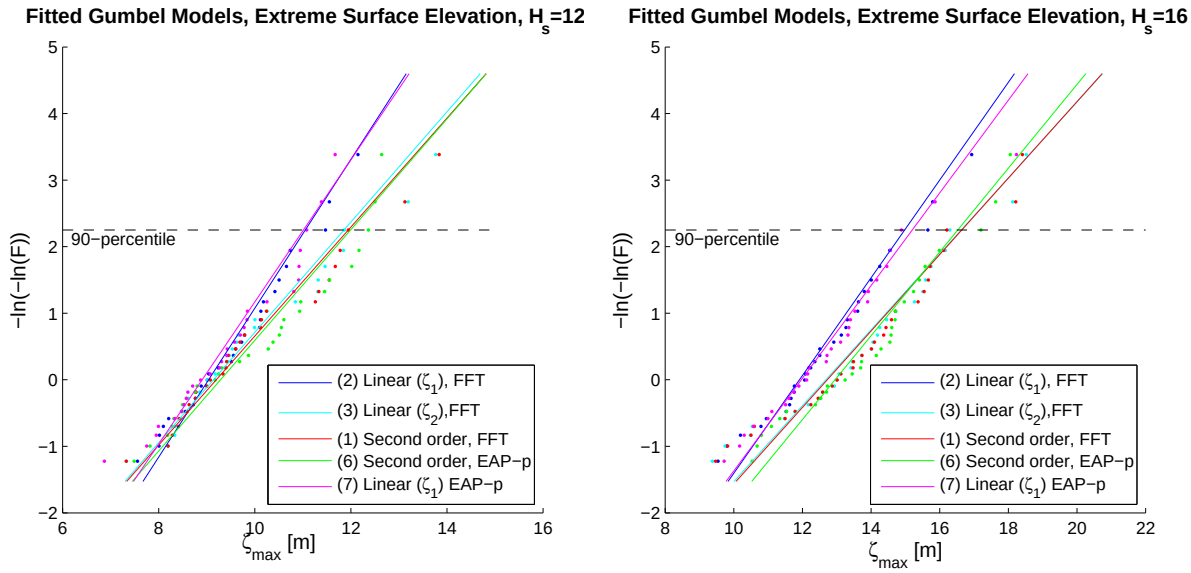

(a) $H_s/T_p = 12m/14s$ (b) $H_s/T_p = 16m/14s$

Figure 63: Gumbel plots of surface extremes, with fitted Gumbel model

8.2.2 Discussions

From the values presented in Table 24 one clearly sees that all three methods which depict a second order sea, both using full second order theory with FFT (1), full second order theory with EAP-p (6) and a Fourier transform of the second order sea (5) agrees well with each other, and the theoretical values. The methods using a linear surface realization (2) and (7) are too low on the mean and variance of extreme crests, and does not show the same positive skewness as the second order models. The reasons have been thoroughly discussed and illustrated in Study 4, and will not be repeated here.

The main observations from the table and plots is that the simplified procedure of using the peaked equal area principle gives very satisfactory surface statistics and extremes. This is further seen in the extreme value distributions, where there is basically no difference between the cyan, red and green coloured lines. The linear models show, however, an error in these plots, as is expected. What can be concluded is that the EAP-p follows the FFT for both linear and second order surface, which strengthen the argument of using the EAP-p for second order simulations of the surface.

An interesting observation is also that the linear realizations tend to have a lower standard deviation of the surface process σ_ζ. A possible reason for this is that in the current program one have used the same cut off frequency for the linear and second order simulations, $\omega_{cut} = \sqrt{2g/H_s}$. The second order *linear* comonents are linearised so as to maintain the variance within this frequency, however some additional variance from sum-frequency contributions at frequencies larger than the cut-off will induce a larger total variance in the sea. It can be discussed whether one should, in fact, use a higher cut frequency for the linear analysis, as the cut frequency used are provide surface kinematics from linear extrapolation in agreement with actual measurements, Stansberg [27]. This effect might lead to slightly lower surface extremes, and hence also low extreme forces. NORSOK N-003 [23] recommends, for instance, to vary the cut frequency of a linear analysis in order to investigate the effect this has on extreme loads. In the further work this is disregarded, and the Stansberg cut-off frequency is applied for both linear and non linear analysis. The Fourier transform of the second order surface is, however, performed with a cut-frequency of $4\omega_p$, in accordance with Wheeler's actual work [35]

8.3 Quasi-static loads

A quasi-static simulation of the mass and drag dominated cylinders are performed, using the 7 methods described previously. As it was found in Study 4 that the overturning moment suffered most from second order effects, this is the response quantity investigated in the following. The result in terms of mean and standard deviation of extreme overturning moment are given in Tables 25 and 26. Furthermore, the populations are fit to Gumbel models in Figures 64 and 65. One could, additionally, compared the 90% values, which are an important quantity for use in i.e. the contour line method, however it is assumed that these values, and the agreement for this values between the various methods, can be seen directly from the Gumbel plots.

Drag dominated	$H_s/T_p = 12m/14s$				$H_s/T_p = 16m/14s$			
	μ_X	Ratio	σ_X	Ratio	μ_X	Ratio	σ_X	Ratio
(1) Stansberg, FFT	25.8	**1.00**	9.1	**1.00**	53.7	**1.00**	19.4	**1.00**
(2) Wheeler (ζ_1), FFT	19.1	**0.74**	5.3	**0.58**	34.9	**0.65**	10.4	**0.53**
(3) Wheeler (ζ_2), FFT	22.0	**0.85**	7.2	**0.80**	43.7	**0.81**	14.8	**0.76**
(4) SELR, FFT	24.1	**0.93**	9.2	**1.02**	52.9	**0.99**	20.3	**1.04**
(5) Increase C_D, FFT	23.9	**0.92**	7.7	**0.85**	45.8	**0.85**	14.9	**0.76**
(6) Stansberg, EAP-p	26.0	**1.00**	8.9	**0.98**	55.2	**1.03**	18.2	**0.94**
(7) Wheeler (ζ_1), EAP-p	19.5	**0.76**	5.0	**0.55**	34.9	**0.65**	9.1	**0.47**

Table 25: Quasi-static extreme overturn moment (X) for a drag dominated cylinder, dimension [MNm]

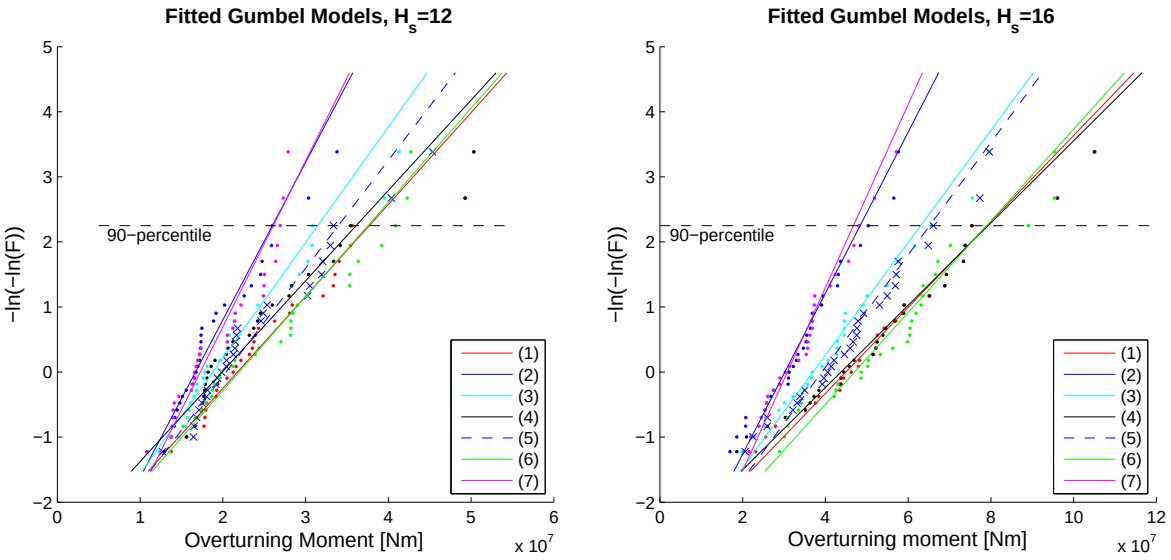

(a) $H_s/T_p = 12m/14s$ (b) $H_s/T_p = 16m/14s$

Figure 64: Gumbel plots of extreme overturning moment, static, drag dominated loads

For the mass dominated load case, the method of increasing C_D to account for second order effects seems pointless, and are therefore not included in the following table and figure.

Mass dominated	$H_s/T_p = 12m/14s$				$H_s/T_p = 16m/14s$			
	μ_X	Ratio	σ_X	Ratio	μ_X	Ratio	σ_X	Ratio
(1) Stansberg, FFT	4.25	**1.00**	0.93	**1.00**	6.69	**1.00**	1.71	**1.00**
(2) Wheeler (ζ_1), FFT	3.75	**0.88**	0.62	**0.66**	5.28	**0.79**	1.00	**0.58**
(3) Wheeler (ζ_2), FFT	4.49	**1.06**	0.93	**1.00**	6.85	**1.02**	1.55	**0.91**
(4) SELR, FFT	4.04	**0.95**	0.93	**0.99**	6.56	**0.98**	1.79	**1.05**
(6) Stansberg, EAP-p	4.17	**0.98**	0.96	**1.03**	6.89	**1.03**	1.68	**0.99**
(7) Wheeler (ζ_1), EAP-p	3.68	**0.86**	0.63	**0.67**	5.43	**0.81**	0.94	**0.55**

Table 26: Quasi-static extreme overturn moment (X) for a mass dominated cylinder, dimension 10^2[MNm]

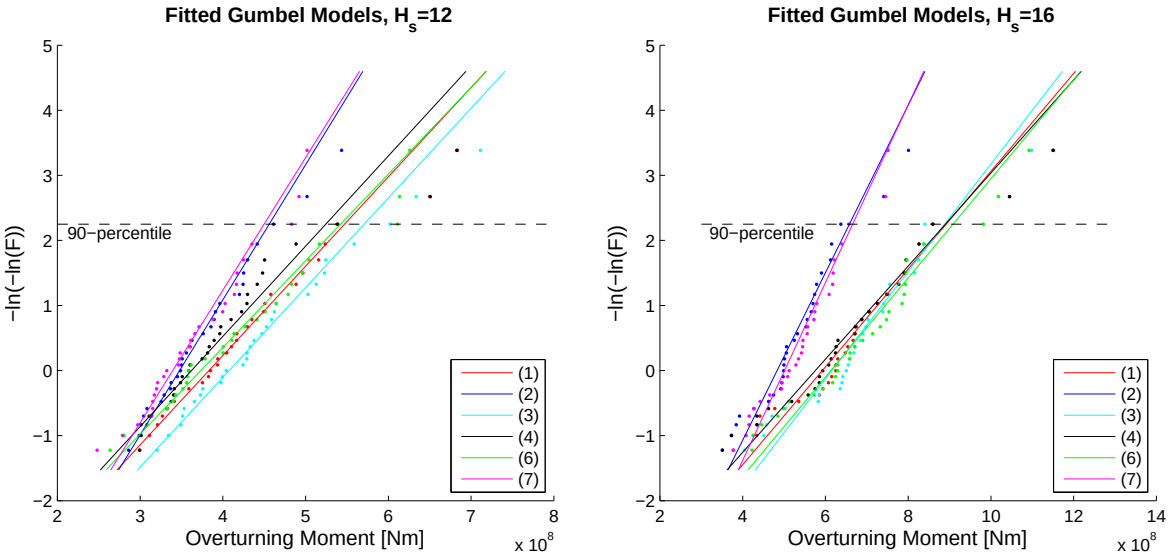

(a) $H_s/T_p = 12m/14s$ (b) $H_s/T_p = 16m/14s$

Figure 65: Gumbel plots of extreme overturning moment, static, drag dominated loads

8.3.1 Discussions

The quasi static behaviour is as expected from the results in Study 4. In general the methods using a linear surface (2 and 7) underestimates heavily the static load level for a drag dominated structure, which is due to both a too low crest height and that Wheeler stretching of a linear surface is fundamentally wrong, and will give large underestimations of the kinematics below a crest. This error increase as the sea steepness increase, and can be seen as wide spread in the Gumbel plots for drag dominated forces. Both the Wheeler stretching of a second order surface (3) and the increased C_D scheme (5) shows improvement, but not enough to completely reach the second order behaviour. While Wheeler stretching the linear components from a second order surface provides a good approximation of the surface velocity, it is low around the mean water level.

For a drag dominated structure, the extremes tend to be found around the largest crest both for dynamic and quasi- static simulations. Therefore the area where the SELR method (4) have second order surface and kinematics is in the area where static results are largest. As the static analysis is basically not influenced by the previous load history, the SELR method will give similar results as those found from the complete second order analysis. Furthermore the simplified method using the EAP-p shows very good agreement with the FFT. The reason being that the surface extremes are dominating in a static analysis, and these were shown previously to be well modelled by the EAP-p.

For the mass governed structure, the differences are not so large between linear and second order approximations. The reason is that the acceleration has its maximum around mean water level rather than a peak, and does therefore not suffer from the stretching. Another important reason is that the second order correction term for the acceleration does not peak at the same instant as the linear term, and the hence the second order surface acceleration will not be much larger than the linear. See Study 4 for more details around these issues.

In terms of the important 90% probability values, one finds a very good agreement between the FFT and EAP-p methods with complete second order kinematics, and also for the SELR method. The other two methods of approximating second order behaviour, Wheeler stretching of ζ_2 and increasing C_D for a linear realization, are more questionable, particularly for a drag dominated structure.

8.4 Dynamic loads

Finally, a dynamic simulation of the described methods are conducted for the cylinders. The results of these simulations in terms of extreme overturning moment are tabulated in Tables 27 and 28. Furthermore a Gumbel model is fit to the population, and plotted together with it in Figures 66 and 67.

Drag dominated	$H_s/T_p = 12m/14s$				$H_s/T_p = 16m/14s$			
	μ_X	Ratio	σ_X	Ratio	μ_X	Ratio	σ_X	Ratio
(1) Stansberg, FFT	41.3	**1.00**	8.2	**1.00**	68.7	**1.00**	14.2	**1.00**
(2) Wheeler (ζ_1), FFT	38.8	**0.94**	6.9	**0.83**	61.0	**0.89**	11.1	**0.78**
(3) Wheeler (ζ_2), FFT	39.4	**0.95**	7.4	**0.90**	63.6	**0.93**	12.4	**0.87**
(4) SELR, FFT	41.1	**0.99**	8.2	**1.00**	68.5	**1.00**	14.8	**1.04**
(5) Increase C_D, FFT	42.9	**1.04**	8.1	**0.99**	69.3	**1.01**	13.4	**0.95**
(6) Stansberg, EAP-p	41.0	**0.99**	9.8	**1.19**	70.8	**1.03**	14.4	**1.02**
(7) Wheeler (ζ_1), EAP-p	38.4	**0.93**	8.0	**0.97**	63.2	**0.92**	10.6	**0.75**

Table 27: Dynamic extreme overturn moment (X) for a drag dominated cylinder, dimension [MNm]

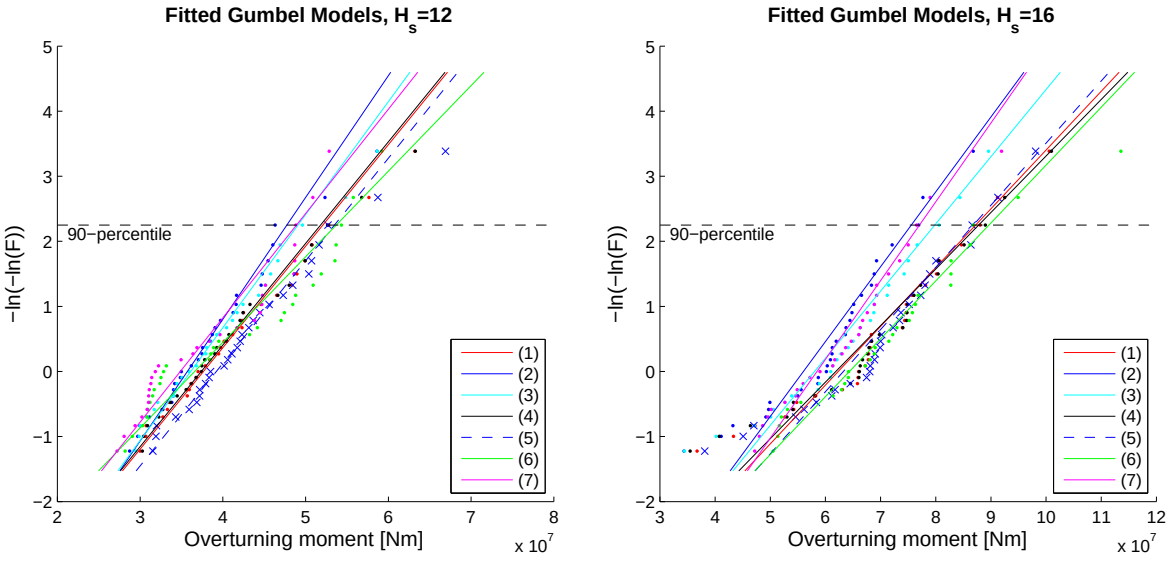

(a) $H_s/T_p = 12m/14s$ (b) $H_s/T_p = 16m/14s$

Figure 66: Gumbel plots of extreme overturning moment, dynamic, drag dominated loads

Mass dominated	$H_s/T_p = 12m/14s$				$H_s/T_p = 16m/14s$			
	μ_X	Ratio	σ_X	Ratio	μ_X	Ratio	σ_X	Ratio
(1) Stansberg,FFT	16.5	**1.00**	2.1	**1.00**	22.7	**1.00**	4.0	**1.00**
(2) Wheeler (ζ_1), FFT	16.6	**1.00**	2.1	**1.03**	22.8	**1.01**	4.1	**1.02**
(3) Wheeler (ζ_2), FFT	16.8	**1.02**	2.1	**1.03**	23.0	**1.02**	3.9	**0.99**
(4) SELR, FFT	16.5	**1.00**	2.1	**0.99**	22.7	**1.00**	4.0	**1.02**
(6) Stansberg, EAP-p, FFT	16.8	**1.02**	2.5	**1.19**	22.5	**0.99**	3.6	**0.91**
(7) Wheeler (ζ_1), EAP-p	16.7	**1.01**	2.4	**1.17**	22.7	**1.00**	3.3	**0.85**

Table 28: Dynamic extreme overturn moment (X) for a mass dominated cylinder, dimension 10^2[MNm]

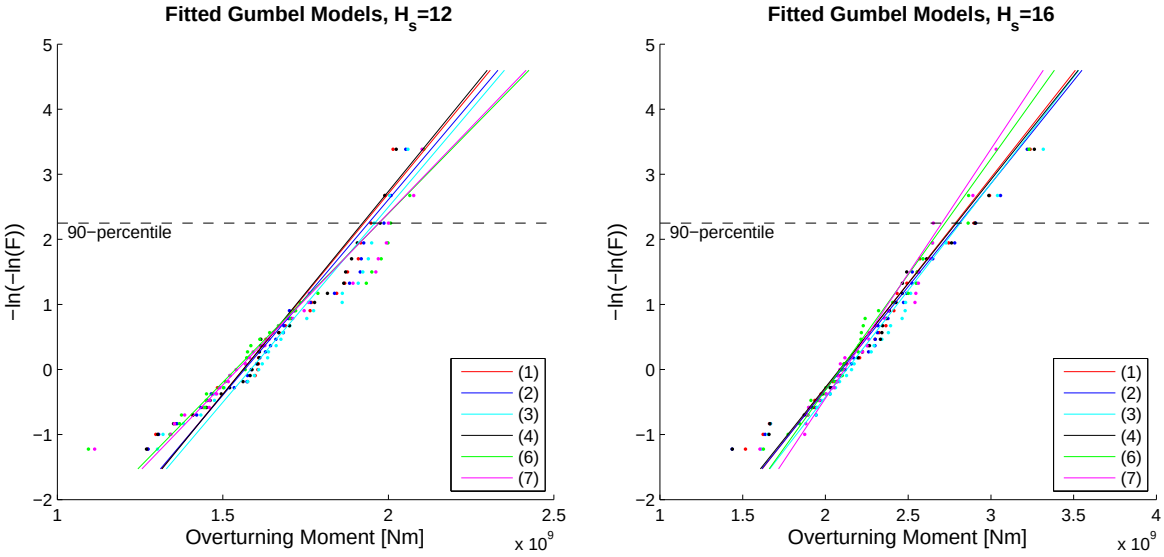

(a) $H_s/T_p = 12m/14s$ (b) $H_s/T_p = 16m/14s$

Figure 67: Gumbel plots of extreme overturning moment, dynamic, mass dominated loads

8.4.1 Discussions

In these discussions it is clearly distinguished between mass and drag dominating loads.

The simulations with mass dominating loading does not show any impact of second order effects in the extreme value statistics, and the Gumbel models lies almost completely on top of each others for all the methods. If one look at the FFT simulations (1 through 4), which origin from the same set of components, frequencies and seeds, and therefore describe the same irregular sea, there is minimal difference between the methods. Similarly, there is minimal difference in the linear and second order EAP-p. There seems therefore not to be any point in using a second order simulation when the target structure/environment is governed by the mass term of Morison's equation. The reason for this is, as discussed previously, that the extreme acceleration are around mean water level, and the second order components are not additive to the acceleration amplitude.

The drag dominated loads shows a far larger spreading in the extreme value distributions. The linear methods (2,7) show an underestimating of mean of extreme, albeit less so than in the static simulations, the reason believed to be an increased focus on the dynamic behaviour in an area where both a linear and a second order surface process will have the same amount of energy (see Study 4). The error produced by from the linear sea grows as the sea state steepness increase, as is seen in Table 27, or by the way the blue and magenta (cyan) Gumbel models are more clearly singled out in plot (b). The increased C_D method provide a powerful correction to the calculated forces for the simulations performed here. There is, however, an issue with using a constant value to account for effects which vary with the severity of the sea. The method overestimates the mean of extremes at $H_S = 12m$, but this overestimation is reduced at $H_s = 16m$. It can therefore be reason to believe that in more extreme sea states (for instance a sea state with return period of 10 000 years), this method might be non conservative.

For other structures than the current cylinder, the effects can also be different. For instance, a moored floating structure tend to have very high natural periods in yaw, surge and sway in an area where there are no linear contribution in the wave spectrum. However, including the second order terms will contain some difference frequency effects, and can hence constitute these slow drift motions. Similarly, for typically Tension Leg Platforms (TLP), the eigenperiods in heave are very small, and can in some cases be excited by sum frequency contributions. For such cases it is expected to be significant underestimation from a linear simulation, regardless of governing loads, and it is not expected that increasing the C_D of such a structure will produce any major corrective effect.

Approximating the second order surface with linear fft components, and performing a stretching of these, are also seen to underestimate the mean and standard deviation of extremes significantly, and provide only a small improvement compared to the completely linear models. On the other side, it seems sufficient to perform second order simulation only in a 20 second area around the linear extreme, as the SELR method (4) shows very little deviations from the complete second order simulation. The black and red line in the drag dominating Gumbel plots are basically identical. It is further seen that performing a second order simulation with EAP-p components provide a very good approximation of the mean of extremes, but with some variations in the standard deviation.

Some rather large discrepancies in the standard deviation for the EAP-p methods are observed for both drag and mass dominated loads, for the sea state with $H_s = 12m$. The errors are not

present in the 16m sea state for drag loads, and on the non-conservative side for the mass loads, which gives some inclination that this is not a consistent error due to an inherent error in the method, but rather due to the particular set of studies performed. One should also remember that the reason why the FFT methods compare so well are that they basically are the same sea state, just with a slightly different approach (i.e. second order corrections). Had one, for instance, redone method (1) with a different set of seeds, one would expect to see some rather different values, in particular for the standard deviation. It is therefore not believed that this is due to an actual error, but rather the statistical uncertainty.

8.5 Time consumption

Second order wave theory suffer from the extreme expenses in terms of computer efforts. In this study the adequacy of simplified procedures, in terms of how well they represent the extreme value distributions have been compared, and found to be adequate. It is therefore of interest to compare how much more effective the methods are in regards to time consumption.

The time consume of the various methods are depending on the computer used to execute the various processes. In this section, the time of assembling one input file of wave kinematics for each method is compared. The same computer is used for all analysis, to obtain comparable results. The time consumption of the analysis in *USFOS* is of secondary importance, as this is small compared to the time it takes to set-up the kinematics in *MATLAB*, and because this is (approximately) the same for all methods.

In Table 29 the time consumption of the various methods are resented, and compared against the complete second order FFT approach. As the number of grid nodes used is dependent on the highest and lowest surface elevation of that particular simulation, it is expected to be slightly higher values for the higher sea state. Therefore both the 12m and 16m H_s sea states are included in the table.

Kinematic Calculation	Spectral Realization	$H_s/T_p = 12m/14s$		$H_s/T_p = 16m/14s$	
		Time [min]	Ratio	Time [min]	Ratio
(1) Stansberg	FFT-500	222	**1.00**	277	**1.00**
(2) Wheeler (ζ_1)	FFT-500	4	**0.02**	4	**0.01**
(3) Wheeler (ζ_2)	FFT-500	5	**0.02**	5	**0.02**
(4) Comboination	FFT-500	12*	**0.05***	14*	**0.05***
(5) Increase (C_D)	FFT-500	4	**0.02**	4	**0.01**
(6) Stansberg	EAP-p-100	20	**0.09**	27	**0.10**
(7) Wheeler (ζ_1)	EAP-p-100	3	**0.01**	3	**0.01**

Table 29: Time consumption of writing grid-wave files for various methods

The SELR method, marked with *, will have some additional time consumption as a linear simulation (2) must be executed first, to decide at which area the second order contributions shall be included. There are, however, significant savings even if both the set up and simulation of the Gaussian sea is included. Furthermore, one can find ways to even better this time, by exploiting the already calculated linear sea. In the studies performed here the total simulation is performed anew, which is not necessary if one inputs the structural motions found in the linear analysis, the total length of the second simulation will be the 30 seconds around the largest linear extreme..

It is apparent that the complete second order kinematics with 500 components is by far the most costly procedure. The 100 component EAP-p simplification has a time consumption at

around 10% of this, and the SELR will be somewhat similar when the mentioned effects are included. The reason for these savings are, of course, the reduction of costly operations, either in terms of total steps of second order analysis (4) or that each step has fewer operations (6). As the number of linear components are reduced by 5 for the EAP-p method, the number of second order corrections are reduced by $5^2 = 25$. The time ratio is a bit higher than what this reduction would suggest, which is mainly thought to be due to inherent slowness in *MATLAB*. In particular will the actual time of writing kinematics be the same for all methods, thus some kind of averaging effect will apply. One can clearly see that this is causing the bulk of time consume for the linear methods, as the difference between the 100 component scheme (7) and the 500 component scheme (2) is not as large as would be expected simply by the number of total operations (5x). The ratio of 5 is very close to the relative time consumption when the complete analysis are performed in *USFOS* for 500 and 100 components.

The second order linear approximation (3) use a bit more than the linear simulation (2), as some additional time is included to set up the sea and perform the Fourier transform of this. The increase in time consume at larger sea states is furthermore found, as expected. When investigating the files, one finds that these are significantly larger for the more severe sea (180 MB vs. 120 MB). This is a direct consequence of the choice of having a very fine vertical mesh between the largest peak and lowest trough (0.1m spacing).

8.6 Summary

In this study various ways of simulating an irregular sea is performed, and the results are compared both in terms of their adequacy in representing the surface and force histories, and in terms of their time consumption.

For a dynamic analysis of a mass dominated cylinder, there is no gain in performing a complete second order simulation. The errors are within a few percent for both sea states when using a linear surface realization with Wheeler stretching of kinematics, compared to the complete second order Stansberg method. This observation is produced both in the EAP-p and FFT simulations, hence it strengthens the argument that second order effects are only important for drag dominating structures.

For a dynamic analysis of a drag dominated cylinder, the linear simulations underestimates the forces significantly. Applying Wheeler stretching to a second order surface profile provides some improvements, however large discrepancies are still present. Increasing the C_D shows good abilities to account for this effect, however an issue is related to using a single constant parameter as a scaling factor for any second order effects. It is seen that the degree of conservatism decays as the sea steepness increase, and it is questionable if satisfactory results can be found for more extreme seas.

The three methods using complete second order theory, at least partly, are presented in terms of deviations in extreme value statistics and time consumption for the sea state of $H_S = 16m$ in Table 30. Both the simplified procedures (4 and 6), compares well with the extreme value statistics from the complete second order FFT. The computational savings of the simplified procedures are huge, and expected to be even larger if incorporated directly in a second order program, as it would remove the inherent slowness of writing to files in *MATLAB*.

		Time [min]	Ratio	$\mu_X[MNm]$	Ratio	$\sigma_X[MNm]$	Ratio
(1) Stansberg	FFT-500	277	**1.00**	68.7	**1.00**	14.2	**1.00**
(4) SELR	FFT-500	20*	**0.05***	68.5	**1.01**	14.8	**1.04**
(6) Stansberg	EAP-p-100	27	**0.10**	70.8	**1.03**	13.4	**1.02**

Table 30: Time consume and accuracy in extreme value overturning moment, drag dominated cylinder

It is hence recommended to perform a linear simulation for mass dominated loads, and use one of the two above methods for drag dominated loads. For other structures than a bottom fixed cylinder, similar studies as performed in this section must be conducted to investigate if the same effects are present.

9 Conclusion

This thesis has dealt with the increased efforts of simulating a second order surface process and possible ways to simplify this simulation. The work has been divided in several parts, where each study builds upon the knowledge gained from the previous. The results of the introductory studies are suggestions for simplified methods of realizing the wave spectrum and other measures to ease the computational cost for second order analysis. These suggestions are tested thoroughly in the final activity, by performing a short term analysis of quasi-static and dynamic extreme statistics using 30 seed variations.

Study 1

It is identified an error in the phase angles generated in the computer software *USFOS*, leading to unrealistic behaviour of the surface process and hence also load levels. The problem is in this report remedied by using *MATLAB* to create the wave components, and simulate these in *USFOS* for force calculations.

Study 2

A study of the required time to avoid transient behaviour of a bottom fixed cylinder is conducted. It is here found that the necessary initiation time to reconstruct the wanted behaviour are strongly dependent on the eigenperiod and governing loads. Mass loads require longer set up time than drag, due to a more consistently high load and motion history. An eigenperiod in the energetic parts of the spectrum will also constitute larger dynamic motions and forces, hence a longer set up time is required. It is not found any difference between a complete FFT and a simplified peaked EAP method. In general, a set up time of 400 seconds was sufficient for all simulations, however for a cylinder with an eigenperiod of $4.5sec$ as low as 50 seconds were found to be sufficient for drag loads.

Study 3

A study of various possible simplifications of realizing the sea spectrum for a linear simulation was performed. The ability of the methods to produce correct statistical parameters for the Gaussian sea elevation was found to be governed by the number of *effective components* within a small frequency range around the peak of the spectrum. Therefore, the equal area principle and peaked equal area principle show best results in terms of statistical parameters of the Gaussian sea. The ability to produce correct dynamic reaction moments were seen to be determined by both the above mentioned issue, and the number of components in the vicinity of the structures natural period *relative to the density of the wave spectrum at this point*. The equal area principle give low force levels for natural periods not in the peak of the spectrum, and the simplified random $d\omega$ FFT approach give low values for periods in the peak of the spectrum. It was also observed that these issues were most pronounced for the mass dominated load case. The main reason for the better estimations for the drag dominated cylinder is that the superharmonic loading excite forces at odd frequency multiples, which for structures with low natural periods will lead to better representation of the dynamic amplification around the natural period.

The equal area principle with increased focus around the natural frequency of the cylinder showed best results in terms of modelling the sea and dynamic forces for an arbitrary structural eigenperiod. The error found were at most 3% in mean of extremes, and 10% in standard deviation of extremes.

Study 4

To verify the *MATLAB* algorithm, a test case for surface statistics and load calculation were performed. The surface statistics were shown to be in compliance with theoretically expected results when 200 realizations were conducted. A further investigation of one of these simulations was further conducted, were a Stokes' V wave was fit to the largest crest. The kinematics and loads produced by the Stokes wave were mostly in agreement with the kinematics calculated from the second order theory. It was also found that a *spool-to-extreme-linear-response* (SELR), where second order kinematics are only included in a small area around the largest linear response, compared well with the complete second order theory. Expected errors from linear theories, using the Wheeler stretching method, were also observed.

Second order simulation

30 different seeds were simulated using linear and second order theory. Additionally, the simplified SELR method was tested, and so was the peaked EAP for a second order surface realization.

In terms of second order surface statistics, the peaked EAP compares very well with the FFT. Both methods show a very good agreement with the Forristall crest height. It is clear that the linear models underestimates the surface extremes, and this effect is more pronounced in steeper seas.

The extreme value statistics of reaction overturning moment obtained in the final study show that the second order contributions can be neglected for mass loads, but must be included when drag loads are dominating. The alternative methods of simulating a second order process, by peaked EAP or by the Spool to Extreme Linear Response show both very good agreement with the complete second order simulation using 500 components in an FFT approach. The time savings of these methods are substantial, and the discrepancies so small, that it is believed that these methods could provide an efficient way of simulating second order seas. Further investigations regarding the applicability of these simplifications to more realistic structural models must however be demonstrated before final conclusions can be made.

10 Recommendations for Further Work

In this study it is shown that alternative methods for simulating both a linear and second order sea might be adequate for certain idealistic structures. Before one can apply these methods in design consideration, further testing must be done, preferably with more realistic structural models. A possible area of applicability for the second order simplifications can be use in design of offshore jacket or jack-ups, as the drag loads were very well modelled by both investigated methods. It is hence recommended that further simulations on one of these structures are performed, to verify the trends observed in this study.

Further studies regarding the second order effects for various structural eigenperiods could be interesting. In particular, how the slowly varying forces for a structure with very high eigenperiod ($\omega_n \to 0$) are accounted for. Towards the end of this study it is realised that the lowest eigenperiod in study 3 is, in fact, outside the frequency-cut from the second order study. It could be very interesting to see how the results of a cylinder with eigenperiod of 4.5 sec acted with the cut-off frequency.

A total of either 800 or 1000 seconds are simulated, for 30-40 random seeds. This may be too little information to base all conclusions upon. In particular, the length of the simulations are short compared to the 3-hours most of the industry is using. Therefore it is recommended to perform similar studies, preferably with actual structural models, for a longer time. One can also perform simulations for more random seeds, which will further reduce the statistical uncertainties in the simulations.

Due to unaffordable computational demands of performing the second order FFT with the recommended 1000 components, it is here used only 500. It is shown in the report that this reduction thus not constitute significant underestimations in terms of surface statistics, however there might be issues regarding the dynamic effects when the forces are calculated, similar to those experienced from the few-component FFT schemes in Study 3. It is therefore recommended to perform additional studies where at least 1000 components are used, to verify the conclusions drawn in this report.

The *MATLAB* algorithm made in this project is not sufficiently tested. A study where the results of these simulations are compared against actual measurements, or other computer software, could produce verification of the program. Furthermore one could compare the kinematics produced from the Stansberg method used in this report with other methods of approximating the second order kinematics. This is somewhat done in the comparison with Wheeler stretching and a fitted Stokes wave, however further verifications are needed.

It is of interest to identify at which sea state the second order effects become important. It is shown in this study that the effect becomes less as the sea steepness decrease, and it can be of importance to identify at which level the linear approximation is sufficient. This can be of importance for both fatigue analysis and long term extreme response analysis for structures with non-linear behaviour.

References

[1] Binner, Ine-Therese, (2011), *Time-domain simulation of floating wind power plants in irregular seas* Department of Marine Technology (NTNU)

[2] Bækkedal, Eivind, (2013), *Time-domain simulation of marine structures in irregular seas* Department of Marine Technology (NTNU)

[3] Cartwright, D.E.m and Longuet-Higgins, M.S., (1952), *The statistical distribution of the maxima of a random function,* Proc. R. Soc. Lond., Series A 1956, XI(3)

[4] Dean, R.G (1965), *Stream function representation of non-linear ocean waves,* J. Geophys, Res., 70,pp 4561-4572

[5] Det Norske Veritas, (2010) *Recommended Practice DNV-RP-C205: Environmental Conditions and Environmental Loads*

[6] Elgar, S; Guza, R.T. and Seymour, R.J., (1985), *Wave group statistics from numerical simulations of a random sea* In: Applied Ocean Research, 1985, Vol. 7, No. 2, pp. 93-96

[7] Faltinsen, O.M. and Zhao, R., (1985), *A comparative study of theoretical models for slowdrift stray motion of a marine structure* In: Journal of Ship Research, 1988, pp. 153-158

[8] Forristall, G., (2000), *Wave cresst distributions: observations and second-order theory* In: Journal of Physical Oceanography, 30, pp. 1931-1943 (2000)

[9] Goda,Y., (1970), *Numerical experiments on wave statistics with spectral simulation,* In: Report of Port and Harbour Res. Inst. 9(3), 3

[10] Haver, Sverre, (2011), *Prediction of Characteristic Response for Design Purpose (PRELIMINARY VERSION)*, Stavanger: Statoil

[11] Haver, S. and Moan, T., (1983) *On some uncertainties related to the short-term stochastic modelling of ocean waves* In: Applied Ocean Research, 1983, Vol. 5, No. 2, pp. 153-158

[12] Hilber,H.M.,Hughes, T.J., and Taylor, R.L. (1977)), *Improved Numerical Dissipation for Time Integration Algorithms in Structural Dynamics,* Earthquake Engineering and Structural Dynamics, 5:282-292

[13] Johannessen, T.B., (2008) *On the use of linear and weakly nonlinear wave theory in continuous ocean wave spectra: Convergence with respect to frequency* In: Proc. 27.th OMAE Conf., Estoril, Portugal

[14] Johannessen, T.B. and Swan,C., (2001) *A laboratory study of the focusing of transient and directionally spread surface water waves* In: Proc. Roy.Soc.Lond. A, 457, pp 971-1006

[15] Langen, Ivar and Sigbjörnsson, Ragnar (1975), *Utdrag fra Dynamisk Analyse av Konstruksjoner*, SINTEF, Avdeling for konstruksjonsteknikk

[16] Larsen, Carl Martin, (2012), *TMR4182: Marine Dynamics* Department of Marine Technology (NTNU)

[17] Larsen, Carl Martin, (2005), *Drag forces in Dynamic Analysis [Lecture Notes]* Department of Marine Technology (NTNU)

[18] Leira, Bernt Johan, (2010), *TMR4235 Stochastic Theory of Sealoads: Probabilistic modelling and estimation* Department of Marine Technology (NTNU)

[19] Longuet-Higgins, M.S., (1963): *The Effect ofNonlinearities on Statistical Distributions in the Theory of Sea Waves,* J.Fluid Mech. 17, pp. 459-480

[20] Moan, Torgeir, (2003) *TMR 4190: Finite Element Modelling and Analysis of Marine Structures* Department of Marine Technology (NTNU)

[21] Muliawan, Jaya; Gao, Zhen and Moan,Torgeir, (2012), *Application of the contour line method for estimating extreme response in mooring lines of a two-body floating wave energy converter* In: Proceedings of the ASME 2012 31st International Conference on Ocean, Offshore and Arctic Engineering

[22] Myrhaug, Dag, (2005), *TMR4235: Stochastic Theory of Sealoads: Statistics of Narrow Band Processes and Equivalent Linearization* Department of Marine Technology (NTNU)

[23] NORSOK standard N-003, (2008), *Action and Action Effects, Edition 2, September 2007*, The Society of Naval Architects and Marine Engineers

[24] Rainey, P. J. and Camp, T. R. (2007), *Constrained non-linear waves for offshore wind turbine design* In: Journal of Physics: Conference Series 75

[25] Rienecker, M. M. and Fenton, J. D.,(1981), *A Fourier approximation method for steady water waves* In: J. Fluid Mech. 104, 119-137

[26] Sharma, J.N. and Dean, R.G., (1981), *Second-Order Directional Seas and Associated Wave Forces* In: Society of Petroleum Engineers Journal, 4, pp, 129-140

[27] Stansberg, C.T., (1993), *Second-order numerical reconstruction of laboratory generated random waves',* In: Proc. 12.th OMAE Conf., Florence, Italy, pp 103-110

[28] Stansberg, C.T., (1998), *Non-Gaussian Extremes in Numerically Generated Second-Order Random Waves in Deep Water* In: Proc. 8.th ISOPE Conf., Vol III, Montreal, Canada, pp 103-110

[29] Taylor, P.H. Jonathan, P. and Harland, I.A., (1995), *Time domain simulation of jack-up dynamics with the extremes of a Gaussian process,* Proc. 14th. Int. Conf. on Offshore Mechanic and Arctic Engineering (oMAE), Vol. 1-A, pp. 313-319

[30] Torsethaugen,K., Haver, S., (2004) *Simplified double peak spectral model for ocean waves* Paper No. 2004-JSC-193

[31] Tromans, P. S. Anaturk, A.R. and Hagermeijer, P., (1991), *A new Model for the kinematics of large ocean waves- application as a design wave* Proceedings of the first International Offshore and Polar Engineering Conference, Edinburgh, UK

[32] Elzinga, T. and Tromans, P.S., (1992), *Validation of 'NewWave' theory and RDWF predictions against measured global loading on a North Sea jacket,* Int. Conf. on the Behaviour of Off-shore Structures (BOSS), University of London, London, pp. 495-505

[33] Tucker, M.J, (1957), *The analysis of finite-length records of fluctuating signals* In: British Journal of Applied Physics, 1984, Vol.8, April 1957, pp. 137-142

[34] Tucker, M.J; Challenor, P.G. and Carter, D.J.T., (1984), *Numerical simulation of a random sea: a common error and its effect upon wave group statistics* In: Applied Ocean Research, 1984, Vol. 6, No.2, pp. 118-122

[35] Wheeler, J.D., (1970), *Method for calculating forces produced by irregular waves* J. Petroleum Technology, 1, pp 359-367

[36] Winterstein, S.R. Ude, T.C. Cornell, C.A. Bjerager, P. and Haver, S. (1993), *Environmental Parameters For Extreme Response Inverse FORM with Omission Factors* In: Proceedings ICOSSAR,

[37] Zhang, J., Hong, K., and Yue, D., (1993), *Effects of wavelength ratio on wave modelling,* J. Fluid Mech., 248, pp 107-127

[38] Zhang, J. & Chen,L., (1999), *General third-order solutions for irregular waves in deep water* J. Eng Mech., 125, No.7, pp 768-446

[39] SINTEF Marintek,(2000) *Release notes for USFOS 7-6*, SINTEF Marintek, Structural Engineering

[40] SINTEF Marintek, (2010), *USFOS Hydrodynamics: Theory Description of use Verification* SINTEF Marintek, Trondheim

[41] SINTEF Marintek, (2001), *USFOS Getting Started* SINTEF Marintek, Trondheim

[42] SINTEF Marintek, (2006), *USFOS User Manual* SINTEF Marintek, Trondheim

[43] SINTEF Marintek, (1993), *USFOS - A Computer Program for Progressive Collapse Analysis of Steel Offshore Structures. Theory Manual* SINTEF Marintek, Trondheim

[44] *Statfjord_Nora10.dat*: Hindcast data for the Statfjord field; Downloaded from itslearning, 20.03.2014

11 Appendix

A Script

Scripting techniques have been used for ensuring an efficient pre processing, running and post processing of the analysis. Additionally, *MATLAB* algorithms have been made to compute wave components for input in Study 1 through 3, and to compute second order wave kinematics.

The complete set of *MATLAB* scripts, and examples of the scripting for efficient use of *USFOS* are given in separate zip-file.

B Input, contour line method

The long term variation of H_s and T_p can often be modelled by the hybrid modell, given in e.g. [10]:

$$\begin{aligned} f_{H_s}(h_s) &= \frac{1}{\sqrt{2\pi}\cdot\alpha\cdot h_s}\cdot exp\left[-\frac{(ln(h_s)-\theta)^2}{2\alpha^2}\right] && h_s \leq \eta \\ f_{H_s}(h_s) &= \frac{\beta}{\rho}\left(\frac{h_s}{\rho}\right)^{\beta-1}\cdot exp\left[-\left(\frac{h_s}{\rho}\right)^{\beta}\right] && h_s > \eta \\ f_{T_p|H_s}(t_p|h_s) &= \frac{1}{\sqrt{2\pi}\cdot\sigma(h_s)\cdot t_p} exp\left[-\frac{1}{2}\left(\frac{ln(t_p)-\mu(h_s)}{\sigma(h_s)}\right)^2\right] \end{aligned} \tag{131}$$

Where

$$\begin{aligned} \mu(h_s) &= a_1 + a_2\cdot h_s^{a_3} \\ \sigma^2(h_s) &= b_1 + b_2\cdot e^{-h_s b_3} \end{aligned} \tag{132}$$

The parameters of the given distribution are found by the method of moments of the various distribution, and by *enforcing continuity* in f_{H_s} and F_{H_s} at $h_s = \eta$. From the Nora10 database of the Statfjord area, [44], the best fit parameters are found and presented in Table 31. These are used to establish the 100 and 10 000 year contours given in Section 2.2.1.

	α	θ	η	β	ρ	
$f_{H_s}(h_s)$	0.5667	0.8278	4	1.4683	2.6613	
	a_1	a_2	a_3	b_1	b_2	b_3
$f_{T_p\|H_s}(t_p\|h_s)$	1.6844	0.3917	0.3864	0.0038	0.1000	0.2683

Table 31: Parameters for joint probability density function $f_{T_p,H_s}(t_p,h_s)$

C Results from various analysis

In this appendix some numerical data and plots that were not directly used in the presentation and discussion of the results in the main report are presented.

C.1 Study 2: Spool-to-extreme-wave

The numerical results from the spool to extreme wave analysis, Section 7.2, is given in the next pages. Green colour is the shortest simulation time satisfying the requirements.

C.1.1 Numerical values from Static simulations

SPOOL-STATIC		FFT 3200				EAP 50				EAP 100				EAP 150			
		Order 1		Order 2		Order 1		Order 2		Order 1		Order 2		Order 1		Order 2	
Loads	TBS	RMSE	Max	RMSE	Max	RMSE	Max	RMSE	Max	RMSE	Max	RMSE	Max	RMSE	Max	RMSE	Max
Drag dominated	25	0.011	0.035	0.001	0.004	0.001	0.002	0.004	0.011	0.005	0.020	0.001	0.002	0.001	0.004	0.002	0.004
	50	0.011	0.035	0.001	0.004	0.001	0.002	0.004	0.011	0.005	0.020	0.001	0.002	0.001	0.004	0.002	0.004
	100	0.007	0.026	0.001	0.004	0.001	0.002	0.004	0.011	0.005	0.020	0.001	0.002	0.001	0.004	0.002	0.004
	150	0.007	0.026	0.001	0.003	0.001	0.002	0.004	0.012	0.005	0.020	0.001	0.002	0.001	0.003	0.002	0.004
	200	0.007	0.026	0.001	0.003	0.000	0.002	0.004	0.012	0.005	0.020	0.001	0.002	0.001	0.003	0.002	0.004
	300	0.007	0.027	0.001	0.003	0.000	0.001	0.004	0.012	0.005	0.020	0.001	0.002	0.001	0.003	0.001	0.003
	400	0.007	0.027	0.001	0.002	0.000	0.001	0.004	0.012	0.005	0.021	0.001	0.002	0.001	0.002	0.001	0.003
	1000	0	0	0	0	0	0	0	0	0	0	0	0	0	0	0	0
Mass dominated	25	0.009	0.033	0.022	0.058	0.006	0.022	0.005	0.014	0.004	0.017	0.006	0.041	0.011	0.021	0.007	0.033
	50	0.009	0.034	0.022	0.058	0.006	0.022	0.005	0.014	0.004	0.017	0.006	0.041	0.011	0.021	0.007	0.033
	100	0.009	0.034	0.022	0.059	0.006	0.022	0.005	0.015	0.004	0.017	0.006	0.041	0.011	0.021	0.007	0.033
	150	0.009	0.034	0.018	0.059	0.006	0.022	0.005	0.015	0.004	0.018	0.005	0.042	0.011	0.021	0.007	0.033
	200	0.009	0.034	0.018	0.059	0.006	0.022	0.004	0.015	0.004	0.018	0.005	0.042	0.011	0.021	0.007	0.033
	300	0.003	0.005	0.012	0.050	0.006	0.023	0.003	0.008	0.002	0.011	0.003	0.042	0.011	0.021	0.007	0.034
	400	0.003	0.004	0.012	0.050	0.002	0.003	0.002	0.008	0.002	0.011	0.003	0.043	0.012	0.021	0.007	0.034
	1000	0	0	0	0	0	0	0	0	0	0	0	0	0	0	0	0
samples used		34		38		36		38		34		34		36		38	

Figure 68: Numerical results from Static Spool-Wave analysis

C.1.2 Numerical values from Dynamic simulations, mass dominated loads

MASS DOMINATED LOADS			25 sec		50 sec		100 sec		150 sec		200 sec		300 sec		400 sec		1000 sec
			RMSE	Max	RMSE	Max	RMSE	Max	RMSE	Max	RMSE	Max	RMSE	Max	RMSE	Max	
Eigenperiod 4.5 seconds	FFT 3200	Order 1	0.132	0.314	0.034	0.074	0.004	0.007	0.002	0.004	0.000	0.001	0.000	0.000	0.000	0.000	0.000
		Order 2	0.077	0.187	0.031	0.056	0.006	0.014	0.002	0.006	0.000	0.001	0.000	0.000	0.000	0.000	0.000
	EAP 50	Order 1	0.045	0.088	0.020	0.040	0.005	0.011	0.001	0.002	0.000	0.000	0.000	0.000	0.000	0.000	0.000
		Order 2	0.030	0.050	0.022	0.053	0.004	0.010	0.001	0.002	0.000	0.001	0.000	0.000	0.000	0.000	0.000
	EAP 100	Order 1	0.045	0.103	0.017	0.033	0.004	0.008	0.001	0.003	0.000	0.000	0.000	0.000	0.000	0.000	0.000
		Order 2	0.040	0.088	0.026	0.052	0.007	0.013	0.001	0.002	0.000	0.000	0.000	0.000	0.000	0.000	0.000
	EAP 150	Order 1	0.068	0.153	0.032	0.067	0.007	0.015	0.001	0.003	0.000	0.000	0.000	0.000	0.000	0.000	0.000
		Order 2	0.067	0.146	0.046	0.088	0.009	0.025	0.002	0.003	0.000	0.001	0.000	0.000	0.000	0.000	0.000
Eigenperiod 9 seconds	FFT 3200	Order 1	0.386	0.561	0.186	0.428	0.105	0.268	0.061	0.192	0.018	0.032	0.004	0.008	0.001	0.001	0.000
		Order 2	0.365	0.549	0.299	1.023	0.123	0.369	0.076	0.215	0.021	0.060	0.007	0.013	0.001	0.003	0.000
	EAP 50	Order 1	0.210	0.383	0.143	0.307	0.099	0.275	0.040	0.096	0.025	0.076	0.005	0.012	0.001	0.002	0.000
		Order 2	0.324	0.626	0.201	0.509	0.089	0.200	0.035	0.085	0.018	0.049	0.006	0.023	0.001	0.002	0.000
	EAP 100	Order 1	0.371	0.795	0.196	0.333	0.110	0.278	0.067	0.220	0.029	0.075	0.005	0.017	0.001	0.003	0.000
		Order 2	0.293	0.552	0.235	0.462	0.128	0.328	0.048	0.113	0.027	0.070	0.003	0.007	0.001	0.002	0.000
	EAP 150	Order 1	0.344	0.664	0.272	0.634	0.164	0.488	0.069	0.222	0.029	0.094	0.006	0.017	0.001	0.002	0.000
		Order 2	0.485	1.320	0.267	0.606	0.135	0.379	0.110	0.360	0.035	0.097	0.006	0.015	0.001	0.003	0.000
Eigenperiod 14 seconds	FFT 3200	Order 1	0.478	0.615	0.235	0.496	0.139	0.337	0.070	0.179	0.035	0.069	0.009	0.016	0.003	0.006	0.000
		Order 2	0.453	0.649	0.259	0.503	0.154	0.335	0.118	0.258	0.045	0.102	0.013	0.022	0.002	0.005	0.000
	EAP 50	Order 1	0.355	0.561	0.254	0.619	0.178	0.413	0.089	0.213	0.032	0.069	0.009	0.018	0.003	0.005	0.000
		Order 2	0.514	1.105	0.503	1.549	0.324	0.884	0.127	0.420	0.055	0.156	0.014	0.028	0.004	0.011	0.000
	EAP 100	Order 1	0.417	0.601	0.257	0.490	0.124	0.400	0.062	0.142	0.029	0.067	0.008	0.019	0.002	0.004	0.000
		Order 2	0.590	1.713	0.422	1.269	0.196	0.643	0.117	0.397	0.026	0.088	0.017	0.045	0.005	0.013	0.000
	EAP 150	Order 1	0.389	0.575	0.192	0.367	0.117	0.239	0.067	0.147	0.034	0.091	0.009	0.018	0.002	0.005	0.000
		Order 2	0.420	1.145	0.189	0.358	0.229	0.459	0.122	0.271	0.086	0.246	0.017	0.044	0.003	0.008	0.000
Eigenperiod 18 seconds	FFT 3200	Order 1	1.120	2.282	0.675	1.585	0.208	0.537	0.149	0.389	0.072	0.179	0.026	0.057	0.006	0.019	0.000
		Order 2	0.387	1.173	0.379	0.689	0.199	0.539	0.109	0.187	0.048	0.125	0.017	0.035	0.005	0.014	0.000
	EAP 50	Order 1	0.527	1.591	0.510	1.892	0.265	0.659	0.072	0.172	0.041	0.116	0.012	0.030	0.004	0.011	0.000
		Order 2	1.103	4.420	0.707	2.906	0.312	1.208	0.109	0.273	0.069	0.147	0.021	0.043	0.005	0.012	0.000
	EAP 100	Order 1	0.621	1.305	0.180	0.308	0.398	1.541	0.094	0.178	0.062	0.180	0.020	0.040	0.004	0.009	0.000
		Order 2	0.548	1.229	0.386	0.898	0.186	0.394	0.146	0.486	0.062	0.143	0.023	0.052	0.004	0.011	0.000
	EAP 150	Order 1	0.948	3.650	0.625	2.379	0.198	0.597	0.077	0.165	0.055	0.114	0.029	0.090	0.006	0.019	0.000
		Order 2	0.780	3.210	0.443	1.522	0.155	0.384	0.107	0.202	0.060	0.135	0.015	0.029	0.005	0.016	0.000

Figure 69: Numerical results from Dynamic Spool Wave analysis with mass dominated loads

C.1.3 Numerical values from Dynamic simulations, drag dominated loads

DRAG DOMINATED LOADS			25 sec		50 sec		100 sec		150 sec		200 sec		300 sec		400 sec		1000 sec
			RMSE	Max	RMSE	Max	RMSE	Max	RMSE	Max	RMSE	Max	RMSE	Max	RMSE	Max	
Eigenperiod 4.5 seconds	FFT 3200	Order 1	0.018	0.036	0.002	0.006	0.000	0.000	0.000	0.000	0.000	0.000	0.000	0.000	0.000	0.000	0.000
		Order 2	0.014	0.030	0.003	0.010	0.000	0.001	0.000	0.000	0.000	0.000	0.000	0.000	0.000	0.000	0.000
	EAP 50	Order 1	0.015	0.034	0.002	0.004	0.000	0.000	0.000	0.000	0.000	0.000	0.000	0.000	0.000	0.000	0.000
		Order 2	0.014	0.036	0.001	0.004	0.000	0.000	0.000	0.000	0.000	0.000	0.000	0.000	0.000	0.000	0.000
	EAP 100	Order 1	0.011	0.022	0.002	0.005	0.000	0.000	0.000	0.000	0.000	0.000	0.000	0.000	0.000	0.000	0.000
		Order 2	0.013	0.030	0.003	0.007	0.000	0.000	0.000	0.000	0.000	0.000	0.000	0.000	0.000	0.000	0.000
	EAP 150	Order 1	0.012	0.038	0.002	0.004	0.000	0.000	0.000	0.000	0.000	0.000	0.000	0.000	0.000	0.000	0.000
		Order 2	0.016	0.037	0.004	0.009	0.000	0.000	0.000	0.000	0.000	0.000	0.000	0.000	0.000	0.000	0.000
Eigenperiod 9 seconds	FFT 3200	Order 1	0.149	0.304	0.074	0.225	0.017	0.045	0.006	0.018	0.001	0.004	0.000	0.000	0.000	0.000	0.000
		Order 2	0.226	0.439	0.135	0.282	0.016	0.050	0.009	0.026	0.001	0.003	0.000	0.001	0.000	0.000	0.000
	EAP 50	Order 1	0.114	0.196	0.039	0.099	0.012	0.033	0.003	0.007	0.001	0.003	0.000	0.000	0.000	0.000	0.000
		Order 2	0.194	0.539	0.057	0.107	0.013	0.023	0.002	0.007	0.001	0.002	0.000	0.000	0.000	0.000	0.000
	EAP 100	Order 1	0.154	0.262	0.064	0.129	0.015	0.034	0.003	0.008	0.001	0.002	0.000	0.000	0.000	0.000	0.000
		Order 2	0.194	0.366	0.088	0.202	0.019	0.033	0.005	0.011	0.001	0.003	0.000	0.000	0.000	0.000	0.000
	EAP 150	Order 1	0.126	0.266	0.074	0.158	0.018	0.040	0.004	0.010	0.001	0.002	0.000	0.000	0.000	0.000	0.000
		Order 2	0.195	0.433	0.069	0.157	0.019	0.047	0.006	0.018	0.001	0.003	0.000	0.000	0.000	0.000	0.000
Eigenperiod 14 seconds	FFT 3200	Order 1	0.359	0.463	0.130	0.268	0.069	0.118	0.022	0.052	0.009	0.021	0.002	0.004	0.000	0.001	0.000
		Order 2	0.343	0.530	0.186	0.342	0.067	0.138	0.047	0.116	0.016	0.036	0.003	0.006	0.000	0.001	0.000
	EAP 50	Order 1	0.267	0.647	0.198	0.629	0.063	0.157	0.027	0.064	0.008	0.017	0.002	0.004	0.000	0.001	0.000
		Order 2	0.293	0.578	0.186	0.410	0.101	0.209	0.034	0.098	0.013	0.039	0.002	0.005	0.000	0.001	0.000
	EAP 100	Order 1	0.284	0.443	0.157	0.333	0.050	0.150	0.017	0.043	0.009	0.022	0.002	0.004	0.000	0.001	0.000
		Order 2	0.339	0.628	0.218	0.486	0.067	0.146	0.038	0.134	0.007	0.020	0.003	0.006	0.000	0.001	0.000
	EAP 150	Order 1	0.262	0.418	0.114	0.245	0.057	0.111	0.023	0.065	0.011	0.036	0.002	0.003	0.000	0.001	0.000
		Order 2	0.334	0.887	0.125	0.341	0.088	0.191	0.041	0.093	0.023	0.071	0.003	0.005	0.000	0.001	0.000
Eigenperiod 18 seconds	FFT 3200	Order 1	0.740	1.715	0.278	0.715	0.080	0.166	0.052	0.125	0.021	0.057	0.007	0.016	0.001	0.002	0.000
		Order 2	0.270	0.537	0.257	0.488	0.076	0.160	0.053	0.085	0.016	0.031	0.006	0.017	0.001	0.001	0.000
	EAP 50	Order 1	0.271	0.763	0.205	0.672	0.088	0.230	0.026	0.076	0.010	0.023	0.001	0.003	0.001	0.001	0.000
		Order 2	0.444	1.118	0.222	0.553	0.075	0.177	0.038	0.069	0.029	0.097	0.005	0.015	0.001	0.002	0.000
	EAP 100	Order 1	0.341	0.805	0.146	0.392	0.119	0.374	0.031	0.075	0.012	0.027	0.003	0.006	0.001	0.002	0.000
		Order 2	0.452	1.101	0.231	0.412	0.097	0.256	0.047	0.109	0.019	0.036	0.005	0.011	0.001	0.002	0.000
	EAP 150	Order 1	0.465	1.556	0.195	0.364	0.086	0.189	0.036	0.090	0.018	0.037	0.004	0.013	0.001	0.003	0.000
		Order 2	0.392	1.344	0.218	0.472	0.096	0.199	0.041	0.093	0.014	0.022	0.003	0.007	0.001	0.001	0.000

Figure 70: Numerical results from Dynamic Spool Wave analysis with drag dominated loads

C.2 Study 3: Methods of simulating the sea spectrum

C.2.1 Gumbel plots of extreme ROM for mass dominated load with eigenperiod 9 and 18

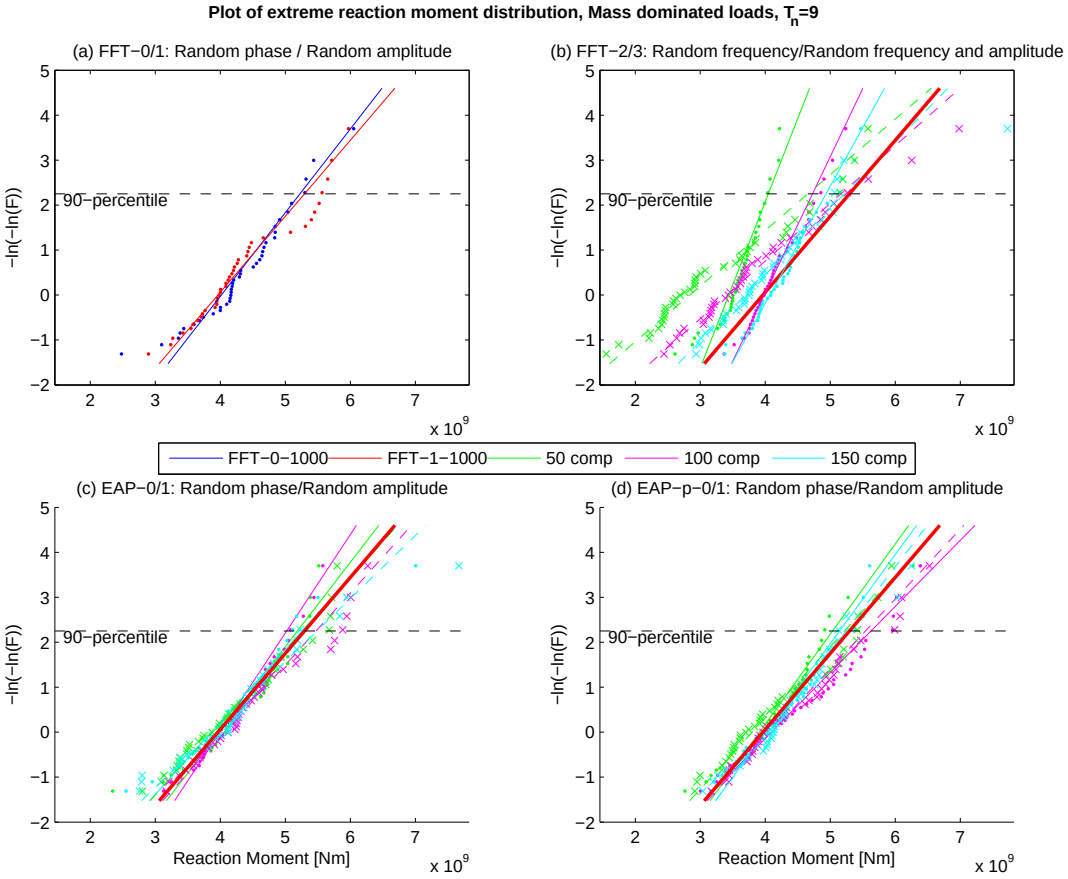

Figure 71: The distributions of extreme reaction moment for mass dominated loads, with $T_n = 9$ sec. Solid lines and dots (.) in Figures (b)-(d) represent the case of deterministic amplitudes, while (x) and dashed lines are from simulations with random amplitudes

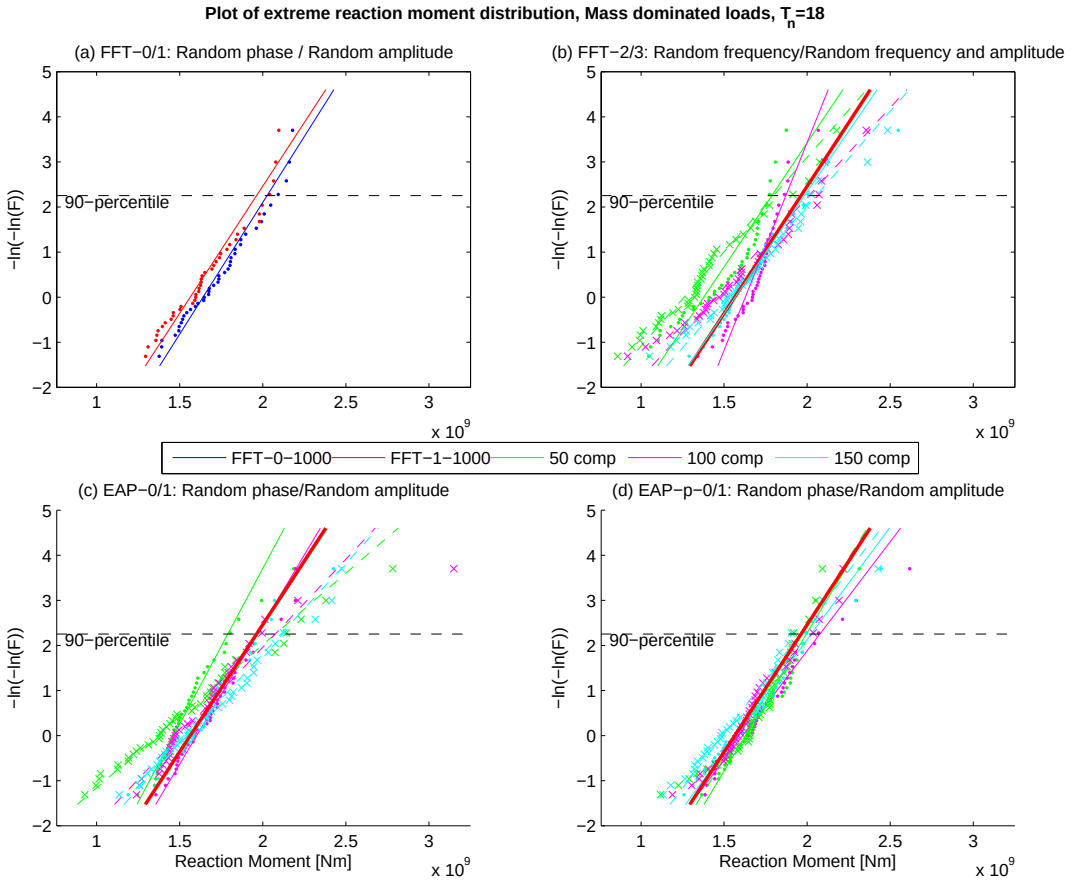

Figure 72: Plot of distributions of extreme reaction moment for mass dominated loads, with $T_n = 18$ sec.Solid lines and dots (.) in Figures (b)-(d) represent the case of deterministic amplitudes, while (x) and dashed lines are from simulations with random amplitudes

C.2.2 Gumbel plots of extreme ROM for drag dominated load with eigenperiod 9 and 18

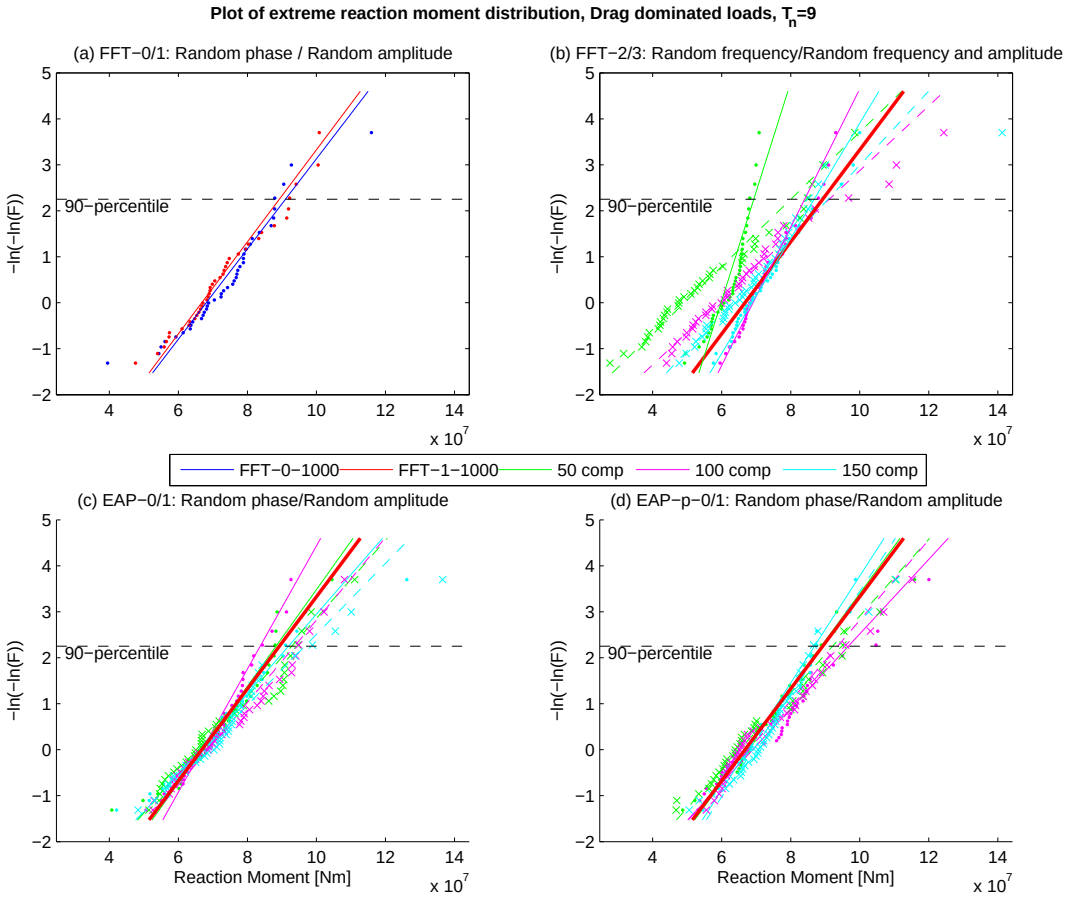

Figure 73: The distributions of extreme reaction moment for drag dominated loads, with $T_n = 9$ sec. Solid lines and dots (.) in Figures (b)-(d) represent the case of deterministic amplitudes, while (x) and dashed lines are from random amplitudes

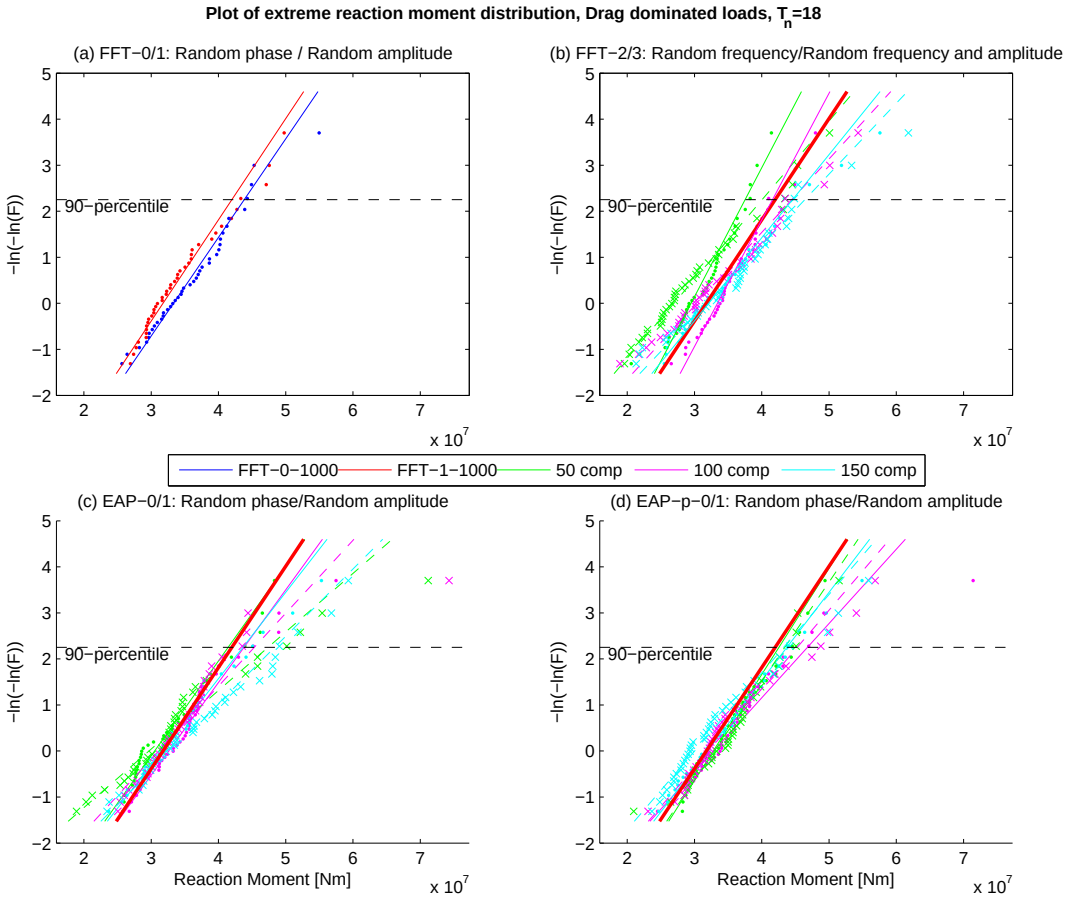

Figure 74: Plot of distributions of extreme reaction moment for drag dominated loads, with $T_n = 18$ sec. Solid lines and dots (.) in Figures (b)-(d) represent the case of deterministic amplitudes, while (x) and dashed lines are from random amplitudes

C.3 Study 4: Wave kinematics and loads

The following Figures are plots of the sea state $H_s/T_p = 14/12$ which were not included in the report. Some general comments regarding these plots are given in Section 7.4.

C.3.1 Kinematics

300 seconds of the time history around the largest peak (largest acceleration is also in this area) is given in Figure 75.

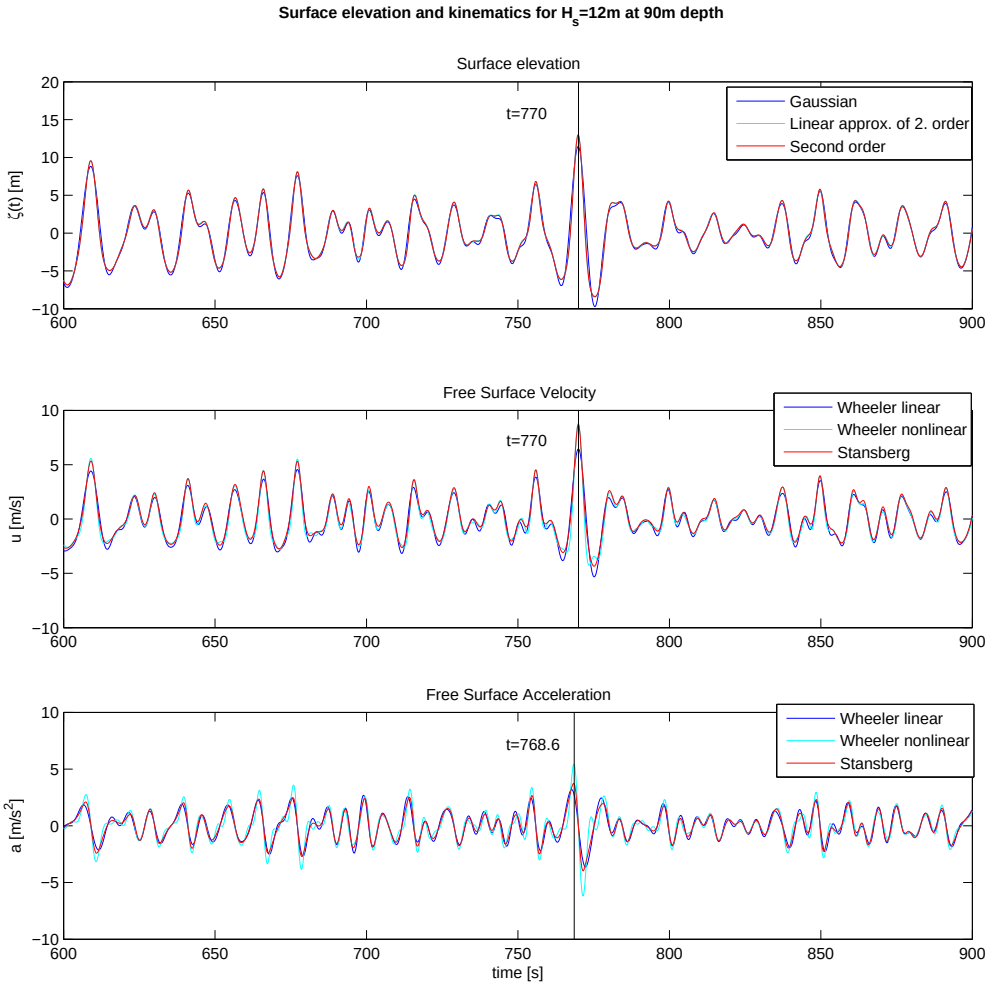

Figure 75: Surface profiles and free surface kinematics from various methods

The profile of the horizontal kinematics over the depth for the time instances marked out in the previous figure is given in Figure 76

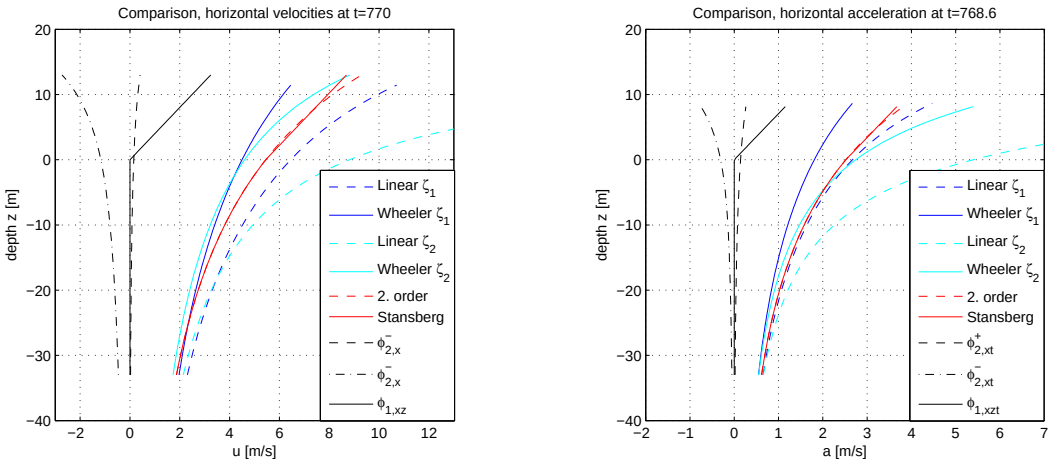

(a) Horizontal velocity profile at t=889.1 s (b) Horizontal acceleration profile at t=889.1 s

Figure 76: Kinematic depth profiles at largest maximum

A Stokes V wave is fitted to the extreme irregular wave profile, and the surface and kinematic profiles at respective maxima are presented in Figure 77.

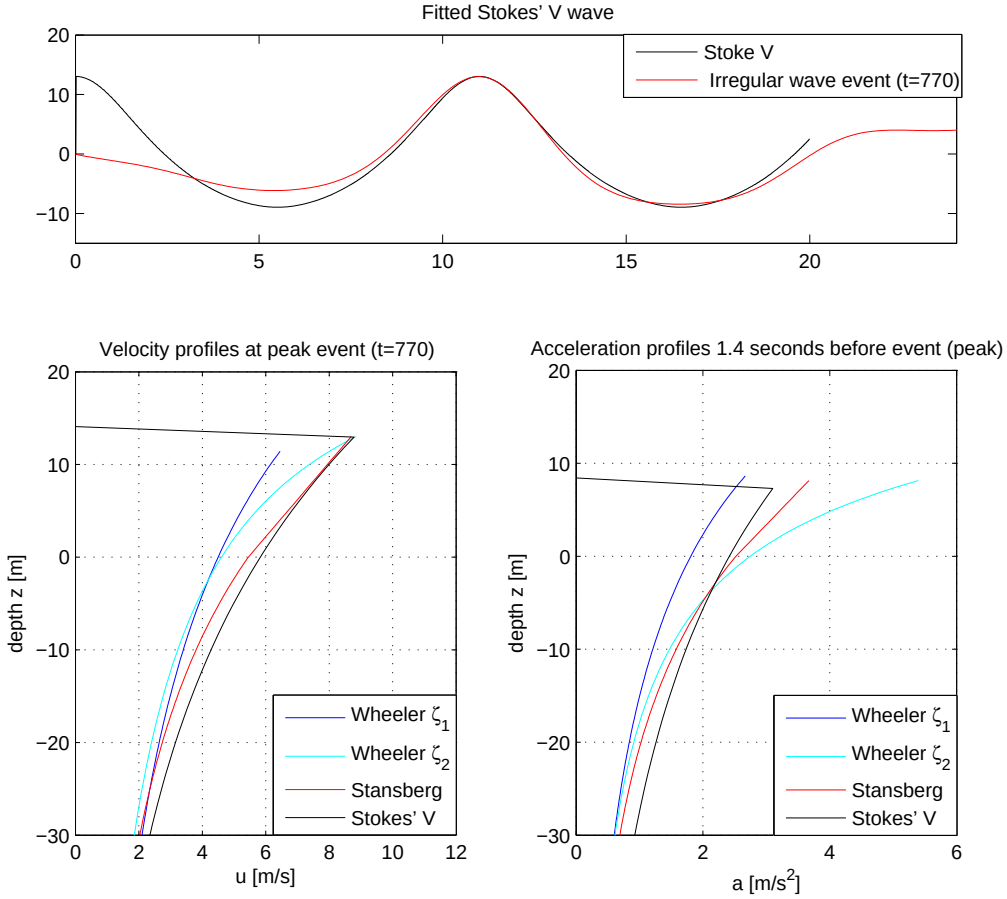

Figure 77: Comparisons with fitted Stokes V wave, H=22m and T=11.3s

C.3.2 Dynamic Reaction Moments

Plots of the dynamic extreme response in terms of overturning moment for the simulation where $H_s = 12m$ are given in the following figures. Note that the extremes occur at the same time as the highest wave for both mass and drag dominated loads, which is not always the case.

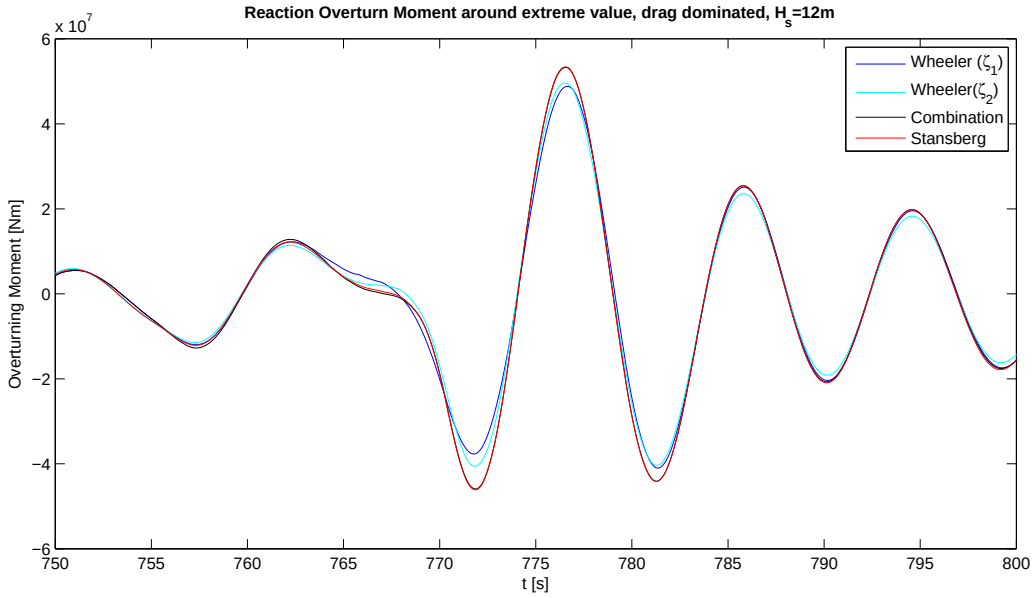

Figure 78: Reaction Overturn Moment around extreme, drag dominated loads

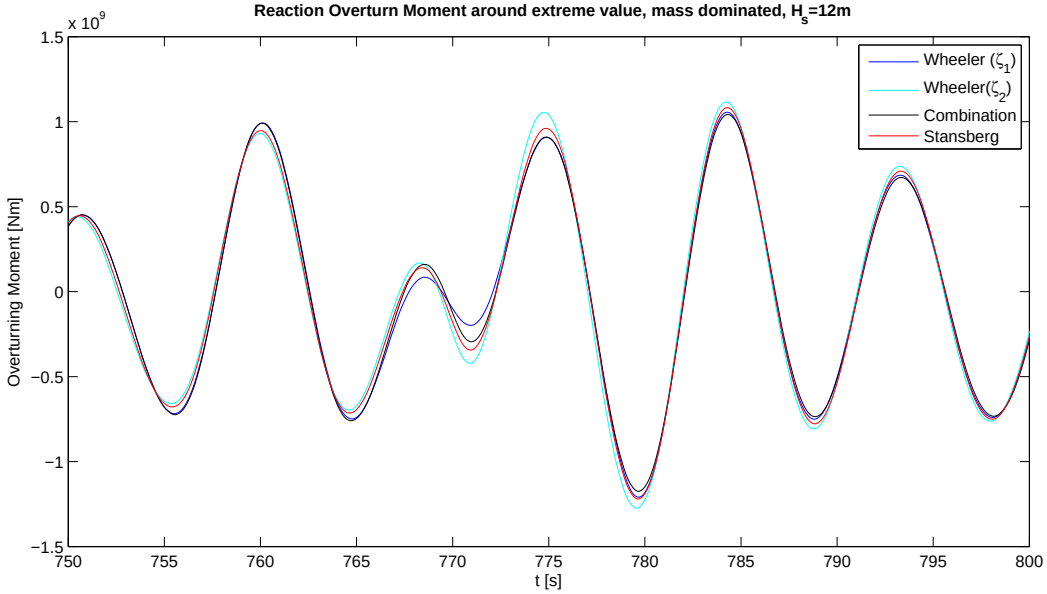

Figure 79: Reaction Overturn Moment around extreme, mass dominated loads